EDARA
European Development And Research Academy

European Development and Research Academy

Journal of Natural and Applied Sciences Ural

Center for Research and Development of Human Resources Ramah- Jordan

ISSN (Print): 2958-8987
ISSN (Online): 2958-8995

Journal of Natural and Applied Sciences URAL

Vol. 2, No. 13, November 2026

A Quarterly Multidisciplinarity Scientific Journal Issued by Center of Research and Human Resources Development Ramah- Jordan and European Development and Research Academy/ Brussels



Editorial Team

Prof. Dr. Ghassan Ezzulddin Arif	**Tikrit University\ College of Education for Pure Science's\ Department of Mathematics.**	**Iraq**	**Editor-in-Chief of the Journal**
Assist. Prof. Baraa Mohammed Ibrahim Al-Hilali	**University of Samarra\ College of Education\ Biology Department**	**Iraq**	**Managing Editor of the Journal**
Asst. Lect. Alyaa Hussein Ashour	**Al-nahrain University College of Medicine**	**Iraq**	**Editorial Secretary of the Journal**

Prof. Dr. Younis A. Rasheed	**Al-Iraqia University, College of Medicine**	**Iraq**
Prof. D. Faeyda Yaseen-ALBadri	**University of Samarra\ College of Education\chemistry Department**	**Iraq**
Assist. Prof. Dr. Hadeer Akram Al-Ani	**Dept. of Public Health Sciences UC Davis School of Medicine**	**USA**
Assist. Prof. Dr. Jawdat Akeel Mohammad Alebraheem	**College of Science Al-Zulfi Majmaah University, Al-Majmaah**	**KSA**
Assist. Prof. Dr. Almbrok Hussin Alsonosi OMAR	**Sebha University**	**Libya**
Assist. Prof. Dr. Saad Sabbar Dahham	**University of Technology and Applied Sciences**	**Sultanate Oman**

Advisory and Scientific Board

Prof. Dr. Ahamed Saied Othman	**Tikrit University**	**Iraq**	**Head**
Prof. Dr. Salih Hamza Abbas	**University of Basrah**	**Iraq**	**Member**
Prof. Dr. Leith A. Majed	**University of Diyala**	**Iraq**	**Member**
Assist. Prof. Dr Ali Fareed Jameel	**Institute of Strategic Industrial Decision Modeling (ISIDM), School of Quantitative Sciences (SQS), University Utara (UUM), 06010 Sintok**	**Malaysia**	**Member**
Assist. Prof. Mustafa Abdullah Theyab	**University of Samarra**	**Iraq**	**Member**
Dr. Modhi Lafta Mutar	**The Open Educational College, Iraqi Ministry of Education, Thi-Qar**	**Iraq**	**Member**
Dr. Asaad Shakir Hameed	**Quality Assurance and Academic Performance Unit, Mazaya University College, Thi-Qar, Iraq.**	**Iraq**	**Member**
Ahmad Mahdi Salih Alaubaydi	**Assist. Lect.; Ph.D Student in the University of Sciences USM, Malaysia**	**Malaysia**	**Member**

Assist. Prof. Dr. Qutaiba Hommadi Mahmood Al.Samarrraie	**University of Samarra/College of Applied Sciences/ Department of Biotechnology**	**Iraq**	**Member**
Ph.D. Ali Mahmood Khalaf	**Gujarat University**	**India**	**Member**
Dr. Amel D. Hussein	**Wasit University**	**Iraq**	**Member**

Focus & Scope:

Journal of Natural and Applied Sciences URAL

Journal welcomes high quality contributions investigating topics in the fields of Biology, physics, computer science, Engineering, chemistry, Geology, Agriculture, Medicine, Mathematics, Pharmacy, Veterinary, Nursing, Dentistry, and Environment.

Publication specializations in the journal	
Biology	**Chemistry**
Physics	**Geology**
Computer	**Agriculture**
Engineering	**Mathematics**
Medicine	**Pharmacy**
Veterinary	**Dentistry Veternity,**
Environment	**Nursing**

The Journal is Published in English and Arabic

General Supervisor of the Journal

Prof. Dr. Khalid Ragheb Ahmed Al-Khatib

Head of the Center for Research and Human

Resources Development Ramah – Jordan

Managing Director:

Dr. Mosaddaq Ameen Ateah AL – Doori

Linguistic Reviewer Team

Prof. Dr. Lamiaa Ahmed Rasheed

Tikrit University/College of Education for Women

Asst. Prof. Ahmed Khalid Hasoon

Tikrit University/ College of Education for Women

Asst. Prof. Dr. Mohammad Burjess

Tikrit University/ College of Education

Administrative Title of the Journal:

Amman\ Jordan\ Wasfi Al-Tal \ Gardens

Phone: +962799424774

Index

No.	Research Title	Researcher	Page No.
.1	The Fractional Delta Atom in a Static Electric Field: Exact Resonance Condition, Polarizability, and Weak-Field Ionization Khalaf M. Al Mufleh Riyadh Schools for Boys and Girls khalafalmufleh@gmail.com	Khalaf M. Al Mufleh	6-24
.2	A Hamiltonian-Inspired Six-Dimensional Extension of the Rössler System: Dynamical Analysis and Evolutionary Parameters Identification .	***Dr. Maysoon M. Aziz , Arqam S. Mahmood***	25-44
.3	An Endpoint-Singularity-Fitted Hybrid Spectral Volterra Method for a Mixed Fractional–Classical Model of Coronary Microvascular Dysfunction	Mohammed Sabah Mahmoud	45-66
.4	An Interface-Consistent hp-Adaptive Spectral Element–Radau IIA Method for Multilayer Dual-Phase-Lag Bioheat Transfer in Clark-II Dynamic Thermography	Almutasim Abdulmuhsin Hamed	67-92
.5	Calculating the Electronic Structure of a Cadmium Telluride Crystal Under High Pressures	Ismael T. Tlayea	93-103
.6	Commuting N − Regular Rings Department of Mathematics College of Computer Sciences and Mathematics	Shahla M. Khalil Shaimaa H.Ahmad Raida D. Mahmood	104-109
7.	A HYBRID FR-HS CONJUGATE GRADIENT METHOD FOR UNCONSTRAINED OPTIMIZATION	Hind H. Mohammed	110-119
8.	Enhanced 4D Hyperchaotic Dynamics via Optimization of Chaotic System Parameters using ICGO	Karam Adel Abed 1, Omar Saber Qasim 2	120-131

9.	Detection of the fungi Aspergillus sp and Candida sp. that cause pneumonia and determining the Dectine2 response against them	Israa. A .Mahmood	132-142
10.	Assessing the Level of Organizational Trust of the Department of Physical Education and Sports Sciences from the Perspective of Faculty Members	Zaid Zuhair Ezzulddin Al-Taiʿ Hussam Ali Ghanim Abdul Kareem	143-154

The Fractional Delta Atom in a Static Electric Field: Exact Resonance Condition, Polarizability, and Weak-Field Ionization

Khalaf M. Al Mufleh
Riyadh Schools for Boys and Girls
khalafalmufleh@gmail.com
ORCID: [https://orcid.org/0009-0001-4178-6674]

The Fractional Delta Atom in a Static Electric Field: Exact Resonance Condition, Polarizability, and Weak-Field Ionization

Khalaf M. Al Mufleh
Riyadh Schools for Boys and Girls
khalafalmufleh@gmail.com
ORCID: [https://orcid.org/0009-0001-4178-6674]

Abstract

We study a particle bound by an attractive delta potential in space-fractional quantum mechanics, with kinetic energy $D_\alpha|p|^\alpha$ $(1 < \alpha \leq 2)$, placed in a uniform static field F. In momentum space the problem reduces to a first-order ODE plus a rank-one term, and it is solved exactly for every α. The Stark resonances are the zeros of a single function built from a "fractional Airy function." We prove that this function has an analytic continuation across the real energy axis for all $1 < \alpha \leq 2$ and that, at weak field, it has exactly one resonance zero near the unperturbed level. A contour-rotated representation makes the exact complex resonance energies computable for fractional α. From the exact condition we obtain two closed-form results. The static polarizability is $\beta = (\alpha+1)(2\alpha+1)\, D_\alpha^{2/\alpha} \kappa^{-1-2/\alpha}/(12\alpha)$, where κ is the binding energy; it is confirmed by two analytic derivations, by the exact complex resonance energies, and by an independent position-space linear-response calculation. The weak-field ionization rate for $1 < \alpha < 2$ follows a power law, $\Gamma \propto F^{2\alpha+1}$, with an explicit prefactor proportional to $\sin^2(\pi\alpha/2)$; it is not exponentially small. The exponential tunneling term, whose exponent $\propto \kappa^{1+1/\alpha}\sin(\pi/\alpha)/F$ agrees with recent semiclassical theory, enters only through a Stokes-smoothed contribution that is exponentially subleading at weak field. The power law comes from the nonlocality of the fractional Laplacian and vanishes at $\alpha = 2$, where the standard exponential law is recovered. Numerically, the exact complex resonance widths agree with the golden-rule formula to 10^{-4} and with the power law to about 2% at the weakest field studied, and an independent position-space calculation (complex absorbing potential and time propagation of the survival probability) reproduces them to within 3%. The numerical verification covers $1.2 \leq \alpha \leq 2$ and $0.01 \leq F \leq 0.1$ in units $\kappa = D_\alpha = 1$; outside this range the results rest on the analytic asymptotics.

Keywords: fractional quantum mechanics; fractional Schrödinger equation; delta potential; Stark effect; polarizability; tunneling ionization; Lévy flights; resonances.

المستخلص :

ندرس جسيمًا مقيّدًا بجهد دلتا جاذب في ميكانيكا الكم الكسرية المكانية، طاقته الحركية D|p|^α حيث 1 < α ≤ 2، وموضوعًا في مجال كهربائي ساكن منتظم F. في فضاء الزخم تُختزل المسألة إلى معادلة تفاضلية من الرتبة الأولى مضافًا إليها حدٌّ من الرتبة الواحدة، وتُحلّ حلًّا دقيقًا لجميع قيم α. رنينات شتارك هي أصفار دالة واحدة مبنية على «دالة إيري كسرية». نبرهن أن هذه الدالة تقبل استمرارًا تحليليًا عبر المحور الحقيقي للطاقة لكل 1 < α ≤ 2، وأن لها في المجال الضعيف صفرًا رنينيًا واحدًا فقط قرب المستوى غير المضطرب، ونقدّم تمثيلًا بتدوير مسار التكامل يتيح حساب طاقات الرنين المركّبة الدقيقة للحالات الكسرية. نحصل على نتيجتين بصيغة مغلقة: الأولى قابلية الاستقطاب الساكنة $\beta = (\alpha+1)(2\alpha+1)\, D^{(2/\alpha)}\, \kappa^{(-1-2/\alpha)} / (12\alpha)$ حيث κ طاقة الربط، وقد تحققنا منها باشتقاقين تحليليين مستقلين، ومن طاقات الرنين المركّبة الدقيقة، وبحساب مستقل للاستجابة الخطية في فضاء الموضع. والثانية معدل التأيّن في المجال الضعيف عندما 1 < α < 2، إذ يتبع قانون قوة $\Gamma \propto F^{(2\alpha+1)}$ بمعامل صريح متناسب مع $\sin^2(\pi\alpha/2)$، فهو ليس صغيرًا صغرًا أسّيًا. أما حدّ النفق الأسّي ذو الأس $\kappa^{(1+1/\alpha)}\, \sin(\pi/\alpha)/F$ المتوافق مع النظرية شبه الكلاسيكية الحديثة، فلا يظهر إلا عبر مساهمة ستوكس المُنعَّمة، وهي مهملة أسّيًا في المجال الضعيف. ينشأ قانون القوة من لاتموضعية اللابلاسي الكسري ويختفي عند α = 2 حيث يُستعاد القانون الأسّي المعروف. عدديًا، تتفق عروض الرنين المركّبة الدقيقة مع صيغة القاعدة الذهبية بدقة $10^{(-4)}$ ومع قانون القوة بدقة 2% عند أضعف مجال مدروس، كما يعيد حسابٌ مستقل في فضاء الموضع (جهد ماصّ مركّب ومحاكاة زمنية لاحتمال البقاء) إنتاجَها ضمن 3%–0.1. يغطي التحقق العددي المدى 1.2 ≤ α ≤ 2 و0.01 ≤ F ≤ 0.1 بوحدات κ = D = 1، وخارج هذا المدى تستند النتائج إلى المفكوكات التقاربية التحليلية.

الكلمات المفتاحية: ميكانيكا الكم الكسرية؛ معادلة شرودنغر الكسرية؛ جهد دلتا؛ تأثير شتارك؛ قابلية الاستقطاب؛ التأيّن بالنفق؛ طيران ليفي؛ الرنينات.

1. Introduction

Space-fractional quantum mechanics replaces the kinetic energy $p^2/2m$ by $D_\alpha|p|^\alpha$, the quantum analogue of replacing Brownian paths by Lévy flights in the path integral [1, 2]. The resulting fractional Laplacian is nonlocal. Its position-space kernel decays only as $|x-y|^{-1-\alpha}$, so a particle can "hop" over long distances in one step. Optical realizations were proposed [3] and have since been demonstrated experimentally [4].

Nonlocality makes exact results scarce and error-prone. Several claimed exact eigenfunctions, such as those for the infinite square well, were later shown to be incorrect because they treated the operator as local [5]. Delta potentials are an exception. Their bound and scattering states are known in closed form

for single and multiple wells and barriers [6–8]. The linear and nonlinear static response of fractional systems has been studied with sum-over-states models [9], but no exact Stark-effect solution is available.

Static-field ionization is an open problem in this setting. Ciappina recently proposed an ADK-type rate whose exponent scales as $I_p^{1+1/\alpha}$ with a factor $\sin(\pi/\alpha)$, obtained from a local imaginary-time action [10]. A natural question is whether long-range Lévy hops, which a local action cannot represent, modify this result.

This paper answers that question exactly for the simplest model, a fractional delta atom in a static field. Our contributions are:

1. An exact resonance condition for all $1 < \alpha \leq 2$, together with a proof that it can be analytically continued to the resonance sheet and that a unique resonance exists at weak field (Section 3).
2. A contour-rotated representation that makes the exact complex resonance energies computable for fractional α (Section 3).
3. A closed-form static polarizability, derived two independent ways and checked independently (Section 5 and Appendix A).
4. A closed-form weak-field ionization rate showing that, for $1 < \alpha < 2$, ionization is dominated by a power law in F, while the exponential tunneling term enters only through a Stokes-smoothed contribution (Section 6).
5. Numerical verification of the main results, including exact complex resonances for fractional α and an independent position-space calculation (Section 7), with an explicit statement of the range that has been verified.

We use units with $\hbar = 1$ throughout.

2. Model and momentum-space formulation

The Hamiltonian is

$$H = D_\alpha |p|^\alpha - g\,\delta(x) + Fx, \qquad 1 < \alpha \leq 2, \quad g > 0, \quad F > 0. \tag{1}$$

We write $K(p) = D_\alpha |p|^\alpha$. At $\alpha = 2$ with $D_2 = 1/(2m)$, H is the ordinary delta atom in a field.

We use the transform pair $\psi(x) = (2\pi)^{-1}\int e^{ipx}\varphi(p)\,dp$, with inner product $\langle\varphi|\chi\rangle = (2\pi)^{-1}\int \varphi^*\chi\,dp$. In this representation the kinetic term is multiplication by $K(p)$; the position operator is $x = i\,d/dp$, so the field term is a first-order derivative; and the delta term becomes the constant $-g\psi(0)$, where $\psi(0) = (2\pi)^{-1}\int \varphi\,dp$. The stationary equation is therefore

$$iF\,\varphi'(p) = \big(E - K(p)\big)\varphi(p) + g\,\psi(0). \tag{2}$$

This is a linear first-order ODE with a constant source. Every nonlocal feature of the fractional Laplacian is carried by the multiplier $K(p)$, and no approximation is needed. The same reduction fails for a generic potential $V(x)$, which becomes an integral operator in momentum space; the delta potential is special because it is rank one.

3. Exact resonance condition

Outgoing solution. Define $\Lambda(p) = D_\alpha \operatorname{sgn}(p)|p|^{\alpha+1}/(\alpha+1)$, so that $\Lambda' = K$, and $S(p) = [Ep - \Lambda(p)]/F$. Under the field, momentum decreases as $dp/dt = -F$, so a decaying state emits amplitude toward $p \to -\infty$ and receives none from $p = +\infty$. The solution of the ODE with this condition is

$$\varphi(p) = \frac{ig\,\psi(0)}{F} \int_p^\infty e^{\,i[S(q)-S(p)]}\, dq. \tag{3}$$

Self-consistency. Inserting this into $\psi(0) = (2\pi)^{-1}\int \varphi\, dp$ and setting $u = q - p$ gives the exact resonance condition

$$1 + g\,G(E) = 0, \qquad G(E) = -\frac{i}{2\pi F}\int_0^\infty d\,u\; e^{iEu/F} J(u), \qquad J(u) = \int_{-\infty}^\infty d\,p\; e^{-i[\Lambda(p+u)-\Lambda(p)]/F}. \tag{4}$$

Here $G(E) = \langle 0|(E - H_0)^{-1}|0\rangle$ is the diagonal Green's function of $H_0 = K + Fx$ at $x = 0$. With $u = Ft$ the integral is the time-domain form $G = -i\int_0^\infty e^{iEt}\,\langle 0\big|e^{-iH_0 t}\big|0\rangle\, dt$, and $J/(2\pi)$ is the free return amplitude in the field.

Spectral form. The eigenfunctions of H_0, normalized to $\delta(\varepsilon - \varepsilon')$, are $\varphi_\varepsilon(p) = F^{-1/2}\exp\{-i[\varepsilon p - \Lambda(p)]/F\}$. Their value at $x = 0$ is $F^{-1/2}A_\alpha(\varepsilon)$, where we define the *fractional Airy function*

$$A_\alpha(\varepsilon) = \frac{1}{2\pi}\int_{-\infty}^\infty e^{\,i[\Lambda(p)-\varepsilon p]/F}\, dp = \frac{1}{\pi}\int_0^\infty \cos\left(\frac{\Lambda(p) - \varepsilon p}{F}\right) dp. \tag{5}$$

It is real because Λ is odd. The local density of states at the origin is $\rho(\varepsilon) = A_\alpha(\varepsilon)^2/F$, and the resonance condition becomes

$$g\,\Sigma(E) = 1, \qquad \Sigma(E) = \int_{-\infty}^\infty \frac{\rho(\varepsilon)\, d\varepsilon}{\varepsilon - E} = -G(E), \tag{6}$$

continued from the upper half-plane to the second sheet (Section 3.1). A root $E = E_r - i\Gamma/2$ gives the Stark-shifted level E_r and the ionization rate Γ.

The case α = 2. Here Λ is a cubic, the p-integral is Gaussian, and

$$J(u) = \sqrt{\frac{\pi F}{iDu}}\; e^{-iDu^3/(12F)}, \qquad A_2(\varepsilon) = \left(\frac{F}{D}\right)^{1/3} \mathrm{Ai}\left(-\frac{\varepsilon}{D^{1/3}F^{2/3}}\right), \tag{7}$$

which reproduces the known Airy-function solution of the ordinary delta atom in a field [11, 12].

Contour-rotated representation for all α. It might seem that $J(u)$ cannot be contour-rotated for $\alpha < 2$ because Λ is not analytic at $p = 0$. In fact it can. For real $u > 0$, split the p-integral in (4) at the two non-analytic points $p = -u$ and $p = 0$. The pieces $p > 0$ and $p < -u$ are equal (substitute $p = -u - s$), and on $-u < p < 0$ we set $p = -uq$. This gives $J(u) = 2J_1(u) + J_2(u)$ with $J_1(u) = \int_0^\infty d\,p \exp\{-iD[(p+u)^{\alpha+1} - p^{\alpha+1}]/\big((\alpha+1)F\big)\}$ and $J_2(u) = u\int_0^1 d\,q \exp\{-iDu^{\alpha+1}h(q)/\big((\alpha+1)F\big)\}$, where $h(q) = (1-q)^{\alpha+1} + q^{\alpha+1}$. Each integrand now contains only principal powers of quantities with positive real part, so both pieces continue analytically into $\arg u < 0$. Rotating u and p together to the ray $\omega = e^{-i\theta}$, $\theta = \pi/[2(\alpha+1)]$, makes $\omega^{\alpha+1} = -i$ and turns every oscillatory exponential into a decaying one:

$$J(s\omega) = \omega\left[2\int_0^\infty d\,r\; e^{-c[(r+s)^{\alpha+1} - r^{\alpha+1}]} + s\int_0^1 d\,q\; e^{-c\,s^{\alpha+1}h(q)}\right], \tag{8}$$

with $c = D_\alpha/[(\alpha+1)F]$, and

$$G(E) = -\frac{i\omega}{2\pi F}\int_0^\infty d\,s\; e^{iE\omega s/F} J(s\omega). \tag{9}$$

Both integrands in (8) are positive and smooth for $s > 0$, and the s-integral in (9) converges absolutely for $\theta < \arg E < \pi + \theta$. This sector contains the negative real axis and the part of the lower half-plane just below it, which is where the resonances lie. At $\alpha = 2$, (8) reproduces (7) on the ray $\arg u = -\pi/6$ to 10^{-14}. The same rotation applied to the half-line form of (5), on the ray $\arg p = +\theta$, gives a rapidly convergent integral for $A_\alpha(\varepsilon)$.

3.1 Convergence, analytic continuation, and existence of the resonance

The following statements put the continuation used above on a firm footing. They hold for every $1 < \alpha \le 2$.

(i) The model is well defined. The quadratic form of $\delta(x)$ is bounded relative to that of K with relative bound zero if and only if $\int dp/(1+|p|^\alpha) < \infty$, that is, if and only if $\alpha > 1$. By the KLMN theorem [13], H is then a well-defined self-adjoint operator. In momentum space, multiplication by $e^{i\Lambda(p)/F}$ is unitary and conjugates $H_0 = K + iF\,d/dp$ into $iF\,d/dp$. Hence H_0 is unitarily equivalent to Fx, and its spectrum is the whole real line and purely absolutely continuous, with the generalized eigenfunctions φ_ε given above. Krein's formula for rank-one perturbations [14],

$$(H-z)^{-1} = (H_0 - z)^{-1} + \frac{g}{1 + g\,G(z)}\,(H_0 - z)^{-1}|\delta\rangle\langle\delta|(H_0 - z)^{-1}, \tag{10}$$

shows that the resonances of H are exactly the zeros of the continuation of $1 + gG(z)$.

(ii) Convergence of (4). As $u \to 0^+$ and $u \to \infty$,

$$J(u) \simeq \frac{2}{\alpha}\,\Gamma\!\left(\frac{1}{\alpha}\right)\left(\frac{F}{iD_\alpha u}\right)^{1/\alpha}, \qquad |J(u)| = O\big(u^{-(\alpha-1)/2}\big). \tag{11}$$

The first follows from $\Lambda(p+u)-\Lambda(p)\simeq uK(p)$. The second is the stationary point $p=-u/2$ of the phase, where its second derivative is $2\alpha D_\alpha(u/2)^{\alpha-1}$. The u-integral in (4) is therefore absolutely convergent for every $\mathrm{Im}E>0$ precisely when $\alpha>1$, the same condition as for the existence of a bound state (Section 4).

(iii) The spectral density is entire. On the ray $\arg p=\theta$ the integrand of the half-line form of (5) is bounded by $\exp\left[-D_\alpha r^{\alpha+1}/\big((\alpha+1)F\big)+|\varepsilon|r/F\right]$. The integral therefore converges uniformly on compact sets of complex ε, so A_α, and with it $\rho=A_\alpha^2/F$, is an entire function that is real on the real axis. Its asymptotics are

$$\rho(\varepsilon)\simeq\frac{1}{\pi\alpha D_\alpha^{1/\alpha}\varepsilon^{1-1/\alpha}}\quad(\varepsilon\to+\infty),\qquad \rho(\varepsilon)=O(F^{2\alpha+1}|\varepsilon|^{-2\alpha-4})\quad(\varepsilon\to-\infty). \tag{12}$$

The first holds up to oscillatory terms; it is the stationary point $K(p)=\varepsilon$, and its mean coincides with the field-free density. The second is the endpoint expansion of Section 6. Hence the integral in (6) converges for every non-real E if and only if $\alpha>1$.

(iv) Continuation to the second sheet. Because ρ is entire, the boundary values $\Sigma(E\pm i0)$ differ by $2\pi i\rho(E)$, and

$$\Sigma_{\mathrm{II}}(E)=\Sigma(E)+2\pi i\,\rho(E),\qquad \mathrm{Im}E<0, \tag{13}$$

is analytic in the whole lower half-plane and joins Σ continuously across the real axis. In the overlap of their domains it coincides with $-G(E)$ computed from (9), which therefore provides the second-sheet function directly. We checked this identity numerically: on the real axis, $\mathrm{Im}G(E+i0)$ from (9) equals $-\pi\rho(E)$ from (5) to better than 10^{-9} in relative terms ($\alpha=1.5,\,1.8,\,2$; $F=0.02,\,0.05$).

(v) Existence and uniqueness of the resonance. Fix $0<r<\kappa_0\sin\theta$, so that the disc $D_r=\{|E+\kappa_0|<r\}$ lies inside the sector of (9). Substituting $s=Ft$ in (9), the integrand is bounded uniformly in F by $e^{-t\,\mathrm{Im}(E\omega)}\left[2\Gamma(1+1/\alpha)(D_\alpha t)^{-1/\alpha}+Ft\right]$, which is integrable because $\alpha>1$. Here we used $(r+s)^{\alpha+1}-r^{\alpha+1}\geq(\alpha+1)s\,r^\alpha$. By dominated convergence, $1+gG_{\mathrm{II}}(E;F)\to 1-g\,c_\alpha(-E)^{1/\alpha-1}$ uniformly on D_r as $F\to 0$. The limit has a simple zero at $E=-\kappa_0$, since its derivative there, $-g\,c_\alpha(1-1/\alpha)\kappa_0^{1/\alpha-2}$, is nonzero. By Hurwitz's theorem, for every sufficiently small F the continued resonance function has exactly one zero $E(F)$ in D_r, and $E(F)\to-\kappa_0$. Because $\mathrm{Im}\Sigma(E)>0$ for $\mathrm{Im}E>0$, there are no zeros in the upper half-plane, so $\Gamma=-2\mathrm{Im}E(F)\geq 0$. Finally, since Σ_{II} is analytic near the real axis, expanding $g\Sigma_{\mathrm{II}}(E)=1$ about E_r gives the narrow-resonance formula (21) below, with relative corrections of order ρ and ρ'.

The constant c_α is defined in (14).

4. Zero-field limit

As $F\to 0$, $\Lambda(p+u)-\Lambda(p)\to uK(p)$, and the u-integral gives $G(E)\to(2\pi)^{-1}\int dp/(E-K)$. With $E=-\kappa<0$, the resonance condition becomes the bound-state condition

$$1 = \frac{g}{\pi}\int_0^\infty \frac{dp}{D_\alpha p^\alpha + \kappa} = g\, c_\alpha\, \kappa^{1/\alpha - 1}, \qquad c_\alpha = \frac{1}{\alpha\, D_\alpha^{1/\alpha}\sin(\pi/\alpha)}. \tag{14}$$

Solving for κ gives the binding energy and ground state

$$\kappa_0 = (g\, c_\alpha)^{\alpha/(\alpha-1)}, \qquad \varphi_0(p) \propto \frac{1}{D_\alpha |p|^\alpha + \kappa_0}, \tag{15}$$

in agreement with [6, 7]. At $\alpha = 2$ and $D = 1/(2m)$ this is the textbook result $\kappa_0 = mg^2/2$.

Two features matter later. First, a bound state exists only for $\alpha > 1$, since the integral diverges otherwise. Second, $\varphi_0(p)$ is not smooth at $p = 0$ when $\alpha < 2$. The cusp $|p|^\alpha$ in momentum space corresponds to a power-law tail $\psi_0(x) \propto |x|^{-1-\alpha}$ in position space, instead of the exponential decay found at $\alpha = 2$. This tail is the fingerprint of Lévy flights.

5. Static polarizability

The level shifts as $E_r = -\kappa_0 - \beta F^2/2 + O(F^4) + O(F^{2\alpha+1})$, with

$$\beta = \frac{(\alpha+1)(2\alpha+1)}{12\,\alpha}\; D_\alpha^{2/\alpha}\, \kappa_0^{-1-2/\alpha}. \tag{16}$$

The non-analytic remainder $O(F^{2\alpha+1})$ is the real-part counterpart of the power-law width of Section 6. It dominates the analytic $O(F^4)$ term when $\alpha < 3/2$. The exact complex roots confirm this: the local exponent of $E_r + \kappa_0 + \beta F^2/2$ at $F \approx 0.005$ is 3.34 for $\alpha = 1.2$ (prediction 3.4) and 4.00 for $\alpha = 1.8$ and 2. At $\alpha = 2$ with $D = 1/(2m)$, the prefactor in (16) is $5/8$ and $\beta = 5/(16m\kappa_0^2) = 5m/(4k_0^4)$, where $k_0 = \sqrt{2m\kappa_0}$. This is the known polarizability of the one-dimensional delta atom. We derive the general result two independent ways. Appendix A gives every intermediate step, so that each can be checked separately.

Derivation 1: Dalgarno–Lewis in the odd sector. The perturbation $V = Fx = iF\, d/dp$ is odd, so the first-order correction φ_1 is odd. An odd function has $\psi_1(0) = 0$, so the delta term drops out of the first-order equation, which becomes algebraic:

$$(K + \kappa_0)\varphi_1 = -iF\,\varphi_0{}' \quad \Rightarrow \quad E_2 = -F^2\,\frac{\int K'^2 (K+\kappa_0)^{-5} dp}{\int (K+\kappa_0)^{-2} dp}. \tag{17}$$

Derivation 2: expansion of the exact condition. Expanding $J(u)$ to order F^2, doing the u-integral, and integrating by parts once gives

$$1 = \frac{g}{2\pi}\int \frac{dp}{K+\kappa} + \frac{gF^2}{2\pi}\int \frac{K'^2\, dp}{(K+\kappa)^5} + O(F^4, F^{2\alpha+1}). \tag{18}$$

The boundary terms vanish because K' is continuous with $K'(0) = 0$ for $\alpha > 1$, and $K'' \propto |p|^{\alpha-2}$ is integrable. Linearizing in $\kappa - \kappa_0$ and using $\int (K+\kappa)^{-2} dp = -\frac{d}{d\kappa}\int (K+\kappa)^{-1} dp$ reproduces E_2 from Derivation 1 exactly.

Closed form. With $p = (\kappa/D_\alpha)^{1/\alpha} s$, both integrals reduce to the standard integral $\int_0^\infty s^{\mu-1}(1+s^\alpha)^{-\nu} ds = \alpha^{-1} B(\mu/\alpha, \nu - \mu/\alpha)$:

$$\frac{\int K'^2 (K+\kappa)^{-5} dp}{\int (K+\kappa)^{-2} dp} = \alpha^2 D_\alpha^{2/\alpha} \kappa^{-1-2/\alpha} \frac{B\left(2-\frac{1}{\alpha}, 3+\frac{1}{\alpha}\right)}{B\left(\frac{1}{\alpha}, 2-\frac{1}{\alpha}\right)} = \alpha^2 D_\alpha^{2/\alpha} \kappa^{-1-2/\alpha} \frac{\Gamma\left(3+\frac{1}{\alpha}\right)}{24\,\Gamma\left(\frac{1}{\alpha}\right)}. \tag{19}$$

The factor $\Gamma(2-1/\alpha)$ cancels between numerator and denominator, and $\Gamma(3+1/\alpha)/\Gamma(1/\alpha) = (2+1/\alpha)(1+1/\alpha)(1/\alpha)$. Then $\beta = -2E_2/F^2$ gives (16).

Independent checks. Table 1 compares the closed form with three independent evaluations: direct quadrature of the Dalgarno–Lewis integrals; the curvature of the exact complex resonance energies of Section 3; and a position-space linear-response calculation that does not use the momentum-space reduction at all (Section 7).

Across $1 < \alpha \leq 2$ the prefactor varies only from 0.50 to 0.625. In natural units, the polarizability is set mainly by the scaling $D^{2/\alpha} \kappa_0^{-1-2/\alpha}$, not by the prefactor.

6. Weak-field ionization rate

For $1 < \alpha < 2$ the weak-field rate is a power law:

$$\Gamma \simeq \frac{2\alpha^2 \sin(\pi/\alpha) \sin^2(\pi\alpha/2)\, \Gamma(\alpha+1)^2}{\pi(\alpha-1)}\; D_\alpha^{2+1/\alpha}\; \frac{F^{2\alpha+1}}{\kappa_0^{2\alpha+2+1/\alpha}}. \tag{20}$$

The rest of this section derives it.

Narrow-resonance formula. When $\rho(\varepsilon)$ is small near E_r, the condition $g\Sigma_{\mathrm{II}}(E) = 1$ can be linearized about the real axis (Section 3.1(v)). Using $\Sigma(E+i0) = P\int \rho/(\varepsilon - E) + i\pi\rho(E)$ gives, to leading order,

$$\Gamma = \frac{2\pi\, \rho(E_r)}{\Sigma'(E_r)} = \frac{2\pi\, A_\alpha(E_r)^2}{F\, c_\alpha (1-1/\alpha)\, \kappa^{1/\alpha - 2}}, \qquad \kappa = -E_r. \tag{21}$$

This is the Fermi golden rule for this model. It is exact in the limit $\Gamma \to 0$. It is checked against exact complex roots for both $\alpha = 2$ and $\alpha < 2$ in Section 7.

Two contributions to $A_\alpha(-\kappa)$. In the classically forbidden region $\varepsilon = -\kappa < 0$, the half-line integral defining A_α has two sources of weak-field asymptotics.

Endpoint at p = 0 (power law). Expanding $\exp\left[iDp^{\alpha+1}/\left((\alpha+1)F\right)\right]$ and integrating term by term against $e^{i\kappa p/F}$, the zeroth term is purely imaginary and drops out of the real part. The first term gives

$$A_\alpha(-\kappa) \simeq \frac{\Gamma(\alpha+1)\sin(\pi\alpha/2)}{\pi}\ D_\alpha\ \frac{F^{\alpha+1}}{\kappa^{\alpha+2}}. \tag{22}$$

The n-th term of the same expansion is of order $F^{n\alpha+1}$, so the relative correction to (22) is $O(F^\alpha)$, with coefficients that grow factorially. This term exists only because $K(p)$ is not analytic at $p=0$. It vanishes identically at $\alpha=2$, where $\sin(\pi\alpha/2)=0$, and inserting it into the narrow-resonance formula gives (20).

Saddle point and Stokes phenomenon (exponential). The phase is stationary where $K(p)=-\kappa$, at $p^* = (\kappa/D)^{1/\alpha}e^{i\pi/\alpha}$, with exponent $i\varphi(p^*) = i\alpha\kappa^{1+1/\alpha}e^{i\pi/\alpha}/\left((\alpha+1)D^{1/\alpha}F\right)$. For $1<\alpha<2$, the steepest-descent path that leaves the endpoint $p=0$ along $\arg p=\pi/2$ bends back into the same valley as the original contour, $0<\arg p<\pi/(\alpha+1)$, without passing through p^*. The saddle is therefore not a separate additive contribution. Its exponential is generated beyond all orders of the endpoint series, and it switches on across the Stokes line $\alpha=2$ (where $\cos(\pi/\alpha)=0$) through Berry's smoothed Stokes multiplier [15]. Combining the Gaussian saddle amplitude with (21) gives the tunneling contribution in the same units as Γ:

$$\Gamma_{\text{tun}} \simeq S_\alpha^2\ \frac{4\alpha\sin(\pi/\alpha)}{\alpha-1}\ \kappa_0 \exp\left[-\frac{2\alpha\sin(\pi/\alpha)}{\alpha+1}\ \frac{\kappa_0^{1+1/\alpha}}{D_\alpha^{1/\alpha}F}\right]. \tag{23}$$

The Stokes multiplier is

$$S_\alpha = 1/2\ \operatorname{erfc}\sigma, \qquad \sigma = |\cos(\pi/\alpha)|\left[\frac{\alpha\,\kappa_0^{1+1/\alpha}}{2(\alpha+1)\sin(\pi/\alpha)\,D_\alpha^{1/\alpha}F}\right]^{1/2}. \tag{24}$$

In (23) an oscillating factor of modulus at most one, $\cos^2\chi$ with $\chi \propto \cos(\pi/\alpha)/F$, has been replaced by its upper bound, so (23) is an envelope. The exponent has the $I_p^{1+1/\alpha}\sin(\pi/\alpha)$ structure found semiclassically in [10]. At $\alpha=2$, $S_2=1/2$ and (23) reduces with $D=1/(2m)$ to $\Gamma = 2\kappa_0\exp(-2k_0^3/3mF)$, the standard weak-field result for the delta atom, which agrees with the exact widths of Table 2 to 10% at $F=0.1$ and 4% at $F=0.05$. For $\alpha=1.99$ and 1.95, at $F=0.05$–0.07, Berry's formula reproduces the remainder of the optimally truncated endpoint series to 0.3–3%. Further from $\alpha=2$, S_α is small and the leading-order smoothing formula is only an order-of-magnitude estimate.

Which one wins. As $F\to 0$, any power of F exceeds $\exp(-\text{const}/F)$, and the factor S_α^2 suppresses the exponential further. So for every $1<\alpha<2$ the power-law channel dominates at weak enough field, and the semiclassical exponential is subleading. Table 4 quantifies this in common units. The power-law regime shrinks as $\alpha\to 2$ because of the $\sin^2(\pi\alpha/2)$ factor, and it disappears at $\alpha=2$. Because the two channels add at the level of amplitudes, the exponential first affects Γ through an interference term of relative size about $2(\Gamma_{\text{tun}}/\Gamma)^{1/2}$.

Physical picture. The $F^{2\alpha+1}$ law has a simple reading. A continuum state at the bound-state energy is localized near the classical turning point $x\approx -\kappa/F$. The bound state's power-law tail gives an overlap

there of order $|\psi_0(-\kappa/F)|^2 \propto (F/\kappa)^{2+2\alpha}$, and the continuum normalization supplies a further factor $1/F$. The particle does not tunnel through the barrier; it reaches the far side in a single Lévy hop. This is precisely the nonlocal effect that a local WKB action cannot capture.

7. Numerical verification

Every analytic result agrees with direct computation, apart from the Stokes-smoothed term (23), which is tested quantitatively only near $\alpha = 2$. The agreement improves as $F \to 0$, where the formulas are asymptotic. We use $D_\alpha = 1$ and choose $g = 1/c_\alpha$ so that $\kappa_0 = 1$; fields are therefore in units of $\kappa_0^{1+1/\alpha} D_\alpha^{-1/\alpha}$. Three independent numerical routes are used:

- **(A) Momentum-space quadrature.** A_α and the Dalgarno–Lewis integrals are computed by adaptive quadrature. This was done in mpmath at 30–50 significant digits and repeated independently in double precision with SciPy.
- **(B) Exact complex resonances.** Roots of $1 + gG(E) = 0$ are found with the rotated representation (8)–(9). The integrals use double-exponential (tanh–sinh and exp–sinh) quadrature, with the inner integration split at $r = s$, and the roots use a complex secant iteration. Halving the quadrature step changes the widths by less than 10^{-15} in absolute terms. This sets the resolution limit of this route: widths below about $10^{-15}\kappa_0$ cannot be resolved in double precision. The $\alpha = 2$ widths at $F \le 0.04$ in Table 2 therefore come from the 30–50-digit calculation of route (A). Route (B) reproduces the $F = 0.05$ and 0.1 rows to the digits shown.
- **(C) Independent position-space calculation.** This route does not use the momentum-space reduction. H is discretized on a uniform grid ($\Delta x = 0.1$; $x \in [-X_L, 60]$ with $X_L = \max(300, 12/F)$). The fractional kinetic operator is applied spectrally, which is exact for $|k| < \pi/\Delta x$, and the delta is a single-site potential whose strength is tuned so that the lattice bound state has $\kappa_0 = 1$ exactly. For the polarizability we solve the linear-response equation $(H_0 - E_0)\phi_1 = -Q\,x\,\psi_0$ (with $Q = 1 - |\psi_0\rangle\langle\psi_0|$) by preconditioned conjugate gradients and evaluate $\beta = 2\langle\psi_0|x\,Q\,(H_0 - E_0)^{-1} Q\,x|\psi_0\rangle$. For the resonances we add a complex absorbing potential (CAP) $-i\eta W(x)$, with $W = [(x_c - x)/(x_c + X_L)]^2$ for $x < x_c = -\max(60, 2/F)$ [16]. We find the complex eigenvalue near -1 by inverse iteration, and verify that it is stationary in η (to $< 10^{-3}$ for $\eta = 0.5$–1). Independently, we propagate the field-free ground state in time with a Crank–Nicolson scheme, and extract the decay rate of the survival probability $P(t) = |\langle\psi_0|\psi(t)\rangle|^2$ by a fit to $\ln P$ at late times.

Zero field. The bound-state condition $g\,c_\alpha \kappa_0^{1/\alpha - 1} = 1$, evaluated by direct quadrature at $\alpha = 1.5$, gives $1 - 6 \times 10^{-18}$.

Table 1. Polarizability prefactor β ($\kappa_0 = D = 1$): closed form (16) versus three independent evaluations — direct quadrature of the Dalgarno–Lewis integrals (17); $-2\lim(E_r + 1)/F^2$ fitted to exact complex resonance energies at $0.004 \le F \le 0.02$; and the position-space linear-response calculation (route C; $\Delta x = 0.0125$, box length 3200).

α	Closed form (α+1)(2α+1)/(12α)	Dalgarno–Lewis quadrature	Exact complex roots	Position-space lattice
1.2	0.519444444	0.519444444	0.519420	0.519715

α	Closed form (α+1)(2α+1)/(12α)	Dalgarno–Lewis quadrature	Exact complex roots	Position-space lattice
1.5	0.555555556	0.555555556	0.555593	0.555562
1.8	0.596296296	0.596296296	0.596297	0.596296
2.0	0.625000000	0.625000000	0.625000	0.625000

The position-space values converge monotonically to the closed form as the grid is refined. For $\alpha = 1.5$ the deviation falls from 2.5×10^{-3} at $\Delta x = 0.2$ to 1.2×10^{-5} at $\Delta x = 0.0125$; for $\alpha = 1.2$ it is still 5×10^{-4} at the finest grid. Convergence is slowest at $\alpha = 1.2$, where the lattice momentum cutoff matters most because $K(p)$ grows slowly.

Table 2. Exact resonances at $\alpha = 2$: complex roots of $1 + gG(E) = 0$, found with the rotated-contour integral (the widths at $F \leq 0.04$ from the 30–50-digit calculation of route A; see Section 7), compared with the perturbative shift $-\kappa_0 - \beta F^2/2$ and the golden-rule width evaluated at the exact E_r.

F	E_r exact	E_r from β	Γ exact	Γ golden rule	Ratio
0.03	−1.00028195	−1.00028125	9.7258×10^{-20}	9.7355×10^{-20}	1.0010
0.04	−1.00050224	−1.00050000	6.4503×10^{-15}	6.4617×10^{-15}	1.0018
0.05	−1.00078679	−1.00078125	5.0228×10^{-12}	5.0368×10^{-12}	1.0028
0.10	−1.00322590	−1.00312500	2.9533×10^{-6}	2.9880×10^{-6}	1.0117

The level shift differs from $-\beta F^2/2$ by an amount of order F^4, as expected at $\alpha = 2$. The golden-rule width converges to the exact width, with a relative error that falls roughly as F^2, which validates the narrow-resonance formula. As a separate check, the numerically computed A_2 matches the Airy-function form to 30 digits.

Table 3. Exact complex resonances for fractional α ($\kappa_0 = D = 1$), computed from the rotated representation (8)–(9), compared with the perturbative level $-\kappa_0 - \beta F^2/2$ and with the golden-rule width (21) evaluated at the exact E_r.

α	F	E_r exact	E_r from β	Γ exact	Γ golden rule	Ratio
1.2	0.01	−1.00002610	−1.00002597	4.067×10^{-7}	4.068×10^{-7}	0.9999
1.2	0.02	−1.00010512	−1.00010389	4.391×10^{-6}	4.392×10^{-6}	0.9996
1.2	0.05	−1.00066866	−1.00064931	1.040×10^{-4}	1.042×10^{-4}	0.9974
1.2	0.10	−1.00265363	−1.00259722	1.075×10^{-3}	1.086×10^{-3}	0.9902
1.5	0.01	−1.00002782	−1.00002778	2.237×10^{-8}	2.237×10^{-8}	0.9999
1.5	0.02	−1.00011165	−1.00011111	3.715×10^{-7}	3.717×10^{-7}	0.9996
1.5	0.05	−1.00071169	−1.00069444	1.723×10^{-5}	1.727×10^{-5}	0.9973
1.5	0.10	−1.00298474	−1.00277778	3.717×10^{-4}	3.760×10^{-4}	0.9887
1.8	0.01	−1.00002983	−1.00002981	4.353×10^{-10}	4.354×10^{-10}	0.9999
1.8	0.02	−1.00011946	−1.00011926	1.089×10^{-8}	1.090×10^{-8}	0.9996
1.8	0.05	−1.00075348	−1.00074537	9.249×10^{-7}	9.274×10^{-7}	0.9973

α	F	E_r exact	E_r from β	Γ exact	Γ golden rule	Ratio
1.8	0.10	−1.00312808	−1.00298148	5.679×10^{-5}	5.746×10^{-5}	0.9884

The golden-rule formula (21) converges to the exact width at the same rate, roughly F^2, as at $\alpha = 2$, reaching 10^{-4} at $F = 0.01$. The level shift agrees with $-\beta F^2/2$ up to the $O(F^4) + O(F^{2\alpha+1})$ remainder of Section 5.

Table 4. Ionization widths for $\alpha < 2$ in common units ($\kappa_0 = D = 1$; all columns are rates with the dimension of energy). Γ_{exact} is the exact complex root; Γ_{PL} is the power law (20); Γ_{tun} is the tunneling contribution (23), including its prefactor and Stokes multiplier S_α.

α	F	Γ exact	Γ power law (20)	Γ exact / Γ power law	Stokes factor S	Γ tunnel (23)	Γ tunnel / Γ exact
1.5	0.01	2.237×10^{-8}	2.192×10^{-8}	1.020	1.6×10^{-5}	1.9×10^{-54}	9×10^{-47}
1.5	0.02	3.715×10^{-7}	3.507×10^{-7}	1.059	1.6×10^{-3}	7.5×10^{-28}	2×10^{-21}
1.5	0.05	1.723×10^{-5}	1.370×10^{-5}	1.257	0.031	9.6×10^{-12}	6×10^{-7}
1.5	0.10	3.717×10^{-4}	2.192×10^{-4}	1.696	0.094	2.8×10^{-6}	8×10^{-3}
1.8	0.01	4.353×10^{-10}	4.300×10^{-10}	1.012	0.080	5.9×10^{-57}	1×10^{-47}
1.8	0.02	1.089×10^{-8}	1.043×10^{-8}	1.045	0.161	7.3×10^{-29}	7×10^{-21}
1.8	0.05	9.249×10^{-7}	7.059×10^{-7}	1.310	0.265	6.3×10^{-12}	7×10^{-6}
1.8	0.10	5.679×10^{-5}	1.712×10^{-5}	3.318	0.329	3.0×10^{-6}	5×10^{-2}
1.95	0.01	9.149×10^{-12}	9.069×10^{-12}	1.009	0.372	4.8×10^{-58}	5×10^{-47}
1.95	0.02	2.803×10^{-10}	2.708×10^{-10}	1.035	0.408	2.8×10^{-29}	1×10^{-19}
1.95	0.05	3.193×10^{-8}	2.413×10^{-8}	1.323	0.442	5.4×10^{-12}	2×10^{-4}
1.95	0.10	9.069×10^{-6}	7.204×10^{-7}	12.589	0.459	3.2×10^{-6}	3×10^{-1}

The ratio of the exact width to the power law approaches 1 as F decreases, confirming (20) and its prefactor with exact resonance widths rather than the golden rule alone. At $F = 0.01$ the tunneling contribution, expressed as a rate with its prefactor, is smaller than the exact width by 46–47 orders of magnitude for $\alpha = 1.5$ and 1.8. The larger ratios at $F = 0.1$ come mainly from the higher-order endpoint terms (relative size $O(F^\alpha)$ with large coefficients) and, near $\alpha = 2$, from the growing Stokes-smoothed exponential. At $\alpha = 1.95$ and $F = 0.1$, Γ_{tun} exceeds the power law itself. This is the shrinking of the power-law regime as $\alpha \to 2$.

Table 5. Independent position-space check (route C: lattice with complex absorbing potential, $\Delta x = 0.1$, $\eta = 1$) against the exact complex roots of route B ($\kappa_0 = D = 1$).

α	F	E_r exact	E_r CAP	Γ exact	Γ CAP	Deviation in Γ
1.2	0.02	−1.0001051	−1.0001058	4.391×10^{-6}	4.512×10^{-6}	+2.76%
1.2	0.05	−1.0006687	−1.0006730	1.040×10^{-4}	1.057×10^{-4}	+1.65%
1.2	0.10	−1.0026536	−1.0026707	1.075×10^{-3}	1.084×10^{-3}	+0.85%
1.5	0.02	−1.0001116	−1.0001117	3.715×10^{-7}	3.751×10^{-7}	+0.97%
1.5	0.05	−1.0007117	−1.0007122	1.723×10^{-5}	1.730×10^{-5}	+0.42%
1.5	0.10	−1.0029847	−1.0029866	3.717×10^{-4}	3.721×10^{-4}	+0.11%
1.8	0.02	−1.0001195	−1.0001195	1.089×10^{-8}	1.094×10^{-8}	+0.43%
1.8	0.05	−1.0007535	−1.0007535	9.249×10^{-7}	9.262×10^{-7}	+0.14%
1.8	0.10	−1.0031281	−1.0031283	5.679×10^{-5}	5.680×10^{-5}	+0.02%
2.0	0.05	−1.0007868	−1.0007868	5.023×10^{-12}	5.029×10^{-12}	+0.13%
2.0	0.10	−1.0032259	−1.0032259	2.953×10^{-6}	2.953×10^{-6}	+0.00%

The deviations are positive and shrink under grid refinement. For example, at $\alpha = 1.5$, $F = 0.05$ they are $+0.60\%$, $+0.42\%$ and $+0.37\%$ for $\Delta x = 0.2$, 0.1 and 0.05. They are largest at $\alpha = 1.2$, for the same cutoff reason as in Table 1. The time-dependent check uses the same lattice Hamiltonian as the CAP calculation, so it tests a different property: whether the decay of the survival probability is a single exponential governed by the resonance pole. Fitting $\ln P(t)$ at late times ($t > 0.3\, t_{\max}$) for $F = 0.1$ yields decay rates 1.084×10^{-3}, 3.721×10^{-4} and 5.680×10^{-5} for $\alpha = 1.2$, 1.5 and 1.8, identical to the lattice CAP widths to all digits shown and within 0.9% of the exact widths 1.075×10^{-3}, 3.717×10^{-4} and 5.679×10^{-5}. The survival probability is a single exponential over three e-foldings (Fig. 2), with initial overlap $|\langle \psi_0 | \psi_{\text{res}} \rangle|^2 > 0.997$ for $\alpha = 1.5$ and 1.8.

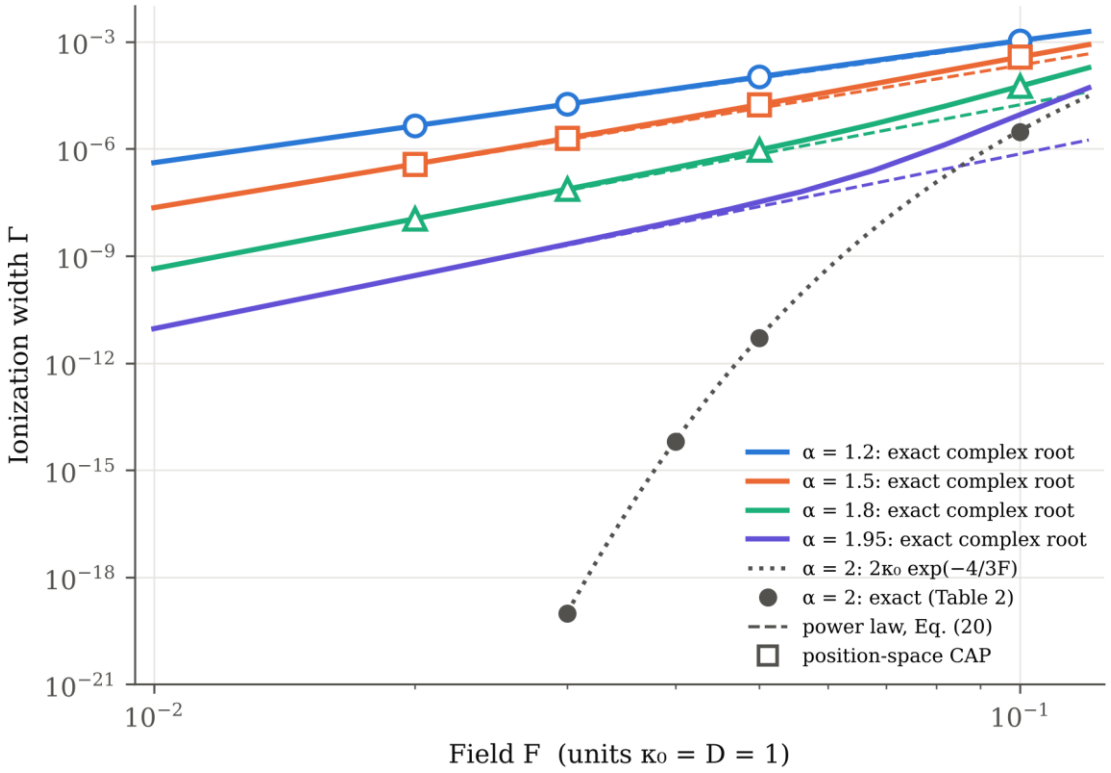


Figure 1. *Weak-field ionization widths. Solid lines: exact complex roots (route B) for* $\alpha = 1.2, 1.5, 1.8$ *and* 1.95. *Dashed lines: power law (20) in the same color. Open symbols: independent position-space CAP calculation (route C). Gray:* $\alpha = 2$, *exact widths (Table 2, dots) and the standard result* $2\kappa_0 e^{-4/(3F)}$ *(dotted). Units* $\kappa_0 = D = 1$.

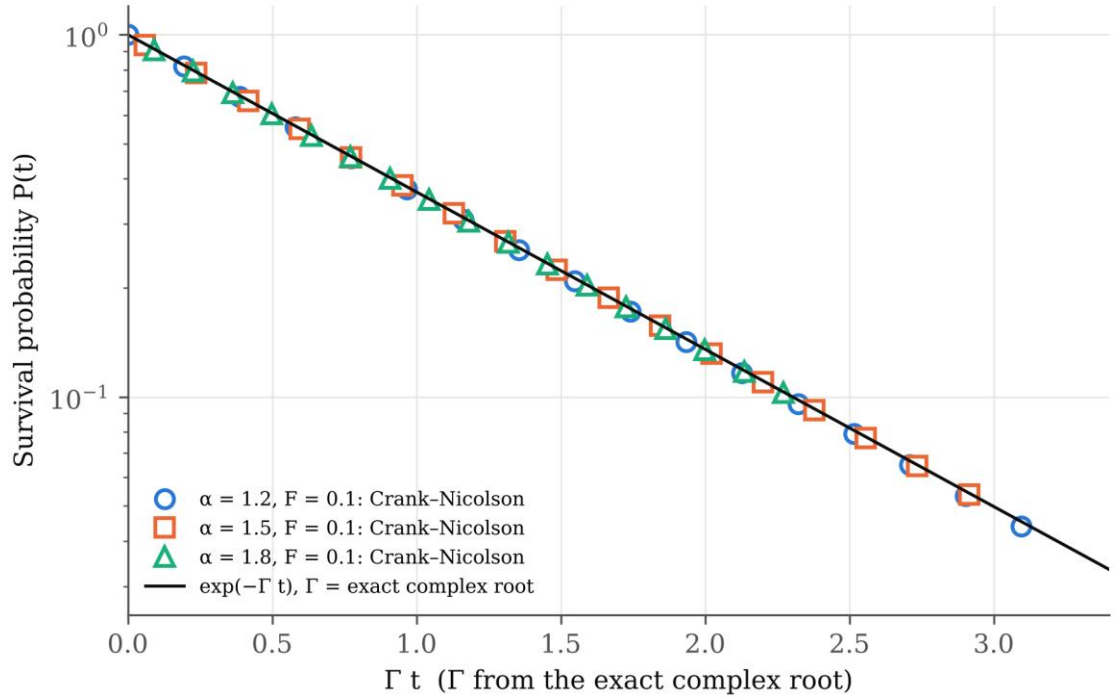


Figure 2. *Survival probability of the field-free ground state after the field is switched on at* $t = 0$*, from Crank–Nicolson time propagation in position space (*$F = 0.1$*). Time is scaled by the exact width Γ from route B. All three cases collapse onto* $e^{-\Gamma t}$ *(black line).*

Scope and limits of the verification. The numerical checks cover $1.2 \leq \alpha \leq 2$ and $0.01 \leq F \leq 0.1$ for the widths, and $0.004 \leq F \leq 0.1$ for the level shifts (units $\kappa_0 = D_\alpha = 1$). The weak-field formulas (16), (20) and (23) are asymptotic statements; outside this window they rest on the analytic derivations alone. In particular, the regime $\alpha \to 1^+$, where κ_0 and the prefactor of (20) become singular, has not been tested numerically. Route (B) is limited to widths above about $10^{-15}\kappa_0$. Route (C) carries lattice-cutoff and finite-box errors of up to 3%, which decrease under refinement. The Stokes-smoothed exponential (23) is tested quantitatively only for $1.95 \leq \alpha < 2$; for smaller α it is an order-of-magnitude estimate. Its role in our conclusions is limited to showing that it is negligible at weak field.

8. Discussion and conclusions

The fractional delta atom in a static field is exactly solvable for every $1 < \alpha \leq 2$. The resonance function can be continued analytically to the second sheet, and at weak field it has a unique resonance zero. A rotation of the integration contour makes the exact complex resonance energies computable for fractional α. The polarizability takes a strikingly simple closed form, confirmed by two analytic derivations, by the exact complex resonances, and by an independent position-space calculation. The weak-field ionization rate behaves qualitatively differently from ordinary quantum mechanics: it is a power law $F^{2\alpha+1}$, not an exponential. This is established by exact complex resonance energies and by an independent position-space calculation, and not only by the golden rule. The exponential tunneling term predicted semiclassically [10] has the predicted $I_p^{1+1/\alpha}\sin(\pi/\alpha)$ structure, but for $\alpha < 2$ it enters only through a Stokes-smoothed contribution that is subleading at weak field.

Generality. The power law comes from the cusp of $K(p)$ at $p = 0$, equivalently from the $|x|^{-1-\alpha}$ tail of the bound state. Bound states of any short-range potential in fractional quantum mechanics are expected to share this tail. We therefore conjecture that $F^{2\alpha+1}$ ionization is generic for $1 < \alpha < 2$, with only the prefactor depending on the potential. If so, ADK-type formulas for fractional systems need a nonlocal, non-exponential term at weak field.

Relation to [10]. The semiclassical treatment of [10] and the present exact result describe different channels. Numerical tests at moderate fields, where the two channels compete, need not conflict with our weak-field result; for α close to 2 and $F \approx 0.1$ the exponential channel is in fact comparable to the power law (Table 4). Our position-space time propagation (Fig. 2) is the type of survival-probability test proposed in [10]. A direct comparison at matched parameters is an important next step.

Limitations. The analytic continuation and the existence of the resonance are proven here for the delta model (Section 3.1); for other short-range potentials, which are not rank one, they remain to be established. The narrow-resonance and power-law formulas are asymptotic, and their numerical verification is restricted to the window stated at the end of Section 7. The saddle-point term for $\alpha < 2$ is described by the leading-order Stokes-smoothing formula (23), which we have tested quantitatively only near $\alpha = 2$. Finally, the physical interpretation of space-fractional quantum mechanics has itself been debated [17, 18]; our results are statements about the Laskin model as defined.

Outlook. The $F^{2\alpha+1}$ scaling and the α-dependence of β are concrete, testable predictions. They could be probed in optical realizations of the fractional Schrödinger equation [3, 4], where a linear potential corresponds to a tilt of the beam.

Data availability. The scripts used for all numerical results (routes A–C) are available from the author on request.

Appendix A. Step-by-step derivation of the polarizability, Eq. (16)

We list the steps of Derivation 1 so that each can be verified independently. Units: $\kappa \equiv \kappa_0$, general $D \equiv D_\alpha$.

A1. Zeroth order. $\varphi_0 = (K + \kappa)^{-1}$ solves $(K + \kappa)\varphi_0 = g\psi_0(0)$ with $\psi_0(0)$ fixed by (14). It is even, and $\varphi_0{}' = -K'(K + \kappa)^{-2}$ is odd and continuous, because $K'(p) = \alpha D\,\mathrm{sgn}(p)|p|^{\alpha-1} \to 0$ at $p = 0$ for $\alpha > 1$.

A2. First order. The first-order equation is $\left(H_0^{(F=0)} - E_0\right)\varphi_1 = -(V - E_1)\varphi_0$ with $E_1 = \langle\varphi_0|V|\varphi_0\rangle = 0$ by parity. Since $V\varphi_0 = iF\varphi_0{}'$ is odd, we seek an odd φ_1. Then $\psi_1(0) = (2\pi)^{-1}\int \varphi_1 dp = 0$ and the delta term does not act, so $(K + \kappa)\varphi_1 = -iF\varphi_0{}'$. This gives $\varphi_1 = iF\,K'(K + \kappa)^{-3}$.

A3. Second order. $E_2 = \langle\varphi_0|V|\varphi_1\rangle/\langle\varphi_0|\varphi_0\rangle$. Integrating by parts once (the boundary terms vanish at $\pm\infty$, and there is no jump at $p = 0$ because $\varphi_0\varphi_1$ is continuous) gives $\int \varphi_0\, iF\varphi_1{}' dp = -iF\int \varphi_0{}'\varphi_1\, dp = -F^2\int K'^2(K + \kappa)^{-5}dp$, which is (17).

A4. Reduction. With $p = (\kappa/D)^{1/\alpha}s$: $K = \kappa s^\alpha$, $K' = \alpha\kappa^{1-1/\alpha}D^{1/\alpha}s^{\alpha-1}$ and $dp = (\kappa/D)^{1/\alpha}ds$. Hence

$$\int_{-\infty}^{\infty}\frac{dp}{(K+\kappa)^2}=\frac{2}{\alpha}\left(\frac{\kappa}{D}\right)^{1/\alpha}\kappa^{-2}\,B(1/\alpha\,,2-1/\alpha),\qquad \int_{-\infty}^{\infty}\frac{K'^2\,dp}{(K+\kappa)^5}=2\alpha\left(\frac{\kappa}{D}\right)^{1/\alpha}\kappa^{-3-2/\alpha}D^{2/\alpha}\,B(2-1/\alpha\,,3+1/\alpha),\tag{25}$$

using $\mu=1,\nu=2$ and $\mu=2\alpha-1,\nu=5$ in the integral quoted before (19).

A5. Result. Taking the ratio, $B(2-1/\alpha\,,3+1/\alpha)/B(1/\alpha\,,2-1/\alpha)=\Gamma(3+1/\alpha)/[24\,\Gamma(1/\alpha)]=(2\alpha+1)(\alpha+1)/(24\alpha^3)$. Therefore $E_2=-F^2(\alpha+1)(2\alpha+1)D^{2/\alpha}\kappa^{-1-2/\alpha}/(24\alpha)$ and $\beta=-2E_2/F^2$, which is (16).

A6. Derivation 2 in detail. With $u=Ft$ and $\Lambda(p+Ft)-\Lambda(p)=F[tK+1/2\,Ft^2K'+1/6\,F^2t^3K'']+\cdots$, expanding the exponential to $O(F^2)$ and using $\int_0^\infty t^n\,e^{i(E-K)t}dt=n!\;i^{n+1}(E-K)^{-n-1}$ ($\mathrm{Im}E>0$) gives $G=G_0+F^2G_2$, where the $O(F)$ term is odd in p and vanishes. Explicitly $G_2=-(2\pi)^{-1}\int[K''(E-K)^{-4}+3K'^2(E-K)^{-5}]dp$. Integrating the K'' term by parts gives $-4\int K'^2(E-K)^{-5}dp$, so $G_2=(2\pi)^{-1}\int K'^2(E-K)^{-5}dp$. At $E=-\kappa$ this is (18). Higher orders involve $K'''\propto|p|^{\alpha-3}$, which is not integrable at $p=0$ for $\alpha<2$; this is the origin of the non-analytic $O(F^{2\alpha+1})$ remainder.

References:

1. N. Laskin, "Fractional quantum mechanics," *Phys. Rev. E* **62**, 3135 (2000).
2. N. Laskin, "Fractional Schrödinger equation," *Phys. Rev. E* **66**, 056108 (2002).
3. S. Longhi, "Fractional Schrödinger equation in optics," *Opt. Lett.* **40**, 1117 (2015). https://doi.org/10.1364/OL.40.001117
4. S. Liu, Y. Zhang, B. A. Malomed and E. Karimi, "Experimental realisations of the fractional Schrödinger equation in the temporal domain," *Nat. Commun.* **14**, 222 (2023). https://doi.org/10.1038/s41467-023-35892-8
5. M. Jeng, S.-L.-Y. Xu, E. Hawkins and J. M. Schwarz, "On the nonlocality of the fractional Schrödinger equation," *J. Math. Phys.* **51**, 062102 (2010).
6. E. C. de Oliveira, F. S. Costa and J. Vaz Jr., "The fractional Schrödinger equation for delta potentials," *J. Math. Phys.* **51**, 123517 (2010).
7. J. D. Tare and J. P. H. Esguerra, "Bound states for multiple Dirac-δ wells in space-fractional quantum mechanics," *J. Math. Phys.* **55**, 012106 (2014). https://doi.org/10.1063/1.4861933
8. J. D. Tare and J. P. H. Esguerra, "Transmission through locally periodic potentials in space-fractional quantum mechanics," *Physica A* **407**, 43–53 (2014). https://doi.org/10.1016/j.physa.2014.03.084
9. N. J. Dawson, "Static hyperpolarizability of space-fractional quantum systems," *J. Opt. Soc. Am. B* **33**, E24–E30 (2016). https://doi.org/10.1364/JOSAB.33.000E24
10. M. F. Ciappina, "Static-field tunneling ionization in space-fractional quantum mechanics," arXiv:2605.05617 [quant-ph] (2026).
11. W. Elberfeld and M. Kleber, "Tunneling from an ultrathin quantum well in a strong electrostatic field: A comparison of different methods," *Z. Phys. B* **73**, 23–32 (1988). https://doi.org/10.1007/BF01312151

12. L. D. Landau and E. M. Lifshitz, *Quantum Mechanics: Non-Relativistic Theory*, 3rd ed. (Pergamon, Oxford, 1977), §§24 and 77.
13. M. Reed and B. Simon, *Methods of Modern Mathematical Physics II: Fourier Analysis, Self-Adjointness* (Academic Press, New York, 1975), Theorem X.17.
14. S. Albeverio, F. Gesztesy, R. Høegh-Krohn and H. Holden, *Solvable Models in Quantum Mechanics*, 2nd ed. (AMS Chelsea Publishing, Providence, 2005).
15. M. V. Berry, "Uniform asymptotic smoothing of Stokes's discontinuities," *Proc. R. Soc. Lond. A* **422**, 7–21 (1989).
16. U. V. Riss and H.-D. Meyer, "Calculation of resonance energies and widths using the complex absorbing potential method," *J. Phys. B* **26**, 4503 (1993).
17. Y. Wei, "Comment on 'Fractional quantum mechanics' and 'Fractional Schrödinger equation'," *Phys. Rev. E* **93**, 066103 (2016).
18. N. Laskin, "Reply to 'Comment on Fractional quantum mechanics and Fractional Schrödinger equation'," *Phys. Rev. E* **93**, 066104 (2016).

A Hamiltonian-Inspired Six-Dimensional Extension of the Rössler System: Dynamical Analysis and Evolutionary Parameters Identification .

Dr. Maysoon M. Aziz **،** ***Arqam S. Mahmood***
aziz_maysoon@uomosul.edu.iq , **arqam.csp117@student.uomousl.edu.iq**

A Hamiltonian-Inspired Six-Dimensional Extension of the Rössler System: Dynamical Analysis and Evolutionary Parameters Identification .

Dr. Maysoon M. Aziz **،** ***Arqam S. Mahmood***
aziz_maysoon@uomosul.edu.iq , **arqam.csp117@student.uomousl.edu.iq**

Abstract:

Developing mathematical models capable of representing complex dynamical behavior is a major challenge in the study of nonlinear systems. Many low-dimensional models lack sufficient degrees of freedom to exhibit all the dynamical properties required by modern applications. Therefore, this research aims to propose a new extension, inspired by the Hamiltonian framework, to transform the classical three-dimensional Rösler system into a six-dimensional system with greater capacity to generate complex dynamical behaviors while preserving the original system's inherent and dissipative properties. The study relied on deriving the proposed mathematical model and analyzing its structural properties by identifying equilibrium points, constructing a Jacobian matrix, extracting the characteristic equation, and studying local and global stability, as well as proving the system's dissipative property. The dynamical behavior of the system was evaluated using numerical simulations in MATLAB, employing phase diagrams, bifurcation diagrams, Lyapunov principles, Kaplan-York dimensions, and the (0-1) chaos test. Additionally, a genetic algorithm was used to estimate the optimal parameters of the system.The results showed that the proposed expansion led to a significant increase in dynamic complexity compared to the original system, while the system retained its dissipative property and exhibited three positive Lyapunov exponents, confirming the existence of hyperchaos. Other dynamic indicators also supported this finding, yielded clear results when comparing the system's numerical data generated from the simulation with real data obtained from electroencephalograms (EEG) of epilepsy patients. The simulation data showed a value of (k.corr=0.9486), while the real data value was (k.corr=0.96418), indicating a clear agreement between the dynamic behavior of the proposed system and the actual data. The main contribution of this research is the estimation of a new expansion framework for the Rösler system, providing six-dimensional models with advanced mathematical and dynamical properties. This framework can serve as a basis for developing more capable models for representing complex nonlinear systems in future applied studies.

Keywords: Rössler system , Hamiltonian-inspired expansion , Hyperchaos , Lyapunov exponents , Genetic algorithm , Nonlinear dynamical systems

1.Introduction:

Nonlinear chaotic systems are among the most important mathematical models used to explain many physical, engineering, and biological phenomena, due to their complex dynamical properties, such as sensitivity to initial conditions, non-periodicity, and unpredictable motion evolution, making them a central focus of modern studies [1–3].

The Rössler system is one of the most widely used chaotic systems for studying nonlinear behavior, given its simple mathematical structure and ability to generate diverse dynamical patterns. However, its three-dimensional limitations have led many researchers to develop it further by increasing

the number of variables or adding new coupling mechanisms to obtain more complex models capable of generating hyperchaos and better representing real-world systems [4–8].
In this context, the generalized Hamiltonian framework provides a structured mathematical basis for expanding dynamical systems by preserving their mathematical structure while increasing the degrees of freedom. However, its application in developing the Rössler system remains limited [9–12].

Therefore, this research proposes a Hamiltonian-inspired extension to transform the three-dimensional Rösler system into a six-dimensional system with more complex dynamic properties. The proposed model was evaluated through equilibrium point, stability, dissipation, Lyapunov exponents, Kaplan-York interval, phase and bifurcation diagrams, and the (0–1) chaos test. A genetic algorithm was also used to estimate optimal parameters, and the simulation results were compared with real EEG data to verify the efficiency of the proposed system and assess its ability to simulate realistic nonlinear neurobiological dynamics associated with real dynamic behavior. The results of this testing are recorded, and their significance is discussed.

Furthermore, all aspects of the analysis, study, and testing of the extended system are supported by graphs and flowcharts that illustrate the results of the study and analysis practically. [13–18]

2. Proposed Hamiltonian 6D From classical Rossler system:

The proposed six-dimensional Hamiltonian framework Rossler system is construct by extending the classical three-dimensional Rossler equations into 6D higher-dimensional coupled structure . as the following :

$\dot{X} = -y - z$, $\dot{Y} = x + ay$, $\dot{Z} = b + z(x - c)$ (classical Rossler system)

The mechanism for expanding the classical system using the Hamiltonian mathematical framework (Hamiltonian-Based):

The basic Hamiltonian rule is : $\dot{X} = (S - R)[X] + [G]$

Where : S : Skew Matrix $n \times n$, R : Symmetric Matrix n * n

[X] : Vector of Variables , [G] : Vector of Constants (independent Param.)

The Rösler three-dimension system is transformed into Hamiltonian matrices as follows:

$$\left(\begin{bmatrix} 0 & -1 & -1 \\ 1 & 0 & 0 \\ z & 0 & 0 \end{bmatrix} - \begin{bmatrix} 0 & 0 & 0 \\ 0 & -a & 0 \\ 0 & 0 & c \end{bmatrix}\right)\begin{bmatrix} x \\ y \\ z \end{bmatrix} + \begin{bmatrix} 0 \\ 0 \\ b \end{bmatrix}$$

S R [X] [G]

After converting the three-part Rösler system to Hamiltonian matrices:
The system is then expanded to 6x6 matrices, and the necessary operations are performed to convert it from a three-part to a six-part system while preserving its fundamental properties and dynamic behavior, as follows:
According to the Hamiltonian formulation S,R and G .can be expanded as the following:

$$\left(\begin{bmatrix} 0 & -1 & -1 & \pm P_{14} & \pm P_{15} & \pm P_{16} \\ 1 & 0 & 0 & \pm P_{24} & \pm P_{25} & \pm P_{26} \\ z & 0 & 0 & \pm P_{34} & \pm P_{35} & \pm P_{36} \\ \mp P_{41} & \mp P_{42} & \mp P_{43} & 0 & \pm f_1 & \pm f_2 \\ \mp P_{51} & \mp P_{52} & \mp P_{53} & \mp f_1 & 0 & \pm f_3 \\ \mp P_{61} & \mp P_{62} & \mp P_{63} & \mp f_2 & \mp f_3 & 0 \end{bmatrix} - \begin{bmatrix} 0 & 0 & 0 & 0 & 0 & 0 \\ 0 & -a & 0 & 0 & 0 & 0 \\ 0 & 0 & c & 0 & 0 & 0 \\ 0 & 0 & 0 & r_{44} & 0 & 0 \\ 0 & 0 & 0 & 0 & r_{55} & 0 \\ 0 & 0 & 0 & 0 & 0 & r_{66} \end{bmatrix}\right)\begin{bmatrix} x \\ y \\ z \\ w \\ u \\ v \end{bmatrix} + \begin{bmatrix} 0 \\ 0 \\ b \\ 0 \\ b \\ -d \end{bmatrix}$$

Where Pij are parameters , fi are functions of variables and r_{ij} are constants.

$$\left(\begin{bmatrix} 0 & -1 & -1 & 0 & 0 & 0 \\ 1 & 0 & 0 & 0 & 0 & 0 \\ z & 0 & 0 & 0 & 0 & 0 \\ 0 & 0 & -d & 0 & 0 & 0 \\ 0 & 0 & 0 & 0 & 0 & x \\ 0 & 0 & 0 & 0 & -x & 0 \end{bmatrix} - \begin{bmatrix} 0 & 0 & 0 & 0 & 0 & 0 \\ 0 & -a & 0 & 0 & 0 & 0 \\ 0 & 0 & c & 0 & 0 & 0 \\ 0 & 0 & 0 & a & 0 & 0 \\ 0 & 0 & 0 & 0 & 0 & 0 \\ 0 & 0 & 0 & 0 & 0 & 0 \end{bmatrix}\right)\begin{bmatrix} x \\ y \\ z \\ w \\ u \\ v \end{bmatrix} + \begin{bmatrix} 0 \\ 0 \\ b \\ 0 \\ b \\ -d \end{bmatrix}$$

S R [Xi] [G]

The Hamiltonian matrices are then converted into mathematical equations to obtain the expanded hexagonal Hamiltonian system, as follows:

$$\left.\begin{aligned} \dot{X} &= -y - z \\ \dot{Y} &= x + ay \\ \dot{Z} &= b + z(x - c) \\ \dot{W} &= dz - aw \\ \dot{U} &= xv + b \\ \dot{V} &= -xu - d \end{aligned}\right\} \quad \text{..... system (1)}$$

It can also be proven that equations (5 & 6) in the system(1) are real, non-random Hamiltonian components, as a follows :

General formula for Hamiltonian systems:

$\dot{X} = J \nabla H$, where $J = \begin{bmatrix} 0 & 1 \\ -1 & 0 \end{bmatrix}$,

then $H = \frac{1}{2} x (u^2 + v^2) + bv + du$ (by partial derivation)

$\frac{\partial H}{\partial v} = xv + d$ and $\frac{\partial H}{\partial u} = -(xu + d)$, using $\dot{X}_5 = \frac{\partial H}{\partial v}$ and $\dot{X}_6 = \frac{\partial H}{\partial u}$ obtaining on :

$\dot{X}_5 = xv + b$ and $\dot{X}_6 = -(xu + d) = -xu - d$

Therefore, this part of the system is real Hamiltonian, satisfying Hamilton's formula. Where a parameter (d) represented Hamiltonian coupling strength.

3. Genetic Algorithm (GA):

Parameter estimation is a fundamental stage in modeling nonlinear dynamical systems, as it depends on the accuracy of the system's representation of real-world behavior through the selection of appropriate values for its governing parameters. With the increasing number of variables and the complexity of nonlinear relationships between system components, traditional parameter estimation methods become less efficient in reaching optimal solutions. This necessitates the use of advanced optimization techniques capable of handling multidimensional search spaces. Among the most widespread and successful optimization techniques in this field is the genetic algorithm, which is based on the principles of natural selection and biological evolution. It establishes an initial set of candidate solutions and

gradually develops them through selection, crossing over, and genetic mutations to reach the best possible solution. This algorithm is distinguished by its ability to avoid local solutions and to handle complex nonlinear functions with high efficiency.
In this chapter, a genetic algorithm was used to estimate the parameters of a modified hexagonal system based on Hamiltonian coupling, represented by the parameters (a,b,c,d) , using real multi-channel EEG data. The fitness function was defined by minimizing the root mean square error (RMSE) between the real signals and the signals generated by the mathematical model, aiming to arrive at a set of parameters that achieves the best possible agreement between the dynamic behavior of the system and the measured biological data.

After solving the 6D system numerically using the set of parameters, the error function and the fitness function used to estimate the system parameters are as follows:
Initially, the value of the root mean square error (RMSE) is calculated for each of the six system variables individually. This measures the deviation between the real signal and the simulated signal. This process can be expressed by the following relationships:

RMSE- i = $\sqrt{\frac{1}{N}\sum_i (i\ real - i\ sim)^2}$ where i= x ,y, z, w, u, v

Where N represents the number of data points, and (real) refers to the actual values of the measured EEG data. (sim) refers to the simulated values generated from the hexagonal system during the numerical solution.
Since the contributions of different channels may not be equal in characterizing the dynamic behavior of the system, a set of weights was adopted to control the effect of each variable within the estimation process. These weights are represented by the following symbols:
Px ,Py ,Pz ,Pw, Pu ,Pv So that the condition is met : $\sum_{i=1}^{6} Pi = 1$
That is : Px + Py + Pz + Pw + Pu + Pv = 1
Based on these weights, the overall error function for the hexagonal system is formed according to the following relationship:
Fitness Function = F(a,b,c,d)= Px.RMSE-x + Py.RMSE-y + Pz.RMSE-z + Pw.RMSE-w + Pu.RMSE-u + Pv.RMSE-v
F represents the total error value between the mathematical model and the real data, directly reflecting the quality of the parameters used in the simulation.
Accordingly, the fitness function F(a, b, c, d) used in the genetic algorithm is defined as the weighted total error value.
Thus, the main objective of the genetic algorithm is to find the parameters (a, b, c, d) that achieve the smallest possible value for the fitness function, i.e., Minimize Fitness (a, b, c, d). This yields the optimal parameters that achieve the highest degree of correspondence between the dynamic behavior of the hexagonal system and the real data. After implementing the genetic algorithm with all its relationships and steps, the best and most optimal values for the 6D system parameters were obtained, as follows:
(a = 0.28 , b= 0.3 , c= 6.7 , d= 0.4)

4.Numerical and graphical analysis :

4.1 Runge-Kutta 4-order Numerical Method:

The proposed 6D system was solved numerically using the fourth-order Runge-Kutta numerical method (RK4) due to its high efficiency and accuracy in solving nonlinear ordinary differential systems. It is a relatively stable method, and a constant time step (h) was used to obtain the time series, phase spaces, and various dynamical analyses.

Description method

To apply this method to the proposed 6D system and simulated data of the system, the relevant formulas and steps are as follows:

Assuming that: $F(x,y,z,w,u,v) = f_i(x)$ Then :

$F(x)=f_1$,$F(y)= f_2$,$F(z)=f_3$,$F(w)=f_4$,$F(u)=f_5$,$F(v)=f_6$

And the step of time =h

Present time=t_n and next time = t_{n+1}

Therefore, the four slopes will be calculated (at the current time) first, and then the step will be calculated at the following time:

$$y_{n+1} = y_n + \frac{1}{6}(k_1 + 2k_2 + 2k_3 + k_4) \quad \text{where :}$$

$k_1 = f(t_n, y_n)$, $k_2 = f\left(t_n + \frac{h}{2}, y_n + h * \frac{k_1}{2}\right)$

$k_3 = f\left(t_n + \frac{h}{2}, y_n + h * \frac{k_2}{2}\right)$, $k_4 = f\left(t_n + \frac{h}{2}, y_n + h\, k_3\right)$ and $\Delta t = h = t_{n+1} - t_n$

From system (1) we have : $\dot{x} = f_1$, $\dot{y} = f_2$, $\dot{z} = f_3$, $\dot{w} = f_4$, $\dot{u} = f_5$, $\dot{v} = f_6$

$$v_{n+1} = v_n + \frac{h}{6}(k_{16} + 2\,k_{26} + 2\,k_{36} + k_{46})$$

Thus, the Runge-Kutta method moves from the current values at time t_n to the new values at the next time t_{n+1} , and then we repeat the same steps over the entire time interval to obtain the complete numerical solution of the hexadecimal system.

4.2 Grahpical Analysis :

It should be noted that the variables x, y, z represent the basic part related to the original system and used in comparison with EEG data, while the variables w, u, v represent additional dynamic variables resulting from the expansion process and have corresponding values in the real EEG data, and also contribute to enriching the dynamic structure of the system and increasing its effective dimensions. By parameters (a = 0.28 , b =0.3, c 6.7 and d= 0.4.) In Figure (1) show the phase space of variables over time.

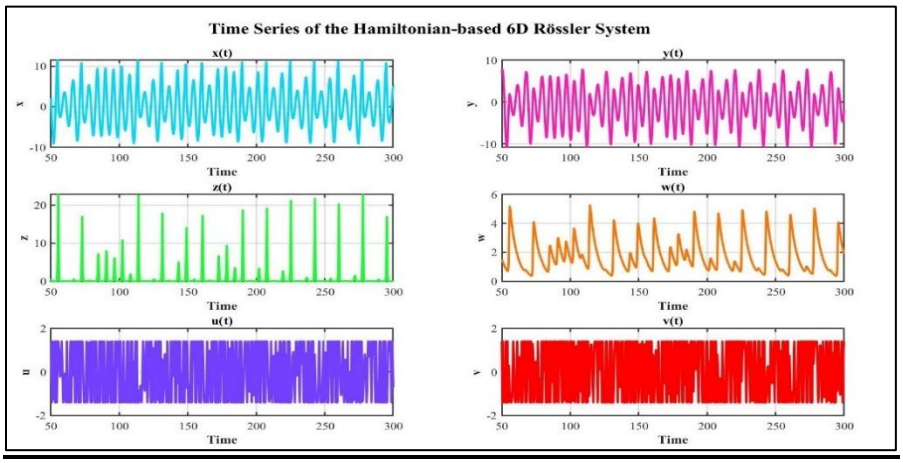


Figure (1): shows aperiodic time series of x(t), y(t), z(t), w(t), u(t) and v(t)

By parameters (a = 0.28 , b =30, c 6.7 and d= 0.4.) In figure (2) shows the two-dimensional phase-space diagrams of the 6D extended system(1), through the projections (x, y), (x, z),(x,w),(x,u),(x,v), (y, z), (y, w), (y,u), (y,v), (z,w),(z,u), (z,v),(w,u),(w,v) and (u, v).

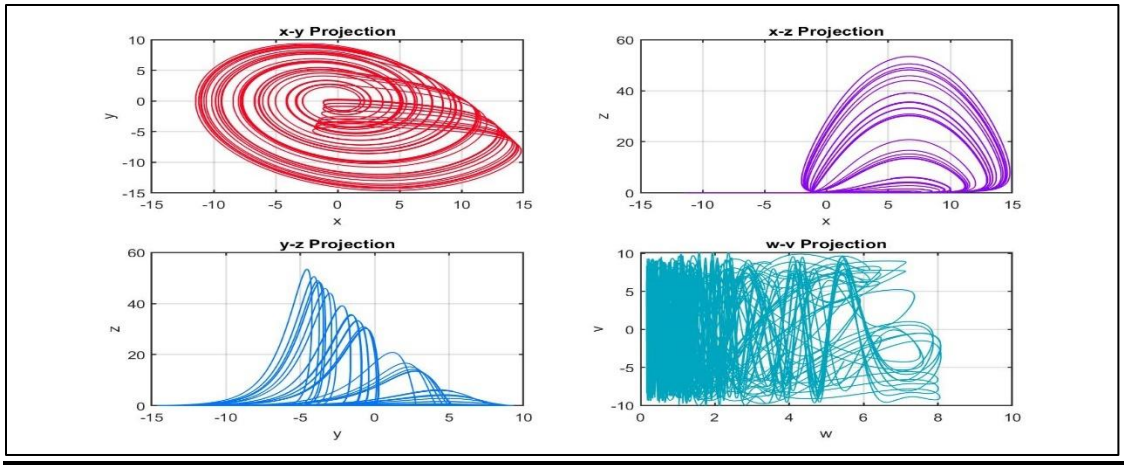
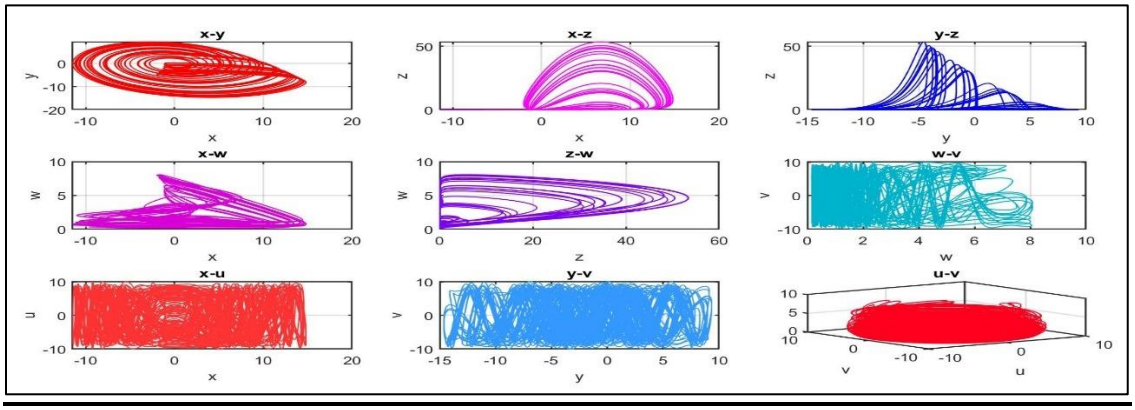


Figure (2): show projections of (x-y),(x-z),(y-z) and (w-v)



Figure(3) : shows the two-dimensional phase-diagrams of the 6D extended system(1).

5. Equilibrium Points :

Put $\dot{x} = \dot{y} = \dot{z} = \dot{w} = \dot{u} = \dot{v} = 0$

From eq.(4) we have $\dot{w} = dz - aw = 0 \rightarrow \quad w = (dz/a)$ (2)

from eq.(1) , we have : $\dot{x} = -y - z = 0 \rightarrow \quad y = -z$ (3)

from eq.(2) , we have : $\dot{y} = x + ay = 0 \rightarrow \quad x = -ay \rightarrow \quad x = az$ (4)

from eq.(3) , we have : $\dot{z} = b + z\,(x - c) = 0 \rightarrow z\,(az - c) + b = 0$

$\rightarrow a\,z^2 - cz + b = 0$ (quadratic equation) (5)

By substituting the values of the parameters into the quadratic equation, we obtain:

$$0.28\,z^2 - 6.7\,z + 0.3 = 0 \qquad (6)$$

By solving the equation (5.), we obtain: $z_1 = 0.04492$, $z_2 = 23.88365$ substitute value of (z) in eqs. (2) , (3) and (4) to obtaining on :

$x = az \rightarrow \quad x_1 = a\,z_1 = 0.0125776\,, \qquad x_2 = a\,z_2 = 6.687422$

$y = -z \rightarrow \quad y_1 = -z_1 = -0.04492\,, \quad y_2 = -z_2 = -23.88365$

$w = \frac{d}{a}\,z \rightarrow \quad w_1 = \frac{0.4}{0.28}\,(0.04492) = 0.06417, \quad w_2 = \frac{0.4}{0.28}\,(23.88365) = 34.1195$

$u = xv + b = 0 \rightarrow \quad v = -\,b/x$ (7)

$$v = -xu - d = 0 \rightarrow u = -{}^{d}/_{x} \quad (8)$$

Then : $v_1 = \frac{-b}{x_1} = \frac{-0.3}{0.0125776} = -23.853$

$v_2 = \frac{-b}{x_2} = \frac{-0.3}{6.6874} = -0.044861$

$u_1 = \frac{-d}{x1} = \frac{-0.4}{0.0125776} = -31.8041$, $u_2 = \frac{-d}{x2} = \frac{-0.4}{6.6873} \approx -0.059814$

Then the equilibrium points are :

$E_1 = \left(a\, z_1 , -z_1 , z_1 , \frac{d}{a}\, z_1 , \frac{-d}{(az_1)} , \frac{-b}{(az_1)} \right)$, $E_2 = \left(a\, z_2 , -z_2 , z_2 , \frac{d}{a}\, z_2 , \frac{-d}{(az_2)} , \frac{-b}{(az_2)} \right)$

(equilibrium points in general, in terms of the variable z and the parameters)

$E_1 = (0.012577, -0.04492 , 0.04492, 0.06417, -31.8041, -23.853)$

$E_2 = (6.6874 , -23.88365 , 23.88365 , 34.1195 , -0.059814, -0.044861)$

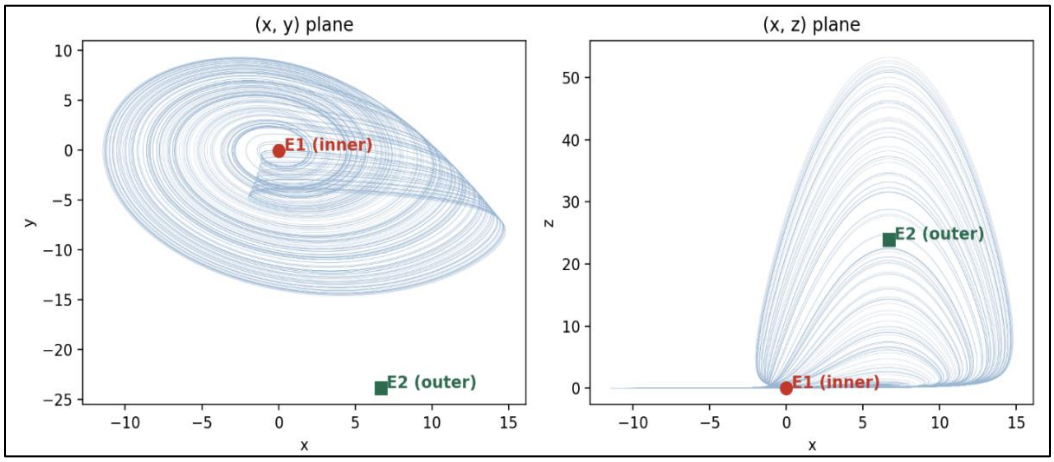
The system possesses two non-hyperbolic unstable equilibrium points.

6. Attractor of extended system (1) :

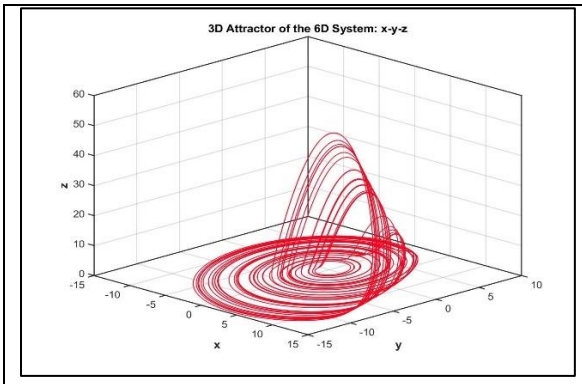
To initially understand the dynamic behavior of a hexagonal system, the trajectories are first represented in state space. The phase attractor allows us to see how the system's variables evolve over time and provides a clear picture of the resulting motion before moving on to mathematical analyses of stability, bifurcation, and chaos.

The attractor is obtained from initial conditions located near the unstable equilibrium points o0f the system, indicating that the attractor's behavior is related to the local structure of these points. Figure (4)(a&b) illustrates the shape of the attractor for the hexagonal system in two and three dimensions.

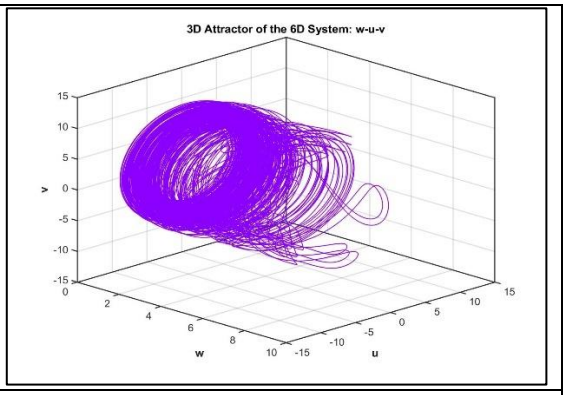
Since the proposed system has unstable equilibrium points and the chaotic attractor can be obtained by choosing initial conditions in the vicinity of these equilibria, the resulting attractor is classified as a self-excited attractor.



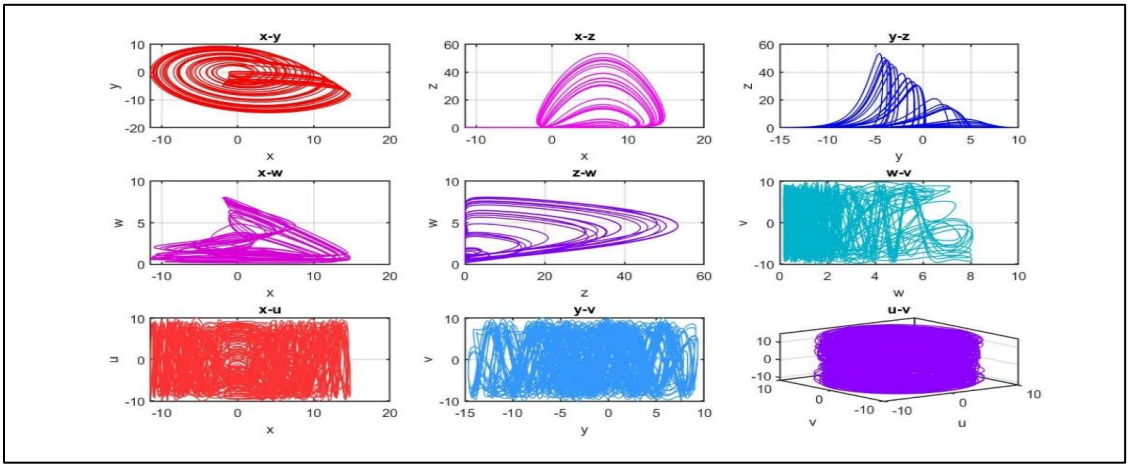
Figure(4) : Position of equilibria relative to the attractor



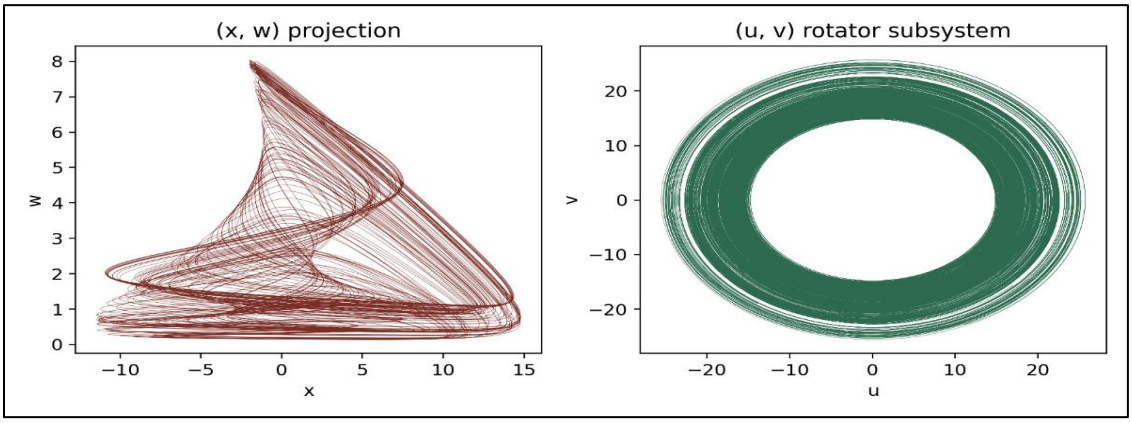
Figure(5)(a) : show the attractor of 6D extended system (1) (x,y,z)



Figure(5)(b) : show the attractor of 6D extended system (1) (w,u,v)



Figure(6) : show 2D trajectories for all two variables of 6D extended system (1) .



Figure(7) : Show 2D trajectories for (x,y) and (u,v) of 6D extended system (1) .

7 Jacobian Matrix and Characteristic equation:

$$J=\begin{bmatrix}0 & -1 & -1 & 0 & 0 & 0\\ 1 & a & 0 & 0 & 0 & 0\\ z & 0 & x-c & 0 & 0 & 0\\ 0 & 0 & d & -a & 0 & 0\\ v & 0 & 0 & 0 & 0 & x\\ -u & 0 & 0 & 0 & -x & 0\end{bmatrix}, \qquad |J-\lambda I|=0 \rightarrow$$

$$\begin{bmatrix}0 & -1 & -1 & 0 & 0 & 0\\ 1 & a & 0 & 0 & 0 & 0\\ z & 0 & x-c & 0 & 0 & 0\\ 0 & 0 & d & -a & 0 & 0\\ v & 0 & 0 & 0 & 0 & x\\ -u & 0 & 0 & 0 & -x & 0\end{bmatrix}-\begin{bmatrix}\lambda & 0 & 0 & 0 & 0 & 0\\ 0 & \lambda & 0 & 0 & 0 & 0\\ 0 & 0 & \lambda & 0 & 0 & 0\\ 0 & 0 & d & \lambda & 0 & 0\\ 0 & 0 & 0 & 0 & \lambda & 0\\ 0 & 0 & 0 & 0 & 0 & \lambda\end{bmatrix}=\mathbf{0}$$

$$\mathrm{M}=\left|\begin{array}{cc}A & B\\ C & D\end{array}\right| \rightarrow \left[\begin{array}{cccc|cc}-\lambda & -1 & -1 & 0 & 0 & 0\\ 1 & a-\lambda & 0 & 0 & 0 & 0\\ z & 0 & (x-c)-\lambda & -d & 0 & 0\\ 0 & 0 & d & -a-\lambda & 0 & 0\\ \hline v & 0 & 0 & 0 & -\lambda & x\\ -u & 0 & 0 & 0 & -x & \lambda\end{array}\right]=0$$

The array is divided into four parts to find its determinant, as follows

Then the following rule is applied: $|J|=\det(d)*det.(A-BD^{-1}C)$

This method is called Schur complement and is used to find the determinants of matrices of size 5×5 or 6×6 ... etc.

$$M=\left[\begin{array}{cccc|cc}-\lambda & -1 & -1 & 0 & 0 & 0\\ 1 & a-\lambda & 0 & 0 & 0 & 0\\ z & 0 & x-c-\lambda & 0 & 0 & 0\\ 0 & 0 & d & -a-\lambda & 0 & 0\\ \hline v & 0 & 0 & 0 & -\lambda & x\\ -u & 0 & 0 & 0 & -x & \lambda\end{array}\right]$$

$$A=\begin{vmatrix}-\lambda & -1 & -1 & 0\\ 1 & a-\lambda & 0 & 0\\ z & 0 & x-c-\lambda & 0\\ 0 & 0 & d & -a-\lambda\end{vmatrix}, B=\begin{vmatrix}0 & 0\\ 0 & 0\\ 0 & 0\\ 0 & 0\end{vmatrix}, c=\begin{vmatrix}v & 0 & 0 & 0\\ -u & 0 & 0 & 0\end{vmatrix}$$

$$D=\begin{vmatrix}-\lambda & x\\ -x & -\lambda\end{vmatrix}$$

$$\det(M)=\det(M)*\det\left(A-BD^{-1}C\right)$$

Since it's: $|B|=0$

Then : det (M) = det (D) * det (A) = [(-λ)(-λ)-(x)(-x)] * det (A)

We note that the fourth column in (A) is: $\begin{vmatrix}0\\ 0\\ 0\\ -a-\lambda\end{vmatrix}$

Therefore, when calculating a specific value (A), it is as follows:

$$\det(A)=(-a-\lambda)*\det(A_1)$$

Where : $A_1 = \begin{bmatrix} -\lambda & -1 & -1 \\ 1 & a-\lambda & 0 \\ z & 0 & x-c-\lambda \end{bmatrix}$

Then $\det(M) = (\lambda^2 + x^2)(-a-\lambda) * -[\lambda^3 + (c-x-a)\lambda^2 + (1 + a(x-c) + z)\lambda + (c-x-az)] = 0$

$= (\lambda^2 + x^2)(\lambda + a)(\lambda^3 + A\lambda^2 + B\lambda + C) = 0$

Where : A= c-x-a , B = 1+a (x-c) + z , C = c-x-az

$\lambda^4 + (A+a)\lambda^3 + (B+aA)\lambda^2 + (C+aB)\lambda + aC = 0$

$\because\ A + a = c - x - a + a = c - x$

$\therefore\ (\lambda^2 + x^2)(\lambda^4 + (c-x)\lambda^3 + (B+aA)\lambda^2 + (C+aB)\lambda + aC) = 0$

$$\rightarrow \lambda^6 + (c-x)\lambda^5 + [B + aA + x^2]\lambda^4 + [C + aB + x^2(c-x)]\lambda^3 + [aC + x^2(B+aA)]\lambda^2 + x^2(C+aB)\lambda + aCx^2 = 0$$

By substituting the values of A, B, and C, we obtain:

$$\rightarrow \lambda^6 + (c-x)\lambda^5 + [1 + a(x-c) + z + a(c-x-a) + x^2]\lambda^4 + [c - x - az + a(1 + a(x-c) + z) + x^2(c-x)]\lambda^3 + \left[a(c-x-az) + x^2\left(1 + a(x-c) + z + a(c-x-a)\right)\right]\lambda^2 + x^2[c - x - az + a(1 + a(x-c) + z)]\lambda + ax^2(c-x-az) = 0$$

Characteristic equation (9)

By substituting the values of the variables from the first equilibrium point E_1, we obtain:

$\lambda_1 = -6.680866$ (strongly stable dimension) , , $\lambda_2 = -0.28$ (stable)

$\lambda_{3,4} = 0.136713 \mp i\ 0.990158$ (unstable- positive real part)

$\lambda_{5,6} = 0 \mp i\ 0.012561$ (center pair)

Therefore, point E_1 is unstable and its type is: Nonhyperbolic-saddle Focus unstable.

By substituting the values of the variables from the second equilibrium point E2 into the characteristic equation, we obtain the following roots:

$\lambda_1 = -0.28$ (stable) , $\lambda_2 = 0.26828$ (real unstable)

$\lambda_{3,4} = -0.00042 \mp i\ 4.988028$ (very weakly stable)

$\lambda_{5,6} = 0 \mp i\ 6.68744$ (center pair)

Therefore, point E_2 is unstable and its type : Non-hyperbolic-Saddle Focus unstable

8 Stability of 6D extended System (1):

After reviewing the dynamic behavior of the system, the focus shifts to studying stability in order to determine the nature of the equilibrium points and their responsiveness to minor disturbances. For this purpose, a set of mathematical tests based on the Jacobian matrix, eigenvalues, and various stability criteria are used to characterize the local behavior of the system.

8.1 Routh stability Criteria :

The Routh criterion is used to directly determine the stability of a system based on its characteristic equation, without needing to calculate the roots of the equation. This involves creating a table known as the Roth table using the coefficients of the characteristic equation, and then analyzing the signals in the first column. Stability is achieved when the signals in the first column are similar. Conversely, changes and differences in the signals in the first column indicate instability at the equilibrium points, and therefore, instability of the system. The polynomial of characteristic equation is :

$p(\lambda) = a_0\lambda^6 + a_1\lambda^5 + a_2\lambda^4 + a_3\lambda^3 + a_4\lambda^2 + a_5\lambda + a6$

Thus, Routh's table is as follows:

λ_6	a_0	a_2	a_4	a_6
λ_5	a_1	a_3	a_5	0
λ_4	b_1	b_2	b_3	0
λ_3	c_1	c_2	0	0
λ_2	d_1	d_2	0	0
λ_1	e_1	0	0	0
λ_0	a_6	0	0	0

Where :

$$b_1 = \frac{a_1 a_2 - a_3}{a_1} \ , \ b_2 = \frac{a_1 a_4 - a_5}{a_1} \ , b_3 = \frac{a_1 a_6 - 0}{a_1} = a_6 \ , \qquad c_1 = \frac{b_1 a_3 - a_1 b_2}{b_1}$$

$$c_2 = \frac{b_1 a_5 - a_1 b_3}{b_1} \ , d_1 = \frac{c_1 b_2 - b_1 c_2}{c_1} \ , d_2 = \frac{c_1 b_3 - 0}{c_1} = b_3 = \ a_6 \ , \ \ e_1 = \frac{d_1 c_2 - c_1 d_2}{d_1}$$

According to Roth's stability condition, all elements in the first column must have the same sign, either all positive or all negative. If there is any difference in the signs of the elements in the first column, then the system is unstable.

$$p_1(\lambda) = \lambda^6 + 6.6874\,\lambda^5 + 0.96668\,\lambda^4 + 6.46858\,\lambda^3 + 0.09924\,\lambda^2 + 0.0010231\,\lambda + 0.000396$$

λ_6	1	0.96668	0.09924	0.000396
λ_5	6.6874	6.46858	0.0010231	0
λ_4	-0.0005988	0.0990870	0.000396	0
λ_3	1113.140	4.423825	0	0
λ_2	0.0990894	0.000396	0	0
λ_1	-0.0247217	0	0	0
λ_0	0.000396	0	0	0

We observe that the elements of the first column have different signs. Therefore, according to Roth's condition, the system is unstable at point E_1.

$$p_2(\lambda) = \lambda^6 + 0.0126\,\lambda^5 + 69.52657\,\lambda^4 + 286.78540\,\lambda^3 + 1103.977\,\lambda^2 + 13.04128\,\lambda - 83.582$$

At the equilibrium point E_2, Routh's table is as follows:

λ_6	1	69.52657	1103.977	-83.582
λ_5	0.0126	286.78540	13.04128	0
λ_4	-22691.2195	68.9548	-83.582	0
λ_3	286.7854	13.0412	0	0
λ_2	1100.8115	-83.582	0	0
λ_1	34.8162	0	0	0
λ_0	-83.582	0	0	0

We note that the signals of the elements of the first column are different, and this indicates, according to Routh's stability condition, that the system is not locally stable at the second equilibrium point E_2.

8.2 Hurwitz stability Criteria :

To reinforce the results of the Routh criterion, the determinants of the Hurwitz criterion are calculated as an additional test of the local stability of the dynamical system. This criterion is based on constructing the Hurwitz matrix from the characteristic equation coefficients and then examining the successive determinants, where the fulfillment of its stability condition is related to the nature of the equation roots and the stability of the equilibrium point as the following :

$$H = \begin{vmatrix} a_1 & a_3 & a_5 & 0 & 0 & 0 \\ a_0 & a_2 & a_4 & a_6 & 0 & 0 \\ 0 & a_1 & a_3 & a_5 & 0 & 0 \\ 0 & a_0 & a_2 & a_4 & a_6 & 0 \\ 0 & 0 & a_1 & a_3 & a_5 & 0 \\ 0 & 0 & a_0 & a_2 & a_4 & a_6 \end{vmatrix} \quad \text{(Hurwitz matrix)} \qquad (10)$$

$$H = \begin{bmatrix} 6.6874 & 6.46858 & 0.001231 & 0 & 0 & 0 \\ 1 & 0.96668 & 0.09924 & 0.000396 & 0 & 0 \\ 0 & 6.6874 & 6.46858 & 0.00101231 & 0 & 0 \\ 0 & 1 & 0.96668 & 0.09924 & 0.000396 & 0 \\ 0 & 0 & 6.6874 & 6.46858 & 0.0010231 & 0 \\ 0 & 0 & 1 & 0.96668 & 0.09924 & 0.000396 \end{bmatrix}$$

Hurwitz parameters are as follows:

$$\Delta_1 = |a_1| = 6.6874 \ , \quad \Delta_2 = \begin{vmatrix} a_1 & a_3 \\ a_0 & a_2 \end{vmatrix} = -0.00400$$

$$\Delta_3 = \begin{vmatrix} a_1 & a_3 & a_5 \\ a_0 & a_2 & a_4 \\ 0 & a_1 & a_3 \end{vmatrix} = -4.4572 \quad , \quad \Delta_4 = \begin{vmatrix} a_1 & a_3 & a_5 & 0 \\ a_0 & a_2 & a_4 & a_6 \\ 0 & a_1 & a_3 & a_5 \\ 0 & a_0 & a_2 & a_4 \end{vmatrix} = -0.44166154$$

$$\Delta_5 = \begin{vmatrix} a_1 & a_3 & a_5 & 0 & 0 \\ a_0 & a_2 & a_4 & a_6 & 0 \\ 0 & a_1 & a_3 & a_5 & 0 \\ 0 & a_0 & a_2 & a_4 & a_6 \\ 0 & 0 & a_1 & a_3 & a_5 \end{vmatrix} = 0.01091861 \ , \Delta_6 = \begin{vmatrix} a_1 & a_3 & a_5 & 0 & 0 & 0 \\ a_0 & a_2 & a_4 & a_6 & 0 & 0 \\ 0 & a_1 & a_3 & a_5 & 0 & 0 \\ 0 & a_0 & a_2 & a_4 & a_6 & 0 \\ 0 & 0 & a_1 & a_3 & a_5 & 0 \\ 0 & 0 & a_0 & a_2 & a_4 & a_6 \end{vmatrix} = 4.32377 \times 10^{-6}$$

Since that $\Delta_2 < 0$, $\Delta_3 < 0$ *and* $\Delta_4 < 0$

Then according to the Hurwitz condition, the system is unstable at equilibrium point one E_1.

Now we find the Hurwitz determinants at the second point E_2. Since we have $a_6 < 0$, the system will already be judged unstable. Therefore, the Hurwitz condition is applied by finding its determinants, stating their values, and judging the system's stability based on them. As follows:

$$H_2 = \begin{bmatrix} 0.0126 & 286.7854 & 13.04128 & 0 & 0 & 0 \\ 1 & 69.52657 & 1103.977 & -83.582 & 0 & 0 \\ 0 & 0.0126 & 286.7854 & 13.04128 & 0 & 0 \\ 0 & 1 & 69.52657 & 1103.977 & -83.582 & 0 \\ 0 & 0 & 0.0126 & 286.7854 & 13.04128 & 0 \\ 0 & 0 & 1 & 69.52657 & 1103.977 & -83.582 \end{bmatrix}$$

$\Delta_1 = |a_1| = 0.0126$, $\Delta_2 = \begin{vmatrix} a_1 & a_3 \\ a_0 & a_2 \end{vmatrix} = -285.909365$

$\Delta_3 = \begin{vmatrix} a_1 & a_3 & a_5 \\ a_0 & a_2 & a_4 \\ 0 & a_1 & a_3 \end{vmatrix} = -81994.6426$, $\Delta_4 = \begin{vmatrix} a_1 & a_3 & a_5 & 0 \\ a_0 & a_2 & a_4 & a_6 \\ 0 & a_1 & a_3 & a_5 \\ 0 & a_0 & a_2 & a_4 \end{vmatrix} = -90260648.6954$

$$\Delta_5 = \begin{vmatrix} a_1 & a_3 & a_5 & 0 & 0 \\ a_0 & a_2 & a_4 & a_6 & 0 \\ 0 & a_1 & a_3 & a_5 & 0 \\ 0 & a_0 & a_2 & a_4 & a_6 \\ 0 & 0 & a_1 & a_3 & a_5 \end{vmatrix} = -3142530027.685384$$

$$\Delta_6 = \begin{vmatrix} a_1 & a_3 & a_5 & 0 & 0 & 0 \\ a_0 & a_2 & a_4 & a_6 & 0 & 0 \\ 0 & a_1 & a_3 & a_5 & 0 & 0 \\ 0 & a_0 & a_2 & a_4 & a_6 & 0 \\ 0 & 0 & a_1 & a_3 & a_5 & 0 \\ 0 & 0 & a_0 & a_2 & a_4 & a_6 \end{vmatrix} = 262658944773.99884$$

Since $\Delta_2 < 0$, $\Delta_3 < 0$, $\Delta_4 < 0$ *and* $\Delta_5 < 0$, the Hurwitz condition is not satisfied, therefore the system (1) is locally unstable at the second equilibrium point E_2.

8.3 Lyapunov Stability Function :

In addition to stability tests based on the characteristic equation, the Lyapunov function can be used to examine the system's behavior from an energetic perspective and track its state evolution over time. Therefore, the Lyapunov function, which is suitable for the expanded hexagonal system, is adopted, and its time derivative is studied in order to assess the global stability in the state space of the dynamical system.

The Lyapunov function formula for 6D extended system as the following:

$$v = \frac{1}{2}(x^2 + y^2 + z^2 + w^2 + u^2 + v^2)$$

The Lyapunov function is positive by definition. $v(x) \geq 0$

When differentiating the function, we obtain: $\dot{v}(x)$

If $\dot{v}(x) < 0$ then the system is stable , $x \neq 0$

If $\dot{v}(x) > 0$ then the system is unstable

Then: $\dot{\mathbf{v}} = x\dot{x} + y\dot{y} + z\dot{z} + w\dot{w} + u\dot{u} + v\dot{v}$

$\dot{\mathbf{v}} = x(-y - z) + y(x + ay) + z\big(b + z(x - c)\big) + w(dz - aw) + u(xv + b) + v(-xu - d)$

The general formula for the derivative of a Lyapunov function

$\dot{v}(x) = -yx - xz + xy + ay^2 + bz + z^2(x - c) + dwz - aw^2 + xuv + bu - xuv - dv$

The final general formula for the derivative of the Lyapunov function with parameters

$$\dot{v}(x) = -xz + 0.28\,y^2 + 0.3\,z + z^2(x - 6.7) + 0.4wz - 0.28\,w^2 + 0.3u - 0.4\,v$$

By substituting for the first equilibrium point E_1 in $\dot{\mathbf{v}}(\mathbf{x})$ we obtain:

$$\dot{v}(E_1) = -(0.012577)(0.04492) + (0.28)(-0.04492)^2 + (0.3)(0.04492) + (0.04492)^2(0.012577 - 6.7) + 0.4(0.06417)(0.04492) - (0.28)(0.06417)^2 + (0.3)(-31.804) - (0.4)(-23.853)$$

$$\dot{v}(E_1) \approx 0.00001788 > 0$$

This confirms that the system is unstable at that point E_1 .

$$\dot{v}(E_2) = -(6.6874)(23.88365) + (0.28)((-23.88365)^2) + (0.3)(23.88365) + (23.88365)^2(6.6874 - 6.7) + (0.4)(34.1195)(23.88365) - (0.28)((34.1195)^2) + (0.3)(-0.059815) - (0.4)(-0.044861)$$

$$\dot{v}(E_2) = 0.0217817 > 0$$

Also, the system is unstable

Since the two equilibrium points are locally unstable according to the Routh and Hurwitz criteria, Therefore, we used the Lyapunov function to study the global instability of the dynamical system.

8 The Dissipativity ($\nabla . F$) :

Dissipative is a fundamental property of nonlinear dynamical systems. It describes the system's ability to shrink the volumetric elements in its state space over time. Studying dispersion is crucial for understanding the long-term behavior of the proposed hexagonal system and for revealing the possibility of finite attractors and chaotic or hyperchaotic structures. Therefore, this section will analyze the dissipative property by calculating the vector field divergence of the system and determining the conditions that cause all dynamic paths to be attracted towards a finite set in the state space.

The value of $\nabla . F$ can be calculated from the following relationship:

$$\nabla . F . = \frac{\partial \dot{x}}{\partial x} + \frac{\partial \dot{y}}{\partial y} + \frac{\partial \dot{z}}{\partial z} + \frac{\partial \dot{w}}{\partial w} + \frac{\partial u}{\partial u} + \frac{\partial \dot{v}}{\partial v} \quad \text{or} \quad \nabla . F . = \sum_{i=j=1}^{6} J_{ij}$$

$$\nabla . F . = 0 + a + (x - c) - a + 0 + 0 \rightarrow \quad \nabla . F . = x - c$$

By substituting the value of parameter (c) and the value of (x) from the first equilibrium point E_1, we obtain:

$$\nabla . F . (E_1) = (0.012577) - (6.7) = -6.687423 < 0$$

Therefore, the system is dissipated at the first equilibrium point E_1.

and substituting the value of parameter (c) and the value of (x) from the first equilibrium point E_1, we obtain:

$$\nabla . F . (E_2) = (6.6874) - (6.7) = -0.0126 < 0$$

The system is dissipated at the equilibrium point E_2 as well,

the dissipation of the system can be expressed by the following derivative relation:

$$\nabla . F . = x - c \rightarrow x - c < 0 \rightarrow \quad x < c$$

If this relationship is established, then the system is dissipated.

Therefore, the system possesses the property of dissipation in the x < 6.7 region, which is the region where chaotic orbits are usually found, thus supporting the possibility of the emergence of a chaotic or super-chaotic attractor within a limited space in state space.

10 The Bifurcation :

After studying the equilibrium and stability points of the dynamic system, as well as the dissipation, we move on to bifurcation analysis to understand how the dynamic behavior of the proposed hexagonal system changes when the value of one of its main parameters is altered. Bifurcation diagrams are an important tool for detecting transitions between periodic, quasi-periodic, chaotic, and hyper chaotic behaviors. They also help identify the parametric domains where the complex dynamics of the system appear.

To study bifurcations in the hexagonal system, the parameter (c) is chosen as the main control parameter within the range [0,10], with the parameters (a = 0.28, b = 0.30, d = 0.40) held constant. The importance of this parameter stems from its direct appearance in the equation of the variable (z), as well as its influence on the dissipation property. Thus, the bifurcation diagram with respect to (c) helps track the dynamic transitions between regular, chaotic, and hyper chaotic behaviors within the system. It is mathematically written as (c versus z_{max}) and then plotted as (c versus z max). Figure (8) illustrates the bifurcation phenomenon of the hexagonal system (1) at $c \in [0,10]$

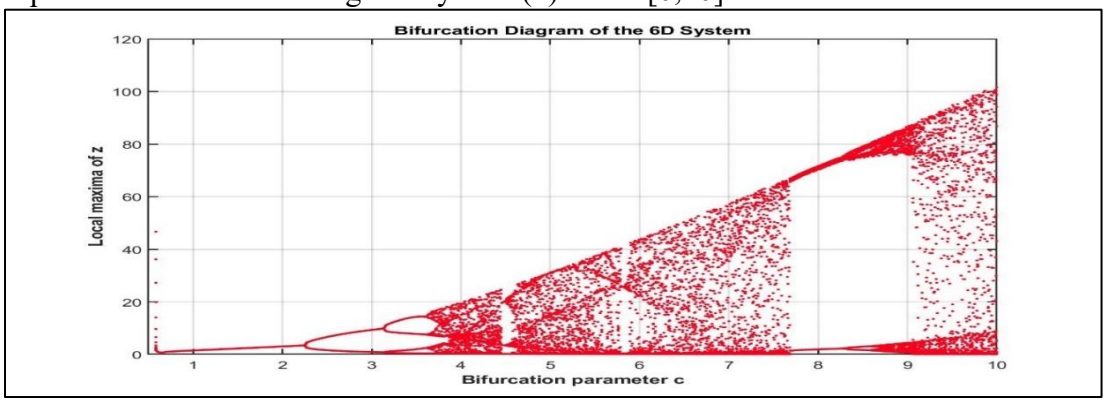


Figure (8): show the bifurcation of the 6D extended dynamical system(1)

11 Chaotic system testing :

11.1 Lyapunov Exponents :

Lyapunov exponents are among the most important quantitative indicators used in the study of nonlinear dynamical systems. They provide a precise description of the rate of divergence or convergence of adjacent paths in state space over time. Their importance lies in their ability to distinguish between orderly and chaotic behavior by measuring sensitivity to initial conditions. Therefore, Lyapunov exponents are widely used to detect disorder and superorganisms and to characterize the dynamical properties of nonlinear attractors. In this section, the spectrum of Lyapunov exponents is calculated for the proposed hexagonal system to determine the nature of its dynamical behavior and to verify the possibility of disorder or superorganism arising within the studied parametric domain. It can be defined mathematically by the following relationship:

$$\lambda_i = \lim_{t\to\infty} \frac{1}{t} \ln\left(\frac{\|\int x_i(t)\|}{\|\int x_i(0)\|}\right) \text{ where i=1,2, …..,n}$$

The spectrum of Lyapunov exponents for the proposed hexagonal system, tested using MATLAB, shows three positive and three negative Lyapunov exponents, with values as follows: $L_i = \{0.1377154093$, 0.0011504383, 0.0005457159 , -0.0006604022 ,
-0.2800080658 , -6.1667887038 } where i = 1, 2, 3, 4, 5, 6

The system is considered hyperchaotic if it possesses at least two positive Lyapunov exponents. Sum. Of Lyapunov exponents = - 6.3080456083

Thus, the fundamental condition for the emergence of hyper chaos is met. Furthermore, the larger positive value (L1) confirms the high sensitivity to initial conditions.
Moreover, the sum of the Lyapunov exponents = -6.3080456083, a negative value, confirms that the system is dispersive. Therefore, it can be concluded that the proposed hexagonal system exhibits hyper chaotic behavior within the studied parameters. the Figure (9) illustrates the case of the Lyapunov exponents for the hexagonal dynamical system (1).

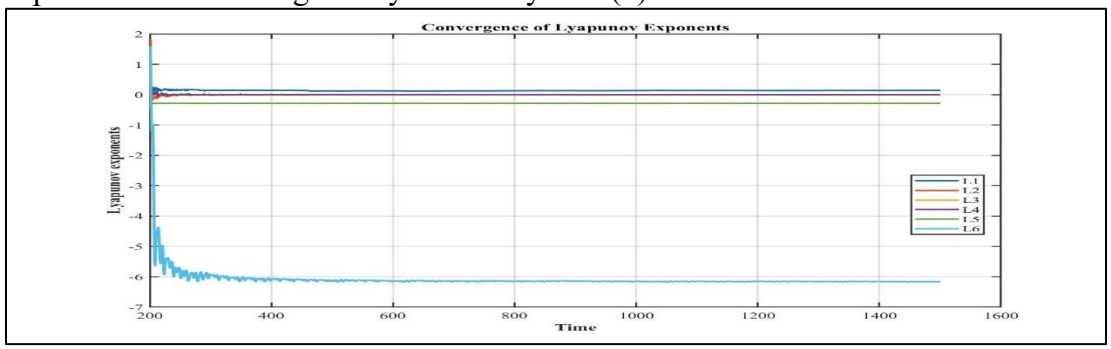


Figure (9): shown the Lyapunov exponents for 6D extended system (1)

11.2 Kaplan –York Dimension :

The dynamical behavior of a system is not limited to Lyapunov principles alone; they can also be used to estimate the fractal dimension of a chaotic attractor using the Kaplan-York dimension. This is a crucial indicator for measuring the geometric complexity of the attractor in state space. It links the spectrum of Lyapunov principles to the fractal structure of the attractor, providing a quantitative description of the number of effective degrees involved in the chaotic or hyperchaotic dynamics of the system under study.

The cumulative sums are now calculated as follows: $\mathrm{DKY} = \mathrm{j} + \frac{\sum_{i=1}^{j} L_i}{|L_{i+1}|}$

Then : $D_{KY} = 4 + \frac{\sum_{i=1}^{j} L_i}{|L_{i+1}|} = 4 + \frac{S_4}{|L_5|} = 4 + \frac{0.1376597295}{|0.2800080658|} \rightarrow$ $\boxed{D_{KY} \approx 4.492}$

This is an excellent value for a super-chaotic hexagonal system because it indicates that the attractor has a fractional structure with a dimension greater than 4 and less than 5, which is perfectly consistent with the existence of three positive exponents for Lyaponov.

Where j is the largest integer that satisfies the condition: $\sum_{i=1}^{j} L_i > 0$ and $\sum_{i=1}^{j+1} L_i < 0$

11.3 The (0-1) Chaos Test :

The (0-1) chaos test is an effective numerical method for distinguishing between orderly and chaotic behavior in dynamical systems without the need to reconstruct the phase space or calculate Lyapunov exponents. Instead, the test relies on direct time series analysis and the extraction of the K-coefficient.
In this chapter, the 1-0 chaos test was also used to verify the dynamic nature of the proposed hexagonal system. It provides a direct means of distinguishing between orderly and chaotic behavior and calculating the K-coefficient.
The K-coefficient ranges from zero to one, where values close to zero indicate orderly behavior, while values close to one indicate the presence of chaos in the system, it works directly with the time series and does not require any phase space reconstruction as the following :

Step(1)- compute translation variables : Given a time series $\boldsymbol{\phi}(j)$, compute the translation variables p(n) and q(n) using $P(n) = \sum_{j=1}^{n} \phi(j) \cos(jc)$, and $q(n) = \sum_{j=1}^{n} \phi(j)\, sin(jc)$, where c is a randomly chosen constant in $(0, \pi)$,n =1,2,…,L

Step(2)- compute Mean Square Displacement (MSD) : calculate M(n) the Mean Square Displacement of the (p,q) trajectory**.**

$M(n) = \lim_{L\to\infty} (\frac{1}{L}) \sum_{j=1}^{L} [(P(j+n) - P(j))^2 + (qn(j+n) - qn(j))^2]$

Where n = 1,2, …. L/10 .

$Vosc(n) = [E(\boldsymbol{\phi})]^2 \times \frac{1-cos(nc)}{1-cos(c)}$,, where $E(\boldsymbol{\phi}) = \lim_{L\to\infty} (\frac{1}{L}) \sum_{j=1}^{n} \phi(j)$

Then D(n) = M(n) ─ Vosc (n) , K corr = Kc = $\lim_{n\to\infty} \frac{log\, Mc(n)}{log\,(n)}$

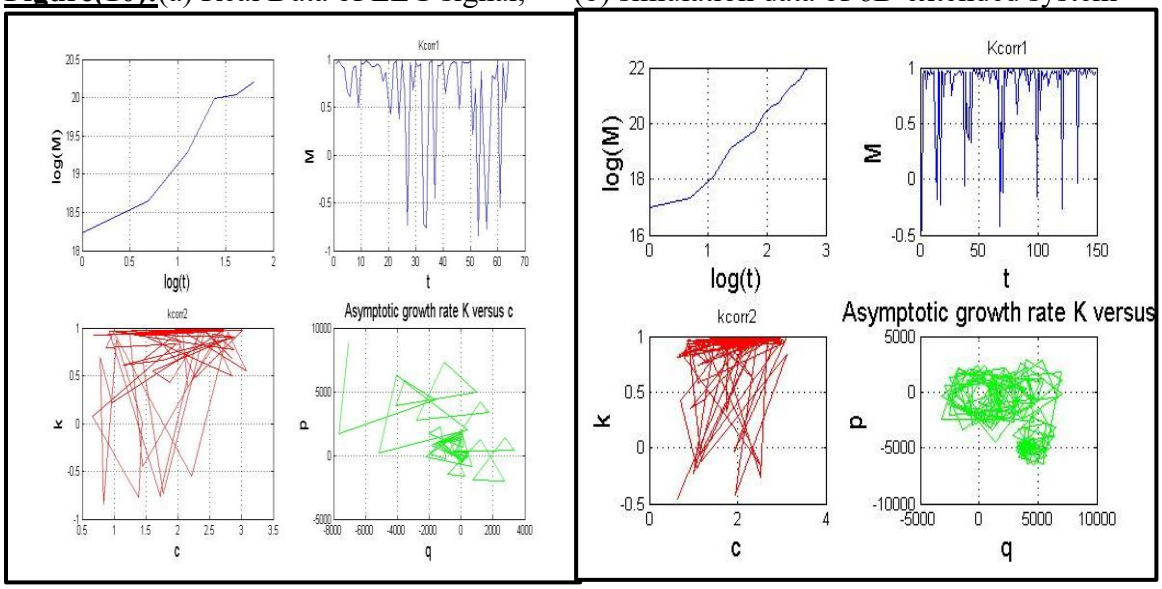
Step(3)- Estimate Growth Rate K: Determine the asymptotic growth rate K of M(n),

Kc states : If $Kc \cong 0$ the dynamic is regular (periodic or quasi-periodic) .

And if Kc ≅ 1 then the dynamic is chaotic . where Kc ∈[0, 1].

By using MATLAB program, we get for simulation data: Kc = Kcorr = 0.94856 ≅ 1 Then the system is a chaotic, getting for real data: Kc = Kcorr = 0.96148 ≅ 1 it is chaotic too. The 0–1 test result obtained from the fractional Rössler simulations exhibit a strong agreement with those taken from the real EEG data, show a high level of similarity in their chaotic signatures. This close correspondence confirms the capability of the fractional model to reliably reproduce the underlying dynamical characteristics of the measured brain signals. The figure (10) a &b shown the compared between real data of (EEG) signal and simulation data of 6D extended system (1) .

Figure(10):(a) Real Data of EEG signal, (b) simulation data of 6D extended system



12.

Conclusions:

The results of this research demonstrate the success of the proposed expansion, inspired by the Hamiltonian framework, in transforming the three-dimensional Rössler system into a hexagonal system with more complex dynamic properties while preserving the dissipative nature of the original system. Mathematical analysis revealed two equilibrium points for the system, and local stability studies showed that the system is unstable at these equilibrium points. Furthermore, the analysis of the Lyapunov function confirmed the global instability of the proposed system, thus providing a suitable environment for the emergence of chaotic attractors.

The dissipation analysis also demonstrated that the sum of the Lyapunov exponents ($\sum L_i = -6.30805$) is a negative value, confirming the contraction of the phase space and the preservation of the dissipative property. Meanwhile, the Lyapunov exponents showed three positive values, confirming the occurrence

of superchaos and a higher degree of dynamic complexity compared to the classical system. The Kaplan-York distance reached approximately (D_{KY}=4.492), reflecting the complex geometric structure of the resulting attractor. Numerical simulation results using MATLAB showed that the system undergoes successive dynamic transitions, beginning with periodic behavior, then chaotic, and finally culminating in superchaotic behavior, as confirmed by bifurcation and phase diagrams. The (0-1) chaos test yielded clear results when comparing the system's numerical data generated from the simulation with real data obtained from electroencephalograms (EEGs) of epilepsy patients. The simulation data showed a value of (k.corr=0.9486), while the real data value was (k.corr=0.96418), indicating a clear agreement between the dynamic behavior of the proposed system and the actual data. The genetic algorithm demonstrated high efficiency in estimating the optimal system parameters, obtaining optimal values of d=0.40, c=6.7, b=0.30, and a=0.28,This contributed to improving the model with the characteristics of the targeted dynamic behavior.

In general, this study presents a new framework for expanding chaotic biological systems based on Hamiltonian structure. It has been shown that systematically increasing the number of variables can lead to the production of high-dimensional models with advanced mathematical and dynamical properties, making them promising candidates for developing more realistic models for studying complex nonlinear systems in the future.

References:

[1] Strogatz, S. H. (2018). Nonlinear dynamics and chaos (2nd ed.). CRC Press.

[2] Ott, E. (2002). Chaos in dynamical systems (2nd ed.). Cambridge University Press.

[3] Sparrow, C. (1982). The Lorenz equations: Bifurcations, chaos, and strange attractors. Springer.

[4] Otto Rössler. (1976). An equation for continuous chaos. Physics Letters A, 57(5), 397–398

[5] van der Schaft, A. J., & Maschke, B. M. (2002). *Hamiltonian formulation of distributed-parameter systems with boundary energy flow*. Journal of Geometry and Physics, 42, 166–194.

[6] van der Schaft, A., & Jeltsema, D. (2014). *Port-Hamiltonian Systems Theory: An Introductory Overview*. Foundations and Trends in Systems and Control, 1(2–3), 173–378.

[7] van der Schaft, A., & Maschke, B. (2018). *Generalized Port-Hamiltonian DAE Systems*.

[8] Goldberg, D. E. (1989). *Genetic Algorithms in Search, Optimization and Machine Learning*. Addison-Wesley.

[9] Haupt, R. L., & Haupt, S. E. (2004). Practical genetic algorithms (2nd ed.). Wiley.

[10] Kuznetsov, N. V. (2016). *Lyapunov dimension and hidden attractors in dynamical systems*. International Journal of Bifurcation and Chaos.

[11] ECE 680 Modern Automatic Control, Routh's Stability Criterion, June 13, 2007, pp.1-6 .

[12] Aziz, M. M., & Mahmood, A. S. (2023, February). Mathematical model of epidemic disease covid-19. In AIP Conference Proceedings (Vol. 2414, No. 1, p. 040072). AIP Publishing LLC.

[13] Aziz, M. M., & Mahmood, A. S. (2021). Analysis of Dynamical Behavior for Epidemic Disease COVID-19 with Application. Turkish Journal of Computer and Mathematics Education, 12(4), 568-577.

[14] Wolf, A., Swift, J. B., Swinney, H. L., & Vastano, J. A. (1985). Determining Lyapunov exponents from a time series. Physica D, 16(3), 285–317.

[15] Barrio, R., Shilnikov, A., & Shilnikov, L. (2015). When chaos meets hyperchaos: 4D Rössler model. Physics Letters A, 379, 2300–2306.Ogata, K. (2010). Modern control engineering (5th ed.). Prentice Hall.

[16] Aziz, M. M., & Mahmood, A. S. (2026). Analysis of a novel fractional-order four-dimensional dynamical system with sinusoidal term for EEG signal: A stability and hyperchaotic perspective. Letters in Biomathematics, 13(2)

[17] Gottwald, G. A., & Melbourne, I. (2009). On the implementation of the 0–1 test for chaos. SIAM Journal on Applied Dynamical Systems, 8(1), 129–145.

[18] Aziz, M. (2023). Mathematical Model for the effect of buoyancy forces on the stability of a fluid flow. European Journal of Pure and Applied Mathematics, 16(2), 983-996.

An Endpoint-Singularity-Fitted Hybrid Spectral Volterra Method for a Mixed Fractional–Classical Model of Coronary Microvascular Dysfunction

Mohammed Sabah Mahmoud
Department of Mathematics – university of mosul
msmt_math@uomosul.edu.iq
https://orcid.org/0009-0006-7291-2801

An Endpoint-Singularity-Fitted Hybrid Spectral Volterra Method for a Mixed Fractional–Classical Model of Coronary Microvascular Dysfunction

Mohammed Sabah Mahmoud
Department of Mathematics – university of mosul
msmt_math@uomosul.edu.iq
https://orcid.org/0009-0006-7291-2801

Abstract:

The underlying mechanisms of coronary microvascular dysfunction (CMD) are the interplay of vascular and inflammatory mechanisms and may be history dependent. This research paper proposes a mixed fractional–classical model where endothelial function and inflammatory burden are modeled by Caputo dynamics, and the microvascular resistance and oxygen supply–demand mismatch are modeled by classical dynamics. The fractional variables are approximated at an endpoint-fitted coordinate and the classical variables are approximated in physical time; barycentric coupling in a Volterra formulation is solved with an analytically assembled block Newton Jacobian. Manufactured tests demonstrate significant improvements in accuracy when the dominant endpoint structure conforms to the mapping, but not for a test purposely "misaligned" (misaligned = non-conforming). The fractional order in the simulations of CMD does not substantially lower the sharpness of the acute peak, but it certainly lengthens the recovery from the stress. Under controlled-kinetics, structured-perturbation and separate-order sensitivity tests, these persistence trends are under control. Polynomial refinement and an independent Adams–Bashforth–Moulton calculation support numerical consistency. The model is normalized and exploratory as opposed to clinically calibrated. The fractional order was lowered from its integer value to 0.7, increasing the recovery time (from 26.08 to 60.86), meaning that the impact of stress exposure has been increasing in length.

1.Introduction:

Coronary microvascular dysfunction (CMD) is defined as a failure of the coronary microcirculation to regulate blood flow, and can potentially cause myocardial ischaemia without the presence of obstructive epicardial coronary artery disease. It is an important mechanism in patients with angina or ischaemia and non-obstructive coronary arteries (ANOCA/INOCA) where symptoms can continue despite the absence of a flow limiting epicardial lesion [1,2]. The abnormalities that have been associated with CMD include endothelial dysfunction, impaired vasomotor control, inflammation, oxidative stress, and structural changes in the coronary microvasculature [2,3]. The presence of these mechanisms implies that the microvascular state may be a reflection of the impact of previous disturbances, as well as of the current physiological demand.

Most mathematical and computational models of the coronary circulation have been concerned with pressure-flow relationships, vascular resistance, compliance, myocardial compression and patient-specific haemodynamics [5,6]. These techniques have proven useful in the description of mechanical regulation of coronary perfusion and the effect of altering resistance or intramyocardial pressure on

blood flow. Pathological processes like chronic endothelial dysfunction and inflammation, however, are not typically included in the same model as interacting dynamical variables. In the case of CMD, this is important because the vascular response may be influenced not only by the current haemodynamic status, but also by the pathological changes that have occurred over longer time scales.

Systems whose evolution is dependent on both their current state and their previous history are naturally described by fractional-order models. The nonlocal structure of fractional derivatives allows to directly include memory and hereditary effects in the governing equations, and this has led to their use in a wide variety of biological and physiological applications [7,8]. In the present study, endothelial function and inflammatory burden are modeled as fractional dynamics, and micro-vascular resistance and oxygen supply–demand mismatch are modeled as first-order dynamics, reflecting the history dependence. This separation is a mathematical one and not an assumption of asymptotic separation of time scales.

The fractional formulation has a numerical difficulty which is not as strong as that of the classical variables. The solutions of Caputo-type problems can be less regular at the initial time and can include fractional power terms, e.g., t^{α}, even if the prescribed data is otherwise regular [9-12]. The polynomial approximation directly in physical time should then be able to resolve this weak endpoint singularity and may converge less well as α decreases. This lack of regularity is especially relevant for global spectral approximations, for which the accuracy is highly sensitive to the smoothness of the approximated solution. The numerical method used here is thus chosen to be able to deal with the fractional endpoint structure explicitly, without increasing the degree of the polynomial to compensate for it.

To address this difficulty, the fractional variables are represented in the transformed coordinate

$$\xi = \left(\frac{t}{T}\right)^{\alpha}$$

which corresponds to the predominant fractional-power dynamics close to the initial point. The classical variables are still displayed in physical time, retaining the smoother temporal structure of the classical variables. The two representations are linked by using barycentric spectral interpolation and are expressed in Volterra integral form, so that the fractional and the classical components are both treated in a single nonlinear system, and that each variable is represented in a way suitable for its regularity.

The proposed framework is explored to understand the role of memory in the endothelial and inflammatory components in subsequent micro-vascular response to transient stress. Special emphasis is on the difference between the acute response to the imposed workload and the maintenance of vascular and metabolic disturbances after the stress has passed. The numerical formulation is tested by manufactured fractional problems and a coupled fractional-classical verification system to verify the accuracy, convergence and conditioning of the numerical formulation before applying it to the CMD model. The changes in the fractional order are then simulated physiologically to find how the magnitude and length of the response change to stress are altered.

To overcome the small order initial regularity of fractional differential equations, several high order strategies have been developed. These include Jacobi polyfractonomial and generalized-Jacobi spectral formulations, fractional pseudospectral differentiation and integration schemes and multi-domain spectral treatments to address nonsmooth temporal behavior. These techniques show that the accuracy of endpoint-adapted approximation spaces can be extremely high, even if the accuracy of standard polynomial spaces is low. The present work is not novel in the field of endpoint adaptation per se. Its value is in the use of an endpoint-fitted representation for the fractional variables and a physical-

time spectral representation for the classical variables in a single nonlinear Volterra system, with barycentric interpolation and an analytically assembled block Newton Jacobian.

In this context the present study is of two-fold contribution. First, it proposes a model of mixed fractional–classical CMD in which the endothelial function and inflammatory burden are memory elements, whereas the microvascular resistance and oxygen supply–demand mismatch are classical. Second, it constructs a hybrid spectral Volterra method that is singularity-fitted to this mixed structure, where the fractional variables are represented in a coordinate that is adapted to their endpoint behavior, while the classical variables are still represented in physical time. The resulting framework is analyzed by analytical properties, verification of manufactured solutions, and simulations of the CMD, with particular focus on the numerical reliability and the ability to maintain post-stress disturbances.

2. Mathematical Formulation of the CMD Model:.

To represent the interaction among pathological and haemodynamic processes,four normalized state variables are introduced. The variable $E(t)$ denotes endothelial function, $I(t)$ represents inflammatory and oxidative burden, $R(t)$ denotes microvascular resistance, and $H(t)$ represents oxygen supply-demand mismatch. All four variables are scaled to the interval $[0,1]$. Larger values of I, R, and H correspond to a less favorable state, whereas a larger value of E represents better endothelial function. This normalization permits variables with different physiological meanings to be coupled within a common dynamical system without assigning artificial physical units to the state variables.

Before introducing the governing equations, time is nondimensionalized using a characteristic scale T_c. Let t_{phys} denote physical time and define

$$t = \frac{t_{\text{phys}}}{T_c}. \tag{1}$$

In this case, t is the dimensionless time that is used throughout the model. This scaling makes the fractional and classical subsystems share a common temporal variable, and does not require the use of physical units that are dependent on the fractional order in the model coefficients for varying α.

There are two external inputs that differentiate pathological and physiological demand. The time-independent parameter $G \in [0,1]$ influences the endothelial and inflammatory responses, and the time-dependent parameter $W(t) \in [0,1]$ influences the vascular and oxygen-mismatch responses. While E and I are given the same fractional order: $0 < \alpha \leq 1$, R and H still have the standard first order dynamics. Separation of mathematical representations for the history dependent and classical parts does not imply separation of time scales. The case $\alpha = 1$ returns to the corresponding fully classical system and it is taken as the reference for the numerical comparisons.

The schematic circuit diagram of the interaction structure of the model is summarized in Fig. 1, where the memory dependent fractional subsystem is separated from the classical subsystem, and the persistent burden G and the transient workload $W(t)$ are entered to the coupled dynamics of the model.

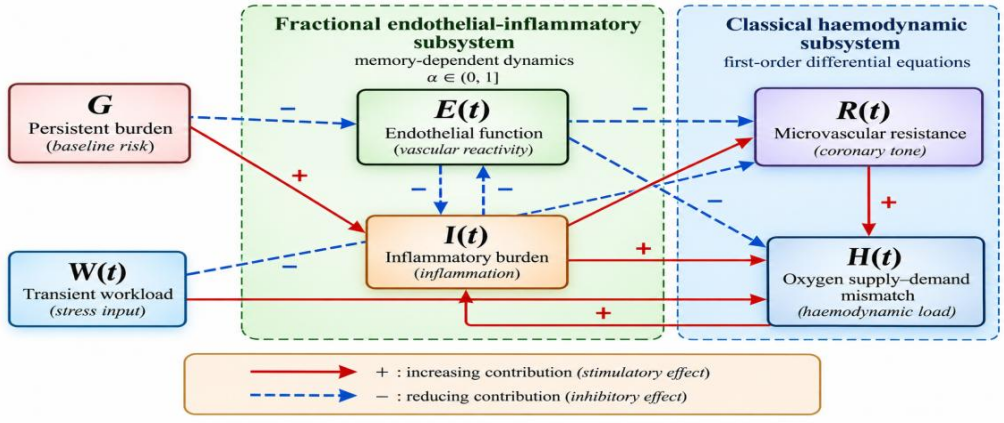


Figure 1. Mixed fractional-classical CMD model with schematic structure: the memory-dependent endothelial-inflammatory subsystem and the classical haemodynamic subsystem as well as the main interactions with persistent cardio metabolic burden G and transient workload $W(t)$. Positive and negative signs denote increasing and reducing contributions, respectively.(Source : The diagram was prepared by the researcher.)

With these definitions, the CMD model is written as

$$c_{D_t^\alpha} E = k_E(1-E) - a_{EI} IE - a_{EG} GE, \quad (2a)$$

$$c_{D_t^\alpha} I = k_I G(1-I) + a_{IH} H(1-I) - d_I I - a_{IE} EI, \quad (2b)$$

$$\frac{dR}{dt} = \frac{1}{\tau_R}[a_R(1-E)(1-R) + b_R I(1-R) - c_R W(t) ER - d_R R], \quad (2c)$$

$$\frac{dH}{dt} = a_H W(t) R(1-H) + b_H I(1-H) - c_H EH - d_H H. \quad (2d)$$

Here, ${}^{C}D_t^\alpha$ denotes the Caputo derivative of order $0 < \alpha \leq 1$. The first two equations define the fractional endothelial-inflammatory subsystem, whereas the last two retain classical first-order dynamics for microvascular resistance and oxygen supply-demand mismatch. The two representations remain fully coupled through the nonlinear interaction terms.

Equation (2a) represents a balance between recovery and impairment. The term $k_E(1-E)$ drives endothelial function toward its normalized upper state, whereas the terms $a_{EI} IE$ and $a_{EG} GE$ represent, respectively, the adverse influences assigned in the model to inflammatory burden and persistent cardio-metabolic stress. The structure is inspired by the widespread linkage between CMD and endothelial dysfunction, inflammation and oxidative stress [2,3] and is bounded normalized formulation of the coupled system.

The total inflammatory and oxidative burden changes is described by equation (2b): the activation from persistent cardiometabolic burden is $k_I\, G(1-I)$; and the activation from additional oxygen supply-demand mismatch is $a_{IH}\, H(1-I)$; $d_I\, I$ is for natural resolution; and $a_{IE}\, EI$ is the regulatory influence attributed in the model to preserved endothelial function. These terms together provide a bounded nonlinear description, with inflammation being caused by a chronic background burden and haemodynamic mismatch, and intrinsic resolution and endothelial regulation being opposed.

Equation (2c) describes the evolution of normalized microvascular resistance. The terms $a_R(1-E)(1-R)$ and $b_R I(1-R)$ represent resistance-promoting effects associated with endothelial impairment and inflammatory burden, respectively. In contrast, the term $c_R W(t) ER$ represents workload-induced vasodilatory regulation, whose effectiveness is modulated by preserved endothelial function. Thus, increasing workload does not directly increase resistance; rather, CMD is represented through an impaired capacity to reduce resistance when endothelial function is compromised. The term $d_R R$ provides additional relaxation toward lower resistance. This formulation is consistent with the reduced coronary vasodilatory reserve and impaired exercise-induced flow augmentation reported in CMD.

Equation (2d) describes the evolution of myocardial mismatch under changing workload and microvascular conditions. The term $a_H W(t) R(1-H)$ represents the combined influence of transient demand and elevated microvascular resistance, while $b_H I(1-H)$ accounts for the contribution assigned to inflammatory burden. In contrast, $c_H EH$ represents the reducing influence associated with preserved endothelial function, and $d_H H$ describes intrinsic relaxation of the mismatch. This structure is consistent with the recognized roles of endothelial dysfunction, altered microvascular resistance, and impaired coronary flow regulation in CMD [1-3].

The model is completed by prescribing the initial state

$$E(0) = E_0, I(0) = I_0, R(0) = R_0, H(0) = H_0, \quad (3)$$

with

$$(E_0, I_0, R_0, H_0) \in [0,1]^4.$$

For $0 < \alpha < 1$, the Caputo derivative appearing in the endothelial and inflammatory equations is defined by

$${}^{C}D_t^\alpha f(t) = \frac{1}{\Gamma(1-\alpha)} \int_0^t \frac{f'(s)}{(t-s)^\alpha} ds \quad (4)$$

where $\Gamma(\cdot)$ denotes the Gamma function. Unlike the ordinary first derivative, this operator depends on the previous evolution of f over the interval $[0, t]$, thereby introducing a nonlocal temporal dependence into the fractional subsystem. In the limiting case $\alpha = 1$, the Caputo derivative reduces to the ordinary first derivative, and the endothelial-inflammatory subsystem becomes classical. This nonlocal structure provides the mathematical basis for representing This nonlocal structure provides the mathematical basis for representing memory in the endothelial and inflammatory variables [7,8].

To represent a temporary increase in physiological demand, the workload is prescribed as the smooth pulse

$$W(t) = W_0 + \frac{A_W}{2}\left[\tanh\left(\frac{t-t_1}{\sigma}\right) - \tanh\left(\frac{t-t_2}{\sigma}\right)\right] \quad (5)$$

$$W_0 \geq 0, A_W \geq 0, W_0 + A_W \leq 1, t_1 < t_2, \sigma > 0.$$

Here, W_0 denotes the baseline workload, A_W controls the additional stress amplitude, t_1 and t_2 define the principal stress interval, and σ determines the smoothness of the transition into and out of that interval. The smooth form avoids an abrupt forcing discontinuity and is well suited to the spectral approximation used later, while also separating the transient stress phase from the subsequent recovery period.

All model coefficients are assumed to be non-negative, with $\tau_R > 0$. Their roles are summarized in Table 1 according to the interactions represented in the governing equations, including endothelial recovery and impairment, inflammatory activation and resolution, microvascular resistance regulation, and the development and relaxation of oxygen supply-demand mismatch. These mechanisms are consistent with the established pathophysiological description of coronary micro-vascular dysfunction [1-3].

Table 1. Model parameters and their interpretation

Parameter	Interpretation
$\boldsymbol{k_E}$	Endothelial recovery rate
$\boldsymbol{a_{EI}}$	Effect of inflammatory burden on endothelial impairment
$\boldsymbol{a_{EG}}$	Effect of persistent cardiometabolic burden on endothelial impairment
$\boldsymbol{k_I}$	Inflammatory activation associated with the background burden
$\boldsymbol{a_{IH}}$	Increase in inflammatory burden induced by oxygen supply-demand mismatch
$\boldsymbol{d_I}$	Natural resolution rate of inflammatory burden
$\boldsymbol{a_{IE}}$	Regulatory effect of preserved endothelial function on inflammation
$\boldsymbol{a_R}$	Contribution of endothelial impairment to microvascular resistance
$\boldsymbol{b_R}$	Contribution of inflammation to microvascular resistance
$\mathbf{c_R}$	Strength of workload-induced, endothelial-modulated reduction in microvascular resistance
$\mathbf{d_R}$	Natural relaxation rate of microvascular resistance
$\boldsymbol{\tau_R}$	Characteristic time scale of the resistance response
$\mathbf{a_H}$	Effect of workload and resistance on oxygen supply-demand mismatch
$\mathbf{b_H}$	Contribution of inflammation to oxygen supply-demand mismatch
$\mathbf{c_H}$	Protective contribution of endothelial function to reducing mismatch
$\mathbf{d_H}$	Natural relaxation rate of oxygen supply-demand mismatch

3. Mathematical Properties

3.1 Positivity and invariant region

Proposition 1. Let

$$\Omega = [0,1]^4$$

be the admissible state region. Assume that all model coefficients are non-negative, $\tau_R > 0, W(t) \geq 0$, and that the initial state satisfies

$$(E_0, I_0, R_0, H_0) \in \Omega.$$

Then every solution of the CMD system remains in Ω throughout its interval of existence; that is,

$$0 \leq E(t), I(t), R(t), H(t) \leq 1.$$

Proof. Consider first $0 < \alpha < 1$, and suppose that a solution exists on $[0, T]$. Assume, for contradiction, that one component leaves Ω for the first time at $t = t^* > 0$. For the fractional variables, the first-contact extremum principle for the Caputo derivative [13] prevents crossing of a lower boundary when the governing right-hand side is non-negative there, and prevents crossing of an upper boundary when it is non-positive. The classical variables are treated by the usual inward-pointing vector-field condition.

For the endothelial variable, at $E = 0$,

$$^C D_t^\alpha E = k_E \geq 0,$$

whereas at $E = 1$,

$$^c D_t^\alpha E = -a_{EI} I - a_{EG} G \leq 0.$$

Hence, $E(t)$ cannot leave the interval [0,1].

For the inflammatory variable, at $I = 0$,

$$^C D_t^\alpha I = k_I G + a_{IH} H \geq 0,$$

whereas at $I = 1$,

$$^C D_t^\alpha I = -d_I - a_{IE} E \leq 0.$$

Therefore, $I(t)$ also remains in [0,1].

For the classical microvascular-resistance variable, the revised resistance equation gives, at $R = 0$,

$$\left.\frac{dR}{dt}\right|_{R=0} = \frac{a_R(1-E) + b_R I}{\tau_R} \geq 0,$$

while at $R = 1$,

$$\left.\frac{dR}{dt}\right|_{R=1} = -\frac{c_R W(t) E + d_R}{\tau_R} \leq 0.$$

Thus, the vector field points inward at both boundaries of the admissible interval for R. Similarly, for the oxygen supply-demand mismatch, at $H = 0$,

$$\left.\frac{dH}{dt}\right|_{H=0} = a_H W(t) R + b_H I \geq 0,$$

whereas at $H = 1$,

$$\left.\frac{dH}{dt}\right|_{H=1} = -c_H E - d_H \leq 0.$$

Hence, $H(t)$ also remains in [0,1].

All four components therefore satisfy inward or tangential boundary conditions on $\partial\Omega$. Consequently,

$$(E(t), I(t), R(t), H(t)) \in \Omega$$

for every t in the interval of existence. When $\alpha = 1$, the fractional equations reduce to ordinary differential equations, and the same conclusion follows directly from the classical inward-pointing boundary argument.

3.2 Existence and Uniqueness.

Proposition 2. Assume that the initial state belongs to the invariant region

$$(E_0, I_0, R_0, H_0) \in \Omega,$$

that all model coefficients satisfy the assumptions of Proposition 1, and that $W(t)$ is continuous and bounded on a finite interval $[0, T]$. Then the CMD system admits a unique solution on $[0, T]$ for the prescribed initial data.

Proof. Let F_E, F_I, F_R, and F_H denote the right-hand sides of Eqs. (2a)-(2d), respectively. The fractional equations are equivalent to the Volterra integral equations for $0 < \alpha < 1$, and the classical equations have the corresponding ordinary integral equations.

$$E(t) = E_0 + \frac{1}{\Gamma(\alpha)} \int_0^t (t-s)^{\alpha-1} F_E(E(s), I(s), G) ds$$

$$I(t) = I_0 + \frac{1}{\Gamma(\alpha)} \int_0^t (t-s)^{\alpha-1} F_I(E(s), I(s), H(s), G) ds$$

The classical equations can be written as

$$R(t) = R_0 + \int_0^t F_R\big(E(s), I(s), R(s), W(s)\big) ds,$$

$$H(t) = H_0 + \int_0^t F_H\big(E(s), I(s), R(s), H(s), W(s)\big) ds.$$

Let $h > 0$ and consider the Banach space $X = C([0, h]; \mathbb{R}^4)$, equipped with the norm

$$\|X\|_\infty = \max_{0 \le t \le h} \max\{|E(t)|, |I(t)|, |R(t)|, |H(t)|\}.$$

The integral relations above define a mixed Volterra operator $\mathcal{T}: X \to X$. Since the right-hand sides are polynomial in the state variables, they are locally Lipschitz on $\mathbb{R}^4$. Choose a closed ball centered at the initial state on which they admit common bounds $M > 0$ and $L > 0$. For sufficiently small h, the corresponding mixed Volterra operator maps the closed trajectory ball into itself and satisfies,

$$\|\mathcal{T}X - \mathcal{T}Y\|_\infty \le L\left(\frac{h^\alpha}{\Gamma(\alpha+1)} + h\right) \|X - Y\|_\infty.$$

Choosing h sufficiently small so that

$$L\left(\frac{h^\alpha}{\Gamma(\alpha+1)} + h\right) < 1$$

makes $\mathcal{T}$ a contraction. The Banach fixed-point theorem thus provides a unique local solution. In a compact region Ω, the same Lipschitz bound is valid for Proposition 1 and the solution stays within this region. This local argument can then be extended to successive subintervals until a fixed time T is reached, for any fixed time T less than infinity. Therefore, the solution is uniquely given on $[0, T]$

3.3 Continuous Dependence and Well-Posedness

Proposition 3. Let

$$X(t) = (E(t), I(t), R(t), H(t))$$

and

$$\tilde{X}(t) = (\tilde{E}(t), \tilde{I}(t), \tilde{R}(t), \tilde{H}(t))$$

be two solutions corresponding to initial states X_0 and $\tilde{X}_0$, with the same model parameters and workload $W(t)$. Let

$$d(t) = \|X(t) - \tilde{X}(t)\|_\infty, d_0 = \left\|X_0 - \tilde{X}_0\right\|_\infty.$$

Because the fractional and classical right-hand sides are Lipschitz continuous on **Ω**, there exist constants $L_f, L_c > 0$ such that

$$d(t) \le d_0 + \frac{L_f}{\Gamma(\alpha)} \int_0^t (t-s)^{\alpha-1} d(s)ds + L_c \int_0^t d(s)ds \quad (7)$$

For $0 < \alpha < 1$ and $0 \le t \le T$,

$$\int_0^t d(s)ds = \int_0^t (t-s)^{\alpha-1}(t-s)^{1-\alpha} d(s)ds \le T^{1-\alpha} \int_0^t (t-s)^{\alpha-1} d(s)ds.$$

Hence

$$d(t) \le d_0 + C_T \int_0^t (t-s)^{\alpha-1} d(s)ds \quad (8)$$

Where

$$C_T = \frac{L_f}{\Gamma(\alpha)} + L_c T^{1-\alpha}.$$

Applying the generalized fractional Gronwall inequality, [15] follows.

$$d(t) \le d_0 \, E_\alpha \, (C_T \, \Gamma(\alpha) t^\alpha \,). \quad (9)$$

Therefore, the solution is dependent on the initial data on each finite interval. If $\alpha = 1$, then the estimate is the classical Gronwall bound. The initial value problem for the CMD is thus well posed in Ω.

4. Hybrid Singularity-Fitted Spectral Volterra Method .

4.1 Volterra representation.

For the numerical treatment, the state vector is separated into the fractional variables E and I and the classical variables R and H. Using the equivalence between a Caputo initial-value problem and its Volterra integral form [14], the fractional subsystem is written as

$$E(t) = E_0 + \frac{1}{\Gamma(\alpha)} \int_0^t (t-s)^{\alpha-1} F_E(E(s), I(s), G)ds \quad (10a)$$

$$I(t) = I_0 + \frac{1}{\Gamma(\alpha)} \int_0^t (t-s)^{\alpha-1} F_I(E(s), I(s), H(s), G)ds \quad (10b)$$

The classical subsystem is represented by

$$R(t) = R_0 + \int_0^t F_R(E(s), I(s), R(s), W(s))ds \quad (10c)$$

$$H(t) = H_0 + \int_0^t F_H(E(s), I(s), R(s), H(s), W(s))ds \quad (10d)$$

Here, F_E, F_I, F_R, and F_H denote the nonlinear right-hand sides of Eqs. (2a)-(2d), respectively. Equations (10a) and (10b) contain the weakly singular kernel $(t-s)^{\alpha-1}$ when $0 < \alpha < 1$. This is a unique characteristic of the fractional integral which needs to be handled separately in the numerical approximation. When a spectral representation is used directly in physical time, the accuracy can therefore become less as the regularity of the endpoints becomes less [9-12]. The formulation developed below only alters the way the fractional variables are represented, the classical variables are still in physical time

4.2 Singularity-Fitted Coordinate and Spectral Representation

Let T denote the final dimensionless time of the computational interval. For the fractional variables, introduce the transformed coordinate

$$\xi = \left(\frac{t}{T}\right)^\alpha, 0 \le \xi \le 1, \quad (11)$$

with inverse mapping

$$t = T\xi^{1/\alpha} \quad (12)$$

The transformation in Eq. (11) is motivated by the type of local structure that is commonly found in fractional solutions close to $t = 0$. In the case of a fractional component, having terms of the form $t^{m\alpha}$, then Eq. (11) yields

$t^{m\alpha} = T^{m\alpha}\,\xi^m.$ (13)

Hence, the terms $t^{m\alpha}$ are just ordinary powers of ξ and are therefore most naturally represented by a polynomial spectral basis. Not all of the terms produced by the coupled system are regularized in the transformation, however. In particular, mixed powers $t^{m\alpha+n}$ are mapped to $\xi^{m+n/\alpha}$ and may retain limited regularity at $\xi = 0$. Consequently, the method is not claimed to provide universal spectral convergence; its accuracy is governed by the regularity of the transformed solution in the fitted coordinate. The mapping also changes the physical distribution of the fractional collocation points, since $t_j^{(f)} = Tx_j^{1/\alpha}$. Hence, comparisons across different values of α use the same polynomial degree and quadrature order but not identical physical node locations. The convergence and conditioning studies reported below are therefore used to verify that this redistribution does not materially affect the reported CMD trends. Related endpoint-adapted spectral strategies for solutions with limited initial regularity are discussed in [9-12].

$E_N(t) = \sum_{n=0}^{N} e_n T_n(2\xi - 1),$ (14a)

$I_N(t) = \sum_{n=0}^{N} i_n T_n(2\xi - 1),$ (14b)

where T_n denotes the Chebyshev polynomial of degree n. By contrast, the classical variables retain the physical-time coordinate

$\eta = \frac{t}{T}, 0 \le \eta \le 1,$ (15)

and are represented as

$R_N(t) = \sum_{n=0}^{N} r_n T_n(2\eta - 1),$ (16a)

$H_N(t) = \sum_{n=0}^{N} h_n T_n(2\eta - 1).$ (16b)

When $\alpha = 1$, Eq. (11) reduces to $\xi = t/T$, so the fitted and classical coordinates coincide. Because the method is formulated through the Volterra integral equations, the mapped coordinate is not differentiated numerically; the singular factor associated with differentiating $t = T\xi^{1/\alpha}$ is therefore avoided.

4.3 Analytical Regularization of the Weakly Singular Kernel.

Consider the fractional Volterra term

$\mathcal{J}_\alpha[F](t) = \frac{1}{\Gamma(\alpha)} \int_0^t (t-s)^{\alpha-1} F(s)ds$ (17)

The factor $(t-s)^{\alpha-1}$ is weakly singular as $s \to t^-$when $0 < \alpha < 1$. To remove this singularity analytically before quadrature, introduce the change of variables

$s = t\left(1 - z^{1/\alpha}\right), 0 \le z \le 1.$ (18)

Then

$t - s = tz^{1/\alpha}\,,\; ds = -\frac{t}{\alpha} z^{1/\alpha - 1} dz.$ (19)

Hence,

$(t-s)^{\alpha-1} ds = -\frac{t^\alpha}{\alpha} z^{(\alpha-1)/\alpha} z^{1/\alpha - 1} dz = -\frac{t^\alpha}{\alpha} dz$ (20)

because

$$\frac{\alpha - 1}{\alpha} + \frac{1}{\alpha} - 1 = 0.$$

After reversing the integration limits, the fractional integral becomes

$$\mathcal{J}_\alpha[F](t) = \frac{t^\alpha}{\Gamma(\alpha+1)} \int_0^1 F\left(t\left(1 - z^{1/\alpha}\right)\right) dz. \quad (21)$$

Thus, the weak endpoint singularity is cancelled exactly before numerical integration is performed. For the fractional CMD subsystem,

$$E(t) = E_0 + \frac{t^\alpha}{\Gamma(\alpha+1)} \int_0^1 F_E(s(z))dz \quad (22a)$$

$$I(t) = I_0 + \frac{t^\alpha}{\Gamma(\alpha+1)} \int_0^1 F_I(s(z))dz \quad (22b)$$

where

$$s(z) = t\left(1 - z^{1/\alpha}\right)$$

Using Gauss-Legendre nodes z_q and weights w_q on [0,1], the regularized integral is approximated by

$$\mathcal{J}_\alpha[F](t) \approx \frac{t^\alpha}{\Gamma(\alpha+1)} \sum_{q=1}^{Q} w_q F\left(t\left(1 - z_q^{1/\alpha}\right)\right) \quad (23)$$

w_q represent gauss-legendre weights at the node z_q, Equation (21) shows that the weak singularity is removed analytically before numerical quadrature is applied. At $t = 0$, the prefactor t^α vanishes and the initial condition is recovered exactly. When $\alpha = 1$, Eq. (18) reduces to $s = t(1 - z)$, and Eq. (21) becomes the standard integral representation of a first-order problem. The regularized form in Eq. (23) is used in the subsequent spectral discretization.

4.4 Collocation grids and barycentric coupling

Let

$$x_j = \frac{1}{2}\left[1 - \cos\left(\frac{j\pi}{N}\right)\right], j = 0, \dots, N. \quad (24)$$

denote the shifted Chebyshev-Gauss-Lobatto points on [0,1]. The fractional variables are collocated at the physical times

$$t_j^{(f)} = T x_j^{1/\alpha}, \quad (25)$$

The classical variables are collocated at the physical-time nodes

$$t_j^{(c)} = T x_j, j = 0, \dots, N. \quad (26)$$

Accordingly, the fractional grid is distributed according to the fitted coordinate introduced in Eq. (11), whereas the classical grid remains distributed directly in physical time. When $\alpha = 1$, Eqs. (25) and (26) generate the same set of temporal nodes.

Because the nonlinear system couples variables represented on different grids, values of the state variables must be evaluated at common quadrature and collocation points. For a fractional variable $Y \in \{E, I\}$, define

$$\xi(s) = \left(\frac{s}{T}\right)^\alpha \quad (27)$$

Its barycentric interpolant is then written as

$$Y_N(s) = \frac{\sum_{j=0}^{N} \frac{\lambda_j Y_j}{\xi(s) - x_j}}{\sum_{j=0}^{N} \frac{\lambda_j}{\xi(s) - x_j}}, \quad (28)$$

where the Chebyshev barycentric weights are

$$\lambda_j = (-1)^j \delta_j, \delta_0 = \delta_N = \frac{1}{2}, \delta_j = 1, 1 \le j \le N - 1. \quad (29)$$

If $\xi(s) = x_k$ for some grid index k, the interpolated value is assigned directly as $Y_N(s) = Y_k$, thereby avoiding the removable singularity in Eq. (28).

For a classical variable $Y \in \{R, H\}$, introduce the normalized physical-time coordinate

$$\eta(s) = \frac{s}{T}. \tag{30}$$

The corresponding barycentric interpolant is

$$Y_N(s) = \frac{\sum_{j=0}^{N} \frac{\lambda_j Y_j}{\eta(s)-x_j}}{\sum_{j=0}^{N} \frac{\lambda_j}{\eta(s)-x_j}}. \tag{31}$$

As in the fractional case, when $\eta(s) = x_k$, the nodal value Y_k is used directly. The fractional equations are collocated at the nodes $t_j^{(f)}$, whereas the classical equations are collocated at $t_j^{(c)}$. The coupling between the two temporal grids is therefore effected entirely through barycentric spectral interpolation. In matrix form, values transferred from the classical grid to the fractional grid and conversely are written as $\mathrm{R}^{(f)} = P_{c\to f}\mathrm{R}^{(c)}, \mathrm{H}^{(f)} = P_{c\to f}\mathrm{H}^{(c)}$, and $\mathrm{E}^{(c)} = P_{f\to c}\mathrm{E}^{(f)}, \mathrm{I}^{(c)} = P_{f\to c}\mathrm{I}^{(f)}$. For numerical evaluation, a target point is treated as coincident with a source node whenever its distance from that node does not exceed $10^{-13}\max(1, |t|)$; the corresponding nodal value is then used directly. Otherwise, the standard barycentric formula is applied. This avoids fragile exact floating-point equality tests while retaining spectral interpolation between the two grids[16].

4.5 Nonlinear algebraic system and exact Newton Jacobian

Let the unknown nodal values be collected in the vector

$$\mathrm{U} = [\mathrm{E}^T, \mathrm{I}^T, \mathrm{R}^T, \mathrm{H}^T]^T, \tag{32}$$

where $\mathbf{E}, \mathbf{I}, \mathbf{R}, \mathbf{H} \in \mathbb{R}^N$ contain the unknown nodal values at indices $i = 1, \dots, N$, with the prescribed initial values at $i = 0$ excluded from the Newton vector. Hence, $U \in \mathbb{R}^{4N}$, ordered as $U = [\mathbf{E}^T, \mathbf{I}^T, \mathbf{R}^T, \mathbf{H}^T]^T$. The residual equations in Eqs. (33a)-(34b) are correspondingly enforced for $i = 1, \dots, N$; E_i and I_i refer to the fractional physical grid $t_i^{(f)}$, whereas R_i and H_i refer to the classical grid $t_i^{(c)}$.

At each fractional collocation point $t_i^{(f)}$, the regularized Volterra equations in Eqs. (22a)-(22b), together with the quadrature rule in Eq. (23), define the residuals

$$\mathcal{R}_{E,i}(\mathrm{U}) = E_i - E_0 - \frac{\left(t_i^{(f)}\right)^{\alpha}}{\Gamma(\alpha+1)} \sum_{q=1}^{Q} w_q F_E\left(s_{iq}\right), \tag{33a}$$

$$\mathcal{R}_{I,i}(\mathrm{U}) = I_i - I_0 - \frac{\left(t_i^{(f)}\right)^{\alpha}}{\Gamma(\alpha+1)} \sum_{q=1}^{Q} w_q F_I\left(s_{iq}\right), \tag{33b}$$

where

$$s_{iq} = t_i^{(f)}\left(1 - z_q^{1/\alpha}\right).$$

For the classical subsystem, Gauss-Legendre quadrature gives

$$\mathcal{R}_{R,i}(\mathrm{U}) = R_i - R_0 - t_i^{(c)} \sum_{q=1}^{Q} w_q F_R\left(\hat{s}_{iq}\right), \tag{34a}$$

$$\mathcal{R}_{H,i}(\mathrm{U}) = H_i - H_0 - t_i^{(c)} \sum_{q=1}^{Q} w_q F_H\left(\hat{s}_{iq}\right), \tag{34b}$$

with $\hat{s}_{iq}$ denoting the corresponding quadrature points on $\left[0, t_i^{(c)}\right]$, where $\hat{s}_{iq} = t_i^{(c)} z_q$.The complete nonlinear algebraic system is written compactly as

$$\mathcal{R}(\mathrm{U}) = 0. \tag{35}$$

Newton iteration is then applied as

$$\mathrm{J}\left(\mathrm{U}^{(m)}\right)\Delta\mathrm{U}^{(m)} = -\mathcal{R}\left(\mathrm{U}^{(m)}\right), \tag{36}$$

followed by

$$\mathrm{U}^{(m+1)} = \mathrm{U}^{(m)} + \Delta\mathrm{U}^{(m)} \quad (37)$$

The Jacobian

$$\mathrm{J}(\mathrm{U}) = \frac{\partial \mathcal{R}}{\partial \mathrm{U}}, \quad (38)$$

is assembled analytically. Since barycentric interpolation is linear in the nodal values, the Jacobian entries follow directly from the interpolation weights and the exact partial derivatives of the nonlinear reaction terms.

For the endothelial equation,

$$\frac{\partial F_E}{\partial E} = -k_E - a_{EI}I - a_{EG}G, \frac{\partial F_E}{\partial I} = -a_{EI}E. \quad (39)$$

For the inflammatory equation,

$$\frac{\partial F_I}{\partial E} = -a_{IE}I, \quad (40a)$$

$$\frac{\partial F_I}{\partial I} = -k_I G - a_{IH}H - d_I - a_{IE}E, \quad (40b)$$

$$\frac{\partial F_I}{\partial H} = a_{IH}(1 - I). \quad (40c)$$

For the microvascular-resistance equation,

$$\frac{\partial F_R}{\partial E} = -\frac{a_R(1-R)+c_R W(t)R}{\tau_R}, \quad (41a)$$

$$\frac{\partial F_R}{\partial I} = \frac{b_R(1-R)}{\tau_R}, \quad (41b)$$

$$\frac{\partial F_R}{\partial R} = -\frac{a_R(1-E)+b_R I+c_R W(t)E+d_R}{\tau_R}. \quad (41c)$$

For the oxygen supply-demand equation,

$$\frac{\partial F_H}{\partial E} = -c_H H, \quad (42a)$$

$$\frac{\partial F_H}{\partial I} = b_H(1 - H), \quad (42b)$$

$$\frac{\partial F_H}{\partial R} = a_H W(t)(1 - H), \quad (42c)$$

$$\frac{\partial F_H}{\partial H} = -a_H W(t)R - b_H I - c_H E - d_H. \quad (42d)$$

All remaining partial derivatives are zero. The resulting Newton matrix therefore has a natural four-block structure associated with the variables E, I, R, and H.

For a prescribed polynomial degree N and quadrature order Q, the fractional and classical collocation grids, barycentric interpolation matrices, and quadrature mappings are assembled once and reused throughout the nonlinear iteration. All computations were performed in MATLAB R2023 using double-precision arithmetic. Newton iteration was terminated when the infinity norm of the full nonlinear residual satisfied $\|\mathcal{R}(U)\|_\infty \leq 10^{-11}$, with a maximum of 60 iterations. The initial solution at $\alpha = 1$ was formed from the prescribed initial state, while subsequent fractional-order cases used continuation in α by interpolating the previously converged solution onto the current grids. Each Newton correction was obtained from the analytically assembled block Jacobian by direct linear solution, and a backtracking line search reduced the damping factor by one half whenever the trial residual failed to decrease; the minimum permitted damping factor was 2^{-14}. The Jacobian conditioning was monitored using MATLAB's reciprocal condition estimator, with 10^{-10} used as a warning level and 10^{-13} as the failure threshold. No explicit scaling or preconditioning was applied.

For the final CMD simulations, $N = 120$ and $Q = 500$ were used for both the regularized Volterra operators and the Gaussian evaluation of integral response metrics. A dense grid of 12,001 points was employed only for diagnostic extrema, plotting, and root bracketing; recovery times were refined from the continuous spectral interpolants rather than read from this grid. The choice $Q = 500$ was supported

by the quadrature study in Section 5.3, where increasing Q beyond approximately 400 produced only marginal changes in the numerical error. All interpolation and quadrature matrices required by a given (N, α) case were preassembled before Newton iteration.

The construction of temporal and physical aggregation networks can be carried out through matrix algebra, quadratic operations, and the determination of residuals for Volterra equations. The system is formulated and solved using a damped Newton iterative method, incorporating the Jacobian matrix. Within the MATLAB environment, any convergent solution leads to the derivation of a new formulation for the fractional derivative.

5. Numerical Verification

5.1 Nonlinear manufactured fractional problem

The first verification problem isolates the fractional component of the method while retaining nonlinear dependence on the unknown solution. Consider

$$ {}^{C}D_t^{\alpha}u(t) + \lambda(t)u(t) + \mu(t)u^2(t) = g(t), \quad 0 < \mathrm{t} \leq 1\,, \tag{43}$$

with

$$\lambda(t) = 0.7 + 0.25t + 0.10\sin(2\pi t), \quad \mu(t) = 0.25 + 0.10\cos(\pi t). \tag{44}$$

The forcing term $g(t)$ is constructed analytically so that the exact solution is

$$u(t) = 1 + t^{\alpha} + 0.4t^{2\alpha} + 0.2t^{3\alpha} + 0.15t^{\alpha+1} + 0.10t^{2\alpha+1}. \tag{45}$$

The required fractional derivatives are evaluated from the Caputo identity

$$ {}^{C}D_t^{\alpha}t^{\beta} = \frac{\Gamma(\beta+1)}{\Gamma(\beta+1-\alpha)}t^{\beta-\alpha}, \beta > 0, \tag{46}$$

which gives $g(t)$ exactly [14].

The exact solution in Eq. (45) contains several fractional-power terms and therefore provides a direct test of the endpoint-fitted representation. The forcing function is obtained by substituting Eq. (45) into Eq. (43) using the identity in Eq. (46). The problem was solved with $Q = 500$ Gauss-Legendre points. Table 2 compares the standard physical-time Chebyshev approximation with the singularity-fitted formulation at $N = 64$.

Table 2. Maximum errors for the nonlinear manufactured fractional problem at $N = 64$ using the standard and singularity-fitted spectral formulations.

α	Standard error	Fitted error	Improvement
0.95	8.72×10^{-6}	7.16×10^{-10}	1.22×10^{4}
0.85	6.38×10^{-5}	1.13×10^{-9}	5.66×10^{4}
0.70	4.79×10^{-4}	4.40×10^{-10}	1.09×10^{6}

The standard approximation deteriorates as α decreases, consistent with the reduced endpoint regularity of the solution. In contrast, the fitted representation maintains errors near $10^{-9} - 10^{-10}$ over the tested range. Newton iteration converged in four to five steps, with final residuals below 10^{-12}.

5.2 Coupled fractional–classical manufactured verification

The second verification problem tests the complete hybrid architecture in a coupled nonlinear setting. On $0 \leq t \leq 1$, consider

$$ {}^{c}D_t^{\alpha}E + a_E E + b_{EI}EI + b_{ER}ER = g_E(t), \tag{47a}$$

$${}^{c}D_t^{\alpha} I + a_I I + b_{IE} EI + b_{IH} IH = g_I(t), \tag{47b}$$

$$\frac{dR}{dt} + a_R R + b_{RE} RE + b_{RI} RI = g_R(t), \tag{47c}$$

$$\frac{dH}{dt} + a_H H + b_{HE} HE + b_{HR} HR + b_{HI} HI = g_H(t). \tag{47d}$$

The coefficients are chosen as

$$a_E = 0.40, b_{EI} = 0.30, b_{ER} = 0.15,$$
$$a_I = 0.35, b_{IE} = 0.25, b_{IH} = 0.20,$$
$$a_R = 0.50, b_{RE} = 0.20, b_{RI} = 0.25,$$
$$a_H = 0.45, b_{HE} = 0.15, b_{HR} = 0.20, b_{HI} = 0.10.$$

The forcing functions are obtained by substituting the exact manufactured solution

$$E(t) = 0.72 + 0.08t^{\alpha} + 0.03t^{2\alpha} + 0.015t^{\alpha+1} \tag{48a}$$

$$I(t) = 0.18 + 0.05t^{\alpha} + 0.025t^{2\alpha} + 0.010t^{\alpha+1} \tag{48b}$$

$$R(t) = 0.24 + 0.05t + 0.02t^2 + 0.01\sin(\pi t) \tag{48c}$$

$$H(t) = 0.10 + 0.04t + 0.015t^2 + 0.008\sin(2\pi t) \tag{48d}$$

The forcing functions g_E, g_I, g_R, and g_H are obtained by substituting Eqs. (48a)-(48d) into Eqs. (47a)-(47d). The corresponding initial values are $E(0) = 0.72, I(0) = 0.18, R(0) = 0.24$, and $H(0) = 0.10$. The fractional derivatives are evaluated using Eq. (46), while the ordinary derivatives of the classical components are obtained directly from Eqs. (48c) and (48d).

$$\mathcal{E}_{\max} = \max\{\|E - E_N\|_{\infty}, \|I - I_N\|_{\infty}, \|R - R_N\|_{\infty}, \|H - H_N\|_{\infty}\}. \tag{49}$$

The fractional orders $\alpha = 0.95, 0.85$, and 0.70 were examined over increasing polynomial degrees. In the standard formulation, all four variables are represented on the physical-time Chebyshev grid, whereas the hybrid formulation applies the fitted coordinate only to E and I, while R and H remain in physical time. Table 3 reports the combined maximum error defined in Eq. (49) at $N = 64$.

Table 3. Combined maximum errors for the coupled fractional–classical manufactured system at $N = 64$ using the standard and hybrid singularity-fitted formulations.

α	Standard $\mathcal{E}_{\infty}$	Hybrid $\mathcal{E}_{\infty}$	Error reduction
0.95	6.97×10^{-7}	7.18×10^{-11}	9.72×10^{3}
0.85	5.10×10^{-6}	1.13×10^{-10}	4.50×10^{4}
0.70	3.83×10^{-5}	4.46×10^{-11}	8.58×10^{5}

The standard approximation loses accuracy as α decreases, whereas the hybrid representation maintains errors near 10^{-10} over the tested range. For $\alpha = 0.70$ and $N = 64$, the hybrid errors in the classical variables were 8.25×10^{-14} for R and 2.12×10^{-14} for H, showing that the fitted treatment of the fractional variables does not degrade the accuracy of the classical components. Newton iteration converged in four iterations in all reported cases, with final residuals at approximately machine precision.

A complementary non-aligned manufactured test was also considered to assess the limitation of the fitted map when the exact solution contains mixed powers that are not integer powers of $\xi = (t/T)^{\alpha}$. In this case, the proposed fitted formulation remained accurate, but it was not uniformly superior to alternative regularity-adapted representations. At $N = 64$, the fitted maximum errors were approximately $3.37 \times 10^{-6}, 3.02 \times 10^{-6}$, and 1.97×10^{-6} for $\alpha = 0.95,0.85$, and 0.70 , respectively, while a power-graded Chebyshev representation achieved errors of order 10^{-8}. This confirms that the principal advantage of the proposed mapping is tied to problems whose dominant endpoint structure is reasonably aligned with $t^{m\alpha}$, rather than constituting a universal accuracy advantage.

5.3 Quadrature sensitivity

Because the regularized Volterra operator is evaluated by Gauss-Legendre quadrature, the influence of the quadrature order Q was examined separately from the spectral degree. For the most demanding tested case, $\alpha = 0.70$ and $N = 80$, the maximum error decreased from 1.10×10^{-9} at $Q = 160$ to 1.94×10^{-10} at $Q = 300$, and to 1.64×10^{-10} at $Q = 400$. Increasing the quadrature order to $Q = 600$ changed the error only marginally, to 1.61×10^{-10}. This behavior indicates that the quadrature contribution becomes negligible once Q is sufficiently large, after which the remaining error is governed primarily by the spectral approximation. On this basis, $Q = 500$ was adopted for the coupled verification problem.

Taken together, the manufactured tests show that the singularity-fitted representation substantially improves the resolution of the fractional endpoint behavior, while the hybrid coupling preserves the accuracy of the classical subsystem. These results provide the numerical basis for the CMD simulations considered next.

6. CMD Numerical Results

6.1 Simulation setting

The CMD system was simulated over the dimensionless interval $0 \le t \le 120$ using the initial state

$$E_0 = 0.82, I_0 = 0.16, R_0 = 0.22, H_0 = 0.08,$$

with a persistent cardiometabolic burden $G = 0.30$. The transient workload was prescribed by Eq. (5) with

$$W_0 = 0.20, A_W = 0.60, t_1 = 10, t_2 = 20, \sigma = 1.5.$$

The model parameters were

$$k_E = 0.20, a_{EI} = 0.50, a_{EG} = 0.22,$$
$$k_I = 0.18, a_{IH} = 0.35, d_I = 0.16, a_{IE} = 0.25,$$
$$a_R = 0.45, b_R = 0.40, c_R = 0.20, d_R = 0.30, \tau_R = 0.80,$$
$$a_H = 0.55, b_H = 0.22, c_H = 0.60, d_H = 0.08.$$

These values define a normalized exploratory regime and are not intended as patient-specific or clinically calibrated parameters. These values define a normalized exploratory regime and are used to examine the response of the mixed fractional-classical system under a controlled parameter setting. Because varying α with fixed coefficients also changes effective fractional kinetics, this issue is examined separately through the controlled-kinetics comparison in Section 6.2. The fractional order was varied over

$$\alpha \in \{1.00,0.95,0.90,0.85,0.80,0.75,0.70\},$$

with $\alpha = 1$ serving as the classical reference case. For each fractional order , two simulations were performed. The control case retained the baseline workload $W(t) = W_0$, whereas the stress case used the transient workload defined by Eq. (5) with the parameter values given above. Stress-induced deviations were then defined relative to the corresponding control trajectory as

$$\Delta E(t) = E_{\text{control}}(t) - E_{\text{stress}}(t) \quad (50a)$$
$$\Delta I(t) = I_{\text{stress}}(t) - I_{\text{control}}(t) \quad (50b)$$
$$\Delta R(t) = R_{\text{stress}}(t) - R_{\text{control}}(t) \quad (50c)$$
$$\Delta H(t) = H_{\text{stress}}(t) - H_{\text{control}}(t). \quad (50d)$$

The signs of $\Delta E, \Delta I$, and ΔH are chosen so that positive values indicate stress-related deterioration. For $\Delta R = R_{\text{stress}} - R_{\text{control}}$, the sign is retained explicitly: negative values indicate workload-induced reduction in microvascular resistance, whereas positive values indicate resistance above the corresponding control trajectory.

For a deviation $\Delta X(t)$, the post-stress accumulated response is defined as the area under its positive part over $[t_2, T]$, namely $\int_{t_2}^{T} \max\{\Delta X(t), 0\} dt$. The 5% recovery time $T_{05,X}$ is defined as the elapsed dimensionless time after stress offset t_2 at which the positive deviation has fallen below 5% of its maximum value and remains below that threshold for the rest of the computational interval. For non-monotone responses or multiple threshold crossings, the final downward crossing is used. Negative portions of the deviation do not contribute to the post-stress AUC or to the recovery threshold. If the 5% level is not reached permanently before T, the recovery time is reported as not reached within the simulated horizon. Threshold crossings are determined from the continuous spectral interpolant rather than from the discrete collocation nodes.

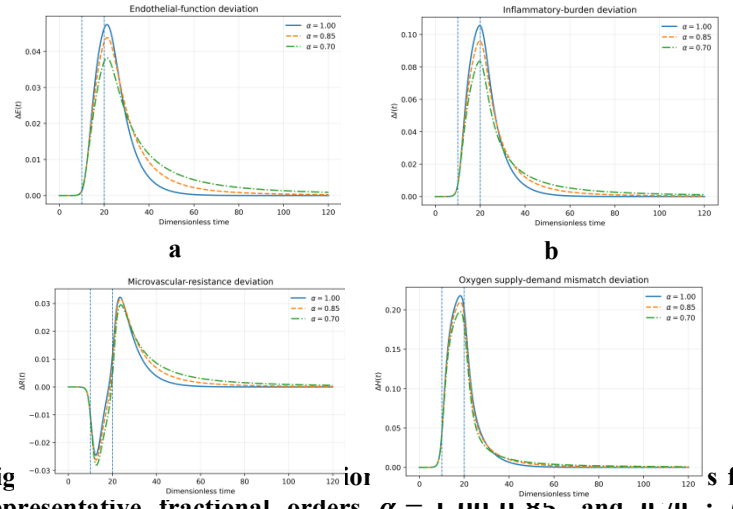


Fig ion s for representative fractional orders $\alpha = 1.00, 0.85$, and 0.70 : (a) endothelial function, (b) inflammatory burden, (c) microvascular resistance, and (d) oxygen supply-demand mismatch. Negative ΔR values indicate workload-induced reduction in resistance relative to the corresponding control trajectory. The vertical markers indicate stress onset and offset. Time is dimensionless.

.

6.2 Fractional-order dependence of the stress response

Figure 2 shows the stress-induced deviations defined in Eqs. (50a)-(50d) for representative fractional orders, while Table 4 summarizes the corresponding response metrics over the full range of α. Decreasing the fractional order from $\alpha = 1.00$ to 0.70 reduces all four positive peak deviations: from

0.0475 to 0.0382 for endothelial function, from 0.1055 to 0.0835 for inflammatory burden, from 0.0323 to 0.0295 for microvascular resistance, and from 0.2179 to 0.1978 for oxygen supply-demand mismatch. The effect of decreasing α is more pronounced after stress offset than during the acute phase. Over the same range, the post-stress AUC increases from 0.5190 to 0.7398 for ΔE, from 0.8714 to 1.0578 for ΔI, and from 0.3644 to 0.5403 for ΔR. The corresponding 5% recovery times also increase for all four state variables. These results indicate that, within the present normalized model, decreasing α has a stronger effect on post-stress persistence than on acute peak magnitude.

Because varying α while keeping all kinetic coefficients fixed can also alter the effective response time of the fractional subsystem, an additional controlled-kinetics comparison was performed. The coefficients in the endothelial and inflammatory equations were rescaled for each α so that their baseline local characteristic times matched the $\alpha = 1$ reference. Under this control, the increase in post-stress persistence was reduced but remained substantial. For $\alpha = 0.70$, the post-stress AUC ratios relative to $\alpha = 1$ were 1.266 for endothelial function and 1.312 for microvascular resistance, while the resistance recovery-time ratio remained 1.901.

These results indicate that the observed persistence cannot be attributed solely to the change in effective kinetics induced by varying the fractional order.

The robustness of these trends was further examined under structured perturbations of five mechanistically important parameters, two alternative initial states, and two alternative workload amplitudes. Each selected parameter was varied independently by $\pm 10\%$, while the fractional orders $\alpha = 1.00, 0.85$, and 0.70 were retained. Across all 15 scenarios, the post-stress AUCs of the endothelial and resistance deviations and the 5% recovery times of resistance and oxygen mismatch increased monotonically as α decreased. From $\alpha = 1.00$ to 0.70 , the corresponding ratios ranged from 1.339-1.518 for endothelial post-AUC, 1.381-1.581 for resistance post-AUC, 2.314-2.352 for $T_{05,R}$, and 1.230-1.340 for $T_{05,H}$. Thus, the principal persistence trends were preserved under moderate parameter, initial-state, and workload perturbations.

As an auxiliary sensitivity check, separate endothelial and inflammatory fractional orders were examined using the fractional Adams-Bashforth-Moulton predictor-corrector scheme [17], because the fitted spectral formulation presented above employs a common fractional order. Relative to the reference case $(\alpha_E, \alpha_I) = (0.85, 0.85)$, reducing only α_E to 0.70 increased the endothelial and resistance post-stress AUCs by approximately 7.0% and 7.6%, respectively, and increased $T_{05,R}$ by 15.0%. Reducing only α_I to 0.70 produced larger changes, increasing the corresponding AUCs by approximately 9.1% and 11.5% and increasing $T_{05,R}$ by 36.7%. These results indicate that the observed persistence trend is not restricted to the common-order assumption, although the inflammatory fractional order has the stronger influence within this limited sensitivity comparison.

Table 4. Stress-response metrics for all state variables at different fractional orders; recovery times are reported in dimensionless time.

α	Peak ΔE	Peak ΔI	Peak ΔR	Peak ΔH	Post-AUC ΔE	Post-AUC ΔI	Post-AUC ΔR	Post-AUC ΔH	T05, E	T05, I	T05, R	T05, H
1.00	0.0475	0.1055	0.0323	0.2179	0.5190	0.8714	0.3644	1.0433	25.14	21.76	26.08	16.54
0.95	0.0464	0.1028	0.0322	0.2157	0.5633	0.9216	0.3963	1.0698	29.21	24.55	29.80	17.50
0.90	0.0453	0.0996	0.0320	0.2129	0.6082	0.9685	0.4293	1.0928	34.16	27.83	34.24	18.48

α	Peak ΔE	Peak ΔI	Peak ΔR	Peak ΔH	Post-AUC ΔE	Post-AUC ΔI	Post-AUC ΔR	Post-AUC ΔH	T05, E	T05, I	T05, R	T05, H
0.85	0.0439	0.0961	0.0316	0.2098	0.6513	1.0090	0.4621	1.1101	40.12	31.64	39.48	19.44
0.80	0.0422	0.0922	0.0311	0.2062	0.6898	1.0398	0.4930	1.1194	47.22	35.97	45.61	20.30
0.75	0.0403	0.0880	0.0304	0.2022	0.7206	1.0572	0.5198	1.1181	55.62	40.80	52.73	20.95
0.70	0.0382	0.0835	0.0295	0.1978	0.7398	1.0578	0.5403	1.1042	65.45	46.03	60.86	21.28

Note: Post-AUC values are computed from the positive part of each stress-induced deviation over [t_2, T]. Recovery times T05,X denote dimensionless elapsed time after stress offset.

All reported 5% recovery thresholds were reached before $T = 120$; the latest was $T_{05,E} = 65.45$ for $\alpha = 0.70$, corresponding to $t \approx 85.45$ after the stress offset at $t_2 = 20$. After the workload returned to baseline, the computed stress-control differences continued to decay toward the common baseline response.

6.3 Numerical convergence and conditioning

The numerical reliability of the revised CMD simulations was examined by polynomial refinement for the representative fractional orders $\alpha = 1.00, 0.85$, and 0.70 , using $N = 80, 100, 120$, and 140 . The solution at $N = 140$ was used as the reference for the final-resolution comparison. Successive refinement produced a consistent reduction in the trajectory differences for all four stress-induced deviations. Between $N = 120$ and $N = 140$, the maximum infinity-norm difference was 6.1×10^{-5}, 6.2×10^{-5}, and 6.3×10^{-5} for ΔH at $\alpha = 1.00, 0.85$, and 0.70 , respectively, while the corresponding differences in $\Delta E, \Delta I$, and ΔR were smaller. The scalar response metrics were also stable at the final refinement: the largest relative difference at $N = 120$ was 0.0142% for $\alpha = 1.00$, 0.0375% for $\alpha = 0.85$, and 0.0751% for $\alpha = 0.70$. These values indicate that $N = 120$ provides a sufficiently resolved representation for the response metrics reported in Section 6.2.

Table 5. Convergence and conditioning indicators for the revised CMD simulations at N = 120, using N = 140 as the reference resolution.

α	$\|\|\Delta H_{120} - \Delta H_{140}\|\|_\infty$	Maximum relative metric difference (%)	Minimum RCOND at N = 120
1.00	6.1×10^{-5}	0.0142	1.58×10^{-3}
0.85	6.2×10^{-5}	0.0375	2.84×10^{-3}
0.70	6.3×10^{-5}	0.0751	2.86×10^{-3}

Note: The N = 140 solution is used only as the reference resolution for this refinement comparison.

All nonlinear solves converged over the tested resolutions, and no violation of the admissible state bounds was detected. At $N = 120$, the final nonlinear residuals remained below the prescribed Newton tolerance, while the minimum reciprocal condition estimates were $1.58 \times 10^{-3}, 2.84 \times 10^{-3}$, and 2.86×10^{-3} for $\alpha = 1.00, 0.85$, and 0.70 , respectively. The values are still considerably higher than the failure limit and do not reveal any deterioration in the conditionings as the fractional order decreases within the range tested. For the final simulations of the CMD, the $N = 120$ discretization was therefore retained, while the $N = 140$ resolution was only used in the refinement study as the reference resolution.

The measured cost remained modest over the tested resolutions: the paired control-stress computations required approximately $0.03 - 0.21$ s per (N, α) case, while the memory associated with the principal preassembled interpolation and Volterra matrices increased from approximately 7.62 MB at $N = 80$ to 13.52 MB at $N = 140$.

As an independent cross-check, the revised CMD system was also integrated using a fractional Adams–Bashforth–Moulton predictor-corrector scheme [17] with 4000 uniform time steps. The maximum difference between this time-stepping solution and the spectral-Volterra solution was 6.2×10^{-5}, 6.3×10^{-5}, and 6.3×10^{-5} for $\alpha = 1.00, 0.85$, and 0.70, respectively. Refining the time-stepping discretization from 2000 to 4000 steps produced changes of only $O(10^{-5})$ or smaller in all four stress-induced deviations, providing an independent numerical consistency check for the CMD simulations.

7. Discussion

Lowering α primarily lengthens recovery rather than amplifying the acute response. From $\alpha = 1.00$ to 0.70, all positive peak deviations decrease, whereas the post-stress AUCs of E, I, and R increase and all four 5% recovery times become longer. Because fractional dynamics are assigned only to E and I, the persistence observed in R and H arises through nonlinear coupling.

The controlled-kinetics, structured-perturbation, and separate-order tests show that this trend is not solely due to changes in the effective kinetics, or to the common-order assumption.

The numerical evidence also helps to make sense of the range of the fitted representation. It works well if the dominant endpoint structure is $t^{m\alpha}$, but not if it is the non-aligned one, as the non-aligned benchmark indicates. Refinement, conditioning and independent time-stepping results suggest that the principle trends in the CMD are not numerical-resolution artifacts.

The model is still in the exploratory stage. Normalizing G and $W(t)$ are not measured variables and combining inflammatory and oxidative effects to the single variable I reduces dimensionality and does not allow the separate contributions of these two effects to be identified. In a calibrated extension, these quantities could be related to suitable cardiometabolic and workload observables, with T_c selected from the physical time scale of the calibration protocol.

8. Conclusion

The mixed fractional–classical CMD model and the singularity-fitted spectral–Volterra method for modelling the coupled dynamics of the model were proposed in this study. The fitted coordinate system is used to get a better resolution when the dominant fractional endpoint structure is parallel to the mapping, whereas the non-aligned benchmark demonstrates that other regularity-adapted representations might be more suitable in other regimes. The reductions in the fractional order in the revised CMD simulations mostly result in longer post-stress recovery, but not in higher acute peak deviations, and this is seen in the controlled-kinetics and the sensitivity tests. The numerical consistency of the results is provided by polynomial refinement, conditioning analysis and independent time stepping. The parameters and external inputs are normalized and not clinically estimated, so the results are to be considered computational evidence from the model, and not predictions of patient-specific results.

Code and Data Availability. The MATLAB source files and numerical data supporting the reported computations are provided as Supplementary Material.

References:

1. Vrints, C., Andreotti, F., Koskinas, K. C., et al. 2024 ESC Guidelines for the management of chronic coronary syndromes. *European Heart Journal*, 45(36), 3415–3537 (2024). doi: 10.1093/eurheartj/ehae177.
2. Kunadian, V., Chieffo, A., Camici, P. G., Berry, C., Escaned, J., Maas, A. H. E. M., et al. An EAPCI Expert Consensus Document on Ischaemia with Non-Obstructive Coronary Arteries. *European Heart Journal*, 41(37), 3504–3520 (2020). doi: 10.1093/eurheartj/ehaa503.
3. Zhu, C., Miao, L., Wei, K., Shi, D., Gao, J. Coronary microvascular dysfunction. *Microvascular Research*, 153, 104652 (2024). doi: 10.1016/j.mvr.2024.104652.
4. Pompei, G., Ganzorig, N., Kotanidis, C. P., Alkhalil, M., Collet, C., Sinha, A., Perera, D., Beltrame, J., Kunadian, V. Novel diagnostic approaches and management of coronary microvascular dysfunction. *American Journal of Preventive Cardiology*, 19, 100712 (2024). doi: 10.1016/j.ajpc.2024.100712.
5. Fan, L., Wang, H., Kassab, G. S., Lee, L. C. Review of cardiac–coronary interaction and insights from mathematical modeling. *WIREs Mechanisms of Disease*, 16(3), e1642 (2024). doi: 10.1002/wsbm.1642.
6. Yong, E., Latief, J., Wang, Y., Erlinge, D., Dahlgren, A., Kotecha, T., Muthurangu, V., Torii, R. A lumped parameter model of the coronary circulation incorporating time-varying resistance, intramyocardial pressure and vascular compliance. *Journal of Biomechanics*, 189, 112679 (2025). doi: 10.1016/j.jbiomech.2025.112679.
7. Calatayud, J., Jornet, M., Pinto, C. M. A. On the interpretation of Caputo fractional compartmental models. *Chaos, Solitons & Fractals*, 186, 115263 (2024). doi: 10.1016/j.chaos.2024.115263.
8. Cusseddu, D. Fractional derivatives in biomathematical models with memory: A critical discussion. *Journal of Mathematical Biology*, 92(3), 39 (2026). doi: 10.1007/s00285-026-02353-x.
9. Algazaa, S. A. T., Saeidian, J. Spectral methods utilizing generalized Bernstein-like basis functions for time-fractional advection–diffusion equations. *Mathematical Methods in the Applied Sciences*, 48(2), 1411–1429 (2025). doi: 10.1002/mma.10390.
10. Zaky, M. A. A new endpoint-adaptive spectral method for nonlinear tempered fractional terminal value problems with non-smooth solutions. *Applied Numerical Mathematics*, 225, 76–86 (2026). doi: 10.1016/j.apnum.2026.02.003.
11. Zayernouri, M., Karniadakis, G. E. Fractional spectral collocation method. *SIAM Journal on Scientific Computing*, 36(1), A40–A62 (2014). doi: 10.1137/130933216.
12. Zayernouri, M., Karniadakis, G. E. Exponentially accurate spectral and spectral element methods for fractional ODEs. *Journal of Computational Physics*, 257, 460–480 (2014). doi: 10.1016/j.jcp.2013.09.039.
13. Luchko, Y. Maximum principle for the generalized time-fractional diffusion equation. *Journal of Mathematical Analysis and Applications*, 351(1), 218–223 (2009). doi: 10.1016/j.jmaa.2008.10.018.
14. Diethelm, K., Ford, N. J. Analysis of fractional differential equations. *Journal of Mathematical Analysis and Applications*, 265(2), 229–248 (2002). doi: 10.1006/jmaa.2000.7194.
15. Ye, H., Gao, J., Ding, Y. A generalized Gronwall inequality and its application to a fractional differential equation. *Journal of Mathematical Analysis and Applications*, 328(2), 1075–1081 (2007). doi: 10.1016/j.jmaa.2006.05.061.

16. Berrut, J.-P., Trefethen, L. N. Barycentric Lagrange interpolation. *SIAM Review*, 46(3), 501–517 (2004). doi: 10.1137/S0036144502417715.
17. Diethelm, K., Ford, N. J., Freed, A. D. A predictor-corrector approach for the numerical solution of fractional differential equations. *Nonlinear Dynamics*, 29, 3–22 (2002). doi: 10.1023/A:1016592219341

An Interface-Consistent hp-Adaptive Spectral Element–Radau IIA Method for Multilayer Dual-Phase-Lag Bioheat Transfer in Clark-II Dynamic Thermography

Almutasim Abdulmuhsin Hamed*
Department of Mathematics, College of Computer Science and Mathematics,
University of Mosul, Mosul, Iraq.
*Corresponding author: almutasim@uomosul.edu.iq
ORCID: https://orcid.org/0000-0001-6289-7376

An Interface-Consistent hp-Adaptive Spectral Element–Radau IIA Method for Multilayer Dual-Phase-Lag Bioheat Transfer in Clark-II Dynamic Thermography

Almutasim Abdulmuhsin Hamed*
Department of Mathematics, College of Computer Science and Mathematics,
University of Mosul, Mosul, Iraq.
*Corresponding author: almutasim@uomosul.edu.iq
ORCID: https://orcid.org/0000-0001-6289-7376

Abstract:

An interface-consistent mesh- and polynomial-degree-adaptive spectral-element method is developed for multilayer dual-phase-lag bioheat transfer and applied to axisymmetric Clark-II dynamic thermography. The discretization fits material interfaces and retains the transmitted physical heat flux as an independent variable, advanced with the temperature field by the two-stage Radau IIA method. This preserves tissue-specific relaxation parameters without a separate temporal approximation at interfaces. Manufactured-solution tests demonstrate spatial convergence, third-order temporal accuracy, and accurate transient dual-phase-lag flux transmission. Under a smooth cooling–rewarming protocol, the tumour-to-healthy surface contrast reaches approximately 0.237–0.240 °C at the end of cooling. Parameter sensitivity is dominated by tumour geometry and perfusion within the tested ranges. For a surface-contrast error below 0.001 °C, adaptive cycle 7 uses 24.1% fewer complete state unknowns than the qualifying uniform discretization, with reductions of 42.5% in assembly-plus-solution time and 39.2% in explicitly stored core matrices. These costs refer to the selected discretizations, not the cumulative adaptive sequence. The results support the numerical formulation for the prescribed model but do not establish experimental distinguishability between the Pennes and dual-phase-lag predictions.

Keywords: Dual-phase-lag bioheat transfer; hp-adaptive spectral element method; Radau IIA; dynamic thermography; multilayer tissue; interface heat flux.

MSC Classification: 65M70, 65M50, 65L06, 92C50

1 INTRODUCTION:

The Pennes bioheat model couples Fourier conduction with blood perfusion and metabolic heat generation (Pennes, 1948). The dual-phase-lag (DPL) model introduces separate delays in the heat flux and temperature gradient to represent non-Fourier thermal responses (Tzou, 1995). Its time-differential formulations depend on the phase-lag parameters and the truncation of the delayed constitutive relation (Quintanilla & Racke, 2006), while reported biological phase lags remain experimentally uncertain (Azhdari et al., 2025; Azhdari et al., 2026). Dynamic thermography provides a setting for examining these effects through the transient response of tumour and healthy tissue to cooling and rewarming (Horvat & Iljaž, 2025).

The spectral element method (SEM) combines high-order polynomial approximation with elementwise geometric flexibility. Since its introduction by Patera (1984), it has been applied to various partial differential equations, including the Pennes bioheat equation studied by Dehghan and Sabouri (2012). The contribution of the present work lies in combining SEM with a DPL-consistent multilayer interface formulation, high-order implicit time integration, and local hp-adaptation.

In multilayer DPL tissue, thermal conductivity, perfusion, metabolic heat generation, and phase-lag parameters may be discontinuous across material interfaces. Perfect thermal contact requires continuity of temperature and transmitted physical heat flux. Because the DPL flux contains both spatial and temporal contributions, continuity of the conductivity-weighted temperature gradient alone does not represent the complete transient transmission condition (Horvat & Iljaž, 2025).

Horvat and Iljaž (2025) developed a boundary-element formulation for multilayer DPL bioheat transfer and applied it to Clark-II and Clark-IV dynamic thermography. Their results showed that the transient tumour-to-healthy contrast depends on the prescribed phase-lag parameters. In their interface treatment, the temporal derivatives entering the DPL relation were approximated by a first-order left-sided difference. The present method instead retains the transmitted physical heat flux as an independent interface variable and advances it with the temperature field using the same Radau IIA scheme. This removes the need for a separate interface time approximation while preserving the relaxation parameters of the adjoining tissues.

Spectral-element adaptivity may increase local resolution through element subdivision, polynomial enrichment, or both (Mavriplis, 1994). Modal information, including the decay of Legendre coefficients, has been used to guide the choice between h-refinement and p-enrichment (Dorao et al., 2009; Galvão et al., 2008). The cited studies do not combine anisotropic hp-adaptation with an independent physical interface-flux variable advanced by the same high-order time integrator as the temperature field in multilayer DPL thermography (Biswas et al., 2020; Dehghan & Sabouri, 2012; Dorao et al., 2009; Galvão et al., 2008; Horvat & Iljaž, 2025; Mavriplis, 1994). The contribution of the present work is the integration of these spatial, temporal, and interface treatments.

The contribution of this study is a multilayer DPL formulation in which temperature and the independent physical interface flux are advanced together by the two-stage Radau IIA method, while anisotropic hp-adaptation controls the spatial resolution. This treatment preserves tissue-dependent relaxation parameters and avoids a separate temporal approximation of the interface flux. Manufactured-solution tests assess spatial convergence, temporal accuracy, and interface transmission. The method is then applied to Clark-II dynamic thermography, and its computational performance is compared with uniform polynomial refinement at a prescribed surface-contrast accuracy.

2 RESEARCH METHOD

2.1 Mathematical Model

2.1.1 Dual-phase-lag Bioheat formulation

Let Ω denote the axisymmetric meridional domain, and let $\Omega_i \subset \Omega$ denote tissue region i . Within Ω_i the density ρ_i specific heat c_{it} thermal conductivity k_i perfusion rate $\omega_{i,}$ metabolic heat source $q_{m,i,}$ heat-flux phase lag τq_i temperature-gradient phase lag τT_i are constant. Their values may differ between adjoining tissues; hence, the model coefficients are piecewise constant over the Clark-II domain (Horvat & Iljaž, 2025).

The local energy balance in each perfused tissue region is written as

$$\rho_i c_i \frac{\partial T_i}{\partial t} = -\nabla \cdot q_i + \omega_i \rho_b c_b (T_b - T_i) + q_{m,i}, x \in \Omega_i \quad (1)$$

In Eq. (1), T_i and q_i denote the tissue temperature and physical heat-flux vector, respectively. The quantities T_β, ρ_β, and c_β are the arterial blood temperature, density, and specific heat. The final two terms represent Pennes perfusion heat exchange (Pennes, 1948) and volumetric metabolic heat generation.

For Fourier conduction, the physical heat flux satisfies

$$q_i = -k_i \nabla T_i.$$

In the DPL description introduced by Tzou (1995), the heat flux and temperature gradient are allowed to respond with distinct phase lags. Within tissue region Ω_i, the delayed constitutive relation is

$$\mathrm{q}_i(\mathrm{x}, t+\tau_{q,i}) = -k_i \nabla T_i(\mathrm{x}, t+\tau_{T,i}), \mathrm{x} \in \Omega_i \quad (2)$$

The parameters $\tau_{q,i}$ and $\tau_{T,i}$ denote the phase lags associated with the heat flux and temperature gradient, respectively. Expanding both sides of Eq. (2) about t and retaining first-order terms gives

$$\mathrm{q}_i + \tau_{q,i} \frac{\partial \mathrm{q}_i}{\partial t} = -k_i \left[\nabla T_i + \tau_{T,i} \frac{\partial}{\partial t}(\nabla T_i)\right] \quad (3)$$

Equation (3) is the first-order time-differential DPL constitutive relation adopted throughout this study.

Different truncations of the delayed relation lead to mathematically distinct DPL models and may exhibit different stability properties (Quintanilla & Racke, 2006). The phase-lag parameters are therefore treated here as prescribed tissue-dependent model quantities rather than universally established material constants; their reported values in biological-tissue studies remain subject to considerable experimental and modeling uncertainty (Azhdari et al., 2026)

For compact notation, define the perfusion heat-transfer coefficient by

$$P_i = \omega_i \rho_b c_b \quad (4)$$

Applying the operator

$$1 + \tau_{q,i} \frac{\partial}{\partial t}$$

to Eq. (1) and eliminating the heat-flux terms through Eq. (3), while assuming that the tissue parameters, T_b, and $q_{m,i}$ are independent of time within each region, gives

$$\left.\begin{aligned} \tau_{q,i}\rho_i c_i \frac{\partial^2 T_i}{\partial t^2} + \left(\rho_i c_i + \tau_{q,i} P_i\right)\frac{\partial T_i}{\partial t} = \\ k_i \nabla^2 T_i + \tau_{T,i} k_i \frac{\partial}{\partial t}(\nabla^2 T_i) + P_i(T_b - T_i) + q_{m,i}\,, \quad \mathbf{x} \in \Omega_i \end{aligned}\right\} \quad (5)$$

Equation (5) is the temperature-based DPL bioheat equation used in the subsequent formulation. When $\tau_{T,i} = 0$ and $\tau_{q,i} > 0$, Eq. (3) reduces to the single-phase-lag Cattaneo-Vernotte form (Azhdari et al., 2026; Tzou, 1995). If both phase lags vanish, Eq. (5) reduces to the classical Pennes equation

$$\rho_i c_i \frac{\partial T_i}{\partial t} = k_i \nabla^2 T_i + P_i(T_b - T_i) + q_{m,i} \quad (6)$$

Thus, the Pennes and DPL formulations considered here share the same local energy balance and differ through the constitutive description of heat conduction

2.1.2 Axisymmetric representation

The multilayer tissue domain and the Clark-II lesion are assumed rotationally symmetric about the z-axis. Hence, the temperature is independent of the azimuthal coordinate, and the Laplacian becomes

$$\nabla^2 T_i = \frac{\partial^2 T_i}{\partial r^2} + \frac{1}{r}\frac{\partial T_i}{\partial r} + \frac{\partial^2 T_i}{\partial z^2} \quad (7)$$

Substitution into Eq. (5) gives

$$\left.\begin{aligned}\tau_{q,i}\rho_i c_i \frac{\partial^2 T_i}{\partial t^2} + \left(\rho_i c_i + \tau_{q,i} P_i\right)\frac{\partial T_i}{\partial t} = k_i\left(\frac{\partial^2 T_i}{\partial r^2} + \frac{1}{r}\frac{\partial T_i}{\partial r} + \frac{\partial^2 T_i}{\partial z^2}\right)\\ +\tau_{T,i} k_i \frac{\partial}{\partial t}\left(\frac{\partial^2 T_i}{\partial r^2} + \frac{1}{r}\frac{\partial T_i}{\partial r} + \frac{\partial^2 T_i}{\partial z^2}\right) + P_i(T_b - T_i) + q_{m,i}\end{aligned}\right\} \quad (8)$$

At $r = 0$, Eq. (7) is interpreted in its regular axisymmetric limit together with the symmetry condition imposed in Section 2.1.5

2.1.3 Multilayer interface conditions

Let Γ_{ij} denote the interface between adjacent tissue regions Ω_i and Ω_j. Under perfect thermal contact, temperature continuity requires

$$T_i = T_j \text{ on } \Gamma_{ij} \quad (9)$$

while conservation of energy requires continuity of the transmitted physical heat flux

$$\mathrm{q}_i \cdot \mathrm{n}_i + \mathrm{q}_j \cdot \mathrm{n}_j = 0 \text{ on } \Gamma_{ij} \quad (10)$$

where n_i and n_j are the outward unit normals of the neighboring subdomains. These are the physical transmission conditions adopted throughout the multilayer model (Horvat & Iljaž, 2025).

For the DPL constitutive law, the normal heat flux in each tissue satisfies

$$q_{n,i} + \tau_{q,i}\frac{\partial q_{n,i}}{\partial t} = -k_i\left(\frac{\partial T_i}{\partial n_i} + \tau_{T,i}\frac{\partial}{\partial t}\frac{\partial T_i}{\partial n_i}\right),$$

with an analogous relation in Ω_j. Thus, the interface condition retains the tissue-dependent relaxation parameters and cannot, in general, be replaced by continuity of $k\partial T/\partial n$ alone.

2.1.4 Clark-II tumour geometry and material properties

The computational domain consists of epidermis, papillary dermis, reticular dermis, subcutaneous fat, and muscle. A cylindrical Clark-II tumour replaces part of the papillary dermis immediately beneath the epidermis. The axisymmetric domain has a radius of 20 mm and a total depth of 11.6 mm , while the tumour has a diameter of 2.0 mm and a thickness of 0.44 mm , occupying $0 \le r \le 1.0$ mm, $0.10 \le z \le 0.54$ mm. The geometry follows the Clark-II configuration reported by Horvat and Iljaž (2025). Figure 1 shows the axisymmetric tissue geometry.

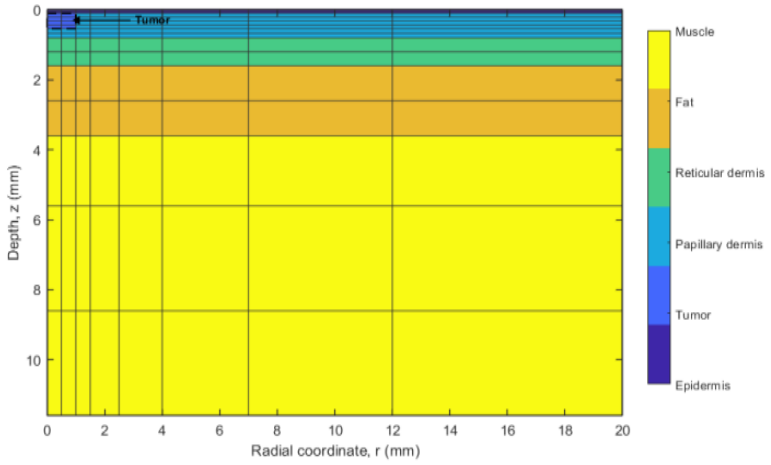


Figure 1. Axisymmetric multilayer Clark-II tissue geometry used in the dynamic-thermography simulations.

The geometrical dimensions, thermophysical properties, and baseline DPL parameters are listed in Table 1. The tissue dimensions and relaxation times follow (Horvat & Iljaž, 2025), whereas the thermophysical properties are adopted from the multilayer skin-tumour model of Iljaž et al. (2019). All parameters are treated as piecewise constant within their respective tissue regions.

Table 1. Geometrical, thermophysical, and DPL parameters adopted for the Clark-II tissue model.

Tissue	h (mm)	ρ (kg m^{-3})	c (J kg^{-1} K^{-1})	k (W m^{-1} K^{-1})	ω (s^{-1})	q_m (W m^{-3})	τ_q (s)	τ_T (s)
Epidermis	0.10	1200	3589	0.235	0	0	0.10	0.05
Tumour, Clark II	0.44	1030	3852	0.558	0.0063	3680	1.00	0.50
Papillary dermis	0.70	1200	3300	0.445	0.0002	368.1	0.77	0.38
Reticular dermis	0.80	1200	3300	0.445	0.0013	368.1	0.82	0.41
Fat	2.00	1000	2674	0.185	0.0001	368.3	0.72	0.36
Muscle	8.00	1085	3800	0.510	0.0027	684.2	0.73	0.37

To examine sensitivity to the phase-lag parameters, both relaxation times in each tissue are scaled by a common factor.

$$\tau_{q,i}^{(s)} = s\tau_{q,i}, \tau_{T,i}^{(s)} = s\tau_{T,i}, s \in \{1,5\} \quad (11)$$

The corresponding cases are denoted DPL-1x and DPL-5x. The common scaling preserves the ratio $\tau_{T,i}/\tau_{q,i}$ within each tissue. DPL-5x is used only as a sensitivity case and is not interpreted as a physiologically calibrated parameter set.

2.1.5 Initial and boundary conditions

The lower boundary is maintained at the arterial/core temperature

$$T(r, H, t) = T_b = 37°\text{C}, 0 \le r \le R. \tag{12}$$

At the skin surface, convective exchange is prescribed in terms of the outward physical heat flux

$$\text{q} \cdot \text{n} = h(t)[T - T_\infty(t)], z = 0 \tag{13}$$

The nominal 30 s cooling-70 s rewarming protocol follows (Horvat & Iljaž, 2025). The changes in the surface data are represented by continuously differentiable transitions of duration $\delta = 1$ s. Define

$$\chi(\xi) = 3\xi^2 - 2\xi^3, 0 \le \xi \le 1,$$

and

$$g(t) = h(t)[T_\infty(t) - T_b].$$

The prescribed boundary data are

$$(h(t), g(t)) = \begin{cases} (h_w, g_w) + (h_c - h_w, g_c - g_w)\chi\left(\frac{t}{\delta}\right), & 0 \le t \le \delta, \\ (h_c, g_c), & \delta < t \le 30, \\ (h_c, g_c) + (h_w - h_c, g_w - g_c)\chi\left(\frac{t-30}{\delta}\right), & 30 < t \le 30 + \delta, \\ (h_w, g_w), & 30 + \delta < t \le 100. \end{cases} \tag{14}$$

where

$$h_c = 50 \text{ W m}^{-2} \text{ K}^{-1}, \qquad T_{\infty,c} = 5°\text{C}, g_c = h_c\left(T_{\infty,c} - T_b\right),$$
$$h_w = 10 \text{ W m}^{-2} \text{ K}^{-1}, \qquad T_{\infty,w} = 22.4°\text{C}, g_w = h_w\left(T_{\infty,w} - T_b\right).$$

The transition function and its first derivative vanish appropriately at the interval endpoints, avoiding an impulsive change in the differentiated DPL boundary term.

Radial symmetry is imposed on the axis, while the outer radial boundary is insulated

$$\frac{\partial T}{\partial r} = 0 \text{ at } r = 0, \text{q} \cdot \text{n} = 0 \text{ at } r = R \tag{15}$$

The transient calculation starts from the steady pre-cooling field $T_0(\text{x})$, obtained under the rewarming ambient conditions. Since all temporal derivatives vanish at equilibrium, the initial DPL conditions are

$$T(\mathbf{x}, 0) = T_0(\mathbf{x}), \frac{\partial T}{\partial t}(\mathbf{x}, 0) = 0 \tag{16}$$

with the corresponding equilibrium heat flux

$$\text{q}(\text{x}, 0) = -k(\text{x})\nabla T_0(\text{x}) \tag{17}$$

2.1.6 Thermal contrast used as the quantity of interest

The quantity of interest (QoI) is the surface-temperature difference between the tumour center and a remote healthy-skin location. With the tumour centered at $r = 0$ and the healthy reference point taken at $r = R$, both on the skin surface $z = 0$, the thermal contrast is defined as

$$\Delta T(t) = T(0,0,t) - T(R, 0, t) \tag{18}$$

A positive value of ΔT therefore indicates that the surface above the tumour is warmer than the selected healthy-skin reference location. The same tumour-center-to-healthy-skin comparison is used in the Clark-II dynamic-thermography configuration of Horvat and Iljaž (2025).

2.2 Interface-Consistent hp-Adaptive Spectral Element-Radau IIA Formulation

2.2.1 Weak form of the multilayer DPL problem

Define the temperature excess above the arterial temperature by

$$\theta_i = T_i - T_b \tag{19}$$

Since T_b is constant, Eq. (5) becomes

$$\tau_{q,i}\rho_i c_i \frac{\partial^2 \theta_i}{\partial t^2} + \left(\rho_i c_i + \tau_{q,i} P_i\right)\frac{\partial \theta_i}{\partial t} - k_i \nabla^2 \theta_i - \tau_{T,i} k_i \frac{\partial}{\partial t}(\nabla^2 \theta_i) + P_i \theta_i = q_{m,i} \tag{20}$$

For an admissible test function w_i integration of the spatial terms by parts over Ω_i, gives

$$\begin{aligned}\left(\tau_{q,i}\rho_i c_i \frac{\partial^2 \theta_i}{\partial t^2}, w_i\right)_{\Omega_i} + \left(\left(\rho_i c_i + \tau_{q,i} P_i\right)\frac{\partial \theta_i}{\partial t}, w_i\right)_{\Omega_i} + (P_i \theta_i, w_i)_{\Omega_i} \\ + (k_i \nabla \theta_i, \nabla w_i)_{\Omega_i} + \left(\tau_{T,i} k_i \nabla \frac{\partial \theta_i}{\partial t}, \nabla w_i\right)_{\Omega_i} \\ - \left\langle k_i \frac{\partial \theta_i}{\partial n_i} + \tau_{T,i} k_i \frac{\partial}{\partial t}\left(\frac{\partial \theta_i}{\partial n_i}\right), w_i \right\rangle_{\partial \Omega_i} = \left(q_{m,i}, w_i\right)_{\Omega_i}.\end{aligned} \tag{21}$$

Here, n_i denotes the outward unit normal to Ω_i. Taking the normal component of the DPL constitutive relation gives

$$q_{n,i} + \tau_{q,i}\frac{\partial q_{n,i}}{\partial t} = -k_i\left[\frac{\partial \theta_i}{\partial n_i} + \tau_{T,i}\frac{\partial}{\partial t}\left(\frac{\partial \theta_i}{\partial n_i}\right)\right], q_{n,i} = \mathrm{q}_i \cdot \mathrm{n}_i \tag{22}$$

Consequently, the boundary contribution in Eq. (21) can be written as

$$\left\langle q_{n,i} + \tau_{q,i}\frac{\partial q_{n,i}}{\partial t}, w_i \right\rangle_{\partial \Omega_i}.$$

This identity fixes the sign convention used below and expresses the boundary term directly in terms of the physical DPL heat flux.

For the axisymmetric domain, the weighted inner products are

$$(u, v)_{\Omega_i} = \int_{\Omega_i} uvrdrdz\,, \langle u, v\rangle_{\partial \Omega_i} = \int_{\partial \Omega_i} uvrds \tag{23}$$

The common azimuthal factor 2π is omitted because it multiplies all terms of the weak formulation. The subsequent Galerkin discretization follows the standard spectral-element and spectral/hp-element framework (Karniadakis & Sherwin, 2005; Patera, 1984).

2.2.2 Spectral element approximation

The axisymmetric domain is partitioned into non-overlapping quadrilateral spectral elements whose boundaries conform to the tissue interfaces and the tumour boundary. Consequently, discontinuous material and DPL parameters remain confined to their respective tissue regions. Within an element Ω_e, the temperature excess is approximated on Legendre-Gauss-Lobatto (LGL) nodes by

$$\theta_h^{(e)}(\xi,\eta,t) = \sum_{a=0}^{p_r^{(e)}} \sum_{b=0}^{p_z^{(e)}} \Theta_{ab}^{(e)}(t)\ell_a(\xi)\ell_b(\eta)\,,(\xi,\eta) \in [-1,1]^2 \tag{24}$$

Here, ℓ_a and ℓ_b are the one-dimensional Lagrange basis functions, while $p_r^{(e)}$ and $p_z^{(e)}$ denote the local polynomial orders in the radial and depth directions. Their independent variation provides the anisotropic resolution used in Section 2.2.6.

For elemental basis functions $\phi_\alpha^{(e)}$, the axisymmetrically weighted mass and diffusion matrices are

$$M_{\alpha\beta}^{(e)} = \int_{\Omega_e} \phi_\alpha^{(e)}\phi_\beta^{(e)} r dr dz \tag{25}$$

and

$$K_{\alpha\beta}^{(e)} = \int_{\Omega_e} k_e \nabla\phi_\alpha^{(e)} \cdot \nabla\phi_\beta^{(e)} r dr dz \tag{26}$$

The remaining coefficients in Eq. (20) are assembled analogously. Element integrals are evaluated using Gauss quadrature of order higher than the local interpolation degree.

2.2.3 Interface flux formulation

Within each homogeneous tissue region, adjacent conforming spectral elements share temperature degrees of freedom (DOF) in the usual continuous Galerkin manner. Across a material interface Γ_{ij}, however, the temperature traces associated with regions Ω_i and Ω_j are retained independently prior to enforcing the transmission conditions (Boffi et al., 2013). For perfect thermal contact, temperature continuity is imposed as

$$\theta_i - \theta_j = 0 \ \text{ on } \Gamma_{ij} \tag{27}$$

Let n_i and n_j denote the outward unit normal of the two adjacent tissue regions, so that $\mathrm{n}_j = -\mathrm{n}_i$ on , Γ_{ij}. A single oriented interface variable is introduced to represent the transmitted physical normal heat flux:

$$\lambda_{ij} = \mathrm{q}_i \cdot \mathrm{n}_i = -\mathrm{q}_j \cdot \mathrm{n}_j \ \text{ on } \Gamma_{ij} \tag{28}$$

This definition fixes the sign convention independently of the local element orientation. Substitution of the normal DPL constitutive relation into the boundary term obtained by integration by parts gives, for region ,Ω_i

$$\langle \lambda_{ij} + \tau_{q,i}\dot{\lambda}_{ij}, w_i \rangle_{\Gamma_{ij}}, \tag{29}$$

whereas the corresponding contribution to the weak equation in Ω_j is

$$-\langle \lambda_{ij} + \tau_{q,j}\dot{\lambda}_{ij}, w_j \rangle_{\Gamma_{ij}} \tag{30}$$

The opposite signs in Eqs. (29) and (30) follow directly from the outward-normal convention in Eq. (28). The same physical flux is transmitted through both tissues, whereas the time-derivative term retains the relaxation parameter of the tissue being tested; therefore, no interfacial averaging is introduced.

The interface variable is discretized in the one-dimensional LGL nodal space associated with the tangential ,Γ temperature trace. On an interface segment

$$\lambda_h(s,t) = \sum_{a=0}^{p_\lambda} \Lambda_a(t)\ell_a(s),$$

where $\boldsymbol{\ell_a}$ denotes the Lagrange polynomial associated with the ath LGL trace node. For a vertical interface, the tangential coordinate is z and the interface polynomial order equals the depthwise trace order; for a horizontal interface, the tangential coordinate is r and the interface order equals the radial trace order. Matching trace spaces are preserved because the adaptive procedure assigns radial and depth wise orders by strips and introduces complete conforming grid lines during h-refinement. Consequently, the adjoining temperature traces have the same tangential polynomial degree, and each interface segment contains $\mathrm{p}\lambda + 1$ flux degrees of freedom.

The interface terms are assembled using the axisymmetrically weighted edge mass matrix:

$$S_{ab}^{\Gamma} = \int_{\Gamma} \ell_a(s)\ell_b(s) r ds$$

With the orientation of Eq. (28), the local contributions to the physical-flux coupling matrix are $+S^{\Gamma}$ on Ω_i and $-S^{\Gamma}$ on Ω_j. The corresponding contributions to the time-dependent flux matrix are $+\tau_{q,i}S^{\Gamma}$ and $-\tau_{q,j}S^{\Gamma}$, respectively. Their global assembly defines the matrices B and B_τ appearing in the semi-discrete formulation of Section 2.2.4. Temperature continuity is enforced independently at coincident LGL trace nodes through the algebraic constraint matrix G, whose interface rows have the form

$$\theta_i(s_a) - \theta_j(s_a) = 0, a = 0, \quad , p_\lambda.$$

At junctions shared by several material interfaces, direct assembly may produce linearly dependent continuity constraints. A rank-revealing QR factorisation of G retains only the independent constraint rows and the corresponding columns of B and Bt, thereby removing redundant constraint-flux pairs without altering the physical transmission conditions.

No mesh-independent inf-sup stability result is claimed for the discrete mixed formulation. Its algebraic stability was instead assessed over the nine reported discretizations from cycles 0-8. Numerical ranks were computed by singular value decomposition without additional row or column scaling. For each matrix A, singular values exceeding max(size(A)) × eps(σmax(A)) were counted, where eps denotes the floating-point spacing at the largest singular value in MATLAB. These checks assess algebraic rank at the stated tolerance; they do not establish mesh-independent inf-sup stability.Each discretization retained conforming interface traces and full interface rank in $G, B, B_\tau, GK^{-1}B$, and $GM_2^{-1}B_\tau$. In the final 45-element discretisation, p_λ ranged from 2 to 5. Removing 17 redundant junction constraints from the initial 94 interface degrees of freedom left 77 independent interface-flux variables, and each of the listed matrices had rank 77. Thus, no algebraic null interface-flux mode was detected. Flux accuracy and temperature continuity are assessed separately by the manufactured-interface test in Section 3.1.

2.2.4 Semi-discrete differential-algebraic system

After assembly of the elemental and interface contributions, the semi-discrete DPL system takes the form

$$M_2\ddot{\mathrm{u}} + C(t)\dot{\mathrm{u}} + K(t)\mathrm{u} + B\lambda + B_\tau\dot{\lambda} = \mathrm{f}(t) \tag{31}$$

subject to the discrete temperature-continuity constraints

$$G\mathrm{u} = 0 \tag{32}$$

Here, u contains the temperature degrees of freedom and λ contains the transmitted interface-flux variables. The matrices B and B_τ couple the interface flux and its time derivative to the neighboring tissue equations, while G imposes temperature continuity. Let C_0, K_0, and f_0 denote the interior contributions, and let S_s and s_s denote the surface mass matrix and load vector. The smoothed convective condition contributes

$$C(t) = C_0 + \tau_{q,s} h(t) S_s,$$
$$K(t) = K_0 + \left[h(t) + \tau_{q,s}\dot{h}(t)\right] S_s,$$
$$\mathrm{f}(t) = \mathrm{f}_0 + \left[g(t) + \tau_{q,s}\dot{g}(t)\right] \mathrm{s}_s,$$

where $\tau_{q,s}$ is the heat-flux relaxation time of the epidermis. These terms follow directly from differentiating the prescribed physical surface flux in the DPL formulation.

Defining $\mathrm{v} = \dot{\mathrm{u}}$ and the state vector $\mathrm{z} = [\mathrm{u}^\top, \mathrm{v}^\top, \lambda^\top]^\top$, Eqs. (31) and (32) can be written in first-order descriptor form as

$$E\dot{\mathrm{z}} = A(t)\mathrm{z} + \mathrm{F}(t) \tag{33}$$

where

$$E = \begin{bmatrix} I & 0 & 0 \\ 0 & M_2 & B_\tau \\ 0 & 0 & 0 \end{bmatrix}, A(t) = \begin{bmatrix} 0 & I & 0 \\ -K(t) & -C(t) & -B \\ G & 0 & 0 \end{bmatrix}, \mathrm{F}(t) = \begin{bmatrix} 0 \\ \mathrm{f}(t) \\ 0 \end{bmatrix}. \tag{34}$$

The zero block in the final row of E represents the algebraic temperature-continuity constraint. For the DPL cases considered here, M_2 is nonsingular because the heat-flux relaxation times are strictly positive. Introducing the transformed variable $w = M_2 v + B_\tau \lambda$ gives

$$\dot{\mathrm{u}} = M_2^{-1}\mathrm{w} - M_2^{-1} B_\tau \lambda,$$
$$\dot{\mathrm{w}} = \mathrm{f}(t) - K(t)\mathrm{u} - C(t) M_2^{-1}\mathrm{w} + [C(t) M_2^{-1} B_\tau - B]\lambda.$$

subject to $Gu = 0$. Differentiating the algebraic constraint once yields

$$G M_2^{-1} w - S_\tau \lambda = 0, S_\tau = G M_2^{-1} B_\tau.$$

If G has full row rank and S_τ is nonsingular, the interface flux is uniquely determined from the differentiated constraint. Under these conditions, the descriptor formulation has differentiation index two and the associated matrix pencil is regular.

For the final cycle- 8 discretization, G has rank 77 , while $\mathrm{S}\tau = \mathrm{GM}_2{}^{-1}\,\mathrm{B}\tau$ is a 77×77 matrix of rank 77 . Its smallest singular value is 6.34×10^{-4}, and the ratio of its smallest to largest singular values is 1.76×10^{-2}, confirming the nonsingularity condition stated above. The initial state is obtained from the constrained steady pre-cooling system $Ku_0 + B\lambda_0 = f_0$ and $Gu_0 = 0$, with $v_0 = 0$. The computed temperature-continuity residual is zero at the reported numerical precision.

2.2.5 Radau IIA time integration

The descriptor system in Eq. (33) is advanced using the two-stage Radau IIA collocation method. To distinguish the Runge-Kutta coefficients from the matrix A in Eq. (34), the Butcher matrix $\mathcal{A}$ is denoted by:

$$c = \begin{bmatrix} 1/3 \\ 1 \end{bmatrix}, \mathcal{A} = \begin{bmatrix} 5/12 & -1/12 \\ 3/4 & 1/4 \end{bmatrix}, b = \begin{bmatrix} 3/4 \\ 1/4 \end{bmatrix} \tag{35}$$

For a time step Δt, the stage states satisfy

$$\mathrm{Z}_i = \mathrm{z}_n + \Delta t \sum_{j=1}^{2} a_{ij} \mathrm{K}_j , \quad i = 1,2 \tag{36}$$

with stage derivatives determined from

$$E\mathrm{K}_i = A(t_n + c_i \Delta t)\mathrm{Z}_i + \mathrm{F}(t_n + c_i \Delta t), i = 1,2. \tag{37}$$

The solution is updated by

$$\mathrm{z}_{n+1} = \mathrm{z}_n + \Delta t \sum_{i=1}^{2} b_i \mathrm{K}_i. \tag{38}$$

The two-stage Radau IIA method is third-order, L-stable, and stiffly accurate (Hairer & Wanner, 1996). Because the interface flux is included in z, its temporal evolution is determined by the same stage equations as the temperature variables; no separate temporal approximation of the interface flux is introduced. The observed temporal order of the present descriptor formulation is verified numerically in Section 3.1.2.

Numerical regularity checks showed that the descriptor pencils $\sigma \mathrm{E} - \mathrm{A}$ were nonsingular for $\sigma = 0.1$, 1.0 , and 10.0 during both cooling and rewarming in the DPL- 1 × and DPL- 5 × cases. The corresponding Radau IIA stage matrices were also nonsingular for $\Delta \mathrm{t} = 0.50$ s and 0.25 s , confirming the solvability of the stage equations for the discretisations used in the simulations.

The transition endpoints at $t = 1{,}30$, and 31 s coincide with time-step endpoints. Within each transition, $h(t), \dot{h}(t), g(t)$, and $\dot{g}(t)$ are evaluated at the Radau IIA stage times. The temperature, its rate, and the transmitted interface flux are therefore advanced continuously through the prescribed changes in the surface data.

2.2.6 hp-Adaptive strategy

The adaptive procedure uses the temperature field at the end of cooling, $t = 30$ s. Within each element Ω_e, the nodal solution is transformed to the tensor-product Legendre representation

$$\theta_h^{(e)}(\xi, \eta) = \sum_{m=0}^{p_r^{(e)}} \sum_{n=0}^{p_z^{(e)}} a_{mn}^{(e)} L_m(\xi) L_n(\eta), \tag{39}$$

where $a_{mn}^{(e)}$ are the local modal coefficients. The relative high-mode content in the radial and depth directions is measured by

$$\eta_r^{(e)} = \left[\frac{\sum_{n=0}^{p_z^{(e)}} \left| a_{p_r^{(e)},n}^{(e)} \right|^2}{\sum_{m=0}^{p_r^{(e)}} \sum_{n=0}^{p_z^{(e)}} \left| a_{mn}^{(e)} \right|^2} \right]^{1/2} , \tag{40}$$

and

$$\eta_z^{(e)} = \left[\frac{\sum_{m=0}^{p_r^{(e)}} \left| a_{m,p_z^{(e)}}^{(e)} \right|^2}{\sum_{m=0}^{p_r^{(e)}} \sum_{n=0}^{p_z^{(e)}} \left| a_{mn}^{(e)} \right|^2} \right]^{1/2} \tag{41}$$

For element marking, the combined high-mode indicator is

$$\eta_e = \left[\frac{\sum_{j=0}^{p_z^{(e)}} \left| a_{p_r^{(e)} j}^{(e)} \right|^2 + \sum_{i=0}^{p_r^{(e)}} \left| a_{i p_z^{(e)}}^{(e)} \right|^2 - \left| a_{p_r^{(e)} p_z^{(e)}}^{(e)} \right|^2}{\sum_{i=0}^{p_r^{(e)}} \sum_{j=0}^{p_z^{(e)}} \left| a_{ij}^{(e)} \right|^2} \right]^{1/2} \tag{42}$$

The corner coefficient is subtracted to avoid counting the highest-order mixed mode twice. Normalization by the total modal energy renders ηe dimensionless and reduces the influence of the local temperature magnitude on element ranking.

Following the bulk-marking criterion (Dörfler, 1996), elements are ranked according to η_e. The smallest marked set $\mathcal{M}$ is selected such that

$$\sum_{e \in \mathcal{M}} \eta_e^2 \geq \vartheta \sum_e \eta_e^2 , \vartheta = 0.65.$$

For the directional refinement decision based on η_e for elements in M, define

$$\eta_{\max} = \max(\eta_r, \eta_z).$$

When $\eta_{\max} > 0.08$, h -refinement is considered. A coordinate direction is subdivided if its directional indicator is at least $0.8\eta_{\max}$ and the corresponding parent interval exceeds the prescribed minimum size. The minimum admissible intervals are 0.20 mm in the radial direction and 0.05 mm in depth. Otherwise, polynomial enrichment is applied in the dominant direction, subject to the maximum polynomial degree.

$$p_{\max} = 6.$$

Radial and depth wise refinement decisions are made independently, permitting anisotropic resolution while preserving the conforming tensor-product interface structure described in Section 2.2.3.

The indicator ηe measures modal high-order content; it is not a goal-oriented error estimator for the tumour-to-healthy surface-temperature contrast. Its reduction therefore need not produce a monotonic decrease in the quantity-of-interest error. The reference solution introduced in Section 3.3 is used only for post-processing error evaluation and does not influence element ranking, bulk marking, or any h- or p-refinement decision.

3 RESULTS AND DISCUSSION

3.1 Numerical Verification and Discretization Sensitivity

The numerical implementation was examined through separate tests of the spatial spectral-element approximation, the Radau IIA time integration, and the transient DPL interface treatment. These tests provide numerical evidence of implementation accuracy and are not intended as analytical convergence or stability proofs.

3.1.1 Spatial verification in a multilayer medium

The spatial discretization was first examined in the steady Pennes limit using a one-dimensional five-layer medium with discontinuous thermal conductivities. A manufactured solution was constructed through the normalized thermal-resistance coordinate

$$\eta(x) = \frac{\int_0^x \frac{1}{k(s)} ds}{\int_0^L \frac{1}{k(s)} ds},$$

with

$$\theta_{ex}(x) = 2\left[1 - \eta(x) + 0.2\sin\left(2\pi\eta(x)\right)\right] \tag{43}$$

Since $k_i d\eta/dx$ is constant throughout the layered domain, Eq. (43) satisfies temperature continuity and conductive heat-flux continuity at every material interface.

The five layers had thicknesses of 0.10,0.70,0.80,2.00, and 8.00 mm and contained 1,2,2, 2, and 4 spectral elements, respectively. The material properties were taken from Table 1. The total thermal resistance is

$$R = \sum_{i=1}^{5} \frac{\ell_i}{k_i}.$$

Substitution of Eq. (43) into the steady Pennes equation yields the following manufactured source in place of the metabolic term:

$$s_i(x) = -k_i \frac{d^2\theta_{\mathrm{ex}}}{dx^2} + P_i\theta_{\mathrm{ex}}(x),$$

or equivalently,

$$s_i(x) = \frac{1.6\pi^2}{k_i R^2} \sin\left(2\pi\eta(x)\right) + P_i\theta_{\mathrm{ex}}(x).$$

Because the outward normal at the surface points in the negative x-direction, the manufactured boundary data are

$$q_n(0) = k_1\theta'_{\mathrm{ex}}(0) = \frac{-2 + 0.8\pi}{R}, h = 15\mathrm{Wm}^{-2}\ \mathrm{K}^{-1}$$

$$\theta_\infty = \theta_{\mathrm{ex}}(0) - \frac{q_n(0)}{h} = T_\infty - T_b, \theta(L) = 0$$

For each uniform polynomial degree from 2 to 8, the maximum temperature error was evaluated as

$$E_\infty = \max_{x\in\mathcal{X}} |\theta_h(x) - \theta_{\mathrm{ex}}(x)|,$$

where $\mathcal{X}$ contains 251 independent evaluation points per element.

Table 2. Spatial error under polynomial refinement for the multilayer manufactured-solution test.

p	Temperature DOF	E_∞
2	22	4.9211×10^{-3}
3	33	3.2807×10^{-4}
4	44	1.4176×10^{-5}
5	55	7.9714×10^{-7}
6	66	2.5360×10^{-8}
7	77	1.0968×10^{-9}
8	88	2.7280×10^{-11}

Table 2 shows that as the polynomial degree increases from 2 to 8, the maximum temperature error decreases by more than eight orders of magnitude. The maximum interface heat-flux jump decreases from approximately $3.96\ \mathrm{W\ m^{-2}}$ to $2.97 \times 10^{-7}\ \mathrm{W\ m^{-2}}$, while the temperature jump remains zero at the reported numerical precision. These results demonstrate rapid spatial error reduction and consistent transmission across the material interfaces.

3.1.2 Temporal convergence of Radau IIA

Temporal accuracy was verified independently using the smooth manufactured solution

$$\theta_{\mathrm{ex}}(x,t) = 2\sin\left(\frac{\pi x}{L}\right) e^{-0.35t} \tag{44}$$

The temporal test used a homogeneous slab of thickness $L = 10\ \mathrm{mm}$ with $\rho = 1030\ \mathrm{kg\ m^{-3}}, c = 3852\ \mathrm{J\ kg^{-1}\ K^{-1}}, k = 0.558\ \mathrm{W\ m^{-1}\ K^{-1}}$, and $\omega = 0.0063\ \mathrm{s^{-1}}$. For the DPL model, $\tau_q = 1.0$ s and $\tau_T = 0.5$ s.

With $\mathrm{P} = \omega\rho\mathrm{bcb}, \mu = \pi/\mathrm{L}$, and $\gamma = 0.35\ \mathrm{s^{-1}}$, direct substitution of Eq. (44) gives the Pennes source,

$$s_{\mathrm{P}}(x,t) = (-\rho c\gamma + k\mu^2 + P)\theta_{\mathrm{ex}}(x,t),$$

and the DPL source

$$s_{\mathrm{DPL}}(x,t) = \left[\tau_q \rho c \gamma^2 - \left(\rho c + \tau_q P\right)\gamma + k\mu^2 - \tau_T k\gamma\mu^2 + P\right]\theta_{\mathrm{ex}}(x,t).$$

The functions sP and sDPL are the complete manufactured forcing terms and replace the metabolic source in these verification tests. If a time-dependent physical heat source Q is specified before eliminating the DPL heat flux, its contribution becomes.

$$Q + \tau_q \frac{\partial Q}{\partial t}$$

Homogeneous Dirichlet conditions were imposed at both boundaries. The initial temperature was taken from Eq. (44) at $t = 0$, and the DPL initial temperature rate was

$$\dot{\theta}(x,0) = -\gamma\theta(x,0).$$

The spatial discretization comprised four spectral elements of polynomial degree $p = 10$. The time steps were $\Delta t = 0.10, 0.05, 0.025, 0.0125$ s. The errors in Table 3 were evaluated at $t = 1$ s using the discrete maximum-

error definition in Section 3.1.1, with 301 evaluation points per element. The observed temporal order was calculated as

$$r = \frac{\ln\left[E_\infty(\Delta t)/E_\infty(\Delta t/2)\right]}{\ln 2}.$$

Table 3. Temporal convergence of the two-stage Radau IIA scheme

$\Delta t(s)$	E_∞ Pennes	Order	E_∞ DPL	Order
0.1000	8.9088×10^{-8}	-	1.8972×10^{-7}	-
0.0500	1.1142×10^{-8}	2.9993	2.4008×10^{-8}	2.9823
0.0250	1.3931×10^{-9}	2.9996	3.0198×10^{-9}	2.9910
0.0125	1.7416×10^{-10}	2.9998	3.7866×10^{-10}	2.9955

The Pennes solution exhibits third-order convergence throughout the refinement sequence. The DPL order approaches the same rate and reaches 2.9955 at the finest time step, confirming the expected third-order accuracy of the two-stage Radau IIA method for the smooth manufactured problem (Hairer & Wanner, 1996).

3.1.3 Verification of the transient DPL interface treatment

A transient multilayer manufactured problem was used to examine the interface formulation when the thermal conductivity and phase-lag parameters differ between adjacent tissues. For a temperature field with temporal dependence $e^{-\gamma t}$, the DPL constitutive relation permits the auxiliary coefficient

$$\kappa_i^* = k_i \frac{1-\gamma\tau_{T,i}}{1-\gamma\tau_{q,i}}, \gamma = 0.25\ \mathrm{s}^{-1} \tag{45}$$

The auxiliary coefficient is used only to construct the manufactured solution; the numerical formulation retains the original material and phase-lag parameters. Define

$$R_* = \sum_{i=1}^{5} \frac{\ell_i}{\kappa_i^*}, \eta(x) = \frac{1}{R_*}\int_0^x \frac{1}{\kappa^*(s)}\,ds$$

For the adopted parameters, the minimum values of $1-\gamma\tau_{q,i}$ and $1-\gamma\tau_{T,i}$ are 0.795 and 0.8975 , respectively. Thus, all κ_i^* are positive, the denominators remain bounded away from zero, and $d\eta/dx = 1/(\kappa_i^* R_*) > 0$ within every layer.

The exact temperature excess is

$$\theta_{\mathrm{ex}}(x,t) = \Phi(\eta(x))e^{-\gamma t},$$

with the spatial profile

$$\Phi(\eta) = 2(1-\eta) + 3\eta(1-\eta), \tag{46}$$

Since

$$\frac{d\eta}{dx} = \frac{1}{\kappa_i^* R_*}, \Phi'(\eta) = 1-6\eta, \Phi''(\eta) = -6$$

the exact physical heat flux in the positive spatial direction is

$$q_{\mathrm{ex}}(x,t) = -\frac{\Phi'(\eta(x))}{R_*}e^{-\gamma t}.$$

Indeed, within each layer,

$$\left(1-\gamma\tau_{q,i}\right)q_{\mathrm{ex}} = -k_i\left(1-\gamma\tau_{T,i}\right)\frac{\partial\theta_{\mathrm{ex}}}{\partial x},$$

which verifies the DPL constitutive relation. Continuity of η across each interface therefore ensures continuity of both the exact temperature and the physical heat flux.

The multilayer interface test used the same five healthy-tissue layers and material data as Table 1, with

$$\tau_q = (0.10,0.77,0.82,0.72,0.73)\mathrm{s}, \tau_T = (0.05,0.38,0.41,0.36,0.37)\mathrm{s}.$$

With $P_i = \omega_i\rho_b c_b$, the corresponding piecewise manufactured source is

$$s_i = \left\{\left[\tau_{q,i}\rho_i c_i\gamma^2 - \left(\rho_i c_i + \tau_{q,i}P_i\right)\gamma + P_i\right]\Phi - k_i\left(1-\gamma\tau_{T,i}\right)\frac{\Phi''}{\left(\kappa_i^*\right)^2 R_*^2}\right\}e^{-\gamma t}.$$

At the surface $x = 0$, the outward normal points in the negative spatial direction. The exact outward heat flux is therefore

$$q_{n,\mathrm{ex}}(0,t) = -q_{\mathrm{ex}}(0,t) = \frac{e^{-\gamma t}}{R_*}.$$

The convective condition

$$q_{n,\mathrm{ex}}(0,t) = h[\theta_{\mathrm{ex}}(0,t) - \theta_\infty(t)]$$

was imposed with

$$h = 15\mathrm{Wm}^{-2}\ \mathrm{K}^{-1}, \theta_\infty(t) = \theta_{\mathrm{ex}}(0,t) - \frac{e^{-\gamma t}}{hR_*},$$

where $\theta_\infty = T_\infty - T_b$. At the deep boundary, $\theta(L,t) = 0$. The exact initial conditions were

$$\theta(x,0) = \Phi(\eta(x)), \frac{\partial\theta}{\partial t}(x,0) = -\gamma\Phi(\eta(x)).$$

Each interface-flux variable was initialized from $q_{\mathrm{ex}}(x_i,0)$, with its sign adjusted to the orientation defined in Eq. (28). These values satisfy both the temperature-continuity constraint and its first time derivative.

The one-dimensional domain was discretized using five spectral elements, one per tissue layer, with polynomial degree $p = 5$ and eight-point Gauss-Legendre quadrature. After imposing the deep-boundary temperature, the system contained 29 temperature unknowns and four interface-flux unknowns, giving 62 variables in the first-order descriptor formulation.

Temperature errors were evaluated at $t = 1$ s using the discrete maximum-error definition in Section 3.1.1, with 301 evaluation points per layer. The interface-flux error was

$$E_q = \max_{i=1,\ ,4}\left|\lambda_{h,i}(1) - \lambda_{\mathrm{ex},i}(1)\right|,$$

where both fluxes use the same interface orientation. The observed convergence orders were calculated using the refinement-ratio formula in Section 3.1.2.

Table 4. Temporal convergence for the manufactured multilayer DPL interface problem.

$\Delta t(s)$	$E_\infty(K)$	Order	Maximum flux error $(\mathrm{Wm^{-2}})$	Flux order
0.200	3.34584×10^{-7}	-	1.09942×10^{-4}	-
0.100	4.32481×10^{-8}	2.9517	1.51083×10^{-5}	2.8633
0.050	5.49962×10^{-9}	2.9752	1.96627×10^{-6}	2.9418
0.025	6.93447×10^{-10}	2.9875	2.50019×10^{-7}	2.9754

As shown in Table 4, the temperature and interface-flux errors both approach third-order convergence. At $\Delta t = 0.025$ s, the respective errors are 6.93×10^{-10} K and 2.50×10^{-7} W m^{-2}, while the temperature-continuity residual remains zero at the reported numerical precision. Increasing the polynomial degree from 5 to 6 changes the temperature and interface flux by only 7.86×10^{-13} K and 5.54×10^{-10} W m^{-2}, respectively, indicating that the reported errors are dominated by the temporal discretization.

3.1.4 Spatial and temporal sensitivity of the two-dimensional Clark-II solution

Residual spatial and temporal discretization effects in the 120-element reference calculation were assessed using DPL-5×, the strongest relaxation case considered. At $\Delta t = 0.25$ s, increasing the uniform polynomial degree from $p = 5$ to $p = 6$ changed the surface contrast by at most 4.07×10^{-7} °C at the reporting times of 10, 30, and 45 s. At $p = 6$, reducing the time step from 0.25 to 0.125 s produced a maximum change of 3.65×10^{-6} °C. The adopted resolution, $p = 4$ and $\Delta t = 0.50$ s, differed from the finest calculation by no more than 1.90×10^{-5} °C, which is less than one-tenth of the smallest reported adaptive error. The interface-continuity residual remained zero at numerical precision; therefore, this resolution was retained for the subsequent Clark-II simulations.

3.2 Clark-II Dynamic Thermography Results and Discussion

The verified formulation was applied to the axisymmetric Clark-II configuration for three constitutive cases: Pennes, DPL-1x, and DPL-5x. The geometry, material properties, initial equilibrium field, and cooling–rewarming protocol were identical in all simulations. DPL-5x is included only as a relaxation-time sensitivity case.

3.2.1 Transient thermal response

All three models start from the same steady temperature field. During cooling, the tumour-center surface temperature decreases rapidly and then recovers during rewarming. In the Pennes model, it decreases from 34.3473 °C initially to 28.7770 °C at 30 s and subsequently reaches 32.4399 °C at 100 s. The largest sampled difference between DPL-5× and Pennes occurs at 4 s, when the DPL-5× temperature is 0.253 °C lower. DPL-5× remains below Pennes during cooling but becomes higher shortly after rewarming begins, indicating that phase-lag effects are concentrated near the changes in the prescribed surface conditions.

3.2.2 Tumour-to-healthy surface thermal contrast

The principal quantity of interest is the tumour-to-healthy surface thermal contrast defined in Eq. (18). Representative values are summarized in Table 5.

Table 5. Tumour-to-healthy surface thermal contrast during the Clark-II thermography protocol

Time (s)	Pennes (°C)	DPL-1x (°C)	DPL-5x (°C)
0	0.063664	0.063664	0.063664
10	0.208890	0.210203	0.203794
30	0.236942	0.237522	0.239947
45	0.116974	0.116622	0.118102
60	0.109173	0.109042	0.108517
100	0.097641	0.097546	0.097172

Cooling increases the Pennes contrast from $0.063664°\mathrm{C}$ initially to $0.236942°\mathrm{C}$ at $t = 30$ s , corresponding to an amplification factor of approximately 3.72. At the same time, DPL-5x gives $0.239947°\mathrm{C}$, approximately 3.01 mK above the Pennes value. The contrast subsequently decreases during rewarming. Figure 2 shows the contrast over the complete cooling–rewarming protocol.

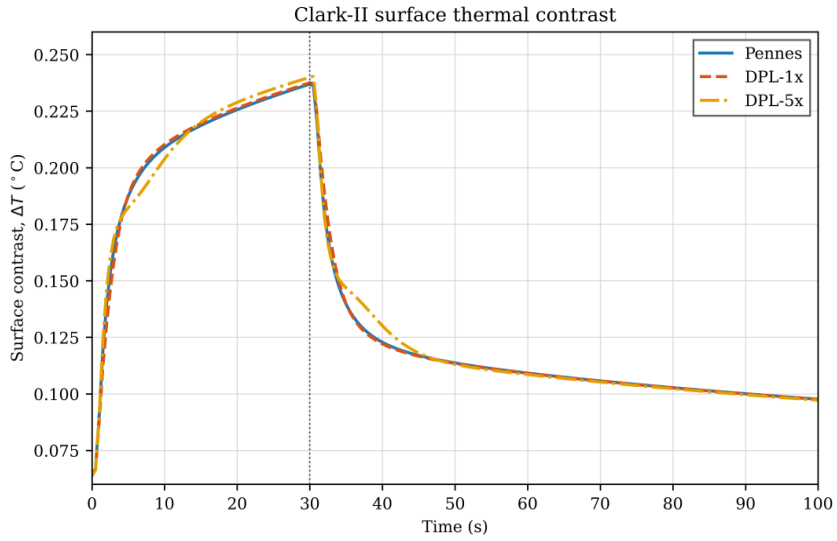


Figure 2. Tumour-to-healthy surface thermal contrast during the cooling-rewarming protocol for the Pennes, DPL-1x, and DPL-5x models

The influence of the relaxation parameters on the surface contrast is time dependent. DPL-5× lies below Pennes at 10 s but above it at 30 s. Values estimated from Fig. 7(a) of Horvat and Iljaž (2025) at 10, 30, and 45 s are approximately 0.2565, 0.2442, and 0.1004 °C for DPL-5×, compared with 0.2038, 0.2399, and 0.1181 °C in the present results. Over these times, the maximum deviations from the published curves are approximately 1.50 mK for Pennes, 2.05 mK for DPL-1×, and 52.74 mK for DPL-5×. The published values were estimated from plotted curves obtained under abrupt boundary changes, whereas the present simulations use 1 s smooth transitions. This difference limits direct quantitative comparison, particularly for DPL-5×. The discretization checks in Section 3.1.4 indicate that the tested

spatial and temporal resolutions do not account for the discrepancy. However, its attribution to boundary smoothing requires a comparison under otherwise identical conditions.

3.2.3 Spatial distribution of the thermal signature

At 30 s , all three models predict the highest surface temperature above the tumour center, followed by a smooth radial decrease toward the healthy-skin level. For Pennes, the surface temperature decreases from 28.7770 °C at the tumour center to 28.5400 °C at 20 mm. The corresponding values are 28.7706 and 28.5331 °C for DPL-1x, and 28.7452 and 28.5053°C for DPL-5x. All three radial profiles remain smooth and monotonic.

The radial profiles are shown in Figure 3.

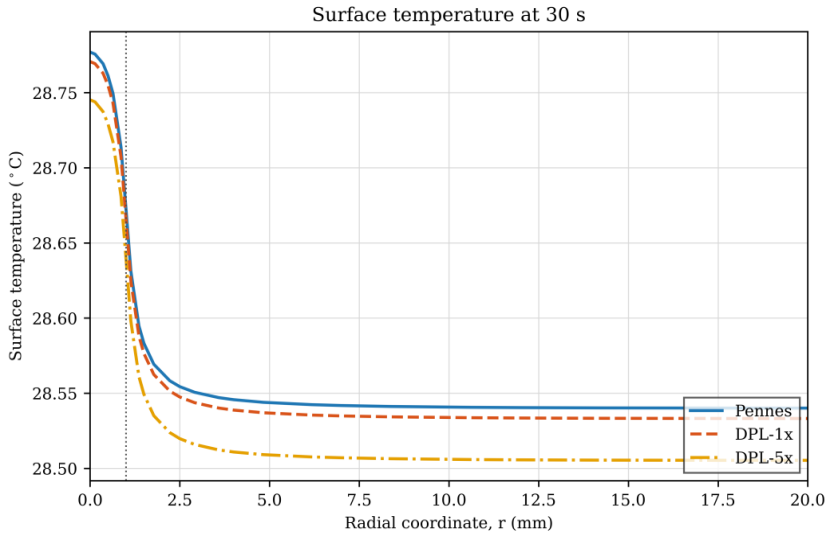


Figure 3. Radial surface-temperature distribution at 30 s for the Pennes, DPL-1x, and DPL-5x models.

The localized surface-temperature elevation results from the tumour-specific material and physiological properties. Their individual effects on the surface contrast are examined in Section 3.2.4.

3.2.4 Interpretation and limitations

At the reporting times in Table 5, the largest difference between the Pennes and baseline DPL-1× contrasts is 1.31 mK. The FLIR A655sc specifies a noise-equivalent temperature difference below 30 mK (Teledyne FLIR, n.d.); however, NETD measures thermal sensitivity rather than absolute accuracy and does not establish experimental detectability. Such an assessment would require experiment-specific uncertainties in measurement noise, drift, emissivity, and tissue properties. The present comparison therefore demonstrates a numerical phase-lag effect but not an experimentally distinguishable advantage over Pennes. Moreover, the geometry and tissue properties are idealized, and DPL-5× is a relaxation-time sensitivity case rather than a physiologically calibrated model.

A one-at-a-time sensitivity analysis varied five parameters individually by $\pm 20\%$ around the DPL- $1\times$ baseline. Tumour invasion thickness was varied while fixing its upper boundary at 0.10 mm , and both geometric variants remained within the papillary dermis. Perfusion and metabolism were varied only within the tumour, whereas the common phase-lag multiplier was applied to all tissues. Each case used an interface-fitted 120-element mesh, the boundary protocol of Section 2.1.5, and an independently computed steady initial state. At $p = 5$ and $\Delta t = 0.25$ s, the baseline contrast at 30 s was 0.237272 °C. Repeating the calculations with $p = 4$ and $\Delta t = 0.50$ s changed every sensitivity increment by less than 0.11% of its magnitude. Within the tested ranges, invasion thickness, tumour radius, and tumour perfusion had substantially greater effects than metabolism or the common phase-lag multiplier. Table 6 summarizes the parameter sensitivity results.

Table 6. Percentage change in end-of-cooling surface contrast under individual ±20% parameter variations.

Parameter	Baseline value	Change at -20%	Change at +20%
Tumour radius (mm)	1.00	-11.957%	+10.269%
Tumour invasion thickness (mm)	0.44	-14.762%	+12.860%
Tumour perfusion $(\mathbf{s^{-1}})$	0.0063	-8.121%	+8.083%
Tumour metabolic source $(\mathbf{W\ m^{-3}})$	3680	-0.195%	+0.195%
Common phase-lag multiplier	1.00	-0.049%	+0.049%

The perturbation ranges are numerical screening choices, not physiological uncertainty bounds.

3.3 hp-Adaptive Accuracy and Computational Efficiency

The final numerical experiment examines whether local hp-adaptation improves the accuracy and computational efficiency of the Clark-II solution relative to uniform polynomial refinement. Comparisons are made using the complete descriptor-state dimension and a prescribed accuracy level. DPL-5× is considered because it produces the strongest phase-lag response among the cases examined in Section 3.2, while the physical model, interface-fitted geometry, thermography protocol, and time step remain unchanged.

Accuracy is assessed through the tumour-to-healthy surface contrast at $t = 10{,}30$, and 45 s . The quantity-of-interest error is defined as

$$E_{\Delta T} = \max_{t\in\{10,30,45\}} |\Delta T_h(t) - \Delta T_{\mathrm{ref}}(t)| \tag{47}$$

The reference values used in Eq. (47) were computed on an interface-fitted mesh comprising 120 quadrilateral elements, with a uniform polynomial degree $\mathrm{p} = 4$ and a time step $\Delta\mathrm{t} = 0.50$ s. After eliminating the prescribed lower-boundary temperatures, the discretization contained 2137 temperature unknowns and 157 independent interface-flux unknowns, giving a complete DPL state dimension of 4431. The resulting tumour-to-healthy surface contrasts were $0.203557{,}0.239706$, and $0.118069°\mathrm{C}$ at 10,30 , and 45 s, respectively.

As shown in Section 3.1.4, the maximum difference between the adopted reference values and the finest validation solution is 1.90×10^{-5} °C, approximately 26 times smaller than the lowest adaptive error. The reference solution is therefore adequate for the present comparison and is used only for post-processing error evaluation; it does not influence the modal indicator, bulk marking, or any h- or p-refinement decision.

3.3.1 Adaptive refinement history

The adaptive calculation starts from a low-order interface-fitted discretization and applies the modal h/p refinement procedure of Section 2.2.6. Table 7 summarizes the evolution of the temperature degrees of freedom and the corresponding quantity-of-interest error.

Table 7. Evolution of the **hp**-adaptive approximation.

Adaptive cycle	Temperature DOF	Maximum $\boldsymbol{Qol\ error}$ ($^{\circ}\boldsymbol{C}$)
0	203	0.019994
1	247	0.019934
2	280	0.019933
3	302	0.019933
4	324	0.019934
5	396	0.002689
6	436	0.004178
7	518	0.000499
8	604	0.001375

The quantity-of-interest error changes only marginally during cycles $0-4$, despite the progressive reduction in the normalized modal estimator. A substantial decrease occurs at cycle 5, followed by a temporary increase at cycle 6. The minimum error of $0.000499°\mathrm{C}$ is attained at cycle 7 , whereas further refinement in cycle 8 increases the error to 0.001375 °C. This nonmonotonic behavior is consistent with the refinement strategy because the modal indicator measures the local spectral representation at 30 s rather than directly minimizing the quantity-of-interest error evaluated at 10, 30, and 45 s. Accordingly, cycle 7 provides the most accurate adaptive approximation within the computed sequence.

A one-at-a-time sensitivity analysis was performed for the empirical adaptive controls using the normalized modal indicator. The Dörfler parameter was varied from 0.55 to 0.75 , the h-refinement threshold from 0.06 to 0.10 , the maximum polynomial degree from 5 to 7, the minimum radial interval from 0.15 to 0.25 mm , and the minimum depth interval from 0.04 to 0.06 mm. All cases used the same sequence from cycles 0 to 8, smooth boundary protocol, and post-processing error tolerance of $1.0 \times 10^{-3}\ °\mathrm{C}$, without using the reference solution in marking or refinement. The baseline case first satisfied the tolerance at cycle 7 with 1104 complete state unknowns. Changing the Dörfler parameter to 0.55 delayed satisfaction to cycle 8 with 1004 unknowns, whereas a value of 0.75 reached it at cycle 6 with 1104 unknowns. Increasing the h-refinement threshold to 0.10 produced a different refinement path and satisfied the tolerance at cycle 5 with 836 unknowns. The tested maximum polynomial degrees and minimum element sizes did not alter the first qualifying baseline discretization. These results show that the tested marking and h-refinement thresholds affect both the refinement path and the state dimension required to meet the prescribed tolerance. The baseline settings therefore define a reference configuration rather than an optimal choice. Cycle 7 gives the smallest QoI error within the baseline sequence, whereas some alternative settings reach the tolerance earlier or with fewer unknowns.

3.3.2 Computational comparison at comparable state size and prescribed accuracy

Because the mixed DPL formulation introduces interface-flux variables in addition to the temperature and temperature-rate unknowns, computational resolution is measured using the complete descriptor-state dimension

$$N_{\text{state}} = 2N_T + N_\lambda,$$

where N_T denotes the number of free temperature degrees of freedom and N_λ the number of independent interface-flux unknowns.

At comparable state size, adaptive cycle 7 contains 518 temperature unknowns and 68 interface-flux unknowns, giving 1104 complete state unknowns. The nearest uniform discretization contains 407 temperature unknowns and 71 interface-flux unknowns, giving 885 state unknowns. Their quantity of interest errors are 4.98595×10^{-4} °C and 4.24151×10^{-3} °C, respectively. Thus, the adaptive discretisation reduces the error by a factor of 8.51 despite having 24.7% more state unknowns. Its execution time is 0.570 s, compared with 0.333 s for the uniform case; therefore, this comparison demonstrates improved accuracy per state variable, but not reduced execution time.

At the prescribed error tolerance of 0.001 °C, the first qualifying uniform discretization and adaptive cycle 7 are compared in Table 8. The adaptive case achieves a slightly smaller error with 24.1% fewer complete state unknowns, 42.5% less assembly-plus-solution time, and 39.2% less storage for the explicitly stored core matrices. Both cases require 91 linear-system solves and six Radau matrix factorizations; the savings therefore reflect the smaller algebraic systems in the selected adaptive discretization. These figures exclude the cumulative cost of generating the adaptive sequence. The storage estimates also exclude internal factorization storage and peak process memory.

Table 8. Computational comparison of the uniform and normalized hp-adaptive discretizations at the prescribed accuracy level of $\mathbf{1.0 \times 10^{-3}\ °C}$.

Method	**Temperature DOF**	**Interface DOF**	**Complete DPL state DOF**	***Qol* Error (°C)**	**Assembly + solve time (s)**	**Explicit core storage (MB)**
Uniform SEM	681	93	1455	0.000513	0.991	16.20
***hp*-Adaptive SEM**	518	68	1104	0.000499	0.570	9.85

Cycle 7 is reported as the first adaptive discretization that satisfies the prescribed tolerance under independent post-processing evaluation; the reference solution does not influence the refinement process.

3.3.3 Spatial distribution of the adaptive resolution

The cycle 8 adaptive discretization shown in Figure 4 contains 45 elements with a nonuniform anisotropic distribution of polynomial orders. In the radial direction, $p_r = 5$ for $r \leq 2.5$ mm and $p_r = 2$ in the outer region. In the depth direction, $p_z = 2$ in the epidermis, $p_z = 3$ in the tumour and dermal layers, and $p_z = 4$ in the fat and muscle layers. Additional depthwise subdivision occurs within the fat and muscle regions.

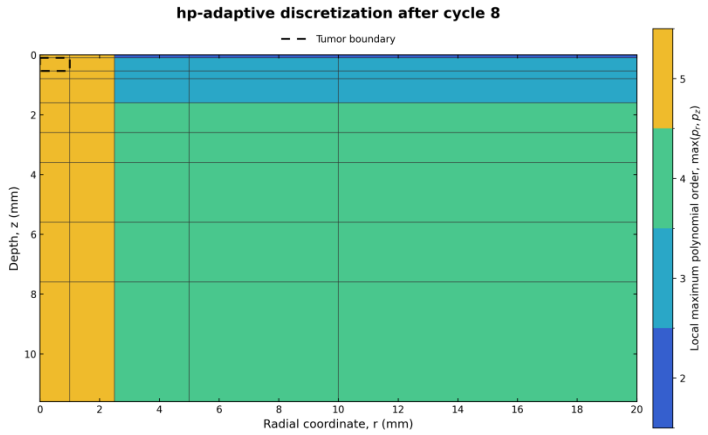


Figure 4. hp-adaptive spectral-element discretization after cycle 8. The colours indicate the larger of the radial and depth wise polynomial orders assigned to each element, while the dashed line denotes the tumour boundary.

4 Conclusions:

The proposed interface-consistent hp-adaptive spectral-element formulation accurately resolved transient DPL heat transfer across discontinuous tissue interfaces. The verification tests demonstrated rapid spatial convergence, third-order temporal accuracy, and consistent transmission of temperature and physical heat flux across material interfaces.

Under the smooth Clark-II cooling–rewarming protocol, the tumour-to-healthy surface-temperature contrast reached approximately 0.237–0.240 °C at the end of cooling. Differences between Pennes and DPL predictions were modest and occurred mainly near changes in the surface conditions. Within the tested parameter variations, tumour invasion thickness, radius, and perfusion had greater effects on the contrast than tumour metabolism or the common phase-lag multiplier.

The adaptive error was nonmonotonic, with cycle 7 providing the smallest quantity-of-interest error within the baseline sequence. Its error was lower by a factor of 8.51 than that of the nearest uniform case in state size. At an error tolerance below 0.001 °C, the selected adaptive discretization required 24.1% fewer state unknowns, 42.5% less assembly-plus-solution time, and 39.2% less storage for the explicitly stored core matrices than the qualifying uniform discretization. These savings exclude the cumulative cost of the adaptive sequence. The findings remain limited to the prescribed geometry, material data, boundary protocol, and parameter ranges; clinical interpretation requires experimentally calibrated relaxation parameters and patient-specific configurations.

Statements and declarations

Funding

This research received no financial support from any institution, organization, or funding agency.

Competing Interests

The author declares that there are no competing interests related to this work.

Author Contributions

The author was responsible for the conception and development of the study, mathematical formulation, numerical methodology, computational implementation, analysis of the results, and preparation of the manuscript. The author read and approved the final version of the manuscript.

Data Availability

The data and computational codes supporting the findings of this study are available from the corresponding author upon reasonable request.

References:

Azhdari, M., Rezazadeh, G., Pathak, R., Tautenhahn, H.-M., Tautenhahn, F., Ricken, T., & Seyedpour, S. M. (2025). Non-Fourier bioheat transfer modeling: An extensive critical review of state of the art, caveats, and future directions. *International Communications in Heat and Mass Transfer, 169*, Article 109509. https://doi.org/10.1016/j.icheatmasstransfer.2025.109509

Azhdari, M., Rezazadeh, G., Pathak, R., Tautenhahn, H.-M., Tautenhahn, F., Ricken, T., & Seyedpour, S. M. (2026). A critical review of non-Fourier heat transfer theories with phase lag in bio-heating: Explaining the variations in reported phase-lag coefficients. *International Journal of Thermal Sciences, 220*, Article 110376. https://doi.org/10.1016/j.ijthermalsci.2025.110376

Biswas, P., Singh, S., & Srivastava, A. (2020). A unique technique for analytical solution of 2-D dual phase lag bio-heat transfer problem with generalized time-dependent boundary conditions. *International Journal of Thermal Sciences, 147*, Article 106139. https://doi.org/10.1016/j.ijthermalsci.2019.106139

Boffi, D., Brezzi, F., & Fortin, M. (2013). *Mixed finite element methods and applications*. Springer. https://doi.org/10.1007/978-3-642-36519-5

Dehghan, M., & Sabouri, M. (2012). A spectral element method for solving the Pennes bioheat transfer equation by using triangular and quadrilateral elements. *Applied Mathematical Modelling, 36*(12), 6031–6049. https://doi.org/10.1016/j.apm.2012.01.018

Dorao, C. A., Fernandino, M., Jakobsen, H. A., & Svendsen, H. F. (2009). hp-adaptive spectral element solver for reactor modeling. *Chemical Engineering Science, 64*(5), 904–911. https://doi.org/10.1016/j.ces.2008.10.027

Dörfler, W. (1996). A convergent adaptive algorithm for Poisson's equation. *SIAM Journal on Numerical Analysis, 33*(3), 1106–1124. https://doi.org/10.1137/0733054

Galvão, Á., Gerritsma, M. I., & De Maerschalck, B. (2008). hp-adaptive least-squares spectral element method for hyperbolic partial differential equations. *Journal of Computational and Applied Mathematics, 215*(2), 409–418. https://doi.org/10.1016/j.cam.2006.03.063

Hairer, E., & Wanner, G. (1996). *Solving ordinary differential equations II: Stiff and differential-algebraic problems* (2nd ed.). Springer. https://doi.org/10.1007/978-3-642-05221-7

Horvat, I. D., & Iljaž, J. (2025). Numerical modeling of non-Fourier bioheat transfer in multilayer biological tissue using BEM to simulate dynamic thermography in skin tumor diagnostics. *Engineering Analysis with Boundary Elements, 179*, Article 106408. https://doi.org/10.1016/j.enganabound.2025.106408

Iljaž, J., Wrobel, L. C., Hriberšek, M., & Marn, J. (2019). Numerical modelling of skin tumour tissue with temperature-dependent properties for dynamic thermography. *Computers in Biology and Medicine, 112*, Article 103367. https://doi.org/10.1016/j.compbiomed.2019.103367

Karniadakis, G. E., & Sherwin, S. J. (2005). *Spectral/hp element methods for computational fluid dynamics* (2nd ed.). Oxford University Press. https://doi.org/10.1093/acprof:oso/9780198528692.001.0001

Mavriplis, C. (1994). Adaptive mesh strategies for the spectral element method. *Computer Methods in Applied Mechanics and Engineering, 116*(1–4), 77–86. https://doi.org/10.1016/S0045-7825(94)80010-3

Patera, A. T. (1984). A spectral element method for fluid dynamics: Laminar flow in a channel expansion. *Journal of Computational Physics, 54*(3), 468–488. https://doi.org/10.1016/0021-9991(84)90128-1

Pennes, H. H. (1948). Analysis of tissue and arterial blood temperatures in the resting human forearm. *Journal of Applied Physiology, 1*(2), 93–122. https://doi.org/10.1152/jappl.1948.1.2.93

Quintanilla, R., & Racke, R. (2006). A note on stability in dual-phase-lag heat conduction. *International Journal of Heat and Mass Transfer, 49*(7–8), 1209–1213. https://doi.org/10.1016/j.ijheatmasstransfer.2005.10.016

Teledyne FLIR (n.d.). *FLIR A655sc: High-resolution science-grade LWIR camera* [Product specifications]. https://www.flir.com/products/a655sc/

Tzou, D. Y. (1995). A unified field approach for heat conduction from macro- to micro-scales. *Journal of Heat Transfer, 117*(1), 8–16. https://doi.org/10.1115/1.2822329

Calculating the Electronic Structure of a Cadmium Telluride Crystal Under High Pressures

Ismael T. Tlayea

Dept. of Medical Instrumentation Techniques Engineering,

Polytechnic College Mosul, Northern Technical University, Mosul, Iraq

ismael.thameen@ntu.edu.iq

Calculating the Electronic Structure of a Cadmium Telluride Crystal Under High Pressures

Ismael T. Tlayea

Dept. of Medical Instrumentation Techniques Engineering,

Polytechnic College Mosul, Northern Technical University, Mosul, Iraq

ismael.thameen@ntu.edu.iq

Abstract:

The study of the energy bands of a zinc blende (ZB) for the cadmium telluride (CdTe) make a significant contribution in many fields, especially in explaining electrical properties and understanding their behavior of electrical conductivity in order to use them in the manufacture of electronic parts. In this research these bands were calculated using the sp^3 tight binding model under pressure within a range of (0 – 50) kbar for the purpose of describing changes in the electronic structure of the crystal. In this study the lattice constant values were calculated as a pressure function and used to determine the interference parameters between atomic orbits that describe the change in the elements of the Hamiltonian matrix and based on these parameters and depending on these parameters a MATLAB is set up to find the eigenvalues that represent electronic energy levels along the pathways between the high symmetry points in the Brillouin region to calculate the energy band structure of the crystal. The results show a shift in the energy eigenvalues at these points: they increase from 3.0509 to 3.2470 eV at the L point, from 5.3500 to 5.6940 eV at the X point, from 4.8850 to 5.1990 eV at the K point, and from 1.6004 to 1.7032 eV at the Γ point as pressure increases. This methodology aims to investigate the effect of pressure on the electronic structure of the crystal and to elucidate the relationship between changes in the crystal structure and variations in the distribution of energy bands, based on a semi-empirical computational model.

Keywords: CdTe, sp^3 model, Energy band structure under pressure, Energy eigenvalues of high symmetry points.

1. Introduction:

Semiconductors have optical and electronic properties that are suitable for many technological applications making them one of the basic materials in solid state physics. These properties depend to a large extent on the electronic structure of the material especially the distribution of energy levels and the formation of valence band and conduction band [1]. Energy bands are important ways to explain the relationship between physical properties and the atomic structure of matter and to clarify the nature of electronic states in crystals [2]. CdTe of the second and sixth group is classified as a compound of binary semiconductor compounds. It has a zinc blind crystalline structure and a direct energy gap which has made it gain importance in studies related to electronic and optical properties [3]. One of the physical factors that can be employed in the study of the behavior of solid materials is the hydrostatic pressure as it reduces the size of the crystal and changes the lattice constant and the spaces between the atoms [4]. This structural change is reflected in the nature of the electronic bonding and the amount of interference between the atomic orbits resulting in a change in the electronic structure of the crystal [5].To study the dependence of energy bands on pressure must be linked between the changes in electronic interactions and the changes in crystal parameters that determine the distribution of energy within the material. One of the mathematical methods used to describe the electronic structure of solid materials is the method of tight binding as it depends on the representation of electronic cases using specific atomic orbits and the description of the interactions between them through the binding parameters [6]. This method enables the build of the

Hamiltonian matrix and finds the energy levels of its eigenvalues at different wave vectors in the Brillouin region. Chadi and Marvin suggested a semi experimental method for calculating energy bands in semiconductors that have a diamond and ZB crystal structures with the determination of the extent to which the interference parameters contribute to the description of the electronic structure [7]. Accordingly sp^3 tight binding model of CdTe study contributes to the description of the interactions associated with the s and p orbitals of the atoms that make up this crystal. To apply this method under pressure it is necessary to determine how the lattice constant and the linking parameters change with the change of distances between the atoms and then these changes are entered into the Hamiltonian matrix. Depending on the calculation of the eigenvalues of the matrix the energy band structure can be created along the paths that connect the high symmetry points in the Brilluoin region at different pressures and analyze the electronic structure changes [8].

2. Literature review:

Many studies addressed the electronic structure of CdTe crystal with a focus on the impact of pressure on the lattice constant, energy gap and phase transitions as well as the use of different mathematical methods to description of the energy bands. As Christensen and Christensen studied the electronic structure of CdTe under pressure using the self-consistent relativistic linear muffin-tin orbital method within the local density approximation. The study included calculating the bulk modulus, equilibrium volumes and energy gaps as well as researching how the crystal was transformed from the structure of ZB to the structure of structural rock salt caused by pressure [3]. While Dunstan et al. studied the impact of hydrostatic pressure on CdTe energy gap using photosynthesis measurements to determine the pressure coefficients associated with the energy gap and extract the deformation potential coefficients [9]. Search Merad et al. in studying how pressure affects the optical and electronic properties of CdTe using sp^3s^* tight binding method using Mornahan's equation of state and the law of interference parameters where they calculated the energy gap, effective charge transverse, ionic property and refractive index [10]. Liu et al. investigated the stability and the electronic and optical properties of CdTe crystal under pressure using first-principles calculations; the researchers employed density functional theory (DFT) to examine the dynamical stability as well as the electronic and optical characteristics of the compound [11]. Kashuba et al. studied the effect of pressure on the electronic spectra of CdTe crystal using the theory of density function the study included the identification of electronic structure, lattice parameters, bulk modulus, energy gap and density of state [12].

The main objective of the research is to study the structure of the energy band of cdTe crystal under pressure in the range (0 – 50) kbar using sp^3 tight binding model and the work includes the calculation of the lattice constant at different pressures and the identification of pressure – dependent tight binding parameter then use these parameters in building the Hamiltonian matrix and extracting energy levels along the path between the high symmetry points in Brillouin region. The importance of the study is to provide an arithmetic description to study the impact of pressure on the electronic structure of the crystal and explain the relationship between structural change and the behavior of energy bands.

3. Theoretical part

3.1 CdTe crystal structure

CdTe is II-VI group semiconductor compound as it is of scientific and applied importance as a result of its optical and electronic properties. Under standard conditions, this compound crystallizes in a zinc-blende structure a type of cubic crystal system consisting of two interpenetrating sub lattices: one for cadmium atoms and the other for tellurium atoms, with a relative displacement between them. The initial structure of ZB includes two atoms of two different types and each atom is surrounded by four adjacent atoms of the other type and distributed over the vertices of the tetrahedral. This geometry plays a fundamental role in determining the nature of chemical bonds and the interactions between atomic orbitals. Furthermore, the interatomic distances and the lattice constant influence the degree of orbital overlap, which in turn shapes the electronic structure of the crystal [3].

Determining the crystal structure is a fundamental step in calculating energy bands, as atomic coordinates and bond vectors are used to define the Hamiltonian matrix elements within the tight binding model. When studying a crystal under pressure, it is assumed that the zinc-blende structure is maintained provided the applied pressure does not induce a phase transition with the lattice constant and interatomic distances updated according to the applied pressure. The distance between the two nearest dissimilar atoms in this structure is calculated using the following relation:[13]

$$\mathrm{d} = \frac{\sqrt{3}}{4}\, a \qquad (1)$$

where d represents the nearest-neighbor distance between the cadmium and tellurium atoms, and a is the cubic lattice constant. This distance is subsequently used to calculate the tight binding parameters and to determine their dependence on pressure.

3.2 Lattice constant under pressure

The lattice constant is an important structural parameter that describes the dimensions of a crystal unit cell; its variation under the influence of pressure leads to changes in the crystal volume and the interatomic distances. When hydrostatic pressure is applied, the crystal undergoes compression, which alters its structural parameters a process that, in turn, affects electronic interactions and energy bands. The relationship between pressure and volume can be described using the Murnaghan equation, which relates pressure to the relative volume change, the bulk modulus, and the first derivative of the bulk modulus with respect to pressure. The equation is expressed as follows [14]:

$$P = \frac{B_o}{B_0'}\left[\left(\frac{V_0}{V}\right)^{B_0'} - 1\right] \qquad (2)$$

Where P is the pressure applied to the crystal, V_0 is its reference volume at atmospheric pressure, V is its volume under applied pressure, B_o is its volumetric elasticity modulus at atmospheric pressure, and its value is 42.4 GPa [15], and B_0' is the first derivative of its volumetric elasticity modulus with respect to atmospheric pressure, and its value is 4.8 [16]. By paraphrasing the equation (2) the ratio of the volume is calculated under pressure to the specific volume of the solid at atmospheric pressure according to the relationship:

$$\frac{V}{V_0} = \left(1 + \frac{B_o' P}{B_o}\right)^{-1/B_o'} \qquad (3)$$

Since the conventional unit cell of CdTe crystal is cubic, its volume is related to the lattice constant by the expression $V=a^3$. Therefore, the lattice constant at a given applied pressure can be determined from the following relationship:

$$a(P) = a_0\left(1 + \frac{B_o' P}{B_o}\right)^{-1/3B_o'} \qquad (4)$$

In which $a(P)$: is the lattice constant under pressure and a_0: is the lattice constant at atmospheric pressure. Equation (4) is used to find the lattice constant at different pressures then calculate the distance of the nearest neighbor at each pressure according to the relationship:

$$\mathrm{d}(P) = \frac{\sqrt{3}}{4}\, a(P) \qquad (5)$$

Thus, the structural changes resulting from pressure are linked to tight binding parameters, which depend on the distances between atoms [17].

3.3 sp^3 type tight binding model

The tight binding model is a semi-empirical theoretical method used to calculate the electronic structure of solids; it represents electronic states using atomic orbitals centered on individual atoms, while accounting for interactions between neighboring orbitals. This model is characterized by its ability to describe energy bands using a limited number of parameters, making it well-suited for studying how the electronic structure depends on structural changes such as those induced by the application of pressure. The sp^3 model is based on four atomic orbitals per atom: one s orbital and three p orbitals (p_x, p_y, and p_z). Since the primitive cell of CdTe crystal contains two atoms, one cadmium and one tellurium the model incorporates eight atomic orbitals, resulting in an 8×8 Hamiltonian matrix (when the spin-orbit interaction is neglected) [7]. In wave vector space, the Hamiltonian is represented by diagonal elements, which correspond to the energies of the atomic orbitals, and off-diagonal elements, which describe the interactions between the various orbitals. The eigenvalue equation is expressed in the general form:

$$H(k)\psi_n(\mathrm{k}) = E_n(\mathrm{k})\,\psi_n(\mathrm{k}) \tag{6}$$

Here, $H(k)$ is the Hamiltonian matrix at wave vector k, $\psi_n(\mathrm{k})$ is the eigenfunction for the nth electronic state, and $E_n(\mathrm{k})$ represents the energy of the corresponding state. When the effect of pressure is introduced, the Hamiltonian matrix also becomes dependent on pressure, due to changes in the lattice constant, interatomic distances, and overlap parameters. The equation can be formulated as follows:

$$H(k,P)\psi_n(k,P) = E_n(k,P)\,\psi_n(k,P) \tag{7}$$

This equation is used to find energy levels at different pressures in order to study the change in the energy bands structure. The method of building Hamiltonian based on the Slater-Koster bases provides an organized process to represent the interactions between the atomic orbits according to their types and geometric directions for bonds. Defining these items is essential to find an appropriate description of the electronic structure of the crystal [18]. The parameters of the tight binding determine the amount of interaction between the atomic orbit and its direction therefore it is considered one of the basic elements that are used to describe the electronic structure. These parameters include the overlap between s and p orbits and the overlap between the opposite p orbits according to the directions of the interconnection between the atoms. These parameters are symbolized by symbols $V_{ss\sigma}$, $V_{sp\sigma}$, $V_{pp\sigma}$, and $V_{pp\pi}$ where sub codes refer to the nature of the overlap and the type of orbit [19]. When the pressure is high the distances between the atoms change which leads to a change in the interference parameters. This change is calculated in the parameters of the matrix elements by using the experimental measurement law which is given in the following relationship [20]:

$$V(P) = V(0)\left(\frac{d_0}{d_P}\right)^2 \tag{8}$$

Where $V(P)$: is the tight binding coefficients at pressure and $V(0)$ is the tight binding coefficients at atmospheric pressure. This relationship is used to update the interference parameters at each pressure and accordingly the Hamiltonian matrix can be created showing the change in electronic interactions resulting from the compression of the crystal lattice.

3.4 Calculation of the energy band structure

Once the lattice constant and tight binding parameters have been determined for various pressures, the Hamiltonian matrix is constructed for each wave vector. Its eigenvalues are then calculated to obtain the electronic energy levels. These calculations are performed along a path connecting high symmetry points within

the Brillouin region such as L, X, K and Γ following the paths appropriate for a cubic crystal structure. By plotting the eigenvalues as a function of the wave vector, the energy band structure is obtained. This process is repeated at different pressures, with the lattice constant and overlap parameters updated for each case, thereby enabling an analysis of the effect of pressure on energy levels, as well as the shape and distribution of the bands [21].

4. Results and discussion

The lattice constant of CdTe crystal at various pressures was calculated using Equation (4), based on the lattice constant value at atmospheric pressure, the bulk modulus, and its first derivative with respect to pressure. A slight decrease in the lattice constant values is observed as pressure increases, as shown in Table 1 and illustrated in Figure 1. Once the lattice constant at different pressures was determined, the distance between the nearest-neighbor atoms in the crystal was calculated according to the relationship provided in Equation (5) as presented in Table 1 revealing variations in these values resulting from the increase in pressure.

Table 1: Lattice constant and bond length values for CdTe crystal at various pressures

Pressure (kbar)	Lattice Parameter (A°)	Bond length (A°)
	This work	This work
0	6.4800[22]	2.8000[23]
10	6.4319	2.7792
20	6.3888	2.7606
30	6.3498	2.7437
40	6.3141	2.7283
50	6.2813	2.7141

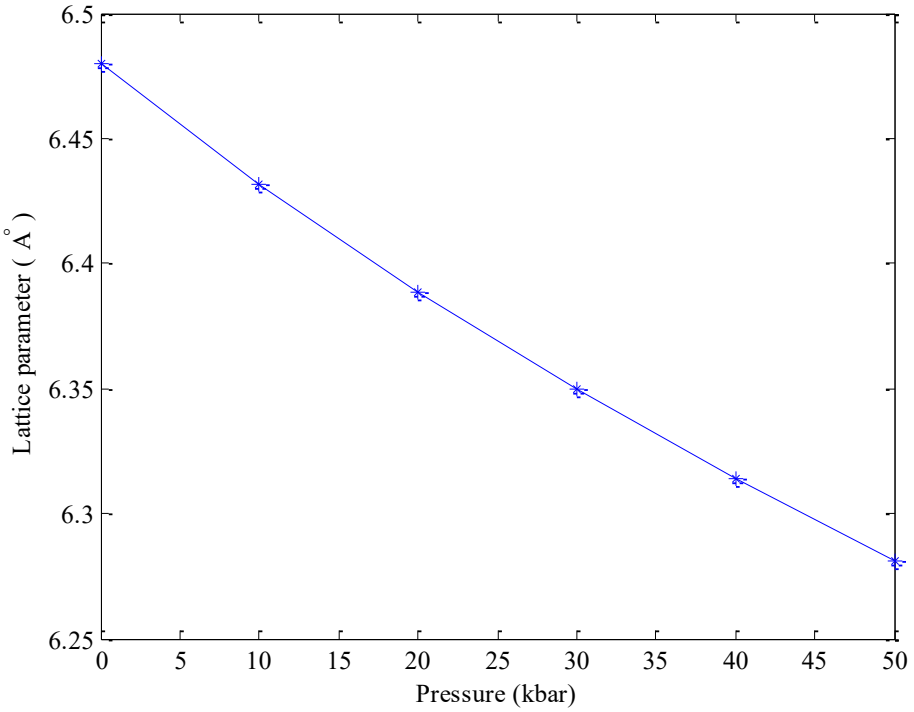


Figure 1. Variation of the lattice constant with pressure for CdTe crystal

Subsequently, the overlap parameters in sp^3 tight binding model were updated based on the variation in interatomic distance with pressure, using Equation (8) and as shown in Table 2.

Table 2: Values of the matrix elements for CdTe crystal under pressure

Matrix Elements	Pressure (kbar)					
	0[24]	10	20	30	40	50
E_{pa}	0.0230	0.0233	0.0237	0.0240	0.0242	0.0245
E_{pc}	5.3170	5.3968	5.4699	5.5374	5.6001	5.6588
E_{sa}	-9.9610	-10.1105	-10.2474	-10.3738	-10.4914	-10.6013
E_{sc}	0.7670	0.7785	0.7891	0.7988	0.8078	0.8163
V_{ss}	-3.1040	-3.1506	-3.1932	-3.2326	-3.2693	-3.3035
V_{xx}	0.3493	0.3545	0.3593	0.3638	0.3679	0.3718
V_{xy}	4.4413	4.5079	4.5690	4.6254	4.6778	4.7268
V_{sapc}	0.7113	0.7220	0.7318	0.7408	0.7492	0.7570
V_{pasc}	5.3832	5.4640	5.5380	5.6063	5.6698	5.7292

Subsequently, the electronic energy levels of CdTe crystal were calculated by solving the eigenvalue equation for the Hamiltonian matrix at the high symmetry points L, X, K and Γ within the Brillouin region. The lattice constant and the tight binding parameters were updated through recalculation at different pressures and represented the energy levels calculated in Figures 2, 3, 4, 5, 6 and 7 to track the change of their locations at the high symmetry points with pressure. Analysis of the figures shows the gradual increase of the conduction bands from the valance bands with the increase in pressure.

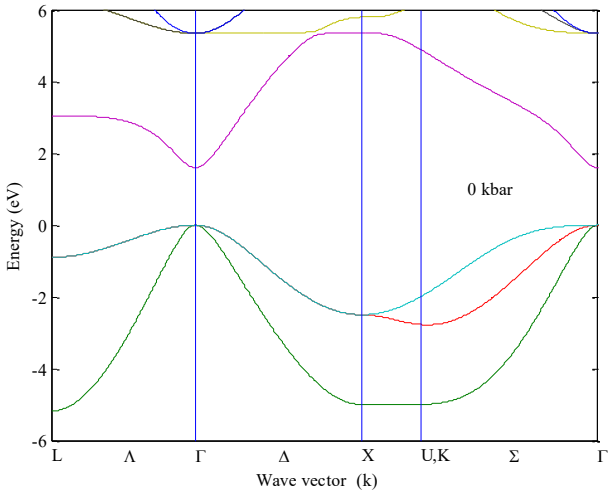


Figure 2. CdTe energy bands structure at 0 kbar

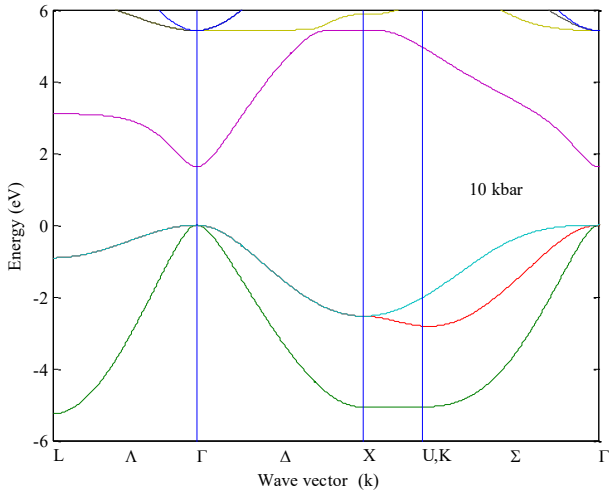


Figure 3. CdTe energy bands structure at 10 kbar

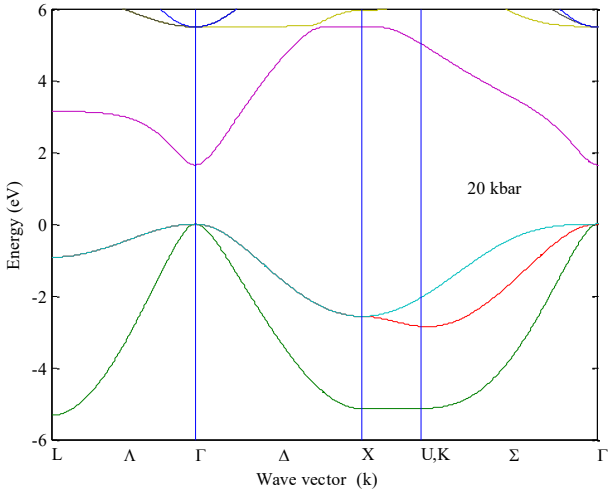


Figure 4. CdTe energy bands structure at 20 kbar

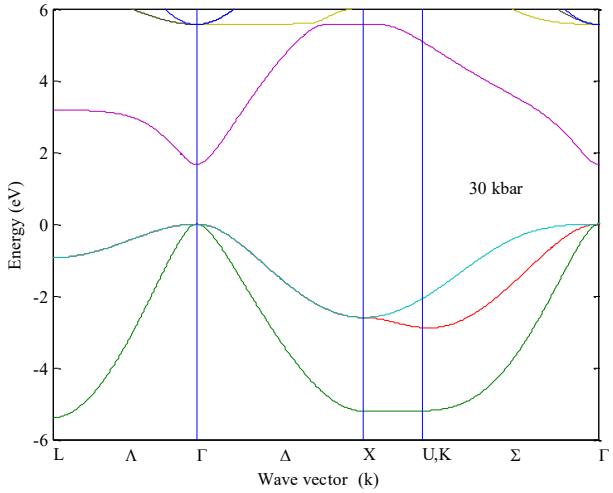


Figure 5. CdTe energy bands structure at 30 kbar

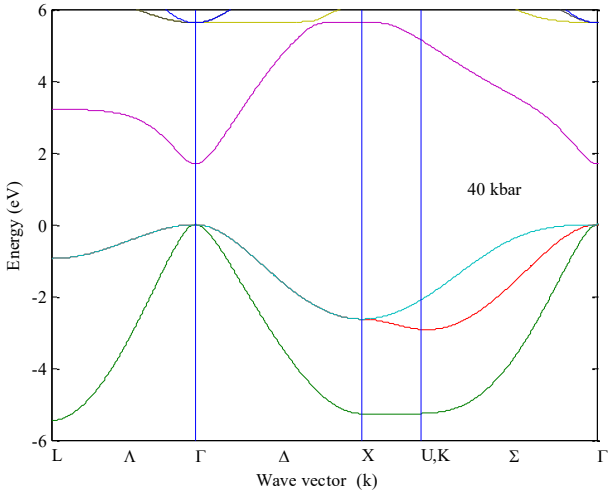


Figure 6. CdTe energy bands structure at 40 kbar

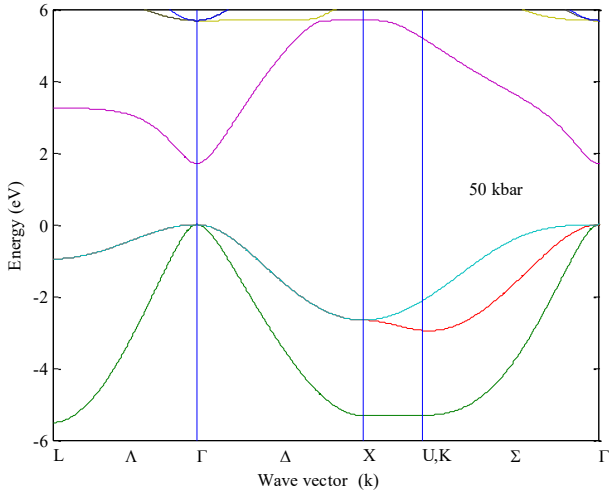


Figure 7. CdTe energy bands structure at 50 kbar

Based on the crystal's energy bands, the energy eigenvalues were calculated at the high symmetry points L, X, K and Γ and subsequently compared with the results obtained by Huang and Ching [25] and Zakharov et al. [26], as presented in Table 3. The findings indicate an upward trend in the values of these parameters as pressure increases, as illustrated in Figure 8.

Table 3: Energy eigenvalues of CdTe crystal at high symmetry points under various pressures

Energy (eV)	Pressure (kbar)						
	0	10	20	30	40	50	P = 0 kbar
L	3.0509	3.0967	3.1386	3.1773	3.2133	3.2470	2.36[25], 2.84[26]
X	5.3500	5.4303	5.5039	5.5718	5.6349	5.6940	2.88[25], 3.46[26]
K	4.8850	4.9583	5.0254	5.0874	5.1450	5.1990	-
Γ	1.6004	1.6244	1.6464	1.6667	1.6856	1.7032	1.60[25], 1.76[26]

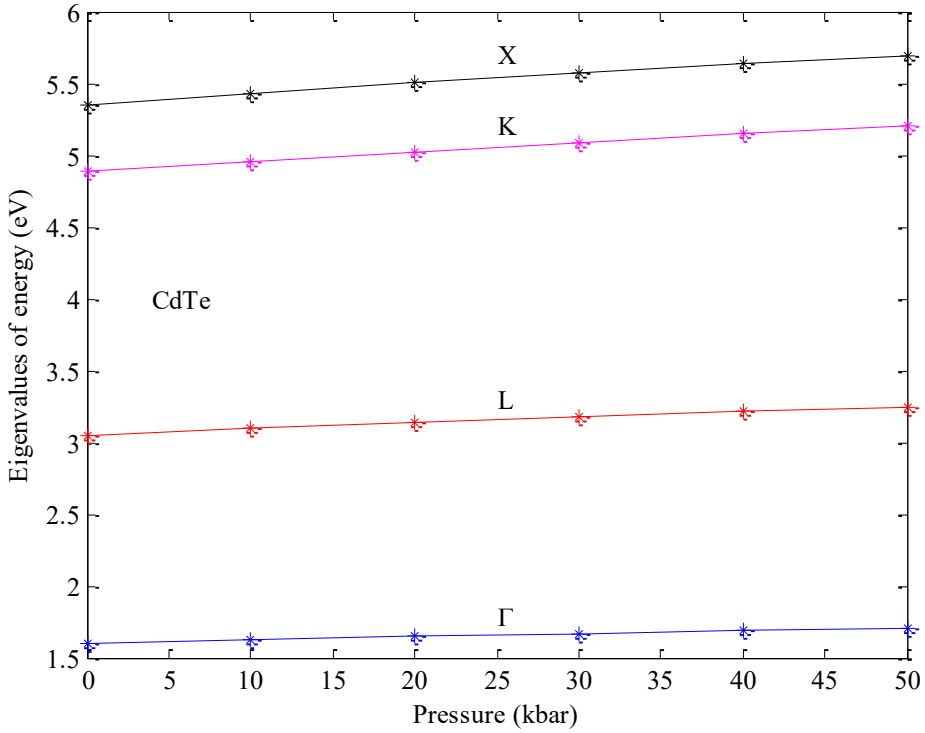


Figure 8. Changes in the energy eigenvalues at high symmetry points of CdTe crystal with pressure

5. Conclusion:

The results obtained from the calculations showed that the increase in external pressure on CdTe crystal from (0 to 50) kbar results in a decrease in the value of the lattice constant from (6.4800 to 6.2813) (A°). This leads to a contraction in the crystal structure and the convergence of the atoms that make up it. This results in a change in the spaces between atoms affecting the values of the interference parameters in the tight binding model. These changes are reflected in the elements of the Hamiltonian in the calculations resulting in a redistribution of energy levels and the change in the structure of electronic energy bands with the increase in pressure. Reflections of these effects appear on the values of energy levels at high symmetry points showing the nature of the connection between pressure and changes in the lattice constant, the tight binding parameters and the electronic structure of the crystal. In conjunction with increased pressure the energy gap values gradually rise at the high symmetry points L, X, K and Γ. The energy gap value increases at L point from (3.0509 to 3.2470) eV, at X point from (5.3500 to 5.6940) eV, at K point from (4.8850 to 5.1990) eV and at Γ point (1.6004 to 1.7032) eV. These results reveal the importance of studying the impact of pressure in understanding the behavior of semiconductor materials and clarifying the mechanism of changes in electronic energy levels in different pressure conditions.

References:

[1] M. Nisoli, *Semiconductor laser photonics*. Cambridge University Press, pp. 16-18, 2022.

[2] N. Y. Tanisa, M. Rahman, A. M. Musa, J. H. Bhuiyan and T. Aziz, "Comprehensive DFT Study of Structural, Mechanical, Dynamical, Electronic, and Optical Properties of ZnX (X= S, Se, Te) Semiconductors", *Advances in Materials Science and Engineering*, vol. 2026, no. 1, p. 2466402, 2026.

[3] N. E. Christensen and O. B. Christensen, “Electronic structure of ZnTe and CdTe under pressure”, *Physical Review B*, vol. 33, no. 7, p. 4739, 1986.

[4] S. Alptekin, “Structural phase transition of CdTe: an ab initio study”, *Journal of molecular modeling*, vol. 19, no. 1, pp. 421-426, 2013.

[5] F. S. Saoud, R. E. Houda Djabou, Y. Al-Douri and R. A. Al-Samarai, “Pressure-tuned structural, electronic, optical and phonon properties of ZnTe in zinc-blende (B3) phase”, *Modern Physics Letters B*, vol. 40, no. 27, p. 2650199, 2026.

[6] I. J. Park and K. Choudhary, “CHIPS-TB: Evaluating tight-binding models for metals, semiconductors, and insulators”, *The Journal of Physical Chemistry.* C, Nanomaterials and Interfaces. vol. 130, no.7, p.2814, 2026.

[7] D. J. Chadi and M. L. Cohen, “Tight-binding calculations of the valence bands of diamond and zincblende crystals”, *Physica status solidi (b)*, vol. 68, no.1, pp. 405-419, 1974.

[8] A. Mujica, A. Rubio, A. Munoz, and R. J. Needs, “High-pressure phases of group-IV, III–V, and II–VI compounds”, *Reviews of modern physics*, vol. 75, no. 3, p. 863, 2003.

[9] D. J. Dunstan, B. Gil and K. P. Homewood, “Hydrostatic and uniaxial pressure coefficients of CdTe”, *Physical Review B*, vol. 38, no.11, p.7862, 1988.

[10] A. E. Merad, M. B. Kanoun, H. Aourag, J. Cibert and G. Merad, “Electronic and optical properties of CdTe under hydrostatic pressure effect”, *Superlattices and microstructures*, vol. 32, no. 1, pp. 25-34, 2002.

[11] D. Liu, J. Feng, M. Tian, Q. Li and R. Sa, “First-principles study of the stability, electronic and optical properties of CdTe under hydrostatic pressure”, *Chemical Physics Letters*, vol. 764, p. 138272, 2021.

[12] A. I. Kashuba, I. V. Semkiv, H. A. Ilchuk and R. Y. Petrus, “Pressure effect on the electronic spectra of CdTe crystal calculated by DFT”, vol. 59, pp. 3-14, 2022.

[13] K. Y. Cheng, *III–V Compound Semiconductors and Devices*, 2020.

[14] F. D. Murnaghan, “The compressibility of media under extreme pressures”, *Proceedings of the National Academy of Sciences*, vol. 30, no. 9, pp. 244-247, 1944.

[15] G. Korotcenkov, *Handbook of II-VI semiconductor-based sensors and radiation detectors*, 2023.

[16] T. Ouahrani, R. Franco, J. M. Menéndez, M. Marqués and J. M. Recio, “Microscopic partition of pressure and elastic constants in CdTe polymorphs, *Journal of alloys and compounds*”, vol. 592, pp. 150-156, 2014.

[17] V. G. Tyuterev and N. Vast, “Murnaghan’s equation of state for the electronic ground state energy”, *Computational materials science*, vol. 38, no. 2, pp. 350-353, 2006.

[18] J. C. Slater and G. F. Koster, “Simplified LCAO method for the periodic potential problem”, *Physical review*, vol. 94, no. 6, p. 1498, 1954.

[19] T. Ismail and M. Hussien, “Band Structure of GaAs Crystal Using the Semiempirical Tight Binding Method”, *appear in Journal of Education and Science*, vol. 30, no. 3, 2021.

[20] S. Froyen and W. A. Harrison, “Elementary prediction of linear combination of atomic orbitals matrix elements”, *Physical Review B*, vol. 20, no. 6, p. 2420, 1979.

[21] Y. Sun, S. E. Thompson and T. Nishida, *Strain effect in semiconductors: theory and device applications*. Springer Science & Business Media, 2009.

[22] N. Tit, "Suitability of II–VI semiconductors for photonic applications: Common-anion versus common-cation superlattices", *Journal of Vacuum Science & Technology A: Vacuum, Surfaces, and Films*, vol. 22, no. 3, pp. 821-825, 2004.

[23] S. G. Shen, "Calculation of the elastic properties of semiconductors", *Journal of Physics: Condensed Matter*, vol. 6, no. 42, pp. 8733-8743, 1994.

[24] Y. R. Wang, C. B. Duke, K. O. Magnusson and S. A. Flodström, "Atomic geometry and electronic structure of CdTe (110) ", *Surface science*, vol. 205, no. (1-2), pp. 760-770, 1988.

[25] M. Z. Huang and W. Y. Ching, "A minimal basis semi-ab initio approach to the band structures of semiconductors", *Journal of Physics and Chemistry of Solids*, vol. 46, no. 8, pp. 977-95, 1985.

[26] O. Zakharov, A. Rubio, X. Blase, M. L. Cohen and S. G. Louie, "Quasiparticle band structures of six II-VI compounds: ZnS, ZnSe, ZnTe, CdS, CdSe", *Physical Review B*, vol. 50, no. 15, 1994.

Commuting N − Regular Rings

Department of Mathematics College of Computer Sciences and Mathematics

University of Mosul, Mosul, Iraq

Shahla M. Khalil **Shaimaa H.Ahmad** **Raida D. Mahmood**

shahlasamer@uomosul.edu.iq

shaymaahatim@uomosul.edu.iq

raida1961@uomosul.edu.iq

Commuting $N-$ Regular Rings

Department of Mathematics College of

Computer Sciences and Mathematics

University of Mosul, Mosul, Iraq

Shahla M. Khalil **Shaimaa H.Ahmad** **Raida D. Mahmood**

shahlasamer@uomosul.edu.iq

shaymaahatim@uomosul.edu.iq

raida1961@uomosul.edu.iq

Abstract:

Let $\Re$ be an associative ring with identity. A ring $\Re$ is called Commuting $N-$ regular (strongly Commuting $N-$regular) if each

$\alpha,\beta \in N(\Re)$, there exists $ą \in \Re$ such that $\alpha\beta = \beta\alpha$ ą $\beta\alpha$. $(\alpha^2 = \alpha^4 ą\, \alpha^4)$ .In this paper, we introduce the concept of Commuting $N-$regular(Strongly Commuting $N-$regular) ring. Moreover, we study various their properties and relationships to $N-$regular and reduced rings.

الملخص:

لتكن $\Re$ حلقة تجميعية ذات عنصر محايد. تسمى الحلقة $\Re$ حلقة منتظمة تبديلية من النمط $N-$ (حلقة منتظمة بقوة تبديلية من النمط $N-$) اذا كان لكل عنصرين $\alpha, \beta \in N(\Re)$ يوجد $ą \in \Re$ بحيث ان $\alpha\beta = \beta\alpha$ ą $\beta\alpha$ ، $(\alpha^2 = \alpha^4 ą\, \alpha^4)$. في هذا البحث نقدم مفهوم الحلقة منتظمة تبديلية من النمط $N-$ (حلقة منتظمة بقوة تبديلية من النمط $N-$). بالإضافة الى دراسة خصائصها المختلفة وعلاقاتها بالحلقات النمط $N-$ والحلقات المختزلة.

Key words and phrases: regular ring, reduced ring, Commuting $N-$regular ring (CNR-ring),$N-$Pure ring,$N-$regular ring.

1-INTRODUCTION

Throughout this article, all rings have an identity element and it is associative . Let $\Re$ be a ring, $\Re$ is called regular ring, if for all $ą \in \Re$, there exists $ƀ \in \Re$ such that $ą = ąƀą$. Some properties of regular

rings and strongly regular has been studied ą = ą²ƀ in [3,7]. In 2004[11] Yamini and Safari defined that a ring is called commuting regular if for each α , $\beta \in \Re$ there exists ą ∈ ℜ such that $\alpha\beta = \beta\alpha$ąą$\beta\alpha$. Also some results on commuting regular rings have been studied in [1,2,4,6]. N denote the set of all nilpotent element in ℜ , J= J (ℜ), Jacobson radical of ℜ , Y (ℜ) right singular ideal and r(ą)(l(ą)) indicate the right (left) annihilator of ą ∈ ℜ. A ring ℜ is said to be a reduced ring if N (ℜ) = {0} . Following [8], ℜ is N-regular if ą ∈ ą ℜ ą for all ą ∈ N(ℜ) and ℜ is known as right (left) N −pure rings if for all ą ∈ N(ℜ), ą ℜ= (ℜą) is a left (right) pure [5].In section 2 we define Commuting N -regular (strongly commuting N -regular) ring and give some basic results about them.

2- Commuting N -regular rings:

Some properties of Commuting N -regular rings are given in this section, along with a discussing of the relationships between Commuting N -regular rings and other types of rings.

Definition 2.1.

A ring ℜ is said to be a Commuting N -regular (CNR-ring) (strongly commuting N – regular)(SCNR-ring) if for all α , $\beta \in N$ (ℜ)**,** there exists ą ∈ ℜ such that $\alpha\beta = (\beta\alpha)$ ą $(\beta\alpha)$ ($\alpha^2 = \alpha^4$ ą α^4), $where\ \alpha = \beta$.

Remarks 2.2.

1- The concepts of N-regular and Commuting N-regular are the same in commutative case.
2- Every reduced ring is CNR-ring.
3- Consider $\Re = \begin{bmatrix} ƶ_2 & ƶ_2 \\ 0 & ƶ_2 \end{bmatrix}$, N (ℜ) = $\left\{\begin{bmatrix} 0 & 0 \\ 0 & 0 \end{bmatrix}, \begin{bmatrix} 0 & 1 \\ 0 & 0 \end{bmatrix}\right\}$

Clearly ℜ is CNR-ring but not Commuting regular. Indeed, let $x = \begin{bmatrix} 1 & 1 \\ 0 & 0 \end{bmatrix}$, $y = \begin{bmatrix} 1 & 0 \\ 0 & 0 \end{bmatrix} \in \Re$, then $xy = \begin{bmatrix} 1 & 0 \\ 0 & 0 \end{bmatrix}$ and $yx = \begin{bmatrix} 1 & 1 \\ 0 & 0 \end{bmatrix}$. If there exists $\begin{bmatrix} ą & ƀ \\ 0 & ç \end{bmatrix} \in \Re$ such that $\begin{bmatrix} 1 & 0 \\ 0 & 0 \end{bmatrix} = \begin{bmatrix} 1 & 1 \\ 0 & 0 \end{bmatrix}\begin{bmatrix} ą & ƀ \\ 0 & ç \end{bmatrix}\begin{bmatrix} 1 & 1 \\ 0 & 1 \end{bmatrix}$, then 1=0 which is a contradiction. Hence ℜ is not commuting regular.

Proposition2.3. Every homomorphic image of CNR-ring is CNR-ring.

Proof: Consider ℜ , ℜ′ be a rings and f: ℜ → ℜ′ be a ring epimerphic Suppose that ℜ is CNR-ring and ą ,ƀ ∈ N (ℜ′) then there exists ç ,đ ∈ N(ℜ) such that ą = f(ç), ƀ = f(đ) . Since ℜ is CNR-ring there exists t such that ç đ = (đç)t(đç) and so ą ƀ = f(ç đ) = f((đ ç)$t$$f$(đ ç)) = f(đ ç)f(t)f(đ ç) = $\big(f(đ)f(ç)\big)f(t)\big(f(đ)f(ç)\big)$ = (ƀ ą)f(t)(ƀ ą)

This completetes the proof. □

Corollary2.4. Let ℜ be CNR-ring and I is any ideal of ℜ. Then ℜ / I is CNR-ring.

Proof: Let $\alpha\beta + I \in \Re / I$, where α , $\beta \in N$ (ℜ) . Since ℜ is CNR-ring, then there exists ƶ ∈ ℜ such that $\alpha\beta = \beta\alpha$ ƶ $\beta\alpha$. Now,

$(\beta\alpha + I)(ƶ + I)(\beta\alpha + I) = \beta\alpha$ ƶ $\beta\alpha + I = \alpha\beta + I$. Therefore ℜ / I is a

CNR-ring. □

Theorem 2.5. If $\Re$ is CNR-ring and (ƀ ą) $\Re$ = $\Re$ $(ƀą)^2$ for every ą ¸ƀ ∈ $N(\Re)$. Then $\Re$ is reduced ring.
Proof: Let ą , ƀ ∈ $\Re$ such that $(ą\ ƀ)^2 = 0$. Since $\Re$ is CNR-ring,there exists ç ∈ $\Re$ such that ą ƀ = ƀą ç ƀą . $Since$ ƀą $\Re$ =$\Re$ (ƀą)^2. Then ƀąç = α(ƀą)^2 for some α ∈ $\Re$. Hence ą ƀ = ƀąçƀą = α(ƀą)^2bą = α ƀą ƀą ƀą = α ƀ(ą ƀ)^{2}ą = 0. So ą ƀ = 0 and $\Re$ is reduced. □

Proposition 2.6. The center of CNR-ring is reduced.

Proof: Assume that $cet(\Re)$ is not reduced, then $0 \neq \alpha, \beta \in N$ $(cet(\Re))$, $\beta\alpha \neq 0$ such that $(\beta\alpha)^2 = 0$. Since $\Re$ is CNR-ring, then there exists ą ∈$\Re$, $\alpha\beta = \beta\alpha$ ą $\beta\alpha$ = ą $\beta\alpha\beta\alpha$ = ą $(\beta\alpha)^2 = 0$, $\beta\alpha \in Cet(\Re)$a contradiction. So $cet(\Re)$ is reduced. □

Corollary 2.7. If $\Re$ is CNR-ring, then so $cet(\Re)$.

Theorem 2.8. Consider $\Re$ = $\Re 1 \times \Re 2$ be a ring . If $\Re 1$ and $\Re 2$ are

CNR-ring. Then $\Re$ is a CNR-ring**.**

Proof: Since $\Re$ 1 and $\Re$ 2 are CNR-ring. Then for every $\alpha, \beta \in N(\Re 1)$, ą ¸ ƀ ∈ $N(\Re 2)$, there exists $w \in \Re 1$, đ ∈ $\Re 2$ such that $\alpha y = \beta\alpha w\beta\alpha$ and ąƀ = ƀąđƀą . Let $z_1 = (\alpha, ą)$ and $z_2 = (\beta.ƀ)$, $z_1, z_2 \in N(\Re)$. Then we have $z_1 \times z_2 = (\alpha, ą)(\beta, ƀ) = (\alpha\beta, ą, ƀ) = \big((\beta\alpha w\beta\alpha), (ƀ\ ą, đ\ ƀ\ ą,)\big) = (\beta\alpha, ƀ\ ą,)(w, đ)(\beta\alpha, ƀ\ ą,) = (\beta, ƀ)(\alpha, ą,)ç\ (\beta, ƀ)(\alpha, ą,) = (z_2z_1)ç\ (z_2z_1)$ when $(w, đ) \in \Re$. Therefore $\Re$ is a CNR-ring. □

Proposition 2.9. If $\Re$ is a SCNR-ring and SXM. then

1) $\Re$ is n-regular.
2) N ($\Re$) ∩ J($\Re$)= 0**.**

Proof:1) $\Re$ is SCNR-ring, for each $\alpha \in N(\Re)$ there exists ą ∈ $\Re$ such that $\alpha^2 = \alpha^4$ą α^4, $\alpha^2(1 - đ\alpha^2) = 0$, α^2ą $\alpha^2 = đ \in \Re, 1 - ą\ \alpha^2 \in r(\alpha^2) = r(\alpha)(\Re\ is\ SXM)$**.** S0 $\alpha = \alpha ą\ \alpha^2 = \alpha ą\alpha\alpha = \alpha ƀ\alpha$. Then $\Re$ is n-regular.

2)If $\alpha \in N$ ($\Re$) ∩ J($\Re$) by (1), $\alpha = \alpha ƀ\alpha$ for some ƀ ∈ $\Re$. Hence $\alpha(1 - ƀ\alpha)$. Since $\alpha \in$ J($\Re$) , ƀ$\alpha \in$ J($\Re$). Hence $1 - ƀ\alpha$ is invertible and so $\alpha = 0$. □

Theorem 2.10. Let $\Re$ SXM, and for all ą , $b \in N(\Re)$, ą $b = b$ą , $\Re$ / r(ąƀ) is CNR-ring. Then $\Re$ is CNR-ring.

Proof: Let $\Re$ / r(ąƀ) be CNR-ring, $then\ for\ all$ ą ¸ƀ ∈ N ($\Re$). ąƀ + r(ą ƀ) = (ą ƀ + r(ą ƀ)$\big(\alpha + r$(ą ƀ)$\big)\big($ą ƀ + r(ą ƀ)$\big)$,for some $\alpha \in \Re$,so(ą ƀ − ą ƀαą ƀ) ∈ r(ą ƀ).Thus ą ƀ(ą ƀ − ą ƀαą ƀ) = 0 = (ąƀ)^2 − (ąƀ)$^2\alpha$ą ƀ. Since $\Re$ is SXM,then$\big(1 - \alpha$(ąƀ)$\big) \in r$(ąƀ)$^2 = r$(ą ƀ) . Therefore ąƀ = (ąƀ)α(ąƀ) and so $\Re$ is CNR-ring. □

Theorem 2.11. If $\Re$ is a CNR-ring and $\alpha\beta = \beta\alpha\ for\ every\ \alpha, \beta \in N$ ($\Re$), then $Y(\Re) = 0$.

Proof: Let $Y(\Re) \neq 0$. Then there exists $0 \neq (\alpha\beta) \in Y(\Re)$ such that $(\alpha\beta)^2 = 0$. Since $\Re$ is a CNR-ring and $\alpha, \beta \in N$ ($\Re$).Then $\alpha\beta = \alpha\beta ƀ\alpha\beta$ for some ƀ ∈ $\Re$, if $r(\alpha\beta) \cap ƀ\alpha\beta\ \Re \neq 0$, then ƶ ∈ $r(\alpha\beta) \cap ƀ\alpha\beta\ \Re$, $\alpha\beta ƶ = 0\ and\ ƶ = ƀ\alpha\beta r\ for\ some\ r \in \Re$, $0 = \alpha\beta ƶ = \alpha\beta ƀ\alpha\beta r = \alpha\beta r$, ƶ = ƀ$\alpha\beta r$ = ƀ0 = 0. Hence $r(\alpha\beta) \cap ƀ\alpha\beta\ \Re = 0$. S0 ƀ$x\beta\ \Re = 0\ and\ ƀx\beta = 0$. Therefore $\alpha\beta = \alpha\beta ƀ\alpha\beta = 0$. Hence $Y(\Re) = 0$. □

Definition2.12. A ring $\mathfrak{R}$ is called right (left) N −duo if for all $ą \in N(\mathfrak{R})$,$ą\,\mathfrak{R}(\mathfrak{R}\,ą)$ is an ideal. [8]

Proposition 2.13. If $\mathfrak{R}$ is N −duo, right N–Pure ring and $\mathfrak{R}ą = \mathfrak{R}\ ą^4$ for any $ą \in N\ (\mathfrak{R})$,then $\mathfrak{R}$ is a $SC\ N$R-ring.

Proof: For any $0 \neq ą \in N\ (\mathfrak{R})$, $ą\ \mathfrak{R}$ is a left pure, $ą = ƀ\,ą$,for some $ƀ \in ą\,\mathfrak{R}$, Multiply left sided by $ą$,

$ą^2 = ąƀ\,ą = ąα\ ą^4 = α\ ą\ ą^4 = ƶ\ ą^4\ ą^4 = ą^4 β\ ą^4$ for some $α, ƶ, β \in \mathfrak{R}$ .So $\mathfrak{R}$ is SCNR-ring. □

Definition 2.14. A ring $\mathfrak{R}$ −module M is called N −injective if for all $ą \in N(\mathfrak{R})$, any $\mathfrak{R}$ –homomorphism $f: ą\,\mathfrak{R} \to M$ can be extended to

$\mathfrak{R} \to M$. [8]

Theorem 2.15. Consider $\mathfrak{R}$ be a ring and $r(ą) = l(ą)$,$\mathfrak{R}\ ą^4 = \mathfrak{R}\ ą^2$ for all $ą \in \mathfrak{R}$ .Then $\mathfrak{R}$ is SCNR-ring. If every maximal right ideal is a left N −injective.

Proof: We shall prove that $ą^4\ \mathfrak{R}\ + r(ą^4) = \mathfrak{R}$, for any $ą \in N(\mathfrak{R})$. If $ą^4\ \mathfrak{R}\ + r(ą^4) \neq \mathfrak{R}$,Then there exists a maximal right ideal $M\ of\ \mathfrak{R}$ such that $ą^4\ \mathfrak{R} + r(ą^4) \subseteq M$ Since M is N −injective ideal, then let $f: ą^4\ \mathfrak{R} \to M$ such that $ą^4 = f(ą^4) = ƀą^4$(for some $ƀ \in M$), $(1 - ƀ)ą^4 = 0$, $(1 - ƀ) \in l(ą^4) = r(ą^4) \subseteq M$, $1 \in M$, a contradiction. Therefore $ą^4\mathfrak{R} + r(ą^4) = \mathfrak{R}$, for any $ą \in N\ (\mathfrak{R})$ $ą^4α + đ = 1$, $α \in \mathfrak{R}$, $đ \in r(ą^4)$, $ą^4αą^2 = ą^2$, since $\mathfrak{R}ą^2 = \mathfrak{R}ą^4$, the $ą^4ƶ\ ą^4 = ą^2$. Hence $\mathfrak{R}$ is SCNR-ring. □

Conclusion:

The ring $\mathfrak{R}$ is reduced, if CNR-ring and $(ƀ\ ą)\ \mathfrak{R} = \mathfrak{R}\ (ƀ\ ą)^2$,for every $ą$, $ƀ \in N\ (\mathfrak{R})$. If $\mathfrak{R}$ is CNR-ring and $α\ β = βα$ for all $α\ β \in \mathfrak{R}$, then $Y(\mathfrak{R}) = 0$. Also we get $\mathfrak{R}$ is SCNR-ring, if every maximal right ideal is a left N –injective and $r(ą) = l(ą)$, $\mathfrak{R}\ ą^4 = \mathfrak{R}ą^2$ for all $ą \in \mathfrak{R}$.

References:

[1] Azadi, M.and Sahebi,Sh. (2013). "Commuting $π$ −regular rings" J- of- linear and Topological Algebra vol.02, No.02, 67-70.

[2] Doosti, H. L. Pourfaraj. (2006). "On minimal ideals of commuting regular rings and semi groups". Int. J. Appl. Math. 19, 201-210.

[3] Huh, Ch. N. K. Kim, Y. Lee. (2004). "Example of strongly $π$ −regular rings". Pure Appl. Algebra. 189, 195-210.

[4] Mahmood, R.D. and Abd, S.A. (2023)."Some Results on strongly commuting regular rings". AIP conf. proc. 2177,040082.

[5] Mahmood, R.D. and Abd, S.A. (2023)."On N-pure ring".AIP conf. proc. 2834,080048.

[6] Marzith,F., Safali,S. and Mahmoud,K. (2013)."Strongly Commuting regular rings"J.Basic and Appl. Sci.Res.,3(1),1078-1081.

[7] Ming, R. yue chi," On Von Neumaun regular rings, III, Monatshefte for Math.,86 (1978),251-257.

[8] wei, J.C. and chen, J.H., (2007),"nil-injective rings". Inter. Ekc. J. of Algebra, vol. 2, pp.1-12.

[9] Saadati, S. and Sh, A. Safali Sabet(2014)"Unit-free Commuting π −regular rings" World J-of Enviro. Blos. Vol.6.

[10] Xiaofeng Yu, shan Jiang, Jingran Xie. 2009. "Commuting regular semi group rings". Int. J. Algebra. 3, No. 15, 739-745.

[11] Yamini, A. H. Sh. A. Safari. Sabet. (2004). "Commuting regular rings". Int. J. Appl. Math. 14(4), 357-364.

A HYBRID FR-HS CONJUGATE GRADIENT METHOD FOR UNCONSTRAINED OPTIMIZATION

Hind H. Mohammed
lecturer, College of Computer Science and Mathematics, University of Mosul, Mosul, Iraq .

hindmath@uomosul.edu.iq

A HYBRID FR-HS CONJUGATE GRADIENT METHOD FOR UNCONSTRAINED OPTIMIZATION

Hind H. Mohammed
lecturer, College of Computer Science and Mathematics, University of Mosul, Mosul, Iraq .

hindmath@uomosul.edu.iq

Abstract:

A Hybrid nonlinear Conjugate Gradient Methods with combining Fletcher–Reeves and Hestenes–Stiefel parameters are achieved by a combination of Fletcher–Reeves and Hestenes–Stiefel parameters with Wolfe-Powell line search for solving unconstrained optimization problems, which is presented in this paper. The proposed approach aims at a semi-convergent focusing, plus the efficiency of a numerical solution. It is ensured that a sufficient descent property is satisfied and under typical conditions the convergence of the sequence is shown using a Zoutendijk-type condition. These numerical experiments are based on the standard unconstrained optimization test problems and involve comparing the proposed method with the Fletcher–Reeves method, Hestenes–Stiefel method and Polak–Ribiére–Polyak method. The outcome indicates that the proposed hybrid technique results competitive performance in the terms of iteration, function and gradient evaluations and the computational time.
Keywords: Conjugate gradient method, descent direction, Convergence Numerical result.

1. Introduction :

It goes without saying that we are dealing with enormous amounts of data in the modern world, which makes modeling an essential responsibility. Continuous optimization models appear in many real-world fields, including machine learning and signal processing.
Because of their ease of use and minimal memory requirements, conjugate gradient methods continue as one of the numerous instruments using to solve unconstrained optimization. They are still well-known among mathematicians and engineers[1, 2]. encountered with problems of the kind:

$$\text{Min } f(x) \ , \ x \in R^n \qquad (1)$$

Where, $f : R^n \to R$ is a continuously differentiable function [3]. In the entire paper, the $\|.\|$ denotes the Euclidean norm on R^n , $g(x) = \nabla f(x)$ symbolizes the gradient of f at x, and. For ease of use, we indicate (x) by f_k, and $\nabla f(x)$ by g_k. Iterative methods are typically used to create a series of points in order to address problems $\{x_k\}$. Beginning with a starting point $x_\circ \in R^n$, using the recurrence

$$x_{k+1} = \alpha_k d_k + x_k \qquad (2)$$

The scalar $\alpha_k > 0$, which, also referred to as the step-size or step length, is determined by performing numerous meticulous computations with the aim of nearly fulfilling the requirement.

$$f(x_k + \alpha_k d_k) \approx \min_{\alpha \geq 0} \{x_k + \alpha \ \ d_k\} \qquad (3)$$

In actuality, because (4) requires extensive calculations in gradient and function evaluations, it is not an efficient line search.
Therefore, we favor using low-cost line search. It's strong Wolfe- Powell line search (SWP) [4, 5], which is provided as:

$$f(x_k + \alpha_k d_k) \leq f(x_k) + \delta \alpha_k g_k^T d_k \qquad (4)$$

$$\left|d_k^T g(x_k + \alpha_k d_k)\right| \leq -\sigma d_k^T g_k \quad (5)$$

Such, $0<\delta<\sigma<1$ are constants. Therefore, by employing SWP line search, we can inherit the benefits of precise line search at a low cost. But different selections of α_k and d_k in (3) suggest several CG techniques. The SWP line search is a very strong enhancement of the Wolfe-Powell (WWP) line search, which is provided by:

$$f(x_k + \alpha_k d_k) \leq f(x_k) + \delta \alpha_k g_k^T d_k \quad (6)$$

$$d_k^T g(x_k + \alpha_k d_k) \geq \sigma d_k^T g_k \quad (7)$$

Conjugate gradient (CG) techniques have garnered particular interest because they only need to store a small number of n-vectors. The following format represents the search directions for the CG techniques.

$$d_\circ = -g_\circ, \; d_{k+1} = -g_{k+1} + \beta_k d_k, \; k = 0,1, \ldots. \quad (8)$$

There are many formulas with completely different computational outcomes for β_k[6, 7, 8]. The manner that conjugate gradient algorithms define the parameter β_k is different. Several selections of β_k have been presented over the years, leading to various conjugate gradient algorithms. Most popular formulas for β_k are Fletcher-Reeves (FR) method[9]

$$\beta_k^{FR} = \frac{g_{k+1}^T g_{k+1}}{g_k^T g_k} \quad (9)$$

Polak-Ribi´ere-Polyak (PRP) method[10]:

$$\beta_k^{PRP} = \frac{g_{k+1}^T y_k}{g_k^T g_k} \quad (10)$$

Hestenes-Stiefel (HS) method[11]

$$\beta_k^{HS} = \frac{g_{k+1}^T y_k}{d_k^T y_k} \quad (11)$$

Dai-Yuan (DY) method[12]

$$\beta_k^{DY} = \frac{g_{k+1}^T g_{k+1}}{d_k^T y_k} \quad (12)$$

High convergence properties of the DY and FR approach are well known from the literature. But it won't necessarily be applicable in a real world situation. However, it can be noted that PRP approaches and HS approaches will do better numerically but may not necessarily converge in general. In view of this, researchers attempt to devise new techniques that exploit both of these techniques, in Section 3. In Section 4, we then compare the numerical results of the novel approach with a couple of other popular approaches. Finally, the conclusion is outlined in Section 5. This has been mainly achieved by using hybrid techniques, that is, two or more of the βk terms in the same conjugate gradient. Hybrids thus attempt to include appealing aspects of many algorithms[13].

One of the crucial requirements for the global convergence of CG methods that can support the convergence structure is the sufficient descent condition. The algorithm's search direction meets the necessary descent requirement when there is a $c > 0$ such that

$$d_k^T g_k \leq -c\|g_k\|^2 \quad (13)$$

This method is existing in the section 2.

2. Motivation and Algorithm:

In this work, we combine the FR and HS approaches. The formula for the parameter $\beta_k$in the hybrid conjugate gradient method of β_k^{FR} FR and β_k^{HS} is as follows:

$$\beta_k^{HI} = (1-\gamma_k)\beta_k^{FR} + \gamma_k\beta_k^{HS} \qquad (14)$$

We will suggest γ_k defined as:

$$\gamma_k = \frac{f_k - f_{k+1}}{-\alpha_k g_k^T d_k} \qquad (15)$$

Following the substitution of parameter values and simplification, we have

$$\beta_k^{HI} = (1-\gamma_k)\frac{g_{k+1}^T g_{k+1}}{g_k^T g_k} + \gamma_k \frac{g_{k+\ \ 1}^T y_k}{d_k^T y_k} \qquad (16)$$

From the equation above, we obtain:

$$\beta_k^{HI} = \frac{g_{k+1}^T g_{k+1}}{g_k^T g_k} - \gamma_k\left(\frac{g_{k+1}^T g_{k+1}}{g_k^T g_k} - \frac{g_{k+1}^T y_k}{d_k^T y_k}\right) \qquad (17)$$

It is widely recognized that the scalar parameter is γ_k. taking into account that if $\gamma_k = 0$ then $\beta_k^{HI} = \beta_k^{FR}$ and if $\gamma_k = 1$, then $\beta_k^{HI} = \beta_k^{HS}$. However, if $0 < \gamma_k < 1$, If the parameters are β_k^{FR} and β_k^{FR}, then β_k^{HI} is a suitable convex combination of them.

Next the method of the proposed technique is presented as stated:

Algorithm 1:

Step 1: Select a starting point $x_\circ \in R^n$, $\in > 0$, $0 < \delta < \sigma < 1$. $k = 0$

Step 2: Compute $g_\circ = \nabla f(x_\circ)$. If $\|g_\circ\| \leq \in$ stop.

Step 3: for $k = 0,1, \ldots$ do

Step 4: Set d_k using (8)

Step 5: Find α_k such that satisfied 6 & 7.

Step 6 : Put $x_{k+1} = x_k + \alpha_k d_k$, and set $k = k + 1$.

Step 7 : If $\|g_k\| \leq \in$ stop.

Step 8 : Compute β_k using equation 17 .

Step 9: end for

3. The Descent property and global convergence:

The new hybrid conjugate gradient approach is sufficient descent condition as well as global convergence under the generalized Wolfe conditions are presented in this section. the following theorem states that the search direction in Algorithm 1 is always sufficient descent.

Theorem 1:
Suppose the algorithm (1) generates sequences $\{g_k\}$,$\{x_k\}$ and $\{\alpha_k\}$,$\{d_k\}$. Then the search direction d_k satisfies:

$$d_{k+1}^T g_{k+1} < -c\|g_{k+1}\|^2 \qquad (18)$$

Proof :

Since $d_\circ = -g_\circ$, it follows $d_\circ^T g_\circ = -\|g_\circ\|^2$, which satisfies the (18), when the (18) holds for an integer k, then we prove that the(18) is satisfied for k + 1, multiplied (8) by g_{k+1}, get:

$$d_{k+1}^T g_{k+1} = -\|g_{k+1}\|^2 + \beta_k d_k^T g_{k+1} \qquad (19)$$

As a result, we get:

$$d_{k+1}^T g_{k+1} = -\|g_{k+1}\|^2 + \left[\frac{\|g_{k+1}\|^2}{\|g_k\|^2} - \gamma_k\left(\frac{\|g_{k+1}\|^2}{\|g_k\|^2} - \frac{g_{k+1}^T y_k}{d_k^T y_k}\right)\right] d_k^T g_{k+1} \qquad (20)$$

Using the Wolfe condition (6) and (7)

$$\gamma_k = \frac{f_k - f_{k+1}}{-\alpha_k g_k^T d_k} \le \frac{-\mu\alpha_k g_k^T d_k}{-\alpha_k g_k^T d_k} = \mu$$

This gives:

$$d_{k+1}^T g_{k+1} \le -\|g_{k+1}\|^2 + \left[\frac{\|g_{k+1}\|^2}{\|g_k\|^2} - \mu\left(\frac{\|g_{k+1}\|^2}{\|g_k\|^2} - \frac{g_{k+1}^T y_k}{d_k^T y_k}\right)\right] \sigma\|g_k\|^2 \qquad (21)$$

Implies:

$$d_{k+1}^T g_{k+1} \le -\|g_{k+1}\|^2 + \sigma(1-\mu)\|g_{k+1}\|^2 + \sigma\mu\left(\frac{g_{k+1}^T y_k}{d_k^T y_k}\right)\|g_k\|^2 \qquad (22)$$

By choosing appropriate Wolfe parameters $0 < \sigma, \mu < 1$ such that

$\sigma(1-\mu) < 1$

we arrive at:

$$d_{k+1}^T g_{k+1} < -c\|g_{k+1}\|^2 \qquad (23)$$

where $\sigma(1-\mu) > 0$,This confirms the sufficient descent property.
To be able to demonstrate the global convergence, The analysis of our approach's global convergence features requires the following standard assumptions to be widely employed in the literature.

Assumption 1.

1. Bounded Level Set: The level set $T = \{x: f(x) \le f(x_\circ)\}$, is bounded namely there exists a constant $a > 0$ such that:

$$\|x\| \le a, \ \forall x \in T \qquad (24)$$

2. **Lipschitz Continuity of the Gradient:** The objective function f is a continuously differentiable and its gradient satisfied Lipschitz continuous in a neighborhood N of T; that is, there is a constant L>0 such that

$$\|\nabla f(x) - \nabla f(y)\| \leq L\|x - y\|, \text{ for all } x, y \in N \qquad (25)$$

3. **Bounded Gradient:** There is a constant b that is positive such that

$$\|\nabla f(b)\| \leq \Gamma, \ \forall x \in N \qquad (26)$$

The famous Zoutendijk condition [14] follows from the following lemma.

Lemma 1: Assume that Assumption 1 is true. The sequence $\{x_k\}$ is given by the new CG method. Where the direction d_k satisfies (13) and step size(6) and (7), Then we have:

$$\sum_{k=1}^{\infty} \frac{(g_k^T d_k)^2}{\|d_k\|^2} < \infty \qquad (27)$$

We now demonstrate the new algorithm's global convergence based on the earlier discussion.

Theorem 2: Consider the sequences $\{x_k\}$ and $\{d_k\}$ generated by HI algorithm. Assumptions(1) is satisfied, then we have:

$$\liminf_{k\to\infty} \|g_k\| = 0 \qquad (28)$$

Proof :

Assume that (28) is false, then there is a constant $\in$>0 that:

$$\|g_k)\| \geq \in, \quad \forall k \geq 0 \qquad (29)$$

Let $D = \max\{\|x - y\| : x, y \in N\}$ be the neighborhood N is diameter of the level set.Then, from (14) we have:

$$\begin{aligned}
|\beta_k^{HI}| &= |(1-\gamma_k)\beta_k^{FR} + \gamma_k\beta_k^{HS}| \\
|\beta_k^{HI}| &\leq |\beta_k^{FR}| + |\beta_k^{HS}| \\
|\beta_k^{HI}| &\leq \frac{\|g_{k+1}\|^2}{\|g_k\|^2} + \frac{\|g_{k+1}\|\|y_k\|}{\mu\alpha_k^2\|d_k\|^2} \\
|\beta_k^{HI}| &\leq \frac{\Gamma^2}{\epsilon^2} + \frac{\Gamma LD}{\mu\alpha_k^2 B^2} = P \qquad (30)
\end{aligned}$$

Thus, from(8)and(30) it follows that:

$$\begin{aligned}
\|d_{k+1}\| &\leq \|g_{k+1}\| + |\beta_k|\|d_k\| \\
\|d_{k+1}\| &\leq \|g_{k+1}\| + |\beta_k|\|d_k\| \\
\|d_{k+1}\| &\leq \Gamma + \frac{P\|x_{k+1} - x_k\|}{\alpha_k} \\
\|d_{k+1}\| &\leq \Gamma + PD = M \qquad (31)
\end{aligned}$$

and this suggests that:

$$\sum_{k\geq 0} \frac{1}{\|d_k\|^2} \geq \frac{1}{M^2} \sum_{k\geq 0} 1 = \infty$$

$$C^4 \in^4 \sum_{k\geq 0} \frac{1}{\|d_k\|^2} \leq \sum_{k\geq 0} \frac{\|g_k\|^4}{\|d_k\|^2} = \sum_{k\geq 0}^{\infty} \frac{(g_k^T d_k)^2}{\|d_k\|^2} < \infty \qquad (32)$$

This is obviously contradictory. Thus, the claim (28) is accurate.

4. Results and Discussion:

In this part, the numerical results obtained for the evaluation of the effectiveness of the proposed approach for solving unconstrained optimization problems are given. The test suite employed consists of 20 unconstrained functions, yielding 107 distinct problem instances. The dimensions range from 2 to 50, encompassing varying levels of difficulty. Some of these are smooth, convex functions—such as the Sphere function, the Quadratic Function (QF1), and the Diagonal 4 function for which most conjugate gradient methods exhibit rapid convergence. Others include functions such as the "Three-Hump Camel," "Six-Hump Camel," Treccani, and Zettl functions; these are non-convex and feature multiple local minima or stationary points, meaning that the convergence of a given method depends on the chosen initial point.

A third group includes extended functions such as the Rosenbrock, Beale, Himmelblau, White & Holst, DENSCHNB, and Tridiagonal 1 functions which are frequently used to test the behavior of algorithms in higher dimensions. Finally, more challenging functions were employed, namely the Powell, Extended Powell, and Extended Wood functions; these are characterized by non-invertible Hessian matrices or level sets with sharp curvature, which slow down the convergence process [15], [16] [17],[18].

The comparisons are made at several performance metrics – No of iterations (NIter), No of Frequency of target function evaluations (NFE), No of Frequency of gradient evaluations (NGE), Sum of CPU time in seconds at the specific test functions and dimensions. Using the same test functions and dimensions, the computational performance of the suggested approach is contrasted with that of the FR, HS, and PRP approaches. All approaches used the same Wolfe condition settings and line search parameters to ensure uniformity. In particular, δ =0.01 and σ =0.3 were used as the line search parameters. The identical starting point is selected for each test function in this comparison, and all computations are stopped when a point x_k satisfies $\|g_k\| \leq 10^{-6}$.

(NIE): HI method consistently outperform the HS,FR and PRP methods in terms of the number of iterations .

(NFE): The number of function evaluations required by the HI method is lower than that of theHS, FR and PRP methods. particularly this suggests that it is proposed technique is more effective in terms of evaluating the objective function during the optimization process.

(NGE) The gradient evaluations, The proposed method outperforms the methods mentioned above in average the derivative calculation.

CPU Time (CPUT): The HI method demonstrate a significant reduction in CPU time compared to the HS, FR and PRP methods. where the HI methods exhibit faster convergence.

The results are summarized in the table1.

Table 1: Advantages of Algorithm 1 in numerical test

Methods	Iterations	Func. Evals	Grad Evals	Time
FR	4657	14118	9441	0.3300
PRP	3028	9233	6183	0.2495
HS	2830	8647	5792	0.2090
HI	2815	8592	5757	0.2103

Figures 1-3 show the performance of new algorithm to solve the unconstrained optimization problems. Figure 1 shows that the HI Algorithm performs better than the other approaches based on the

number of iterations because the HI curve is primarily near the top of the HS, PRP, and FR CG curves. Generally, the HI technique is better than alternative techniques. Figure 2 compares the techniques depending on how many

function evaluations, where the HI technique again outperforms the HS, PRP, FR methods in most cases. Figure 3 provides a comparative analysis of the HI approach as opposed to HS, PRP and FR techniques. In terms of CPU time, the novel Algorithm HI outperformed all other approaches, as this graphic shows. This demonstrates unequivocally how successful the HI approach is.

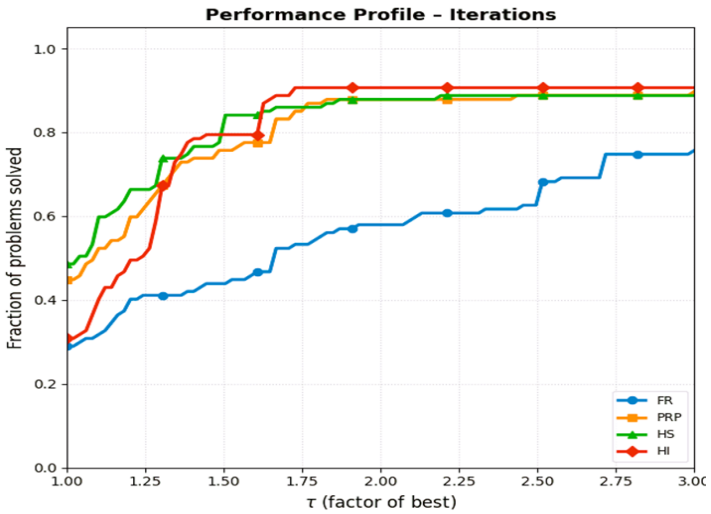


Figure 1: Performance based on NIE

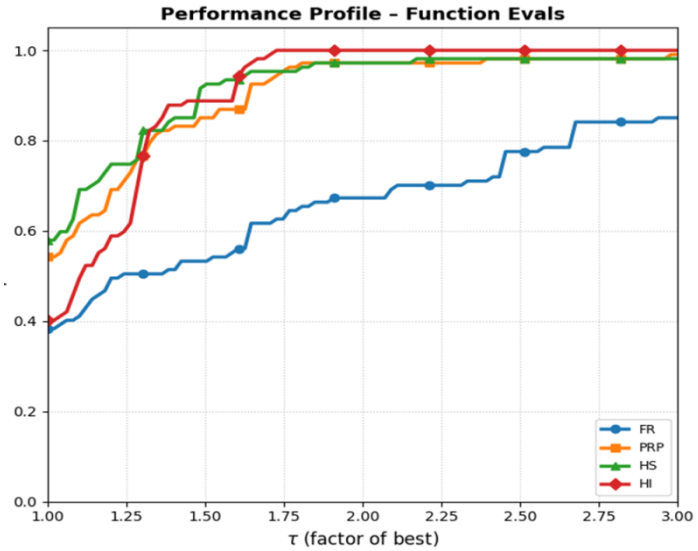


Figure 2: Performance based on NFE

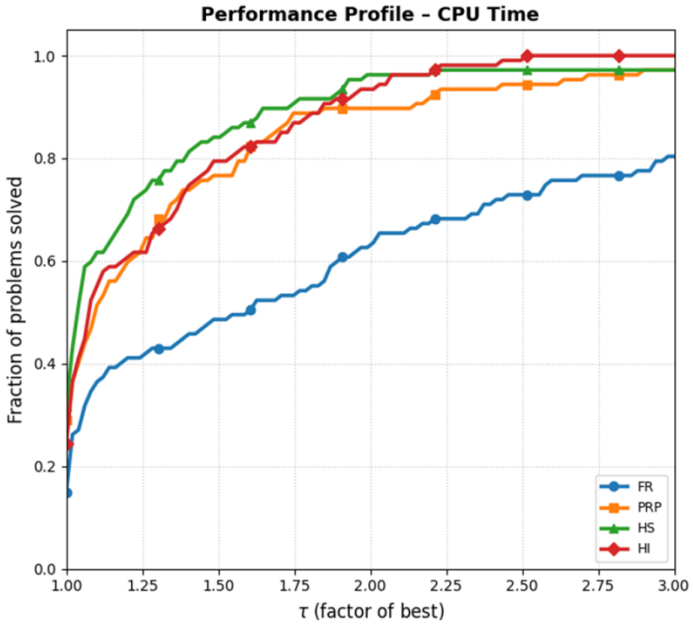


Figure 3: Performance based on CPU

5. Conclusion

We introduce a new solution approach in this research suitable for solving the optimization problems in a quick way and effectively. Both the descent and convergence properties are satisfied by the suggested approach. Furthermore, through numerical results it was proved that the proposed method is reliable and effective compared to Hestenes-Stiefel (HS), Polak-Ribi´ere-Polyak (PRP) and Fletcher-Reeves (FR). This new approach will not only provide us with new ideas for further development of even better approaches, but it could also be a viable alternative to the current approaches. To explore their potential in this area, we plan to use This technique in machine learning applications in future studies.

References:

1. Babaie-Kafaki S. , A survey on the Dai-Liao family nonlinear conjugate gradient methods. Journal Rairo operations research, Rairo-oper. Res. 57, 43–58, (2023).
2. Moyi A. U., . Leong W. J and Ibrahim S., On the application of three – term conjugate gradient method in regression analysis. International Journal of Computer Applications, 102 (8), 1 - 4. https://doi.org/10.5120/17832-8517,(2014).
3. Yu C. , Hong Y. and Chenyun M. , Applications of two sufficient descent spectral conjugate gradient methods in image denoising. Journal AIMS Mathematics, 11(3): 8635–8654, (2026).
4. Wolfe P. , Convergence conditions for ascent methods. SIAM Review, 11(2):226–235, (1969).
5. Wolfe P. , Convergence conditions for ascent methods. ii: Some corrections. SIAM Review, 13(2):185–188, (1971).
6. Andrei N. , Numerical comparison of conjugate gradient algorithms for unconstrained optimization. Stud. Inform. Control 16,333–352, (2007).
7. Babaie-Kafaki S. , On the sufficient descent condition of the Hager–Zhang conjugate gradient methods. 4OR 12, 285–292, (2014).
8. Hagar W. W. and Zhang H. , A survey of nonlinear conjugate gradient methods. Pacific J. Optim. 2, 35–58, (2006).

9. Fletcher R. and Reeves G. , Function minimization by gradients computer. Journal, Vol(7). 149-154 (1964).
10. Polak, E. and Ribiere,G. , Not sur la convergence de directions conjugate. Rev. Franaisse Informants. Research operational, 3e Anne., 16. 35-43 (1969).
11. Hestenes, M and Stiefel, E. , Methods of CG for solving linear Systems. J. Research Nat. Bar . stan. Sect. B. ,49. 409-436 (1952).
12. Dai Y. and Yuan Y. , A Nonlinear conjugate gradient method with a strong global convergence property. SIAM J, Optim10, 177-182 (1999).
13. Kaelo P. and Mtagulwa P. & Thuto M. V. , A globally convergent hybrid conjugate gradient method with strong Wolfe conditions for unconstrained optimization. Math. Sci. (Springer),14, 1–9(2020).
14. Zoutendijk G. , Nonlinear programming, computational methods. In Integer and Nonlinear Programming, pages 37–86, (1970).
15. Bongartz, A. R. , Conn N. G., and Toint P. L., "CUTE: Constrained and unconstrained testing environment." ACM Trans. Math. Softw, vol. 21, no. 1, pp. 123–160, Mar. doi: 10.1145/200979.201043, (1995).
16. Moré J. J., Garbow B. S., and Hillstrom K. E., "Testing unconstrained optimization software." ACM Trans. Math. Softw, vol. 7, no. 1, pp. 17–41, Mar, (1981).
17. Gould N. I. M. , Orban D. , and Toint P. L. , CUTEr and SifDec:A constrained and unconstrained testing environment, revisited. ACM Trans. Math. Softw., vol. 29, no. 4, pp. 373-394, Dec. https://doi.org/10.1145/962437.962439,(2003).
18. Jamil M., and Yang X. S., A Literature Survey of Benchmark Functions For Global Optimization Problems, Int, Journal of Mathematical Modelling and Numerical Optimisation Vol. 4(2) (2013) 150-194. http://dx.doi.org/10.1504/IJMMNO.055204,(2013).

Enhanced 4D Hyperchaotic Dynamics via Optimization of Chaotic System Parameters using ICGO

Karam Adel Abed [1], Omar Saber Qasim [2]

[1] Department of Operations Research and Intelligence Techniques, College of Computer Sciences and Mathematics, University of Mosul, Iraq

[2] Department of Mathematics, College of Computer Science and Mathematics, University of Mosul, Mosul, Iraq

Email: karamadel@uomosul.edu.iq

Enhanced 4D Hyperchaotic Dynamics via Optimization of Chaotic System Parameters using ICGO

Karam Adel Abed [1], Omar Saber Qasim [2]

[1] Department of Operations Research and Intelligence Techniques, College of Computer Sciences and Mathematics, University of Mosul, Iraq

[2] Department of Mathematics, College of Computer Science and Mathematics, University of Mosul, Mosul, Iraq

Email: karamadel@uomosul.edu.iq

ABSTRACT

In this research, an analytical and design research of an enhanced hyperchaotic system, which is basically the three-dimensional Sprott C model is performed. To increase dynamic and structural complexity, the basic framework was upgraded to a four-dimensional model by employing a state feedback control technique. This Article of the new system's dynamic behavior demonstrated a confirmed transition from the conventional chaotic state to a state of increased higher-dimensional chaotic complexity, aiming to enhance levels of dynamic and physical complexity. To adjust parameters and optimize the system's dynamic behavior, the hybrid algorithm ICGO_Game_Chaotic was utilized. Analyses of the dynamic characteristics proved that the system effectively transitions from ordinary chaos to hyperchaos. Numerical results indicate that this four-dimensional system possesses exceptional flexibility, extreme sensitivity to variables, and a higher level of chaos compared to the original version.

Keywords:

Sprott-C system, Parameter estimation, ICGO algorithm.

1. INTRODUCTION

Recent decades have seen significant progress in chaos theory as researchers have extensively investigated chaotic systems, which have found use across a range of areas, including NNTs[1-4], synchronization [5], communications [6], encryption [7-8], engineering [9-11]. The chaotic signal is regarded as an optimal candidate for secure communication systems, Chaotic systems and with different dynamic properties are used in order to enhance complexity and take advantage of their ease of implementation and unpredictability. [12-18]. The discovery of the chaotic attractor is attributed to Lorenz in 1963 [19], This was followed by the announcement of a range of 3D and 4D systems, including the Sprott in 1976, 1979, 1999, 2004, and 2021, respectively [20]. In 1994, J.C. Sprott designed a set of systems featuring nonlinear boundaries and observed various chaotic phenomena. [21], Many researchers have worked on refining it; the Sprott-A system was presented as a system with a hidden attractor. [22]. They are classified into four categories: (a) those that do not contain equilibrium points. [23-27], (b) with stable the points [28-29], (c) with a curve [30-31], and (d) with point circles

[32]. It can be utilized to classify chaotic systems [33]. The adopted chaotic system was studied. (Sprott, 2011), With a focus on improving the new system, given the rich, chaotic characteristics it possesses.

Multi-dim highly chaotic systems have consistently remained a primary area of interest within the field of chaos theory [34]. A chaotic system was extended to a four-dimensional system and a study of its structure and analysis of its dynamic properties led to highly complex hyperchaotic behavior [35]. To design hyperchaotic systems having complex physical characteristics, a lot of attention has been paid to Sprott-S system, which is extended to a four-dimensional system by implementing linear feedback control (LFC) strategy [36-37].

This is an article on the design of a new 4D chaotic system derived from Sprott-C system, which contains seven terms. The selection of chaotic system parameters is discussed; an optimization process was performed on the parameters of an expanded 4D chaotic system derived from the established 3D system using the proposed algorithm, resulting in a hyperchaotic system. This system features a more compact structure and fewer parameters compared to similar hyperchaotic systems, alongside rich complex dynamic properties and compliance with Sprott's second criterion by exhibiting previously unobserved behavior. The following are the major contributions to the study:

1. We designed a new 4D system that is based on the 3D Sprott-C system, with the particular characteristics of having two positive Lyapunov exponents.
2. The proposed system is very simple both structurally and in terms of the number of terms needed: only seven terms are used, and only two of these are nonlinear.
3. The basic dynamics of the system is thoroughly examined. This includes an extensive study of the Jacobian array, stability and classification of the equilibrium points, Lyapunov metrics, and the D_{KY}, both before and after the parameter estimation.
4. The ICGO algorithm was used to optimally tune the parameters of the model in a strategic manner in order to obtain a robust hyperchaotic.

This study has six main axes. The second axis is devoted to the display of an innovative, highly chaotic, 4D model starting from the environment Sprott-C system. The third axis then provides an in-depth analytical study of this model. The developed algorithmic methodology is detailed in the fourth axis. The fifth axis explores the dynamic behavior of the system and then evaluates its parameters using the aforementioned algorithm. The paper concludes in the sixth axis by summarizing the most important findings of the research.

2. DESCRIPTION SIMPLE 4D HYPERCHAOTIC SYSTEM

The Sprott C 3D system is defined as follows:

$$\begin{cases} \dot{x} = yz \\ \dot{y} = x - y \\ \dot{z} = 1 - x^2 \end{cases} \quad (1)$$

Sprott (1994) established a seminal series comprising nineteen elementary 3D chaotic systems series [22] The generation of new systems often relies on combining or interconnecting these baseline models, alongside leveraging established analytical approaches. Derived from the Sprott-C prototype, the present study introduces a streamlined chaotic system composed of seven terms, including two nonlinear teams, as expressed in Equation (2):

$$\begin{cases} \dot{x} = yz \\ \dot{y} = x - y - a_1 x_4 \\ \dot{z} = 1 - x^2 \\ \dot{u} = a_2 z \end{cases}$$

(2)

Considering (a_2) as a positive non-zero constant $(a_2 \neq 0)$. the new system exhibits a simple structure consisting of only seven terms, thus satisfying one of Sprott criteria (Sambas et al., 2021) [30]. as illustrated Fig. 1.

$$(a_1, a_2) = \underbrace{(-1.000142, -0.003)}_{\text{Typical parameters}}$$

(3)

$$(x_0, y_0, z_0, u_0) = \underbrace{(0.3, 0.2, 0.3, 0.1)}_{IC} \quad (4)$$

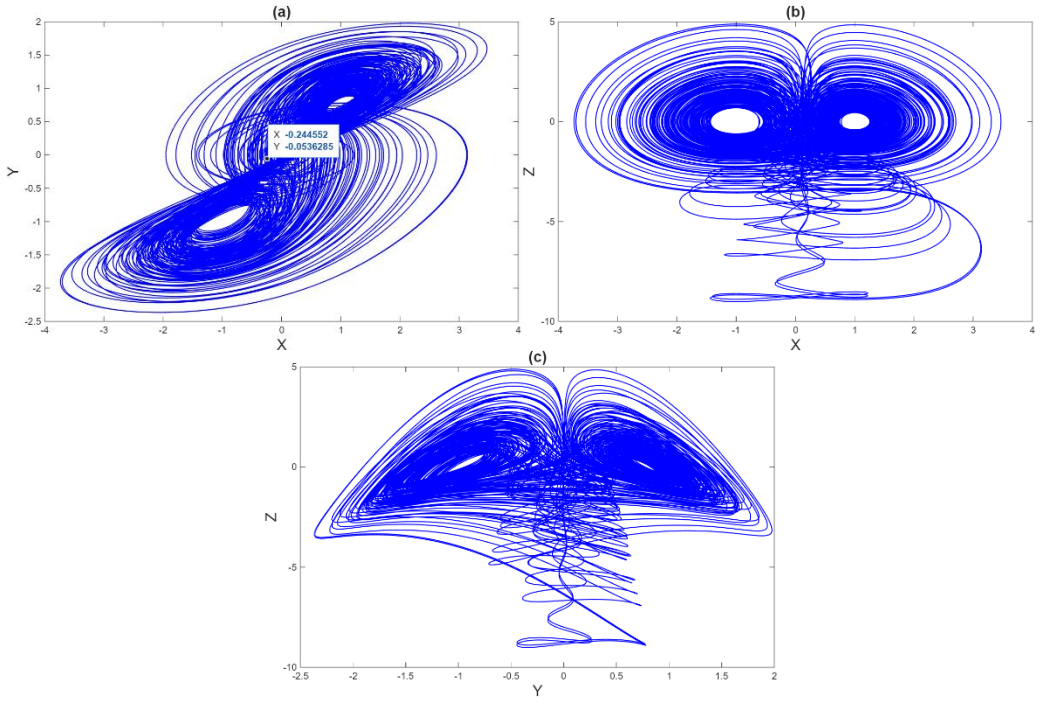


Fig. 1.2D phase trajectories for the proposed Sprott-C across different projections:$(a)\ x-y, (b)\ x-z, (c)\ y-z$.

Analytical and computational studies will be conducted on the key physical properties of system (2).

2.1. DISSIPATIVE

The system (2) is divergent (trace of a Jacobian matrix) and its value is:

$$Trace = \sum_{i=1}^{4} \frac{\partial \dot{x}_i}{\partial x_i} = -1 \quad (5)$$

2.2. EQUILIBRIA POINTS

Equilibria Points constitute the central pillar in the analysis of dynamical systems, where opposing effects balance out to bring the system to a state of stability. This state embodies the point where disturbances vanish, paving the way to study and monitor variables in an efficient and scientific manner. In the Sprott-C system, assuming ($\dot{x} = \dot{y} = \dot{z} = \dot{u} = 0$), as shown in Equation (6):

$$\begin{cases} yz = 0 \\ x - y - a_1 u = 0 \\ 1 - x^2 = 0 \\ a_2 z = 0 \end{cases} \tag{6}$$

Solving the system mentioned above yields two equilibrium, $E_{1,2} = (\pm 1, 1 - au, 0, 0)$. Meanwhile, the array of the new system at $(E_{1,2})$, along with the characteristic equation:

$$J = \begin{bmatrix} 0 & z & y & 0 \\ 1 & -1 & 0 & -a_1 \\ -2x & 0 & 0 & 0 \\ 0 & 0 & a_2 & 0 \end{bmatrix} = \overrightarrow{J(E_{1,2})} \begin{bmatrix} 0 & 0 & 1 - a_1 u & 0 \\ 1 & -1 & 0 & -a_1 \\ \pm 2 & 0 & 0 & 0 \\ 0 & 0 & a_2 & 0 \end{bmatrix} \tag{7}$$

$$\lambda + (\lambda + 1) + \lambda^2 + 2(1 \pm a_1 u)\lambda = 0 \tag{8}$$

Four eigenvalues control the dynamics of the system. There are two fixed parameters ($\lambda_1 = 0, and\ \lambda_2 = -1$), a zero root for marginal stability and a negative for stable convergence. The other two roots depend on the parameters $\lambda_{3,4} = \pm\sqrt{2(1 - a_1 u)}$. Varying this parameter will alter the behaviour of the system, from an unstable saddle (where the roots are real and of opposite sign) to the sustained oscillations (where the roots are purely imaginary) and eventually a collapse to zero at a certain critical value.

2.3. LYAPUNOV EXPONENETS

The Lyapunov exponents are fundamental quantities that show the average rate of exponential divergence of nearby trajectories. Furthermore, these exponents are used to determine D_{KY}, another measure of system complexity. System (2) was simulated using MATLAB 2024b and the ODE45 numerical solver. Based on the model parameters (3) and I.C. (4), the calculated (LE_s) values are:

$$\begin{cases} LE_1 = 0.1101104 \\ LE_2 = \mathbf{-0.0003752} \\ LE_3 = -0.0067313 \\ LE_4 = -1.1030040 \end{cases}, \sum_{i=1}^{4} LE_i = -1.0468942 \tag{9}$$

$$D_{KY} = J + \frac{\sum_{I=1}^{J} LE_I}{LE_{i+1}} = 3.0535 \tag{10}$$

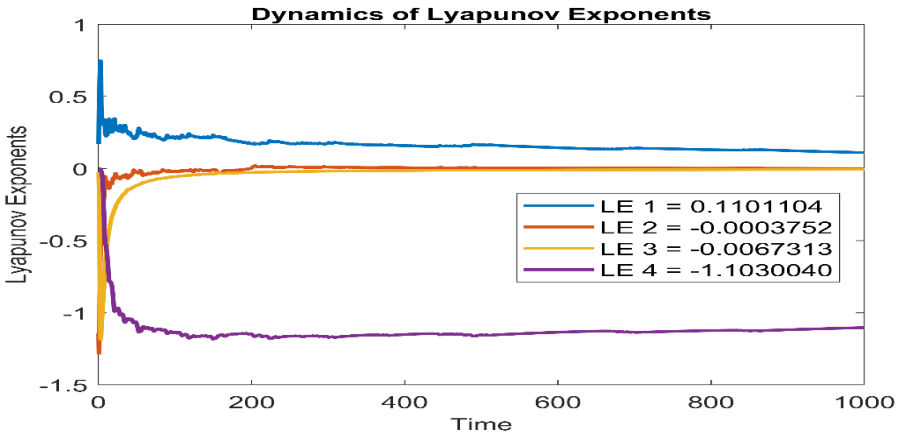


Fig. 2. $LE_s$of the system (2) for $(a_1, a_2) = (-1.000142, -0.003)$

3. IMPROVING (ICGO) ALGORITHM

ICGO represents an improvement on the CGO algorithm which was proposed by the same person, and is based on the fractal geometry [38]. However, the traditional version has its own problems, such as local convergence, and the lack of solution variety, so chaotic maps and dynamic learning parameters were added, which increased the convergence speed and improved the efficiency of the solution space exploring [39].

3.1. THE COMPUTATIONAL MODEL

The ICGO algorithm is an algorithm that combines the use of chaotic initialization of the population with the use of dynamic updating of search positions.

3.2. INITIALIZATION VIA CHAOTIC MAPS

The initial position of the solutions (X_i) is not a random vector $r \in U(0,1)$ as it is in the classic approach, but is a nonlinear chaotic sequence (x_k) which makes it possible to ensure that the solutions are not randomly positioned but are distributed ergodically in the search space [40].

$$y_{k+1} = \mu \,.\, y_k \,.\, (1 - y_k) + \frac{4-\mu}{4} \,.\, \sin(\pi y_k) \qquad (11)$$

Where $y_0 \in (0,1)$ and $\mu \in (0,1]$

3.3. POSITION UPDATE RULE

In each operation are moved in the direction of the selected vector (V), that consists of the Best Global Vector (GB), Best Individual Vector (P_i) and the Average Vector (MG)[41].

$$Y_i^{new} = Y_i^{old} + \alpha_k . (\beta . V - \gamma . Y_i^{old}) \qquad (12)$$

Where:

- $[Y_{NEW}^I]$ and $[Y_{CURRENT}^I]$ They refer to the solution and update vectors, respectively.
- $[V_{seed}]$ seed vertex to the search space.

- $[M_t]$ represents a movement vector at step [t], replacing standard random variables.
- $[\beta]$ and $[\gamma]$ coefficients balancing local exploitation and global exploration.

4. THE PROPOSED TECHNIQUE

Bypass the high computational cost of conventional methods used to convert them into hyperchaotic systems, nature-inspired algorithms offer an efficient alternative by tuning system parameters to enhance complexity and elevate the Lyapunov exponent. This study employs the ICGO algorithm which relies on a three-stage feedforward mechanism (exploration, migration, and exploitation) to achieve the following:

1. Enhancing chaotic behavior by searching the parameter space to increase phase space complexity and chaotic dimension.

2. Testing system dynamics by examining how different factors influence various chaotic systems.

3. Facilitating practical applications by converting standard chaotic systems into hyperchaotic ones to expand their use across various scientific fields.

5. A NEW 4D HYPERCHAOTIC SYSTEM WITH ICGO

Due to the drawbacks of the traditional algorithm, the algorithm ICGO is used which can overcome the defects of the traditional algorithm and has the advantages of escaping from local minimum, fast convergence rate, high accuracy and reliability in chaotic dynamics.

$$\begin{cases} \dot{x} = yz \\ \dot{y} = x - y - a_1 u \\ \dot{z} = 1 - x^2 \\ \dot{u} = a_2 z \end{cases} \tag{13}$$

where $(x, y, z\ and\ u)$ are state variables.

$$(a_1, a_2)^{ICGO} = \underbrace{(-0.051476090541331, 0.192175435433803)}_{\text{Typical parameters}} \tag{14}$$

$$(x_0, y_0, z_0, u_0) = \underbrace{(0.3, 0.2, 0.3, 0.1)}_{IC} \tag{15}$$

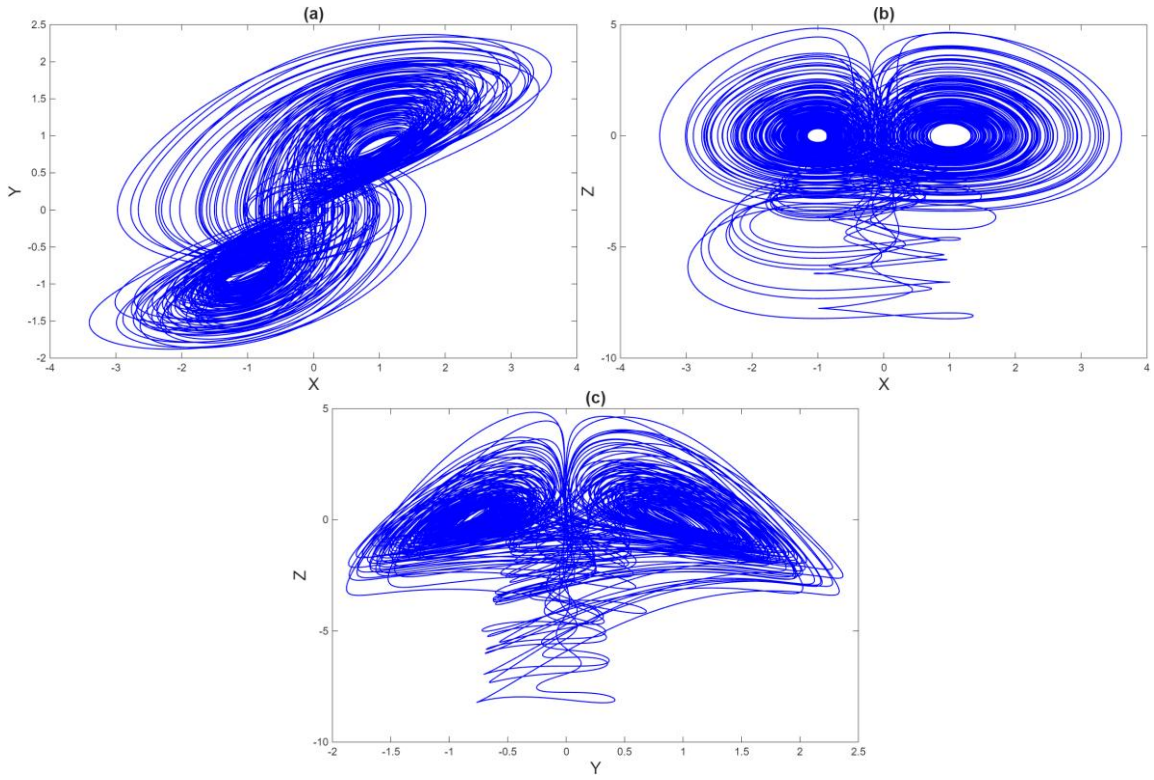


Fig. 3.2D phase trajectories for the proposed Sprott-C across different projections:$(a)\ x-y, (b)\ x-z, (c)\ y-z$.

5.1. DISSIPATIVE WITH ICGO

The optimal values for the parameters of the hyperchaotic system will be selected to study its dynamic characteristics. The div. ($Trace\ (J\ )^{ICGO}$) of the system (2) is computed as:

$$Trace^{ICGO} = \sum_{i=1}^{4} \frac{\partial \dot{x}_i}{\partial x_i} = -1 \tag{16}$$

5.2. EQUILIBRIUM WITH ICGO

$$E_{1,2}^{ICGO} = (\pm 1, 1 - a_1 u, 0, 0) \tag{17}$$

The Jacobian array of the new system at the points $(E_{1,2})$ as follows:

$$J = \begin{bmatrix} 0 & z & y & 0 \\ 1 & -1 & 0 & -a_1 \\ -2x & 0 & 0 & 0 \\ 0 & 0 & a_2 & 0 \end{bmatrix} = \overrightarrow{J(E_{1,2})} \begin{bmatrix} 0 & 0 & 1 - a_1 u & 0 \\ 1 & -1 & 0 & -a_1 \\ \pm 2 & 0 & 0 & 0 \\ 0 & 0 & a_2 & 0 \end{bmatrix} \tag{18}$$

$$\lambda + \underbrace{(\lambda + 1)}_{E_1} + (\underbrace{\lambda^2}_{E_2} + \underbrace{2(1 \pm a x_4)\lambda}_{E_3} = 0 \tag{19}$$

The points are unstable when $(au > 1)$, or $(au < 1)$. Finally, upon reaching the critical value $(au = 1)$, these roots converge exactly to zero.

5.3. LYAPUNOV EXPONENTS

The dynamic behaviors are analyzed by the Lyapunov exponent (LE), with a positive (LE) value denoting chaos and a multiple positive LE value denoting hyperchaos. An improved ICGO algorithm, related to system complexity through the D_{KY}, was employed to determine the optimal parameters to maximize the complexity of Eq. (2).

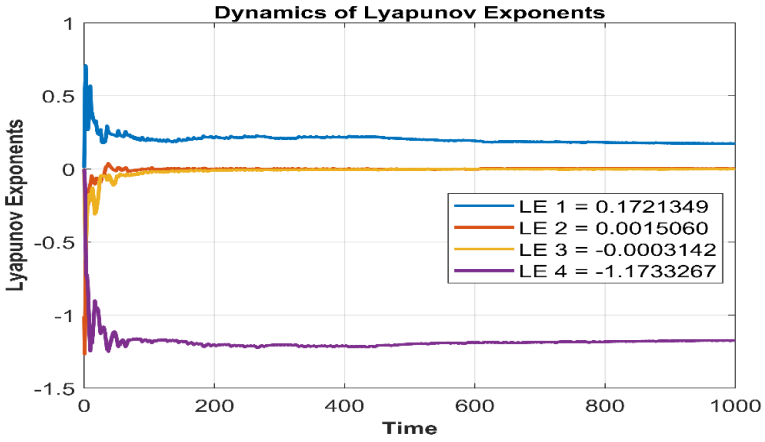


Fig. 4. LE_s of the system (2) for $(a_1, a_2) = (-0.051476090541331, 0.192175435433803)$

$$\begin{cases} LE_1 = 0.1721349 \\ LE_2 = 0.0015060 \\ LE_3 = \mathbf{-0.0003142} \\ LE_4 = -1.1733267 \end{cases}, \quad \sum_{i=1}^{4} LE_i = -1 \tag{20}$$

$$D_{KY}^{ICGO} = J + \frac{\sum_{I=1}^{J} LE_I}{LE_{i+1}} = 3.1733267 \tag{21}$$

6. CONCLUSION

This paper introduces a new 4D chaotic system with (7- terms), including two nonlinear ones. The system is constructed using state feedback control linear, and its chaotic dynamics are thoroughly examined through key physical characteristics. These include unstable equilibrium points associated with self-excited and dissipative attractors, linear stability analysis, (LE_s), the D_{KY}, All of these attractors and there are as many as you need – meet the requisite $(n-1)$ criterion typical of chaotic systems. In order to obtain a system that satisfies the $(n-2)$ condition, the ICGO algorithm is used to search for optimal parameter values and this is extended to a hyperchaotic regime. These physical properties play an important role in determining the behavior of the system and its interactions; hence, they are essential to model, analyses and predict the behavior of this type of systems. The chaotic properties are obvious in the algorithm, which is ICGO, for 2-positives (LE_s), there is strong sensitivity to the parameter choices. The results of the work will be useful for further advancement in cryptography and secure communications, and have applications in many branches of engineering.

ACKNOWLEDGMENTS

This research was done with an institutional support from the College of Computer Science and Mathematics, University of Mosul, Iraq.

REFERENCES

1. Wan Q, Yan Z, Li F, Chen S, Liu J. Complex dynamics in a Hopfield neural network under electromagnetic induction and electromagnetic radiation. Chaos. 2022;32(7):073107.
2. Shen H, Yu F, Kong X, Mokbel AAM, Wang C, Cai S. Dynamics study on the effect of memristive autapse distribution on Hopfield neural network. Chaos. 2022;32(8):083133.
3. Lin H, Wang C, Sun Y, Wang T. Generating n-scroll chaotic attractors from a memristor-based magnetized hopfield neural network. IEEE Trans Circuits Syst II Express Briefs. 2023;70(1):311-315.
4. Shen H, Yu F, Wang C, Sun J, Cai S. Firing mechanism based on single memristive neuron and double memristive coupled neurons. Nonlinear Dyn. 2022;110(4):3807-3822.
5. Ma M, Lu Y, Li Z, Sun Y, Wang C. Multistability and phase synchronization of Rulkov neurons coupled with a locally active discrete memristor. Fractal Fract. 2023;7(1):82.
6. Lin H, Wang C, Cui L, Sun Y, Zhang X, Yao W. Hyperchaotic memristive ring neural network and application in medical image encryption. Nonlinear Dyn. 2022;110(1):841-855.
7. Yu F, Kong X, Mokbel AAM, Yao W, Cai S. Complex dynamics, hardware implementation and image encryption application of multiscroll memeristive Hopfield neural network with a novel local active memeristor. IEEE Trans Circuits Syst II Express Briefs. 2022;70(1):326-330.
8. Li X, Zhou L, Tan F. An image encryption scheme based on finite-time cluster synchronization of two-layer complex dynamic networks. Soft Comput. 2022;26(2):511-525.
9. Korolj A, Wu HT, Radisic M. A healthy dose of chaos: Using fractal frameworks for engineering higher-fidelity biomedical systems. Biomaterials. 2019;219:119363.
10. Lin H, Wang C, Cui L, Sun Y, Xu C, Yu F. Brain-like initial-boosted hyperchaos and application in biomedical image encryption. IEEE Trans Ind Inform. 2022;18(12):8839-8850.
11. Yu F, Shen H, Yu Q, Kong X, Sharma PK, Cai S. Privacy protection of medical data based on multi-scroll memristive Hopfield neural network. IEEE Trans Netw Sci Eng. 2022;1-14.
12. Yu F, Kong X, Chen H, Yu Q, Cai S, Huang Y, et al. A 6D fractional-order memristive hopfield neural network and its application in image encryption. Front Phys. 2022;10:847385.
13. Azam A, Aqeel M, Sunny DA. Generation of multidirectional mirror symmetric multiscroll chaotic attractors (MSMCA) in double wing satellite chaotic system. Chaos Solitons Fractals. 2022; 155:111715.
14. Ai W, Sun K, Fu Y. Design of multiwing-multiscroll grid compound chaotic system and its circuit implementation. Int J Mod Phys C. 2018;29(8):1850049.
15. Yu F, Chen H, Kong X, Yu Q, Cai S, Huang Y, et al. Dynamic analysis and application in medical digital image watermarking of a new multi-scroll neural network with quartic nonlinear memristor. Eur Phys J Plus. 2022;137(4):434.
16. Abed, K. A. (2024). A better approximation to Sawada-Kotera via differential transform method with hybrid grey Wolf and Cuckoo algorithm. *Journal of Interdisciplinary Mathematics*, *27*(6), 1231-1241.
17. Abed, K. A., Al-Azzawi, S. F., & Saber Qasim, O. (2025). Electronic circuit and image encryption using a novel simple 4D hyperchaotic system. *Physica Scripta*, *100*(1), 015210.
18. Abed, K. A., Qasim, O. S., & Al-Azzawi, S. F. (2026). Optimizing parameters for 4D hyperchaotic system using Walrus Optimizer Algorithm. *Informatyka, Automatyka, Pomiary w Gospodarce i Ochronie*

Środowiska, *16*(2), 107-112.
19. Lorenz EN. Deterministic nonperiodic flow. J Atmos Sci. 1963;20(2):130-141.
20. Al-Hayali MA, Al-Azzawi FS. 4D hyperchaotic Sprott S system with multistability and hidden attractors. J Phys Conf Ser. 2021;1879(3):032031.
21. Zhang S, Zeng Y. A simple Jerk-like system without equilibrium: Asymmetric coexisting hidden attractors, bursting oscillation and double full Feigenbaum remerging trees. Chaos Solitons Fractals. 2019;120:25-40.
22. Sprott JC. Some simple chaotic flows. Phys Rev E. 1994;50(2):R647-R650.
23. Vaidyanathan S, Dolvis LG, Jacques K, Lien CH, Sambas A. A new five-dimensional four-wing hyperchaotic system with hidden attractor, its electronic circuit realisation and synchronisation via integral sliding mode control. Int J Model Ident Control. 2019;32(1):30-45.
24. Vaidyanathan S, Pham VT, Volos CK. A 5-D hyperchaotic Rikitake dynamo system with hidden attractors. Eur Phys J Spec Top. 2015;224(8):1575-1592.
25. Wang Z, Cang S, Ochola EO, Sun Y. A hyperchaotic system without equilibrium. Nonlinear Dyn. 2012;69(1):531-537.
26. Yang Q, Chen C. A 5D hyperchaotic system with three positive Lyapunov exponents coined. Int J Bifurcation Chaos. 2013;23(6):1350109.
27. Zhang S, Zeng Y, Li Z, Wang M, Xiong L. Generating one to four-wing hidden attractors in a novel 4D no-equilibrium chaotic system with extreme multistability. J Math Anal Appl. 2018;28(1):013113.
28. Deng Q, Wang C, Yang L. Four-wing hidden attractors with one stable equilibrium point. Int J Bifurcation Chaos. 2020;30(6):2050086.
29. Singh JP, Rajagopal K, Roy BK. A new 5D hyperchaotic system with stable equilibrium point, transient chaotic behaviour and its fractional-order form. Pramana. 2018;91(3):1-10.
30. Sambas A, Vaidyanathan S, Tlelo-Cuautle E, Abd-El-Atty B, Abd El-Latif AA, Guillen-Fernandez O, et al. A 3-D multi-stable system with a peanut-shaped equilibrium curve: Circuit design, FPGA realization, and an application to image encryption. IEEE Access. 2020;8:137116-137132.
31. Sambas A, Vaidyanathan S, Bonny T, Zhang S, Hidayat Y, Gundara G, et al. Mathematical model and FPGA realization of a multi-stable chaotic dynamical system with a closed butterfly-like curve of equilibrium points. Appl Sci. 2021;11(2):788.
32. Sambas A, Vaidyanathan S, Tlelo-Cuautle E, Zhang S, Guillen-Fernandez O, Hidayat Y, et al. A novel chaotic system with two circles of equilibrium points: multistability, electronic circuit and FPGA realization. Electronics. 2019;8(11):1211.
33. Singh JP, Roy BK. Coexistence of asymmetric hidden chaotic attractors in a new simple 4-D chaotic system with curve of equilibria. Optik. 2017;145:209-217.
34. Sprott JC. A proposed standard for the publication of new chaotic systems. Chaos Solitons Fractals. 2011;21(9):2391-2394.
35. Peng Z, Yu W, Wang J, Zhou Z, Chen J, Zhong G. Secure communication based on microcontroller unit with a novel five-dimensional hyperchaotic system. Arab J Sci Eng. 2022;47(1):813-828.
36. Yan S, Li L, Gu B, Cui Y, Wang J, Song J. Design of hyperchaotic system based on multi-scroll and its encryption algorithm in color image. Integration. 2023;88:203-221.
37. Al-Hayali MA, Al-Azzawi FS. A 4D hyperchaotic Sprott S system with multistability and hidden attractors. J Phys Conf Ser. 2021;1879(3):032031.
38. Talatahari S, Azizi M. Chaos Game Optimization: a novel metaheuristic algorithm. Artif Intell Rev. 2021;54(2):917-1004.

39. Liu Y, Zheng R, Yu B, Liao B, Song F, Tang C. An improved chaotic game optimization algorithm and its application in air quality prediction. Axioms. 2025;14(4):235.
40. Mehrabi Hashjin N, Amiri MH, Mohammadzadeh A, Mirjalili S, Khodadadi N. Novel hybrid classifier based on fuzzy type-III decision maker and ensemble deep learning model and improved chaos game optimization. Cluster Comput. 2024;27(7):10197-10234.
41. Oueslati R, Manita G, Chhabra A, Korbaa O. Chaos game optimization: A comprehensive study of its variants, applications, and future directions. Comput Sci Rev. 2024;53:100647.

Detection of the fungi *Aspergillus* sp and *Candida* sp. that cause pneumonia and determining the Dectine2 response against them

Israa. A .Mahmood
University, Tikrit ,Iraq.
College of Medicine
Israa .a. mahmood @ tu.edu.iq

Detection of the fungi *Aspergillus* sp and *Candida* sp. that cause pneumonia and determining the Dectine2 response against them

Israa. A .Mahmood
University, Tikrit ,Iraq.
College of Medicine
Israa .a. mahmood @ tu.edu.iq

Abstract:

155 clinical samples (sputum, blood) were collected from patients suffering from various respiratory diseases (asthma, tuberculosis, chest allergies, and chest infections) from the consultation clinic for chest and respiratory diseases in Tikrit. The total number of infected samples was 70, and the number of uninfected samples was 85. The age groups comprised males and females aged between 10 and 65 years. The presence of fungal species belonging to the genus *Aspergillus* was found in 48 samples (68.57%), including *A. niger*, *A. fumigatus*, *A. hiratsukae*, and *A. flavus*. The presence of yeasts belonging to the genus *Candida* was also detected in 22 samples, representing 63.64%, and including *C. albicans*, *C. dublinensis,* and *C. parapsilosis*. Immunological tests were performed on the blood serum of the same people infected with the pathogenic fungi. The immune response was diagnosed with antibodies (Dectine2) Due to systemic fungal infection , and a significant increase was observed at the probability level (0.05, 0.01, and 0.001) when comparing the serum of healthy people (20 samples of male and female).

We noticed that it was high in the serum of people infected with the fungus, with the exception of the elderly, those with chronic diseases, and those with cancer, as its percentage in their serum was low.

Keywords: *Aspergillus, Candida*, Dectine2

Introduction:

Fungal pneumonia is considered one of the most common and deadly diseases among invasive fungi, as it affects a large number of patients who suffer from immunodeficiency and various other accompanying diseases. Yeasts and molds are the main causes of fungal pneumonia (Kontoyiamis, 2023). The genus *Candida* is the most common cause of fungal infections worldwide, as (Bongomin *et.al*. 2017) pointed many species coexist harmlessly in the host's body, including humans. However, when the barriers are broken, mucous membrane or weakened immune system, can invade and cause disease, known as opportunistic infection. Candida is present on most mucosal surfaces and mainly in the gastrointestinal tract, as well as infecting the skin (Gupta *et.al* 2012). *Candida albicans* is the most commonly isolated species and can cause infection (candidiasis or thrush) in humans (Calderone *et.al*

2012). It is accompanied by some chronic lung diseases that are a trigger for infection, such as pulmonary tuberculosis, asthma, lung abscesses, as well as chronic or acute bronchitis (Al-Janahi, 2012; Al-Waisi, 2021).

Fungal infections of the lung are usually contagious and cause deaths, especially in patients who suffer from a defect in the immune system, which weakens the host's immune response to the disease (Bellocchio *et.al*., 2004; Jose *et.al*., 2012), as increasing data indicate. It has been recorded that many cells and molecules are responsible for regulating the host's response to fungal infection in the lung. When the infection begins, the host's defenses are stimulated, represented by B cells, macrophages, dendritic cells (Dc), and neutrophils, as the first line of defense, represented by phagocytosis and secretion. Cytokines, and natural killer cells have a role in controlling the spread of fungi in the lung through direct and indirect killing of fungal cells as well as the role of adaptive T cells (Saag *et.al*., 2000; Manavath *et.al*., 2004).

The increasing rate of resistance of fungi to antifungals and the toxic side effects of these antibiotics, which still pose potential risks to the patient, have helped in the spread of invasive fungi (Fisher *et.al.,* 2018), so immune receptors have an effective role in controlling fungi, as they work Dectine1 and Dectine2 receptors stimulate the immune response towards fungi, especially towards Aspergillus and Candida (Griffiths *et.al*., 2018)

Materials and Methods

Samples collection: 155 sputum and blood samples were collected from patients attending the consultation clinic for chest and respiratory diseases in Tikrit city, Salah al-Din Governorate, who suffer from a cough accompanied by sputum that persists for a long time and does not respond to treatment. Sputum samples were collected first by sterilizing the mouth and gargling with a saline solution early in the morning. A sample was taken from each patient and placed in vials. Blood samples were also drawn from each patient. The samples were collected during the period from August 2022 until December 2022.

Samples Culture : The samples were grown on Potato Dextrose Agar (PDA) medium, and the presence of fungi was initially detected by microscopic examination using 10% potassium hydroxide (KOH) by sterilized wooden swabs by passing them over the surface of Petri dishes containing the solid culture medium (PDA). The plates were incubated at 37 °C for 24 hours (Atlas, 1995). The study included the following:

Detecting the immune response to Dectine2: The Dectine2 immune response was detected through its presence in the blood serum of infected patients, using the ELISA device as in the steps below:

Standard has been added to the Wells, and the quantity of Standard must be equal to the quantity of Serum, and usually the number is 6. The enzyme was added on top of the Standard and Serum and mixed well. Then, washing solution (preservative and trace agent) was added. And finally base material was added

The purpose of using the washing solution is to get rid of unbound antibodies and other unbound foreign antigens, leaving only the required Antigen bound to the antibody present in the wall, and in this case Antigen-antibody is formed. As for the purpose of using Substrate, every enzyme needs A base material binds to it, meaning the base material binds to the enzyme, and the color of the samples changes from colorless to blue, while the wall (Well) is Its concentration is zero, meaning it does not give color. As for the purpose of Stop solution, the Stop solution (contains hydrochloric acid) is added at the end of the first minute to stop the reaction, and the color of the samples turns from blue to yellow according to the wavelength of the device, and it enters the reading stage of 450-630, the existing pits. They are antibodies, while Antigen is present in the serum in which the hormones or other components in it are to be measured.

Biostatic analysis: The Statistical Analysis System (SAS) program (2018) was used to detect the effect of the different groups (patient group and control group) on the study criteria. The T-test and LSD - least significant difference - were used to compare the means. The Chi-square was used to compare the percentages. (Probability 0.05 and 0.01) In this study, the ANOVA Tow Way program was also used.

Results and Discussion

155 sputum samples were collected from patients suffering from various respiratory infections (pulmonary tuberculosis, asthma, chest allergies, pneumonia), and the results of direct microscopic examination showed the presence of 64 positive samples, representing 41.29% of the total samples, while 91 of samples were negative (58.71%). Regarding the results of culturing the samples in SDA medium, 70 infected samples were recorded as positive (45.16%) and 85 samples were negative (54.84%) in which no growth was observed, as shown in Table (1). These results agreed with the results of Al-Ghalbi (2006), Al-Janahi (2012), Hamid (2021) and Al-Samarrai (2021), who indicated that the results of the culture examination was higher than the results of direct examination. The results disagreed with results of Muhammad(2015), as the result of direct microscopic examination was 70%, while the result of laboratory culture was 65%.

Table (1): Number and percentages of laboratory examination of samples.

Type of examination	positive samples	Percentage	negative samples	Percentage	Total
Direct microscopic examination	64	41.29	91	58.71	100%
Agricultural inspection	70	45.16	85	54.85	100%
		NS Chi-Square= 2.575 P- Value 0.109			

NS* No significant differences

Through the results of the statistical analysis, no significant differences were observed, *P value* = 0.109. The reason for the appearance of negative samples may be attributed to the fact that the cause of the disease is not fungal in patients who suffer from diseases of the respiratory system. It may be due to bacterial, viral, or Genetic factors, and the reason for the difference in the results of direct microscopic examination may be due to the type of microscope used in the examination, or the reason may be due to the type of dyes used in the examination and the method used to collect the sample because direct microscopic examination cannot be relied upon in the test to detect the presence or absence of fungi (Niazi, 2000; Al-Waisi, 2021). This is what was confirmed by Collee and his group (1996). There are negative results in laboratory tests for many reasons, including diagnosis. Clinical analysis is inaccurate as it does not give accurate results, as the infection may not be fungal, or it may be due to patients infected with fungi taking anti-fungal drugs without consulting a specialist doctor.

Table (2) shows the numbers and percentages of fungi isolated during the study after conducting all the above-mentioned tests, where several species belonging to the genus *Aspergillus* were diagnosed at a rate of 68.57%, with a number of isolates amounting to 48 isolates distributed among four types, the most frequent of which was type *A. fumigatus*, where the number of isolates was 21(43.75%) followed by *Aspergillus niger*, where the number of isolates was 13 (27.08%) while the number of isolates *A. flavus* and *A .hiratsukae* were 7 for each type, at a rate of 14.58%. The results agreed with the study of Hamid (2021), which was recorded 43.18% of *Aspergillus fumigatus* and 25% of *A. niger*. The results disagreed with the study of Zohri and his group (2017), which found that the highest infection rate was recorded for *A. niger*, with 30 isolates, and15 isolates of fungus *A. fumigatus*, meaning that the number of *A. niger* isolates was higher than the number of *A. fumigatus* isolates.

Table (2): Numbers and types of molds isolated

	Mold type	N	Percentage
1	*A . fumigatus*	21	43.75
2	*A .niger*	13	27.08
3	*A . flavus*	7	14.58
4	*A . hiratsukae*	7	14.58
Total		48	100

Table (3) shows the numbers and percentages of yeasts isolated during the study after conducting all the above-mentioned tests, as the number of *Candida* isolates was 22 isolates, distributed into three species; 14 isolates (63.64%) of *C. albicans*, 4 isolates (18.18%) of each *C. parapsilosis*, and *C.*

dublineinsis. The results were consistent with the study of Al-Khafaji (2021) and Al-Samarrai (2021). They found that the percentage of *C. albicans* was higher than other yeast isolates.

Table (3): Numbers and types of yeasts isolate

	Yeast type	N	Percentage
1	*C. albicans*	14	63.64
2	*C .dublineinsis*	4	18.18
3	*C . parapsilosis*	4	18.18
Total		22	100

Immunity test

Immunological tests were performed on serum samples of patients infected with fungi in the respiratory system, which were detected through laboratory culture examination.

Table (4) shows the level of the immune receptor Dectine2 compared to the healthy group, as we notice its increase in patients infected with fungi compared to healthy people not infected with systemic fungi, as the level of Dectine2 in people infected with respiratory fungi was 1180.01±79.39, while its level in healthy people not infected With fungi 17.79±8.01 The table shows that there are significant differences at a significance level of P≤0.01, that Dectine2 has an important immune role against systemic fungi, as it acts as an antifungal against them. (Saijo *et.al*.,2011) indicated that Dectine2 is the functional receptor for the existing α-mannans In the walls of fungal cells, Dectine2 is characterized by its ability to bind to many fungi, whether they are in the form of molds or yeasts (McGreal *et al.,* 2006).

Table (4) Dectine2 level in groups of patients and healthy controls

Groups	C .Type Lectine (Dectine2) Pg/ml
Patients	1180.01±79.39
Healthy people (Control)	17.79±8.01
T .test	340.44**
P .Value	0.0001
	P≤0.01

We note from Table 5 that the level of the immune receptor Dectine2 in males is higher than its level in females, as its level in males was 1460.10±103.65, while its level in females was 907.92±101.51 at a significance level of P≤0.01, as male immunity is often higher than females, and this may be due to the fact that the physical structure of males is stronger than the physical structure of females, meaning that the infection of females was higher than the infection of males, and this is consistent with the study (Al-Hamdani and his group, 2010) and the study (Al-Saadi, 2012).

We note from Table 5 that the level of the immune receptor Dectine2 in males is higher than its level in females, as its level in males was 1460.10±103.65, while its level in females was 907.92±101.51 at a significance level of P≤0.01, as male immunity is often higher than females, and this may be due to the fact that the physical structure of males is stronger than the physical structure of females, meaning that the infection of females was higher than the infection of males, and this is consistent with the study (Al-Hamdani and his group, 2010) and the study (Al-Saadi, 2012).

Table (5): Measurement of the immune variable Dectine2 according to gender, males and females

Groups	Gender-specific (male and female) (Dectine2 pg/ml)
Male	1460.10±103.65
Female	907.92±101.51
T .test	225.01**
P value	0.0001
	Significant No NS P ≤ 0.01

Table (6) shows us that there are significant differences between the rates of increase in the level of Dectine2 among the age group groups, as it was shown that the level of cytokine was at its highest levels in the age groups younger than 40 years, as its highest level in this age group was 1494.87±93.16 a, and also in the groups and age groups from 40-50 years, as its level was 1180.91±90.21 a, while we note that its lowest levels are in the age groups older than 50 years, as its level was 669.65±150.52 b, and this percentage was consistent with the study (Al-Wisi 2021). They may have been infected due to mixing with sick people infected with respiratory fungi, which facilitates the transmission of infection to them. Also, the high infection rates in people within the age group may be due to a weakness in their immune system because they are elderly and also due to their infection with chronic diseases such as diabetes, which leads to a weakness in the immune system due to their taking steroid medications. The lowest infection rate was recorded in the age groups (19-29 years) at 8.58%, and this rate was consistent with what was stated in the study (Hamid, 2021). This may be due to the fact that they are young and are the most active, and also due to the strength of their immune systems (Jassim *et.al* 2010; Abood; 2014).

Table (6): Dectine2 level according to age groups in infected people

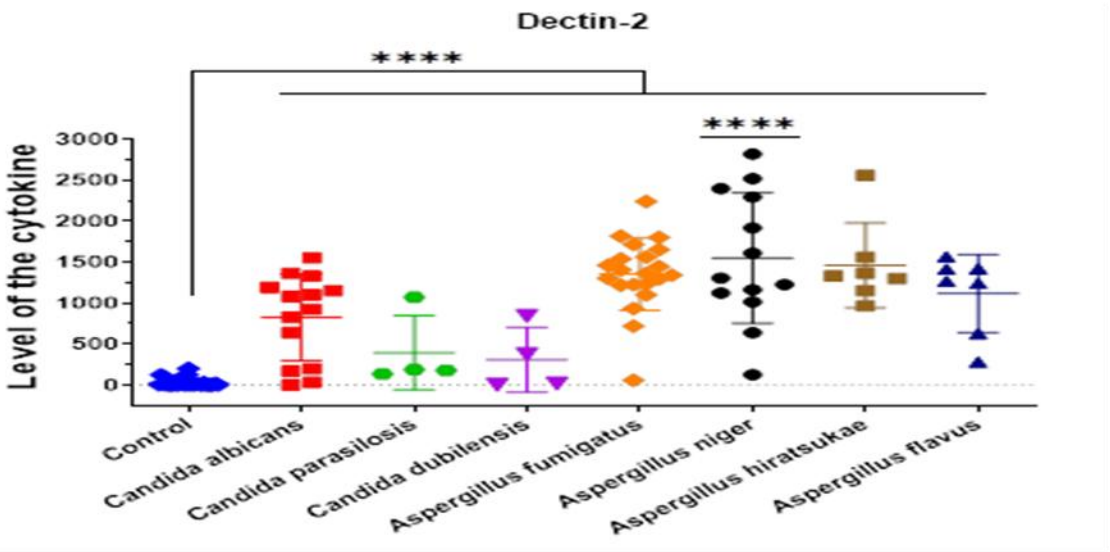
Groups	C Type Lectin (Dectine2) pg/ml
<40 yr	1494.87±93.16 a
40 -50 yr	1180.91±90.21 a
>50 yr	669.65±150.52 b
T .test	333.17 **
P. Value	0.0001
	*P ≤ 0.05 ** P ≤ 0.01

Measurement of the proportion of the immune variable dectine2 according to the type of fungal infection

Figure (1) shows the concentration levels of the cytokine Dectine2 when infected with fungi isolated from the respiratory system, where its highest concentration level was when infected with *A. niger*, then with *A. hiratsukae*, then with *A. fumigatus*, and its lowest level was when infected with *A. flavus*. It was found that there were significant differences at a significance level of 0.0001, as the Dectine2 immune receptor recognizes mannan to activate the final immune responses, as the Dectine2 immune receptor is primarily associated with fungal hyphae and is coupled to the Fc(FcR gamma gamma receptor chain to stimulate the production of inflammatory cytokines (Graham *et al.,* 2012).

In the case of Candida infection, its highest level was in the case of infection with *C. albicans*, then infection with *C. parapsilosis*, and then its lowest level in the case of infection with *C. dublineinsis*, and this confirms that the immune receptor Dectine2 has an important role in defending the body against *Candida albicans* by stimulating Th17 differentiation (Sajio, and Yoichiro 2011) (and there were also significant differences at a significance level of 0.0001, where a one-way analysis of variance test (Bartlett's test) was conducted, where the value of Bartlett's statistic (corrected) reached 133.8 and the value of $P < 0.0001$

Figure (1) Dectine2 values changing according to infection with different fungi



Conclusion:

As a conclusion of this study, *Aspergillus* and *Candida* sp. were the most common types of fungi that cause pneumonia. But the Aspergillus fungus species were higher than the Candida species , The values of the immune Dectine2, are higher than their normal levels in people infected with respiratory fungi. It has been found that there are differences in the values according to the different fungal species, Its level was high in the case of infection with the species *Candida albicans*, *Candida dublineinsis, Aspergillus fumigatus*, *Aspergillus flavus*, and *Aspergillus hiratsukae*, and its level was low in the case of infection with the species *Candida parapsilosis* and *Aspergillus niger*, as well as according to the ages and genders of the infected patients. We concluded that the level of the was high in the blood serum of patients infected with fungi compared to healthy people. The level was similar almost in males and females, and its highest level was in the age group between 40-50 years.

References:

1- Abood ,M.S.(2014). Immunological and Molecular study of Candida spp. Causing Vulvovaginal Candidiasis and the Role of Lactic acid Bacteria as Probiotic Invivo and Invitro. Ph. D .Thesis ,college of Science. Baghdad University. Iraq.
2- Al-Ghalibi, Haider Habib Hoteit (2006). Study of the effect of some plant extracts and antifungals on some skin fungal infections of pathological samples in the city of Kirkuk. Master's thesis, Tikrit University. Iraq.
3- Al-Janahi, Farqad Abdul-Ilah (2012). The effect of Cordia myxa extracts on the growth of fungi isolated from patients with pulmonary infections in the city of Diwaniyah, Master's thesis, College of Education - Al-Qadisiyah University.

4- Al-Khafaji, Dhofar Subeih Baqir. (2021). Detection of the susceptibility of Candida species isolated from cases Different clinical studies in biofilm formation. Master Thesis. The amount of education for the pure general population. Biology Tikrit University. Iraq
5- Al-Samarrai, Muhammad Amer Saad Al-Din (2021). Isolating and identifying yeasts associated with urinary tract infections in the city of Samarra and investigating the active content and biological activity of the Agaricus gennadi mushroom extract against them, Master's thesis - College of Education for Pure Sciences - Tikrit University.
6- Al-Waisi, Hadeel Abdullah Saleh (2021). Histological comparison of the lung and liver of the white mouse experimentally infected with the fungus Aspergillus fumigatus after using the antifungal amphotericin B and the alcoholic extract of the fungus Trametes sp.
7- Atlas, R. M., Williams, J. F., & Huntington, M. K. (1995). Legionella contamination of dental-unit waters. Applied and environmental microbiology, 61(4), 1208-1213.
8- Bellocchio S, Moretti S Perruccio K, Fallarino F, Bozza S, Montagnoli C, et al ., TLRs govern neutrophil activity in aspergillosis . J Immunol. (2004) 173:7406-15 .doi: 10.4049/ jimmunol .173.12.7406
9- Bongomin F, Gago S, Oladele R, Denning D. Global and Multi-National Prevalence of Fungal Diseases-Estimate Preci sion. J Fungi (Basel) 2017; 3: 57.
10- Calderone RA, Clancy CJ, editors. Candida and Candidiasis. Washington: American Society of Microbiology Press. 2012.
11- Collee, J.; Frase, A.; Marmion, B.& Simon, A. (1996). Makie and McGartney practical medical microbiology. 14th. Ed. Churchill Livingstone. New York. 978
12- Fisher MC, Hawkins NJ, Sanglard D, Gurr SJ. Worldwide emergence of resistance to antifungal drugs challenges human health and food security Science .(2018) 360:739-42.10.1126/science aap7999 . Google Scholar
13- Gupta P, Gautam P, Rai N, Kumar N. An emerging hope to combat *Candida albicans*: plantbased therapeutics. Biotechnol Int2012; 5: 85-114
14- Graham LM, Gupta V, Schafer G, Reid DM, Kimberg M, Dennehy KM, et al. The C-type lectin receptor CLECSF8 (CLEC4D) is expressed by myeloid cells and triggers cellular activation through Syk kinase. J Biol Chem 2012;287: 25964-25974. Google Scholar
15- Griffiths JS, Thompson A, Stott M, et al.. Differential susceptibility of Dectine-1 isoforms to functional inactivation by neutrophil and fungal protease . FASEB J 2018; 32:3385-97.
16- Hamid, Kanan Adnan Abdullah. (2021). Phenotypic and molecular diagnosis of some species of the genus Aspergillus spp isolated from chronic lung infections in Saladin Governorate - Iraq, Master's thesis, College of Education for Pure Sciences - Tikrit University.
17- Jassim, A.N. ; Majeed ,H.A and Habib, K.A. (2010). Effect of Some predisposing factors on Vulvovaginal Candidiasis. Baghdad journal for sciences , 7(3) :1087-1090.
18- Jose RJ, Brown JS, Opportunistic and fungal infections of the lung . Medicine .(2012) 40:335-9.:10.1016/j.mpmed.2012.03.013
19- Manavathu EK, Ramesh MS, Baskaran I, Ganesan LT, Chandraskar PH . A comparative study of the post-antifungal effect (PAFE) of amphotericin B, triazoles and echinocandins on Aspergillus

fumigatus and Candida albicans J Infect antimicrobe Chemother . (2004) 53:386-9.10. 1093/jac/dkh066 Google Scholar

20- McGreal E.P , Rosas M,. Brown GD , Zamze S,. Wong S.Y.C, Gordon S, Martinez-Pomares L, Taylor P.R.(2006). The carbohydrate-recognition domain of Dectin-2 is a C-type lectin with specificity for high mannose Glycobiology, Volume 16, Issue 5, May 2006, Pages 422–430, https://doi.org/10.1093/glycob/cwj077 Published: 19 January 2006.

21- Muhammad, Nour Jassim (2015). Molecular characterization of some causes of skin infections in Diwaniyah Governorate and the effect of silver particles on their growth. Master's thesis, College of Science, Al-Qadisiyah University)

22- Niazi, B. H., Rozema, J., Broekman, R.A., & Salim, M. (2000). Dynamics of growth and water relations of fodder beet and sea beet in response to salinity . Journal of Agronomy and Crop Science, 184(2), 101-110.

23- Saijo S, Ikeda S, Yamabe, et al. Dectin-2 recognition of alpha-mannans and induction of Th17 cell differentiation is essential for host defense against Candida albicans, Immunity, 2010, , vol., 32, pg 681.

24- Saijo S, Yoichiro , I . Dectin-1 and Dectin-2 in innate immunity against fungi International Immunology, Volume 23, Issue 8, August 2011, Pages 467–472, https://doi.org/10.1093/intimm/dxr046. Published: 15 June 2011 Article history.

25- SAS. 2018. Statistical Analysis System, User's Guide. Statistical. Version 9.6th ed. SAS. Inst. Inc. Cary. N.C. USA.

26- Saag MS, Graybill RJ, Larsen RA, Pappas PG, Perfect JR, Powderly WG, et al.. Practice guidelines for the management of cryptococcal disease . Infectious Disease Society of America. Clin Infect Dis.(2000) 30:710-8. 10.1086/313757 Google Scholar .

27- Zohri AN, About-Nasr MB ,Adam m, mustafa Am ,Amer Em (2017).Impact of Enzymes and Toxin potentiqlity of four Aspergillus species to cause .Aspergillosis ,Biol ,med,(Aligarh)9:409

تقييم مستوى الثقة التنظيمية لقسم التربية البدنية وعلوم الرياضة من جهة نظر أعضاء الهيئة التدريسية

م.م زيد زهير عزالدين داؤد الطائي، م.م حسام علي غانم عبد الكريم
Zaid Zuhair Ezzulddin Al-Tai، Hussam Ali Ghanim Abdul Kareem

Email:zaid.zuhair@uomosul.edu.iq

Assessing the Level of Organizational Trust for the Department of Physical Education and Sports Sciences from the Perspective of Faculty Members

Zaid Zuhair Ezzulddin Al-Tai، Hussam Ali Ghanim Abdul Kareem

Email:zaid.zuhair@uomosul.edu.iq

Abstract

The significance of this research lies in the fact that organizational trust is a key managerial concept that has become a subject of scholarly inquiry; it reflects the prevailing culture and organizational climate within the sports institution, in addition to the positive impacts of implementing this concept in a practical setting.

Based on the foregoing, the research problem is articulated through the following question:

- What is the state of organizational culture within the Department of Physical Education and Sports Sciences at the University of Mosul?

The current research aims to achieve the following:

Adapting the organizational trust scale for faculty members in the Department of Physical Education and Sports Sciences at the College of Basic Education, University of Mosul.
- Determining the level of organizational trust among faculty members in the Department of Physical Education and Sports Sciences at the College of Basic Education.

The researcher employed the descriptive method, as it was suited to the nature of the current study.
The research population and sample consisted of (30) faculty members from the Department of Physical Education and Sports Sciences for the 2025–2026 academic year, holding various academic degrees and ranks.
The researcher concluded the following:
- The organizational trust scale was adapted for faculty members in the Department of Physical Education and Sports Sciences at the College of Basic Education, University of Mosul.
- The validity dimension achieved the highest score, followed by the other dimensions of the questionnaire.

Keywords: Assessment, organizational trust, faculty members.

تقييم مستوى الثقة التنظيمية لقسم التربية البدنية وعلوم الرياضة من جهة نظر أعضاء الهيئة التدريسية

م.م زيد زهير عزالدين داؤد الطائي، م.م حسام علي غانم عبد الكريم
Zaid Zuhair Ezzulddin Al-Tai، Hussam Ali Ghanim Abdul Kareem

Email:zaid.zuhair@uomosul.edu.iq

المستخلص:

تكمن أهمية البحث في أن الثقة التنظيمية تعد من المفاهيم الإدارية المهمة التي بدأ الباحث بالكتابة عنها والبحث فيها، فهي تعكس واقع الثقافة السائدة والمناخ التنظيمي داخل أروقة المؤسسة الرياضية، فضلاً عن التأثيرات الإيجابية لتطبيق هذا المفهوم على الواقع الميداني.

ومن خلال ما سبق وتبرز مشكلة البحث في تقديم التساؤل الآتي:

- ما واقع الثقافة التنظيمية في قسم التربية البدنية وعلوم الرياضة في جامعة الموصل؟

يهدف البحث الحالي إلى ما يأتي:

- تكييف مقياس الثقة التنظيمية لأعضاء الهيئة التدريسية في قسم التربية البدنية وعلوم الرياضة في كلية التربية الأساسية/ جامعة الموصل.
- التعرف على مستوى الثقة التنظيمية لدى أعضاء الهيئة التدريسية في قسم التربية البدنية وعلوم الرياضة في كلية التربية الأساسية.

واستخدم الباحث المنهج الوصفي لملاءمته طبيعة البحث الحالي.

واشتمل مجتمع البحث وعينته على (30) عضواً من الهيئة التدريسية في قسم التربية البدنية وعلوم الرياضة للعام الدراسي (2025-2026)، علماً أنهم يحملون شهادات وألقاب علمية مختلفة.

واستنتج الباحث

- تم تكييف مقياس الثقة التنظيمية لأعضاء الهيئة التدريسية في قسم التربية البدنية وعلوم الرياضة في كلية التربية الأساسية/ جامعة الموصل.
- حصول بعد الصدق على اعلى نسبة يليه بقية الابعاد الخاصة بالاستبانة.

الكلمات المفتاحية: تقييم، الثقة التنظيمية، أعضاء الهيئة التدريسية

1- التعريف بالبحث

1-1 المقدمة وأهمية البحث

تعد الثقة التنظيمية من المفاهيم المحورية في حقل الإدارة الرياضية، لما لها من دور أساسي في بناء بيئة عمل فعالة داخل المؤسسات الرياضية، ومع تزايد التحديات الإدارية والفنية التي تواجه المنظمات الرياضية المعاصرة، برزت الحاجة إلى ترسيخ علاقات قائمة على الثقة بين مختلف المستويات التنظيمية، في السياق الأكاديمي الرياضي، ينظر إليها على أنها حالة من الاطمئنان النفسي والتوقعات الإيجابية التي يحملها الأفراد تجاه سلوك القيادات وزملاء العمل داخل المؤسسة الرياضية، بحيث يفترض أن هذه الأطراف ستتصرف بنزاهة وكفاءة وعدالة، وتعد هذه الثقة عاملاً حاسماً في تعزيز التواصل الفعال، ودعم العمل الجماعي، وتقليل مستويات الصراع التنظيمي، كما تحظى الثقة التنظيمية باهتمام واسع في دراسات علم النفس الرياضي، حيث ترتبط بشكل مباشر بدافعية اللاعبين، والرضا الوظيفي، والانتماء للفريق، أن ارتفاع الثقة داخل الفريق الرياضي يسهم في التماسك الجماعي، ويعزز من قدرة الأفراد على التكيف مع الضغوط التنافسية.

يعد المجال الرياضي مرآة يعكس مدى الرقي والثقافة التي تسود مجتمع معين، فلا بد من أن تكون علاقات القيادي مع الأخرين علاقة تتمثل بالحيوية والتفاعل لضمان نجاح المنظمة في تحقيق أهدافها، والقائد الذي ينجح في إقامة علاقات إنسانية سليمة تمكن الإدارة من وضع سياسات أفضل تساعد في استقطاب طاقات بشرية متميزة تخدم تطلعات وأهداف المؤسسات الرياضية.

إذ يؤكد (الشتوي، 2016) أن التزام القادة بالمبادئ الأخلاقية السامية تعمل على تقديم الدعم للمرؤوسين للالتزام بالسلوكيات الأخلاقية، إذ لا يكون ذلك عفوياً أو تلقائياً، بل يكون مخططاً ومدروساً، مما يساعد في بناء الثقة التنظيمية الجيدة، التي تهدف لبناء أخلاقي للمؤسسة لذا يقوم على تبادل الثقة بين الأطراف ذات العلاقة كلها (الشتوي، 2016، 38).

تُعد الثقة التنظيمية بين الأطراف المعنية (الأفراد، والمنظمة) عاملاً أساسياً داخل المنظمات، وعاملاً مهماً في تحقيق التكامل للمنظمة، ومفتاحاً رئيساً متوقع للسلوك، في أي شكل للتفاعل الإنساني، إذ يحتاج العمل مع الأخرين إلى الاعتماد المتبادل بينهم وبطرائق مختلفة لإنجاز أهدافهم الشخصية والتنظيمية، لذا تُعد الثقة أساسية وجوهرية لفهم السلوك الجماعي والفردي بين الأفراد والفعاليات الإدارية والتبادل الاقتصادي والاستقرار الاجتماعي أو السياسي. كما أنها تمثل عنصراً محورياً وعاملاً مهماً في تحقيق التكامل في المنظمات، وكذلك من الأدوات الإدارية الأكثر فاعلية، لأنها تهيئ الظروف اللازمة لنجاح المنظمات، بخلق مناخ تنظيمي جيد يقوم على أساس الثقة المتبادلة بين القول والفعل (الساقي، 2015، 47). فضلاً عن أنها إحدى الدعائم الأساسية في علاقات العمل التي تساعد المنظمات على تدعيم فاعليتها وتحقيق أهدافها.

(Kalleberg and Schmitt, 2004, 105)

ومن خلال ما سبق يرى الباحث أن أهمية هذا البحث تكمن في أن الثقة التنظيمية تعد من المفاهيم الإدارية المهمة التي بدأ الباحث بالكتابة عنها والبحث فيها، فهي تعكس واقع الثقافة السائدة والمناخ التنظيمي داخل أروقة المؤسسة الرياضية، فضلاً عن التأثيرات الإيجابية لتطبيق هذا المفهوم على الواقع الميداني.

2-1 مشكلة البحث

تعد الثقافة التنظيمية من العوامل الجوهرية التي تؤثر في أداء المؤسسات التعليمية، إذ تشكل منظومة القيم والمعتقدات والسلوكيات التي تحكم عمل الأفراد داخل المنظمة، وفي ضوء ذلك يواجه قسم التربية البدنية وعلوم الرياضة في جامعة الموصل تحديات متعددة تتعلق بمدى وضوح هذه الثقافة وانسجامها مع أهداف القسم، فقد تظهر تباينات في فهم العاملين للرسالة والرؤية، مما ينعكس سلباً على مستوى التنسيق والتعاون بينهم، كما أن ضعف تبني القيم التنظيمية المشتركة قد يؤدي إلى انخفاض مستوى الالتزام الوظيفي والانتماء المؤسسي، وتبرز المشكلة بشكل أوضح في ظل التغيرات المتسارعة في البيئة التعليمية والرياضية التي تتطلب مرونة تنظيمية عالية، إضافة إلى ذلك، قد تسهم أنماط القيادة السائدة في تعزيز أو إضعاف الثقافة التنظيمية داخل القسم، ومن هنا تبرز الحاجة إلى دراسة واقع الثقافة التنظيمية وتحليل مكوناتها وأبعادها المختلفة، كما تتطلب هذه المشكلة الكشف عن مدى تأثير الثقافة التنظيمية في تحسين الأداء الأكاديمي والإداري، وتسعى الدراسة أيضاً إلى تحديد المعوقات التي تحد من تطوير ثقافة تنظيمية إيجابية داخل القسم.

ومن خلال ما سبق وتبرز مشكلة البحث في تقديم التساؤل الآتي:

- ما واقع الثقة التنظيمية لدى أعضاء الهيئة التدريسية في قسم التربية البدنية وعلوم الرياضة في كلية التربية الأساسية/ جامعة الموصل؟

1-3 أهداف البحث

يهدف البحث الحالي إلى ما يأتي:

1-3-1 تكييف مقياس الثقة التنظيمية لأعضاء الهيئة التدريسية في قسم التربية البدنية وعلوم الرياضة في كلية التربية الأساسية/ جامعة الموصل.

2-3-1 التعرف على مستوى الثقة التنظيمية لدى أعضاء الهيئة التدريسية في قسم التربية البدنية وعلوم الرياضة في كلية التربية الأساسية/ جامعة الموصل

1-4 مجالات البحث

1-4-1 المجال البشري: اشتمل هذا المجال على أعضاء الهيئة التدريسية في قسم التربية البدنية وعلوم الرياضة.

2-4-1 المجال الزماني: الفترة الزمنية الممتدة من 2026/8/1 لغاية 2026/10/1.

3-4-1 المجال المكاني: قسم التربية البدنية وعلوم الرياضة في كلية التربية الاساسية/ جامعة الموصل.

1-5 تحديد المصطلحات

1-5-1 الثقة التنظيمية

تعرف (الطائي، 2007) الثقة التنظيمية بأنها إيمان الفرد بالأهداف والقرارات والسياسات التنظيمية والقائد التنظيمي بالأفراد العاملين معه جميعهم في المنظمة، بما يعكس رضا والتزام الفرد تجاه منظمته (الطائي، 2007، 61).

يعرف الباحث الثقة التنظيمية نظرياً بأنها توقع إيجابي لدى الأفراد بأن الآخرين داخل المنظمة الرياضية سيتصرفون بنزاهة وكفاءة وعدالة، ولن يستغلوا المواقف بشكل يضر بالفريق أو المؤسسة الرياضية.

2- اجراءات البحث

1-2 منهج البحث

استخدم الباحث المنهج الوصفي لملاءمته طبيعة البحث الحالي.

2-2 مجتمع البحث

اشتمل مجتمع البحث وعينته على (34) عضواً من الهيئة التدريسية في قسم التربية البدنية وعلوم الرياضة للعام الدراسي (2025-2026)، علماً أنهم يحملون شهادات وألقاب علمية مختلفة.

3-2 عينتي التطبيق والتجربة الاستطلاعية

اشتملت عينة التطبيق النهائي لمقياس الثقة التنظيمية على (30) عضواً من الهيئة التدريسية العاملين في قسم التربية البدنية وعلوم الرياضة للعام الدراسي (2025-2026)، وتمكن الباحثان من الحصول على (26) استمارة صحيحة، ويمثل هذا الرقم نسبة (86.6 %) من المجتمع الكلي. أما عينة التجربة الاستطلاعية فقد ضمت (4) أعضاء الهيئة التدريسية العاملين في قسم التربية البدنية وعلوم الرياضة.

4-2 مقياس الثقة التنظيمية

نظراً لوجود أداة تقيس متغير الثقة التنظيمية في المجال الرياضي، ولأجل أن يتمكن الباحث من تحقيق أهداف البحث، لجأ الباحث إلى مقياس الحوافز المالية والمعنوية الذي صممه (اليوزبكي 2022) كأداة لجمع البيانات من عينة البحث الحالي، اذ يتكون المقياس من

(27) فقرة تكون موزعة على **(4)** محاور تكون الاجابة وفق **(5)** بدائل هي **(موافق بشدة، موافق، غير متأكد، غير موافق، غير موافق بشدة)** وتعطي الاوزان (1,2,3,4,5) على التوالي.

2-5 الصدق الظاهري

يعرف (الجنابي، 2019) الصدق الظاهري بأنه "نوع من أنواع الصدق الذي يتم إيجاده على المظهر الخارجي للمقياس، أي أن يظهر أن المقياس يقيس الصفة أو السمة التي وضع من أجلها (الجنابي، 2019، 86). كما يذكر (الطائي والعبادي، 2018) أنه للتحقق من الصدق الظاهري للاستبيان وصلاحيته في قياس ما وضع من أجله، وبيان قدرة العبارات على تغطية الموضوع المبحوث، يتم عرض أداة الدراسة على عدد من المحكمين والمختصين في مجال عنوان البحث وتخصصه (الطائي والعبادي، 2018، 144). لذا قام الباحث بعرض الصورة الأولية للمقياس على عدد من المحكمين في تخصص الإدارة الرياضية الواردة أسمائهم في (الملحق 2) وبعد جمع وتحليل آراء السادة المختصين، تبين أن نسبة اتفاق الخبراء على صلاحية عبارات المقياس تراوحت ما بين (80 % إلى 100 %) كما اجمعوا على صلاحية نموذج بدائل الاجابة الخماسي وأوزانه.

2-6 التجربة الاستطلاعية

من أجل تشكيل صورة متكاملة عن المقياس، لجأ الباحث إلى تطبيق التجربة الاستطلاعية على عينة ضمت (4) من أعضاء الهيئة التدريسية في قسم التربية البدنية وعلوم الرياضة في كلية التربية للبنات ممن يحملون شهادات وألقاب علمية متنوعة، وقد تبين للباحث من خلال هذا الإجراء وضوح العبارات وطريقة الإجابة عليها، كما تم احتساب متوسط زمن الإجابة والذي بلغ (12) دقيقة، علماً تم تطبيق هذا الإجراء يوم الاحد الموافق 2026/8/6.

2-7 الثبات

لإيجاد معامل ثبات مقياس الثقة التنظيمية، لجأ الباحث لاستخراج معامل الثبات من خلال تطبيقه على (30) من أعضاء الهيئة التدريسية العاملين في كلية التربية البدنية وعلوم الرياضة، يوم الإثنين الموافق 2026/8/10 ومن ثم تم إعادة تطبيق الاختبار مرة ثانية يوم الأحد الموافق 2026/8/23. وبذلك تم استخراج معامل ارتباط الاختبارين لمقياس الحوافز المالية والمعنوية والبالغ (0,85).

2-8 التجربة الرئيسة

تم تطبيق التجربة الرئيسة لأداتي البحث على عينة التطبيق البالغة (30) عضواً من أعضاء الهيئة التدريسية في قسم التربية البدنية وعلوم الرياضة / كلية التربية الأساسية، وقد حصل الباحث على (26) إستمارة صالحة، علماً أن فترة تطبيق التجربة 2026/8/27 لغاية 2026/9/4.

2-9 الوسائل الإحصائية

- الوسط الحسابي.
- الانحراف المعياري.
- معامل الارتباط بيرسون.
- النسبة المئوية.

3-عرض النتائج ومناقشتها

سوف يتطرق الباحث في هذا الباب إلى عرض النتائج ومناقشتها التي وصل إليها على وفق الأهداف التي تم وضعها في الباب الأول وحسب التسلسل.

3-1 عرض نتائج الهدف الاول

اشتمل **الهدف الاول** على تكييف مقياس الثقة التنظيمية لأعضاء الهيئة التدريسية في قسم التربية البدنية وعلوم الرياضة في كلية التربية الأساسية/ جامعة الموصل، وقد تم التحقق من الهدف الثاني في مجموعة من الإجراءات العلمية المعتمدة في الباب الثالث.

2-3 عرض نتائج الهدف الثاني

التعرف على مستوى الثقة التنظيمية لدى أعضاء الهيئة التدريسية في قسم التربية البدنية وعلوم الرياضة في كلية التربية الأساسية/ جامعة الموصل.

الجدول رقم (1)

يبين الاوساط الحسابية والانحرافات المعيارية والنسب المئوية والمستويات لأبعاد الثقة التنظيمية

ت	الأبعاد	الوسط الحسابي	الإنحراف المعياري	النسبة المئوية	المستوى	التسلسل
.1	النزعة الخيرية	25.3	5,4	% 72,2	جيد	الثاني
.2	القدرة الذاتية	21,2	5,1	% 70,6	جيد	الثالث
.3	المشاعــر	28,2	6,1	% 70,5	جيد	الرابع
.4	الصـدق	21,9	4,9	% 73	جيد	الأول
.5	**الثقة التنظيمية**	96,8	19,8	71,7	**جيد**	

- يتبين من الجدول (1) حصول بعد **الصدق** على وسط حسابي (21,9) وبانحراف معياري قدره (4,9)، إذ جاء بالتسلسل الأول ضمن أبعاد الثقة التنظيمية بنسبة مئوية قدرها (73%) بمستوى إجابة **جيد**.
- يجد الباحث أن ذلك مؤشراً إيجابياً في العمل الإداري يعكس مدى القيم والمبادئ العادلة والمنصفة التي تتحلى بها إدارة القسم في التعامل مع المواقف والظروف المتنوعة التي تعاني منها بمنهج عادل دون تمييز أو تفضيل، فالصدق يعد من السلوكيات والفضائل الإنسانية التي لها انعكاسات إيجابية على نوعية الأداء داخل المؤسسة الرياضية، فهي تعزز حالة الثقة لدى الأعضاء تجاه المنظمة التي ينتمون إليها. إذ يشير (Robert and Angelo, 2001) إلى أن المدراء بحاجة إلى التركيز على ست طرائق من لبناء الثقة التنظيمية ومنها العدل، إذ يجب أن يكون المدير موضوعياً وغير منحاز وبعيداً عن التصرف بمحاباة لان هذه السلوكيات يصعب التسامح معها وتكون مدمرة بشكل كبير للثقة (Robert & Angelo, 2001, 423). كما يتطلب بناء الثقة التنظيمية إتباع عدد من الإستراتيجيات، منها الإنصاف، إذ لا يمكن للمدراء أن يكونوا منحازين وهم يأملون في بناء الثقة (David and Stanley, 1997, 229-230)
- لذا فإن الصدق أساس ثقة الناس وهو نواة مجتمع تسوده الثقة المتبادلة بين الأعضاء والإحترام والتقدير، لذا يرتفع الأداء البشري على جميع المستويات (السليفاني، 2010، 43).
- يتبين من الجدول (1) حصول بعد **النزعة الخيرية** على التسلسل الثاني ضمن أبعاد الثقة التنظيمية بنسبة مئوية بلغت (72,2%) إذ بلغ الوسط الحسابي (25,3) والإنحراف المعياري (5,4) بمستوى إجابة **جيد**.
- فالنزعة الخيرية بحسب ما يراها (الساقي، 2015) هي إمتلاك إدارة الإتحاد لنوايا إيجابية فكرية وسلوكية يمكن أن تترجم على وفق إجراءات واقعية تخدم العاملين وتدعم طموحاتهم وتتوافق مع تطلعاتهم تجاه تطوير العمل التحكيمي والتنظيمي والرياضي (الساقي، 2015، 52).
- ومن خلال النتائج في الجدول أعلاه يرى الباحث أن النزعة الخيرية تتمثل في الصفات والسلوكيات الإيجابية التي تصدر عن إدارة القسم للمواقف والأحداث التي تنشأ في المواقف الرياضية والإدارية المختلفة، اذ تعكس حالة الثقة والتعاون بين الأطراف المتفاعلة داخل الوسط الرياضي وتعبر عن مدى المساعدة والإنصاف التي يتلقاها العاملين من قبل الإدارة، ويشمل الإحسان معالي الأخلاق إطلاقاً، لأنه يشمل العفو والصفح والتسامح وإصلاح ذات البين، ويدور حول معالي الأمور (علوش، 2002، 72). كما يؤكد (Pillai, 1999) أن النزعة الخيرية تتمثل بتلك التوقعات الإيجابية الواثقة للمرؤوسين تجاه مشرفهم في العمل وفقاً للعلاقات المتبادلة بين الطرفين (Pillai, 1999, 898).
- يتبين من الجدول (1) حصول بعد **القدرة الذاتية** على مستوى إجابة **جيد**، إذ بلغت النسبة المئوية (21,2) بإنحراف معياري قدره (5,1)، لذا جاء بالتسلسل الثالث ضمن أبعاد الثقة التنظيمية بنسبة مئوية بلغت (70,6%).

- يجد الباحث أن القدرة الذاتية للقسم تتمثل بمجموعة من الكفاءات والخبرات الرياضية والإدارية التي يمكن أن يستثمرها الإتحاد بصورة صحيحة للإرتقاء بالإداء الإداري، فالإدارة الكفؤة والناجحة تستطيع إستثمار كافة الإمكانات والقدرات المتاحة لتنفيذ السياسات والإستراتيجيات في توظيف المصادر والعلاقات الرسمية وغير الرسمية كافة لصالح نجاح العمل وإلمام القائد بمكونات العمل المناطة به وخصائصه وقدرته على حل مشكلات بكفاءة يخلق الثقة لدى مرؤوسيه ويمنحه قوة التأثير فيهم، فالمرؤوس يولي إهتماماً كبيراً للمعرفة والخبرة الفنية الجيدة لدى رئيسه وقائده، ذلك لأنها تشعره بالأمان وبأن من يوجهه ويشرف عليه ويحل مشكلات ويطور أداءه إنسان ذو مهارة فنية عالية قادر على العمل بشكل جيد (العقيلي، 1996، 382-383).
- يتبين من الجدول (1) حصول بعد **المشاعر** على التسلسل الأخير ضمن أبعاد الثقة التنظيمية، إذ كان الوسط الحسابي (28,2) والإنحراف المعياري (6,1)، جاء بمستوى إجابة **جيد** وبنسبة مئوية (70,5).
- يجد الباحث أنه على الرغم من حصول بعد المشاعر على التسلسل الأخير ضمن أبعاد مقياس الثقة التنظيمية ولكن بفارق بسيط عن بقية الأبعاد، فلتلك النتيجة مردودات إيجابية على واقع العمل في المؤسسة الأكاديمية، إذ أنها تعد دافعاً إيجابياً تدفع بالعاملين على تنفيذ الواجبات والمهام من دون ملل أو تقصير، فالرياضيون يمتلكون قدرات ومهارات بدنية وعقلية تتفاوت من شخص لأخر، لذا يتطلب من الإدارة حتى تنجح في مهامها، توظيف هذا المفهوم بصورة صحيحة في إختيار الوقت والطريقة المناسبين في التعامل مع هذه الشريحة لكسب ثقتهم وتحقيق حالة من الإستقرار النفسي مما يجعلهم مؤمنين بأهداف وسياسات الإتحاد ويعملون على صيانتها والحفاظ عليها.
- ويؤكد (الحسني، 1986) أن الرياضيون يختلفون فيما بينهم إذ قدراتهم وإستعداداتهم العقلية والجسمية، يوجد مستويان أو ثلاثة مستويات من الرياضيين من ناحية إستيعابهم وقدراتهم على الأداء، فلذلك تكون مهمة العاملين أو المدرب إختيار ما يناسب جميع المستويات مراعياً في ذلك الفروق الفردية بين الرياضيين (الحسني، 1986، 46). فالمشاعر هي مجموعة من المهارات العاطفية التي تختلف من شخص لأخر، والشخص الذي لا يعرف قوة مشاعره لا يمكنه التنبؤ بمدى تأثيرها في نفسه والآخرين من حوله(إبراهيم، 2001، 90-91).

4 – الاستنتاجات والتوصيات

4-1 الاستنتاجات

4-1-1 فاعلية مقياس الثقة التنظيمية لأعضاء الهيئة التدريسية في قسم التربية البدنية وعلوم الرياضة في كلية التربية الأساسية/ جامعة الموصل.

4-1-2 حصول بعد الصدق على اعلى نسبة يليه بقية الابعاد الخاصة بالاستبانة.

4-2 التوصيات

4-2-1 اعتماد مقياس الثقة التنظيمية بشكل دوري لتقييم درجة ثقة أعضاء الهيئة التدريسية في قسم التربية البدنية وعلوم الرياضة في كلية التربية الأساسية/ جامعة الموصل بالقيادة الخاصة بالقسم.

المصادر العربية:

1. إبراهيم، يحيى عبدالحميد (2001): التحديات الإدارية وإعداد قيادات المستقبل، دار التوزيع والنشر الإسلامية، السيدة زينب، القاهرة، مصر.
2. الجليحاوي، صلاح وهاب شاكر (2013): المبادئ الإدارية لطلاب التربية الرياضية، الأيك للطباعة والنشر والتوزيع، بغداد، العراق.
3. خضر، أحمد ادريس محمد (2022): الثقة التنظيمية لرؤساء المنظمات الرياضية في محافظة نينوى من وجهة نظر أعضاء هيئاتها الإدارية، بحث منشور، مجلة الرافدين للعلوم الرياضية، المجلد (25)، العدد (77)، جامعة الموصل، العراق.
4. الخطيب، أحمد ومعايعة، عادل سالم (2009): الإدارة الحديثة نظريات واستراتيجيات ونماذج حديثة، عالم الكتب الحديث للنشر والتوزيع، أربد، الأردن.
5. الراوي، إبراهيم يونس وهمام، وليد خالد (2019): مفاهيم في الإدارة الرياضية الحديثة، ط1، دار نون للطباعة والنشر والتوزيع، العراق.

6. الزهراني، أحمد (2012): الثقة التنظيمية لدى مديري المدارس الثانوية بالطائف وعلاقتها بالسلوك الإداري الإبداعي، رسالة ماجستير غير منشورة، قسم الإدارة التربوية والتخطيط، كلية التربية، جامعة ام القرى، مكة المكرمة.
7. الساعدي، مؤيد يوسف نعمة (2002): بناء مقياس الثقة بالآخرين، بحث منشور، مجلة العلوم الاقتصادية والإدارية، المجلد 9، العدد 31، كلية الإدارة والاقتصاد، جامعة بغداد.
8. الساقي، أحمد رعد إبراهيم (2015): سياسات الاتحاد العراقي المركزي لإدارة الضغوط المهنية ودورها في الثقة التنظيمية لحكام كرة السلة، أطروحة دكتوراه غير منشورة، كلية التربية البدنية وعلوم الرياضة، جامعة الموصل.
9. السكارنة، بلال (2010): القيادة الإدارية الفعالة، ط1، دار المسيرة للنشر والتوزيع والطباعة، عمان، الأردن.
10. السليفاني، نزار محمد علي (2010): الثقة التنظيمية ودورها في تعزيز سلوك المواطنة التنظيمية دراسة لآراء عينة من العاملين في دار ابن الأثير للطباعة والنشر/ جامعة الموصل، رسالة ماجستير غير منشورة، كلية الادارة والاقتصاد، جامعة الموصل.
11. شاكر، صلاح وهاب (2013): المبادئ الإدارية لطلاب التربية الرياضية، ط1، الأيك للطباعة والنشر والتوزيع، بغداد، العراق.
12. الشتوي، سلمان (2016): القيادة الأخلاقية القوة الناعمة، مجلة التدريب والتنمية، الرابط الإلكتروني http://tra-dev.info
13. الشكرجي، أسماء طه نوري (2008): اثر العدالة التنظيمية والثقة التنظيمية في الإحتراق النفسي للعاملين، رسالة دكتوراه غير منشورة، كلية الإدارة والاقتصاد، جامعة بغداد.
14. الشملان، خالد بن عبد العزيز حمد (2016): دور سلوكيات القيادة الأخلاقية في تعزيز فعالية الإرشاد الأكاديمي دراسة مقارنة، بحث منشور، مجلة كلية التربية، المجلد (27)، العدد (106)، جامعة بنها، مصر.
15. الطائي، رنا ناصر صبر (2007): الأنماط القيادية والثقة التنظيمية وأثرها في تحقيق الالتزام التنظيمي، رسالة ماجستير غير منشورة، كلية الإدارة والاقتصاد، جامعة بغداد.
16. الطائي، نور محمد جاسم (2020): الثقة التنظيمية بإدارة مسابح مدينة الموصل على وفق الكفايات التعليمية لمدرباتهم من وجهة نظر متعلمات السباحة، رسالة ماجستير غير منشورة، قسم التربية البدنية وعلوم الرياضة، كلية التربية الأساسية، جامعة الموصل.
17. العقيلي، عمر وصفي (1996): الادارة اصول واسس ومفاهيم، دار زهران للنشر والتوزيع، عمان، الاردن.
18. العنزي، سعد والساعدي، مؤيد يوسف نعمة (2004): الثقة بين الإطار الشخصي لها والمفهوم التنظيمي الحديث، المجلة العراقية للعلوم الإدارية، المجلد 2، العدد 5، جامعة كربلاء.
19. عودة، أحمد سليمان (1999): القياس والتقويم في العملية التدريسية، جامعة اليرموك، الأردن.
20. عويس، خير الدين علي أحمد (1999): دليل البحث العلمي، دار الفكر للطباعة والنشر، القاهرة.
21. فتحي، محمد (2003): 766 مصطلح إداري إيضاح وبيان، دار التوزيع والنشر الإسلامية، السيدة زينب، القاهرة، مصر.
22. الميداني، عبد الرحمن حسن حنبكة (1987): الأخلاق الإسلامية وأسسها، ط2، ج1، دار القلم للطباعة والنشر والتوزيع، دمشق، سوريا.
23. نجم، نجيب عبد المجيد وكريم، خوله صدر الدين (2014): دور الثقة التنظيمية في تعزيز سلوك المواطنة التنظيمية دراسة تشخيصية تحليلية لأراء عينة من العاملين في مديرية بلدية كركوك، مجلة آداب الفراهيدي، العدد 19، المعهد التقني، الحويجة.
24. Kalleberg, A; Appelbaum, E.; Sleigh, S. and Schmitt, j. (2004): For better or worse: union and citizenshipbehaviors. Paper Presented at Industrial.
25. Pillai ,Chnechiem ,C.A., and Williams , E.C.,(1999) , Fairness Perceptions and Trust as Mediator for Transformational and Transactional Leadership Atwo Sample Study, Journal of Management. Vol.25, No.6..
26. Robert, Kreitner & Angelo, Kinicki, (2001), Organizational Behavior, 5th ed., New York, San Francisco.
27. Spector, M. D., & Jones, G. E., (2004), Trust in the Workplace: Factors Affecting Trust Formation between Team Members, Journal of Social Psychology, Vol. 144, No. 3.
28. Straiter, K. L., (2005), The Effects of Supervisor's Trust of Subordinates and Their Organizations on Job Satisfaction and Organizational Commitment, International Journal of Leadership Studies, Vol. 13, No. 1.

ملحق (1)

جامعة الموصل
كلية التربية الأساسية
قسم التربية البدنية وعلوم الرياضة

مقياس الثقة التنظيمية

تحية طيبة..

يروم الباحث إجراء البحث الموسوم بـ **(تقييم مستوى الثقة التنظيمية لقسم التربية البدنية وعلوم الرياضة من جهة نظر أعضاء الهيئة التدريسية)** ولتحقيق أهداف البحث يضع الباحث بين أيديكم مقياس الثقة التنظيمية المعد من (اليوزبكي، 2022) راجياً من جنابكم الكريم الإطلاع على فقرات المقياس وقراءتها بدقة وعناية، والإجابة عن فقراته وذلك بوضع علامة **(√)** أمام العبارة وتحت البديل الذي تراه مناسباً.

الثقة التنظيمية "هي توقعات ومعتقدات ومشاعر إيجابية يحملها الأفراد تجاه المنظمة التي ينتمون إليها، والمرتبطة بالممارسات والسلوكيات الإدارية المطبقة، والتي روعي فيها الإلتزام بالقيم الأخلاقية العامة والإدارية الخاصة، والإبتعاد عن كل ما يضر بالمصالح المشتركة".

وتقبلوا مني فائق الشكر والإحترام..

التوقيع:
التحصيل الدراسي:
اللقب العلمي:
التخصص العلمي:
التاريخ:

ت	الفقرة	موافق بشدة	موافق	محايد	غير موافق	غير موافق بشدة
.1	يعتمد القسم أساليب فاعلة تجاه القضايا التي تخصه.					
.2	يلتزم القسم بالإيفاء بوعوده ذات الشأن بالقسم.					
.3	يحاول القسم إشراك الأعضاء ببعض القضايا التي تتعلق بأعمالهم.					
.4	يتمكن القسم من دعم بعض أهدافه في مختلف الظروف.					
.5	يتبنى القسم سياسات إدارية واضحة فيما يخص عمله.					
.6	يطبق القسم الأفكار الإبداعية التي تطرح من قبل الأعضاء.					
.7	يؤمن القسم المعلومات المطلوبة للأعضاء عند الحاجة ويزودهم بها في الوقت المناسب.					
.8	يجيد القسم توظيف العلاقات غير الرسمية في ميدان عمله.					
.9	يتبنى القسم قرارات ذات أهمية تخص تطوير برامجه وأهدافه الأكاديمية والرياضية.					
.10	يثق القسم بقدرة الأعضاء على تفهم متطلبات عملهم وتنفيذها.					
.11	يمتلك القسم القدرة على تحمل المسؤوليات وحل المشكلات التي تحدث.					
.12	يعمل القسم على تنمية قدراته الذاتية لتلبية إحتياجات ومتطلبات سوق العمل.					
.13	يستطيع القسم إيجاد أرضية مشتركة بين الأقسام المناظرة.					
.14	يقوم القسم بمناقشة المشكلات والعمل على حلها.					
.15	يكشف القسم عن نتائج تقييم الأداء للأعضاء بشفافية.					
.16	يركز القسم على تأمين العدالة بين الأعضاء.					
.17	يستثمر القسم طاقات الأعضاء على نحو أفضل.					
.18	يبدي القسم إهتماماً جدياً في فهم وجهة نظر الأعضاء التي تتعلق بالعمل.					
.19	يستحضر القسم إمكانات الأعضاء عند وجود الحاجة إليها.					
.20	يهتم القسم بالحفاظ على أسرار عمل الأعضاء.					
.21	يحرص القسم على متابعة تنفيذ القرارات.					
.22	يقدم القسم الحقائق للأعضاء.					
.23	يتعامل القسم بصدق بعيداً عن التحيز مع الأعضاء.					
.24	يساعد القسم الأعضاء على تجاوز الأزمات في العمل.					
.25	يعمل القسم على خدمة مصالح الأعضاء والكلية.					
.26	يسمح القسم بمشاركة الأعضاء لتقديم أفكار بناءة.					
.27	يكيف القسم أهدافه وقراراته على وفق التغيرات البيئية.					

ملحق رقم (2)

أسماء السادة الخبراء والمختصين

ت	الأسم	التخصص العلمي	مكان العمل
.1	ا.د وليد خالد همام النعمة	إدارة وتنظيم	جامعة الموصل / كلية التربية الأساسية قسم التربية البدنية وعلوم الرياضة
.2	أ.د ثابت إحسان أحمد	إدارة وتنظيم	جامعة الموصل / كلية التربية للبنات قسم التربية البدنية وعلوم الرياضة
.3	أ.م.د محمد خالد أحمد	إدارة وتنظيم	جامعة الموصل / كلية التربية الأساسية قسم التربية البدنية وعلوم الرياضة
.4	أ.م.د ياسر بازل محمد	إدارة وتنظيم	جامعة الموصل / كلية التربية الأساسية قسم التربية البدنية وعلوم الرياضة
.5	أ.م.د منتصر معيوف ذنون	إدارة وتنظيم	جامعة الموصل / كلية التربية البدنية وعلوم الرياضة